Czech Technical University in Prague

Faculty of Electrical Engineering

Doctoral Thesis

October 2020 *Ing. Pavel Karlovský*

Czech Technical University in Prague

Faculty of Electrical Engineering
Department of Electric Drives and Traction

SENSORLESS PREDICTIVE CONTROL OF INDUCTION MOTOR DRIVE

Doctoral Thesis

Ing. Pavel Karlovský

Prague, October 2020

Ph.D. Programme: Electrical Engineering and Information Technology, P2612
Branch of study: Electric Machines, Apparatus and Drives, 2642V004

Supervisor: Prof. Ing. Jiří Lettl, CSc

Declaration

I hereby declare that I have written my doctoral thesis on my own and I have used only the literature listed at the end of the doctoral thesis in the references.

……………………………………….

Pavel Karlovský

Acknowledgement

This thesis is the result of my Ph.D. studies at the Department of Electric Drives and Traction, Faculty of Electrical Engineering, Czech Technical University in Prague. They provided me with support, equipment and help. The submitted work was also partly supported by the internal student grants of the CTU in Prague.

I would like to give my thanks to my colleagues, who helped me during my study at the university, and created a pleasant atmosphere at the department. Namely, they are Ing. Ondřej Lipčák, Ing. Jan Bauer, Ph.D., Ing. Bc. Pavel Kobrle, Ph.D., Ing. Jakub Zedník, Ing. Petr Pichlík, Ph.D., Ing. Filipp Frolov, Ing. Pavel Skarolek and Ing. Tomáš Košťál.

Further, I would like to thank my supervisor, prof. Ing. Jiří Lettl, CSc, for his support, guidance, and the advices he gave me during my Ph.D. studies.

Finally, I would like to express my gratitude to my parents, my family, my close friends, and my girlfriend for their care and support.

Abstract

The electric drives nowadays consume a significant part of the world's electric energy, so power savings are an important aspect. Most of the high-power drives are realized with AC motors. The speed and torque control of an AC drive is a sophisticated topic, for which many strategies were developed. However, the increased torque and current ripple represent the drawbacks of many control strategies. A model predictive control is a new control method in the area of electric drives. Such control enables the optimization of multiple selected parameters at once. The thesis deals with the model predictive control, and its possibility of decreasing the torque and current ripples, and machine's energy losses. The proposed solution lies within the DC-link voltage optimization of induction motor drive fed from the voltage-source inverter.

The thesis first describes the model of the IM, principles of the most popular methods for the sensorless speed determination, and the IM drive control.

Then, it deals with predictive control. Its classification is provided, and the main characteristics are described. The predictive torque control method is selected for further examination. Since this method shares many properties with the direct torque control method, a comparison of these two methods is performed. The comparison is based on the switching patterns of the transistors. It explains the reasons for the lower torque ripple of the predictive torque control. The possibilities of further torque and current ripples decreases within the predictive control method are then analyzed.

Then, the influence of the DC-link voltage on the torque and current waveforms is analyzed, and the derivation of its limits is performed. Based on the analysis, a method optimizing the DC-link voltage is proposed and designed. The optimization method uses the model predictive control principle, and by using the DC-link voltage adjustment it aims to lower the torque and flux error compared to their respective references. Finally, its integration into the predictive torque control method is provided.

The last part is dedicated to the simulation and experimental verifications of the proposed voltage optimization. The simulations are carried out on a mathematical model of IM drive in the Matlab Simulink environment. The experiments are performed on a laboratory IM drive of 5.5 kW output power that is controlled by means of the dSpace platform. Since the optimization method requires an active rectifier, a thyristor bridge rectifier is utilized instead of a conventional diode rectifier. In many applications, the speed sensor elimination is often required, so the experiments are performed with, as well as without the speed sensor. The gained simulation and experimental results confirm the benefits of the predictive torque control with the proposed DC-link voltage optimization in terms of lower torque ripple, lower current THD, and lower machine losses.

Keywords

Induction Motor, Variable Frequency Drive, Sensorless Control, Predictive Torque Control, DC-Link Voltage Optimization

Abstrakt

Významný podíl světové elektrické energie v dnešní době spotřebovávají elektrické pohony. Úspora elektrické energie je tedy v této oblasti důležitým aspektem. Většina velkých elektrických pohonů využívá střídavé motory. Řízení otáček a momentu takového pohonu představuje velmi sofistikovaný úkol a pro jeho splnění bylo vyvinuto mnoho strategií. Často se vyskytujícím nepříznivým jevem je zvýšené zvlnění výstupního momentu a fázových proudů. Prediktivní řízení představuje v oblasti řízení elektrických pohonů jednu z nových metod. Toto řízení umožňuje současnou optimalizaci více sledovaných parametrů. Tímto způsobem řízení a možnostmi snižování zvlnění momentu, proudů a redukcí ztrát v motoru se zabývá předkládaná dizertační práce. Navrhované řešení spočívá v optimalizaci velikosti napětí ve stejnosměrném meziobvodu napájecího nepřímého měniče kmitočtu.

V práci je popsán použitý model asynchronního motoru, základní principy bezsenzorového zjišťování otáček a nejčastěji používaných metod řízení.

Dalším tématem práce je prediktivní řízení. Je uvedena základní klasifikace typů prediktivního řízení a jejich hlavní vlastnosti. Jako stěžejní je vybrána metoda prediktivního řízení momentu. Vzhledem k podobnosti vybrané metody s metodou přímého řízení momentu je provedeno porovnání obou metod, které je založeno na rozboru spínacích sekvencí střídače. Je vysvětlen důvod nižšího zvlnění momentu v případě prediktivního řízení. Následně jsou rozebrány další možnosti snižování zvlnění momentu a proudu pomocí predikce.

V další kapitole je odvozen vliv velikosti napětí ve stejnosměrném meziobvodu na průběh momentu a proudu a jsou stanoveny limitní hodnoty tohoto napětí. Na principu prediktivní regulace je navržena optimalizační metoda velikosti napětí v meziobvodu minimalizující odchylky momentu a toku od svých referenčních hodnot. Je popsán způsob integrace metody do prediktivního řízení momentu.

Poslední část práce je věnována simulačnímu a experimentálnímu ověření navržené optimalizační metody. Simulace jsou provedeny na matematickém modelu pohonu v prostředí Matlab Simulink. Experiment je realizován na laboratorním pohonu s asynchronním motorem o výkonu 5.5 kW, řízeném pomocí platformy dSpace. Potřeba aktivního usměrňovače si vyžádala nasazení tyristorového můstkového usměrňovače místo klasického diodového usměrňovače. Častým požadavkem v mnoha aplikacích je provoz bez otáčkového čidla, a proto je experimentální ověření realizováno jak s čidlem otáček, tak bez něj. Simulační i experimentální výsledky prokázaly nižší zvlnění průběhu momentu, nižší THD fázových proudů i nižší ztráty v motoru při řízení pohonu s navrženou napěťovou optimalizací.

Klíčová slova

asynchronní motor, pohon s frekvenčním řízením, bezsenzorové řízení, prediktivní řízení momentu, optimalizace napětí ve stejnosměrném meziobvodu

List of Content

List of Figures

List of Tables

Abbreviations

AC	alternating current
ADC	analog digital converter
AFE	active front end
BEMF-MRAS	back electromotive force model reference adaptive systems
CAN	controller area network
CB-MRAS	current based model reference adaptive systems
CEITEC	Central European Institute of Technology
CS-MPC	continuous set model predictive control
CTU	Czech Technical University
DAC	digital analog converter
DC	direct current
DSP	digital signal processor
DTC	direct torque control
ECPE	European Center for Power Electronics
EKF	Extended Kalman filter
FEE	Faculty of Electrical Engineering
FFT	fast Fourier transform
FOC	field-oriented control
FPGA	field-programmable gate array
FS-MPC	finite set model predictive control
GUI	graphical user interface
HVDC	high voltage direct current
IEC	International Electrotechnical Commission
IEEE	Institute of Electrical and Electronics Engineers
IGBT	insulated gate bipolar transistor
IM	induction motor
KF	Kalman filter
LO	Luenberger observer
MPC	model predictive control
MRAS	model reference adaptive systems
PCC	predictive current control
PFC	power factor correction
PI	proportional integral
PID	proportional integral derivative
PMSM	permanent magnet synchronous motor
PTC	predictive torque control
PWM	pulse width modulation
RF-MRAS	rotor flux model reference adaptive systems
RICE	Regional innovation centre for electrical engineering
RMS	root mean square
RP-MRAS	reactive power model reference adaptive systems
SCR	silicon controlled rectifier
SG	synchronous generator
SM-MRAS	sliding mode model reference adaptive systems

SVM	space vector modulation
THD	total harmonic distortion
UPS	uninterruptible power supply
VSI	voltage source inverter
WoS	Web of Science

Nomenclature

$\boldsymbol{\psi_1}, \boldsymbol{\psi_2}$	Stator and rotor flux linkage vectors
$\boldsymbol{v_1}$	Stator voltage vector
$\boldsymbol{i}_1, \boldsymbol{i}_2, \boldsymbol{i}_\mathrm{m}$	Stator, rotor, and magnetizing current vectors
R_1, R_2	Stator and rotor resistances
L_1, L_2, L_m	Stator, rotor, and magnetizing inductances
$T, T_\mathrm{e}, T_\mathrm{L}$	Torque, developed torque, and load torques
p_p	Number of pole pairs
J	Moment of inertia
$\mathbf{A}, \mathbf{B}, \mathbf{C}, \mathbf{D}$	System, input, output, and feedback matrices
$\mathbf{I}, \mathbf{0}$	Identity and zero matrices
$\omega, \omega_\mathrm{r}, \omega_\mathrm{s}, \omega_\mathrm{sl}$	Mechanical, electrical, synchronous, and slip rotational speeds
ω_k	Rotational speed in a general coordinate system
$\boldsymbol{u}, \boldsymbol{x}, \boldsymbol{y}$	System input, state, and output vectors
t	Time
$\mathbf{L}$	Observer correction matrix
$l_1 \ldots l_4$	Gains of the observer correction matrix
l	Observer correction constant
e	Error
$K_\mathrm{p}, K_\mathrm{I}$	Proportional and integral gains of the PI controller
$\mathbf{F}, \mathbf{H}$	State and output matrices of Kalman filter
$\mathbf{K}$	Kalman gain
$\mathbf{P}, \mathbf{Q}, \mathbf{R}$	Covariance, state noise, and output noise matrices
f	Frequency
k	Discrete time sample
$\tau_\mathrm{s}, \tau_\mathrm{r}$	Stator and rotor time constants
R_1', L_1', k_r	Recalculated motor parameters
$\sigma, L_\sigma, R_\sigma, \tau_\sigma$	Leakage factor and recalculated constants
j	Imaginary unit
g	Cost function
g_DN	Cost function demand
V_DC	DC-link voltage
T_s	Sampling time
$\mathrm{V0} \ldots \mathrm{V7}$	Voltage vectors
$\mathrm{S1} \ldots \mathrm{S6}$	Flux sectors
P, Q	Active and reactive power
$k_\mathrm{DC}, k_\mathrm{th}, k_\mathrm{crit}, k_\mathrm{opt}$	Coefficients of DC-link decrease, threshold, critical, and optimum values
$\boldsymbol{c}_\mathrm{sw}$	Vectors corresponding to the switching state
$\Im$	Imaginary part
Δ	Difference
$\gamma, \delta, \varepsilon$	Angles of the stator voltage, current, and flux
φ, ϑ, ξ	Angles between the voltage and current, current and stator flux, and voltage and rotor flux vectors
$C_1 \ldots C_8$	Coefficients with IM parameters
v_1fw	Magnitude of the fundamental voltage waveform

n	Number of the considered candidate
$k_{\mathrm{CF}}, k_I, k_F, k_{\mathrm{v}}$	Cost function’s weighting factors
P_0	Input power
$P_{\mathrm{c}}, P_{\mathrm{mech}}, P_{\mathrm{Fe}}, P_{\mathrm{Cu}}$	Constant, mechanical, iron, and copper, losses
$\times$	Cross product
x'	Denotes the reduced voltage
x^*	Denotes the reference
$\bar{x}$	Complex conjugate vector
$\hat{x}$	Estimated variable
$\dot{x}$	Derivation of the variable
x_{k}	Denotes the voltage optimization
x_α, x_β	Links to the respective component of the variable in the stationary coordinates
x_d, x_q	Links to the respective component of the variable in the rotating coordinates

1. Introduction

The drives with electric motors nowadays consume a significant part of the world's electric energy. Therefore, energy-savings in this area are a big challenge among researchers. Two types of electric motors are distinguished, DC (direct current) and AC (alternating current) motors. The advantage of DC motors against AC motors lies within the torque and speed control simplicity. The torque of the DC motor can be easily controlled by the current and the speed by the applied DC voltage. Modern drives usually rely on AC motors, mainly induction or synchronous. The control of the torque and speed is a much more complicated task within AC motors, from both the hardware and the software perspective. Moreover, the wide speed range control, including very low and very high speed areas as well as fast transients, are often required. In specific applications, other requirements, such as high efficiency, online fault diagnostics, or sensorless operation, may be demanded. The traditional scalar control is not sufficient for these requirements. In such cases, the field-oriented control or direct torque control are usually utilized. Both of them are now standards in industrial applications, and both utilize the drive near the maximum reachable efficiency.

A different approach is the model predictive control (MPC). However, in the area of power electronics, this approach was not gaining much publicity among researchers or companies for a long time. This changed around the year 2000. Since then, a number of MPC publications related to power electronics started to increase exponentially in the IEEE (Institute of Electrical and Electronics Engineers) Xplore database and reached about 550 new publications in the year 2019. This increase is depicted in Fig. 1.

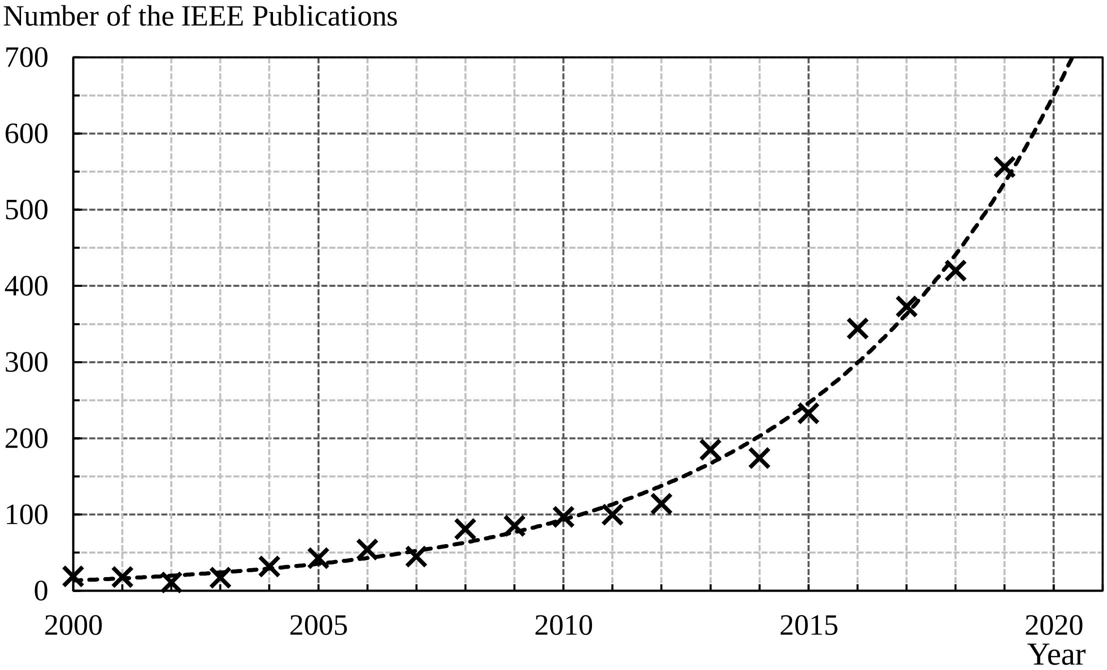

Fig. 1. Number of publications in IEEE Xplore related to MPC applications in power electronics.

Recently, many applications of power electronics utilizing MPC have been developed, particularly in the control of electric drives [1]. Beside it, other important MPC applications including active front-end rectifier (AFE) [2], uninterruptible power supply (UPS) [3], high voltage DC transmission system (HVDC) [4], matrix converter [5], StatCom systems [6] or DC-DC converter [7] have been deployed.

Therefore, much work has been done in the area of MPC of power electronics, and further progress is possible mainly within the small improvements. One of these small improvements may be found, among others, in the DC-link voltage optimization, which is one of the thesis topics.

1.1. Motivation

One of the focuses of the Department of Electric Drives and Traction of Faculty of Electrical Engineering (FEE) Czech Technical University (CTU) in Prague, is the control of electric drives. During my master's study at the Department, I was interested in the progress of modern AC drives control, and I even dealt with the IM (induction machine) drive control in my master thesis.

The development of model predictive control is moving forward very quickly. Compared to conventional control algorithms, predictive control methods have many advantages. First of all, their concept is much easier to understand. If the system is known, the predictive control can be easily applied to the system control, and even the system nonlinearities can be considered in the predictive model. Moreover, multivariable control with constraints can be included by means of the so-called cost functions. On the other hand, the computational requirement is the disadvantage of this approach. However, modern fast microcontrollers enable its implementation. Another disadvantage may arise from the complexity of the cost function if multivariable control is required.

In the case of a variable speed drives, the AC motors are usually powered from a frequency converter. The converter consists of a rectifier, voltage DC-link, and VSI (voltage-source inverter). The conventional approach uses an uncontrolled rectifier. It means that the full voltage is present in the DC-link. That is required to reach the AC motor nominal power. However, in other operating points, the lower DC-link voltage may be sufficient and more beneficial. The lower DC-link voltage reduces negative features from the point of inverter and motor losses and motor insulation stress.

Therefore, it was a very interesting topic for me to investigate the DC-link voltage optimization possibilities of electric drive predictive control strategies. Mainly, I chose to focus put an emphasis on the torque and current waveforms improvement because the torque ripple and current THD (total harmonic distortion) are the main problems of the commonly utilized control methods. In the thesis, the integration of the DC-link voltage optimization into the predictive control strategy of the IM drive is the subject of interest.

1.2. State of Art

The control of variable speed IM drives has developed rapidly in recent years. The two main approaches are nowadays the field-oriented control (FOC) and direct torque control (DTC) [8]. The FOC is a very common control method among variable frequency drives of a higher power. The method originates in Germany in the year 1972 [9]. It uses the transformation of quantities into rotational coordinates and separates the current vector into two components, which are then separately regulated. The control method is fast and precise. However, the topology contains controllers in cascades (which need to be appropriately tuned), multiple mathematical transformations, and precise knowledge of the motor parameters to achieve proper alignment of the d-axis. DTC is another modern control method. It was simultaneously developed in Germany and Japan in 1986 [10], [11]. It brings simple control loops containing hysteresis controllers with fast dynamic responses. However, it is dependent on the sampling period, the switching frequency is not constant, and high torque and current waveforms ripples are introduced. The high-frequency torque components can cause problems in applications where the smooth torque waveform is demanded. The comparison between FOC and DTC is a common topic among researchers [8].

Another modern control strategy of AC drive is model predictive control (MPC). The MPC concept is used in many industrial applications [12]. It was first used in the chemical industry, i.e., petrochemical plants, where it still plays an important role [12], [13]. At that time, only a few attempts within the predictive control of electric drives were realized in the field of electric drives [14], [15], [16]. The further usage of MPC in the AC drive area was not possible for a long time; it started becoming popular recently thanks to modern fast microcontrollers with sufficient computational power [17], [18]. Two main types of MPC can be distinguished: the continuous set MPC (CS-MPC) and the finite set MPC (FS-MPC) [19], [20]. In the case of the basic implementation of FS-MPC with a two-level inverter, only the eight fundamentals voltage vectors are considered as the feasible candidates. Therefore, the modulator can be omitted. The system outputs are predicted only for a limited number of possible inputs, which makes the searching for the optimal voltage vector simpler. Usually, the control variables are the developed torque and stator flux amplitude. This type of control is called predictive torque control (PTC) and reminds the DTC because the same variables are controlled, and no modulator is used [21]. Sometimes, the combination of both algorithms is utilized [22]. Another common implementation of FS-MPC chooses the stator current as the control variable. The stator current vector is divided into two components utilizing the coordinate transformation. Those components are then separately regulated. This approach is called predictive current control (PCC) and is similar to the FOC [23], [24]. In the case of CS-MPC, the infinite number of voltage vectors is considered as the feasible inputs. The search for the optimal voltage vector is then a more challenging task and requires advanced mathematical operations. With the two-level inverter, the feasible voltage vectors are limited by the amplitude of the DC-link voltage only. The final voltage vector is then applied through a PWM (pulse width modulation) modulator [20]. The most common implementation of CS-MPC is PCC. The performance of these strategies has been analyzed and compared by many authors [25], [26], [27]. In the case of IM drive with a two-level inverter, the most often examined predictive method is PTC, which is also the subject of this thesis.

Since the PTC has some control ideas analogical with the DTC, they share some disadvantages as well. One of them is the higher torque waveform ripple and high current THD. Similarly, as in the case of the conventional DTC, many methods for suppressing this disadvantage were proposed in the literature so far. The easiest way is to decrease the sampling time, which reduces the waveform ripple, but, on the other hand, it increases the switching frequency [28]. This is not admissible in many applications, especially in high-power applications, where the low switching frequency is required since the semiconductor's cooling is the limiting factor. Another source of undesired waveform ripple is the model parameters mismatch. This problem can be eliminated by offline or online parameter identification [29]. Another approach lies in the MPC cost function design. The cost function is a specific set of rules that evaluate the effects of all candidates. Usually, it is expressed as an equation. The cost function determines the behavior of the whole drive, and its design can optimize many parameters at the same time, for instance, the switching frequency [19]. Further, it can shape the harmonic spectrum [30] of the selected quantities or even suppress the motor acoustic noise [31]. By the cost function design, the further ripple reduction [32] can be achieved.

In the case of two-level VSI, there are eight fundamental switching combinations creating eight input candidates that are to be considered by the PTC. If the set of generable voltage vectors is increased, the smoother waveforms control is reachable. This can be achieved by modulation techniques such as space vector modulation (SVM) [33]. However, this leads to a higher switching frequency and increases the microcontroller's computational burden. With the hardware modification, more feasible voltage vector candidates can be achieved by a multi-level inverter [34], [35], or a matrix converter [5]. Both of them share the advantage that the switching frequency does not rise on the contrary to the SVM. However, a greater number of basic voltage vectors are available at the price of higher costs. Another important aspect of MPC is the prediction horizon choice [36]. Then, the cost function can be designed to follow the reference trajectory during more sample times rather than within the next step only [37]. However, in the case of the examined system, only a small improvement is achieved by a prolonged prediction horizon. It could be beneficial mainly at very small switching frequencies [38]. Moreover, its price is the very high computational burden since the number of candidates increases exponentially with the prediction horizon number. An interesting approach to reduce the current and torque ripples is to decrease the virtual amplitude of the basic voltage vector by utilizing modulation techniques [39]. Literature [40] proposes optimal duty cycle control at which the passive voltage vector is applied after the selected voltage vector within one sampling time. The time durations of the selected and passive voltage vectors are based on the deadbeat torque control principle. Such an approach virtually decreases the amplitude of the applied vector. To reach the same effect, literature [41] proposes a similar approach. However, the calculation of the selected voltage vector time duration is managed by another cost function, the so-called tracking cost index.

In the case of predictive control of electric drives, the prediction of control variables requires the knowledge of the rotational speed. The conventional approach employing a speed sensor suffers from several issues. The encoder increases hardware complexity, and it is vulnerable to harsh environmental conditions. To overcome this problem, an encoderless (often called sensorless) solution may be desired. Most common sensorless methods linked with predictive control are model reference adaptive systems (MRAS) [42], observers [43], [44], [45], [46] and Kalman filters [47]. An interesting approach lies within implementing prediction into sensorless speed determination [48].

The world's research on the predictive control of AC drives is nowadays conducted mainly by the academic sphere. The best research is conducted in multiple universities around the world. One of the most famous is University Andres Bello in Chile, where Jose Rodriguez [1], [3], [12], [13], [17], [19] published hundreds of scientific papers indexed in IEEE, and wrote multiple books. Also, in Chile, Patricio Cortes [2], [3], [19], [30] from Technical University Federico Santa Maria is cooperating with Jose Rodriguez. Another well-known research university is located in Germany at Technical University Munich, where many publications arisen within the team led by professor Ralph Kennel [16], [17], [23], [37], [46]. Other great personalities in MPC of electric drives research are Sergio Vazquez [1], [3], [18] from University Sevilla in Spain, Fengxiang Wang [17], [24], [25], [26], [42] from Chinese Academy of Sciences, Zhenbin Zhang [25], [43], [49] from Shandong University in China, Petros Karamanakos [38], [50], [51], [52] from Tampere University in Finland, Daniel Quevedo [2], [30], [36] from the Queensland University of Technology in Australia and Marian Kazmierkowski [13], [53] from Warsaw University of Technology in Poland.

European Center for Power Electronics (ECPE) [54], of which CTU in Prague is a member, has recently experienced an increasing interest in this topic. The ECPE workshops and tutorials concerning MPC in power electronics are being held from the year 2016. In 2011, in München, Germany, Workshop on Predictive Control of Electrical Drives and Power Electronics (PRECEDE) [55] was organized for the first time. The second event was a joint event with the IEEE International Symposium on Sensorless Control for Electrical Drives (SLED) in 2013 [56], and in 2015 became a separate biannual conference under IEEE. In that year, it was held in Pilsen, Czech Republic, at the University of West Bohemia.

Besides the universities, some private companies are also participating in this research. A good example is ABB corporation [57] in Switzerland, where Tobias Geyer [36], [38], [58] is not only publishing results of his research but is also presenting the company's implementation of model predictive control in real applications. Their most significant achievement in the MPC implementation on a real drive is the control of large compressors (up to 50 MW) for natural gas long pipelines [59].

In the Czech Republic, few universities deal with predictive control. It is mainly the University of West Bohemia, where the Regional Innovational Centre for Electrical Engineering (RICE) was established. Among other topics, it deals with predictive control of modern electric drives. Within RICE, especially Zdenek Peroutka and Vaclav Smidl are involved. Many works about MPC for multiple IMs connected to single inverter [60], about predictive control of IM acoustic noise [31], and about predictive control of permanent magnet synchronous motor (PMSM) drives [61] were published. At the Brno University of Technology, the IM drive control research is done by Pavel Vaclavek and Petr Blaha within the consortium of six universities and research institutes based in Brno (CEITEC). In the field of predictive control, they mainly focus on PMSM drives [62]. At the Technical University of Ostrava, the research on the control of AC drives is being conducted mainly by Pavel Brandstetter, Petr Chlebis, and Martin Kuchar. However, their main focus is speed and flux estimation [63] rather than the drive control. Another group dealing with power electronics control is at the Czech Academy of Sciences in Prague, where, among others, Viktor Valouch is dealing with predictive control [64].

Finally, at Czech Technical University in Prague, few people are dealing with high-speed PMSM drives at Faculty of Mechanical Engineering [65]. Concerning my home department, the Department of Electric Drives and Traction at Faculty of Electrical Engineering, there is a group of people participating in the IM drive control methods research. They are Jiri Lettl, Jan Bauer, Ondrej Lipcak, and I [66].

1.3. Thesis Objectives

The topic of the thesis is the sensorless predictive control of induction motor drive. Within that, the machine's performance improvement is defined as the main objective. It is planned to achieve this goal by utilizing predictive control's ability to optimize certain parameters. The influence of the DC-link voltage will be examined and will be the subject of the optimization. Since the predictive control shares the same control idea with the direct torque control method, and both methods have many similar aspects, their comparison should be included. Since the predictive control methods require the speed information and the elimination of the speed sensor is a common requirement in many applications, the method should work with and also without the speed sensor (sensorless). The individual tasks were defined as follows:

1. Sensorless IM drive predictive control method design.
2. IM drive predictive torque control and direct torque control comparison.
3. Predictive controlled IM drive VSI DC-link voltage optimization.
4. Proposed algorithms verification in Matlab Simulink environment.
5. Experimental verification of proposed DC-link voltage optimization algorithm on laboratory IM drive with the speed sensor.
6. Experimental verification of proposed DC-link voltage optimization algorithm on laboratory IM drive without the speed sensor.
7. Reduction of the torque ripple, stator current THD, and drive losses.

2. Mathematical Model of the Controlled System

For the predictive control and for sensorless speed estimation of the IM drive, the knowledge of the IM mathematical model is important. Multiple mathematical models can be utilized. The most widely used ones are the so-called T-model, Γ-model, and inverse Γ-model. They are all equivalent, and their mutual conversions were analyzed [67]. The equations used throughout the thesis are usually based on the T-model, which is described in this section. In the real IM drive system, not all the required quantities are directly measurable. Many variables, usually the magnetic flux, are not measured and must be somehow estimated. The latter part of this section is therefore dedicated to the description of the observer used for the estimation of these non-measurable motor quantities.

2.1. IM Model

The so-called T-equivalent circuit of the IM is depicted in Fig. 2 and is utilized for the mathematical description of the machine [68]. In the figure, the symbols $\boldsymbol{\psi}_1$ and $\boldsymbol{\psi}_2$ denote the stator and rotor flux linkage space vectors, respectively, $\boldsymbol{v}_1$ represents the stator voltage space vector, $\boldsymbol{i}_1$ and $\boldsymbol{i}_2$ are the stator and rotor current space vectors, respectively, $\boldsymbol{i}_\mathrm{m} = \boldsymbol{i}_1 + \boldsymbol{i}_2$ is the magnetizing current, R_1 and R_2 denote the stator and rotor resistance, respectively, ω_r is the rotor mechanical angular speed, L_m is the magnetizing inductance. The stator inductance L_1 is defined as $L_1 = L_\mathrm{m} + L_{1\sigma}$, where $L_{1\sigma}$ is the stator leakage inductance and the rotor inductance L_2 is defined as $L_2 = L_\mathrm{m} + L_{2\sigma}$, where $L_{2\sigma}$ is the rotor leakage inductance. The symbol j represents the imaginary unit for which the equivalence $\mathrm{j}^2 = -1$ applies. In the presented model, a squirrel-cage rotor is considered, so the rotor voltage is zero, and the equivalent resistance representing the core losses is not considered.

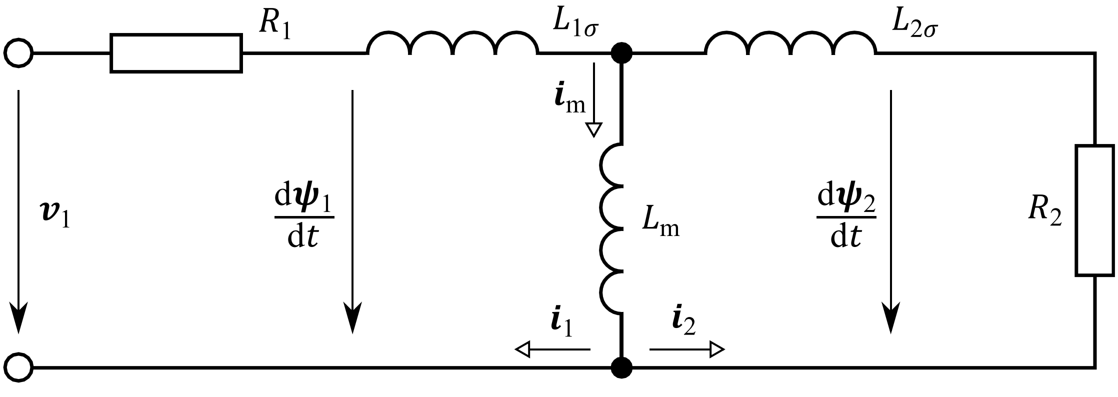

Fig. 2. T-equivalent circuit of induction motor.

According to the scheme presented in the figure, the equations of the IM equivalent circuit can be defined. They are following

$$\boldsymbol{v}_1 = R_1\boldsymbol{i}_1 + \frac{\mathrm{d}\boldsymbol{\psi}_1}{\mathrm{d}t}, \tag{1}$$

$$0 = R_2\boldsymbol{i}_2 + \frac{\mathrm{d}\boldsymbol{\psi}_2}{\mathrm{d}t} + \mathrm{j}\omega_\mathrm{r}\boldsymbol{\psi}_2,$$

$$\boldsymbol{\psi}_1 = L_1\boldsymbol{i}_1 + L_\mathrm{m}\boldsymbol{i}_2,$$

$$\boldsymbol{\psi}_2 = L_2\boldsymbol{i}_2 + L_\mathrm{m}\boldsymbol{i}_1.$$

The described equivalent circuit equation set would be incomplete without the torque producing equation

$$T = \frac{3}{2}\frac{L_\mathrm{m}}{L_2}p_\mathrm{p}|\boldsymbol{\psi}_2 \times \boldsymbol{i}_1| = \frac{3}{2}\frac{L_\mathrm{m}}{L_2}p_\mathrm{p}\left(\psi_{2\alpha}i_{1\beta} - \psi_{2\beta}i_{1\alpha}\right), \tag{2}$$

where T is the torque generated by the IM and p_p denotes the number of pole pairs. The subscripts α and β denote the individual elements of the appropriate space vector in the static non-rotating coordinate system, and the symbol × denotes the cross product between two vectors. Finally, the motion equation to calculate the speed of the motor ω_r is

$$\omega_\mathrm{r} = \int \frac{T - T_\mathrm{L}}{J}\mathrm{d}t, \tag{3}$$

where T_L is the load torque. The damping factor is neglected.

2.2. Flux Observer

The most easily measurable quantity of induction motor drive is the stator current. The stator voltage can be reconstructed from the measured DC-link voltage and the known switching state of the inverter, and the speed can be measured with an encoder. However, modern control strategies require the knowledge of more quantities. Since some of them are very hard to measure or even non-measurable, they must be estimated. A common way of obtaining those quantities is an observer and, in the case of IM, Luenberger observer (LO) [69]. LO belongs to a group of closed-loop deterministic observer types. It is an IM model that utilizes the actual motor as a reference model and its output for feedback. According to the difference between the observed and the real output, the states of the system are corrected. The correction gain matrix must be designed according to Lyapunov’s asymptotic stability theory and must be faster than the observed system [70].

The general description of a linear system can be written as

$$\begin{aligned}\dot{\boldsymbol{x}}(t) &= \mathbf{A}\boldsymbol{x}(t) + \mathbf{B}\boldsymbol{u}(t)\\ \boldsymbol{y}(t) &= \mathbf{C}\boldsymbol{x}(t) + \mathbf{D}\boldsymbol{u}(t),\end{aligned} \tag{4}$$

where, in case of IM, the input $\boldsymbol{u}$ is the stator voltage vector $\boldsymbol{v}_1$, output $\boldsymbol{y}$ is the stator current vector $\boldsymbol{i}_1$, $\boldsymbol{x}$ is the state variable vector, and $\dot{\boldsymbol{x}}$ is its derivative. Many equivalent state variables $\boldsymbol{x}$ choices within IM exists. The most common way is the stator current $\boldsymbol{i}_1$ and rotor flux vectors $\boldsymbol{\psi}_2$ as

$$\boldsymbol{x}(t) = \begin{bmatrix} \boldsymbol{i_1} \\ \boldsymbol{\psi_2} \end{bmatrix}. \tag{5}$$

Other matrices describe system behavior. The system matrix **A**, input matrix **B**, output matrix **C** and feedback matrix **D** are defined as

$$\begin{gathered}
\mathbf{A} = \begin{bmatrix} -\frac{1}{\tau_\mathrm{s}}\mathbf{I}_2 & \left(\frac{k_\mathrm{r}}{\tau_\mathrm{r}{L_1}'} - \mathrm{j}\frac{k_\mathrm{r}p_\mathrm{p}\omega_\mathrm{r}}{{L_1}'}\right)\mathbf{I}_2 \\ \frac{L_\mathrm{m}}{\tau_\mathrm{r}}\mathbf{I}_2 & \left(-\frac{1}{\tau_\mathrm{r}} + \mathrm{j}p_\mathrm{p}\omega_\mathrm{r}\right)\mathbf{I}_2 \end{bmatrix}, \\
\mathbf{B} = \begin{bmatrix} \frac{1}{{L_1}'}\mathbf{I}_2 \\ \mathbf{0}_2 \end{bmatrix}, \\
\mathbf{C} = [\mathbf{I}_2 \quad \mathbf{0}_2], \\
\mathbf{D} = [\mathbf{0}_2],
\end{gathered} \tag{6}$$

where $\mathbf{I}_2$ is the unity matrix with rank two and $\mathbf{0}_2$ is the zero matrix with the same rank, and the constants are

$$R_1' = R_1 + R_2\frac{{L_\mathrm{m}}^2}{{L_2}^2}, \tau_\mathrm{s} = \frac{{L_1}'}{R_{1'}}, \tau_\mathrm{r} = \frac{L_2}{R_2}, k_\mathrm{r} = \frac{L_\mathrm{m}}{L_2}, L_1' = \sigma L_1, \tag{7}$$

where $\sigma = 1 - L_\mathrm{m}^2/L_1L_2$ is the leakage factor. Because the system matrix **A** changes with the speed of the motor ω_r, this matrix must be numerically calculated in every sampling time.

The state-space description of the observer [70] is

$$\begin{gathered}
\dot{\hat{\boldsymbol{x}}}(t) = \mathbf{A}(\omega_\mathrm{r})\hat{\boldsymbol{x}}(t) + \mathbf{B}\boldsymbol{u}(t) + \mathbf{L}[\boldsymbol{y}(t) - \mathbf{C}\hat{\boldsymbol{x}}(t)] \\
\hat{\boldsymbol{y}}(t) = \mathbf{C}\hat{\boldsymbol{x}}(t),
\end{gathered} \tag{8}$$

where **L** is the correction matrix, and $\hat{\boldsymbol{x}}$ is the observed state variable vector defined as

$$\hat{\boldsymbol{x}}(t) = \begin{bmatrix} \hat{\boldsymbol{i}}_\mathbf{1} \\ \hat{\boldsymbol{\psi}}_\mathbf{2} \end{bmatrix}, \tag{9}$$

and $\hat{\boldsymbol{y}}$ is the observed output $\hat{\boldsymbol{\imath}}_\mathbf{1}$.

The observer poles are then defined by the correction matrix design. The typical approach is to place the poles of the observer to the left compared to the poles of the motor [71]. The particular observer that was utilized within this thesis was described in [72], where also the stability of the observer was investigated. The used gain matrix is

$$\mathbf{L} = \begin{bmatrix} (l_1 + \mathrm{j}l_2)\mathbf{I}_2 \\ (l_3 + \mathrm{j}l_4)\mathbf{I}_2 \end{bmatrix}, \tag{10}$$

where the constants l_1, l_2, l_3, and l_4 are defined as

$$l_1 = \frac{l-1}{1-\sigma}\left(\frac{1}{\tau_\mathrm{r}} - \frac{l}{\tau_\mathrm{s}}\right), \tag{11}$$

$$l_2 = \frac{(l-1)\sigma}{1-\sigma}\omega_\mathrm{r},$$

$$l_3 = -\frac{l-1}{\sigma}\left(\frac{1}{\tau_\mathrm{r}} + \frac{1}{\tau_\mathrm{s}}\right),$$

$$l_4 = (l-1)\omega_\mathrm{r},$$

and l (often also marked as k) is a positive number usually within the range of 1 – 1.5, depending on the particular used motor and uncertainty of IM parameters. Since the correction matrix **L** is speed-dependent, it must also be numerically recalculated in every step.

The block diagram of the used flux observer is shown in Fig. 3.

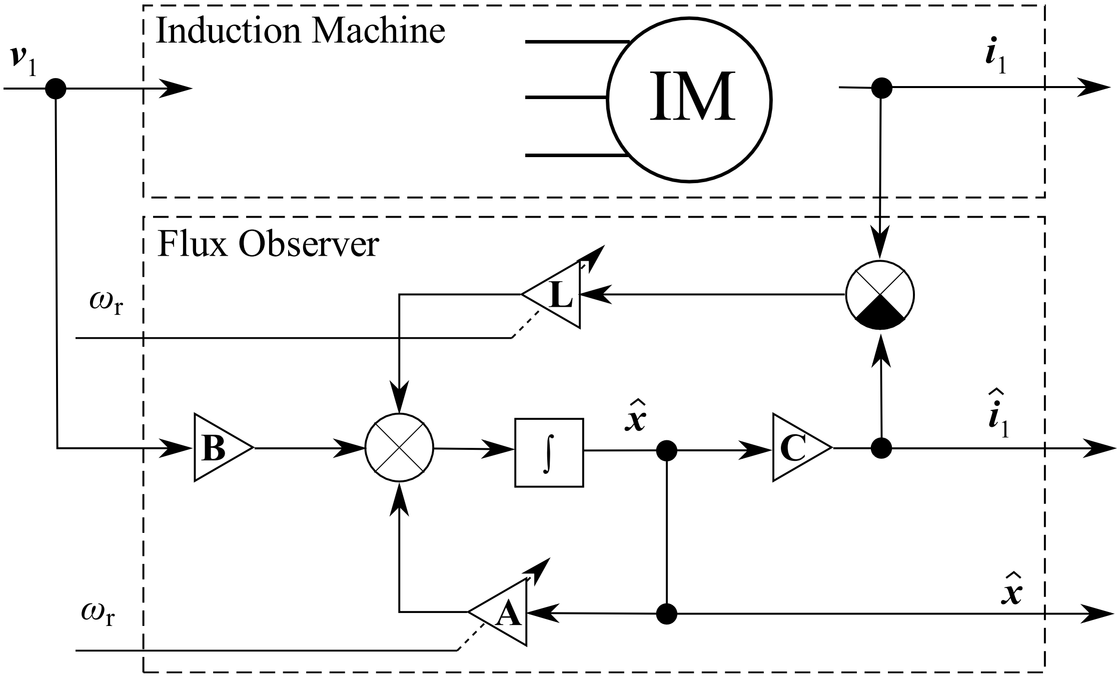

Fig. 3. Scheme of flux observer.

The system poles [49] of the induction motor itself and of the observer for different rotational speeds and correction constants k were examined in Matlab and are shown in Fig. 4.

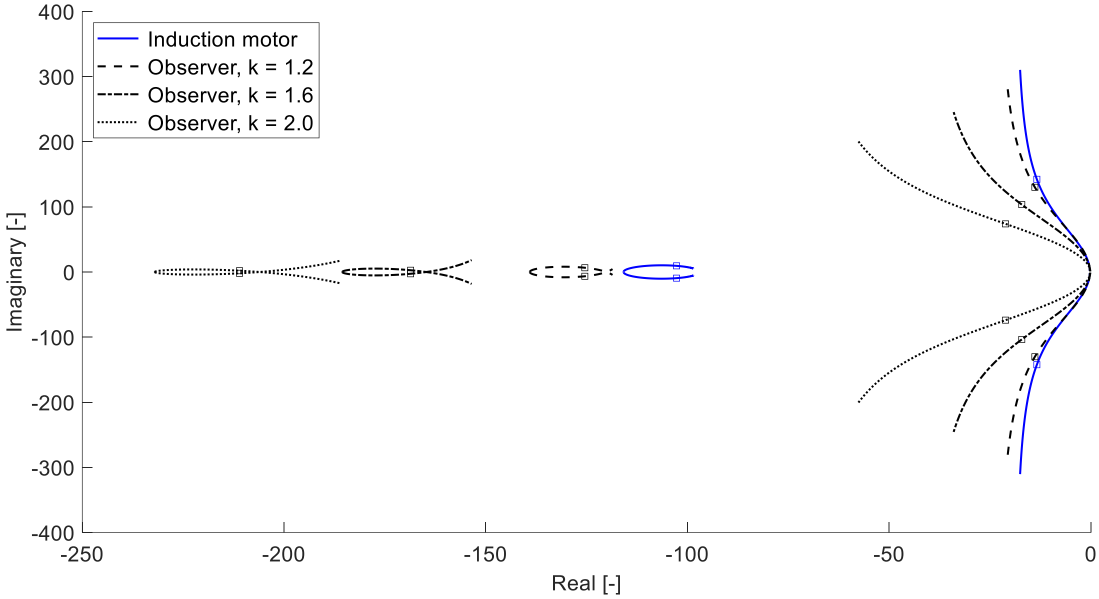

Fig. 4. Motor's and observers' poles for motor speed range from 0 to 1500 rpm. Marked points refer to the IM rotational speed 750 rpm.

Other frequently required non-measurable IM quantities are the stator flux vector $\hat{\boldsymbol{\psi}}_1$ and the developed torque $\hat{T}$. They can be obtained from the estimated quantities and IM equivalent circuit as

$$\hat{\boldsymbol{\psi}}_1 = \frac{L_\mathrm{m}}{L_2}\left(\hat{\boldsymbol{\psi}}_2 - \left(L_\mathrm{m} - \frac{L_1 L_2}{L_\mathrm{m}}\right)\boldsymbol{i}_1\right),$$

$$\hat{T} = \frac{3}{2}p_\mathrm{p}\left|\hat{\boldsymbol{\psi}}_1 \times \boldsymbol{i}_1\right| = \frac{3}{2}p_\mathrm{p}\left(\hat{\psi}_{1\alpha} i_{1\beta} - \hat{\psi}_{1\beta} i_{1\alpha}\right). \tag{12}$$

where the subscripts αβ denote the corresponding vector component in stationary coordinates.

This technique was used throughout the whole thesis for the stator and rotor flux vector and the developed torque estimations. The practical implementation of the observer in Matlab is added in Appendix A3.

3. Determination of IM Speed without the Speed Sensor

The knowledge of the actual speed of the controlled IM drive is an important aspect of most of the control strategies, especially if the speed control is requested. The conventional approach uses the speed sensor. It is a very good solution and reaches high precision. However, it suffers from a few disadvantages. The significant disadvantage of this solution is the increased probability of failure, especially in the aggressive environment where the sensor might be fault-prone [73]. Moreover, the sensor causes additional expenses, and it takes up space in the drive. For this reason, a speed sensorless solution is gaining its popularity in modern drive control. The most popular methods [74], [75] are an open-loop estimation, model reference adaptive systems (MRAS), different types of observers, and high-frequency signal injections into to supply voltage. The disadvantage of such methods is usually a complex tuning of controllers and lower accuracy than a case with a speed sensor [73]. However, in many applications, these are not significant issues. The classification of the sensorless speed determination techniques is depicted in Fig. 5.

One goal of the thesis is the verification of the proposed algorithms in an operation that does not use the speed sensor. Therefore, the performance of the most common methods are discussed in the following section.

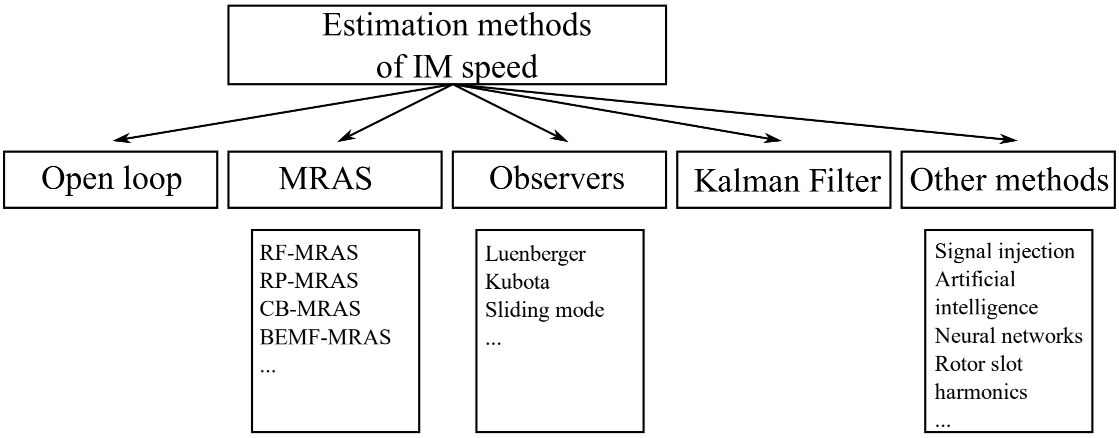

Fig. 5. Sensorless methods classification.

3.1. Open Loop Methods

The IM is described by a set of equations. The open-loop methods rely on the idea that speed can be directly calculated from these equations [76]. Most of these methods involve complicated mathematical operations, such as integration, in order to obtain the magnetic flux. However, an integrator can be saturated by DC offset or distorted due to present signal noise [77]. Replacing the integrator by a low-pass filter can partly eliminate the offset, but on the other side, it may bring another error to the estimated speed [78]. Moreover, these methods assume that all parameters are known and are constant during the motor operation. In open-loop operation, this causes error in the calculated speed [79]. Generally, the open loops methods are easier to implement but show higher inaccuracy than the closed-loop algorithms, so they will not be further described in the thesis.

3.2. MRAS Methods

The model reference adaptive systems method is a robust technique often used to calculate the speed of the rotor [42], [80], [81], [82], [83]. In principle, it is based on two models of the motor that both calculate the same variable. The first model is called the reference model, and it calculates the quantity from known quantities. The second is called the adjustable model, and it calculates the same chosen variable from the estimated output. This output is the goal of the estimation process. It is adjusted by an adaptive mechanism from the error between the two models' output. When the estimated variable is set correctly, the error between the models is zero, and, therefore, the desired variable is estimated correctly as well. The accuracy of the method and its speed of convergence are strongly dependent on the correct adjustment of the adaptation mechanism and the knowledge of the IM parameters [84], [85]. The general working principle of the method is depicted in Fig. 6.

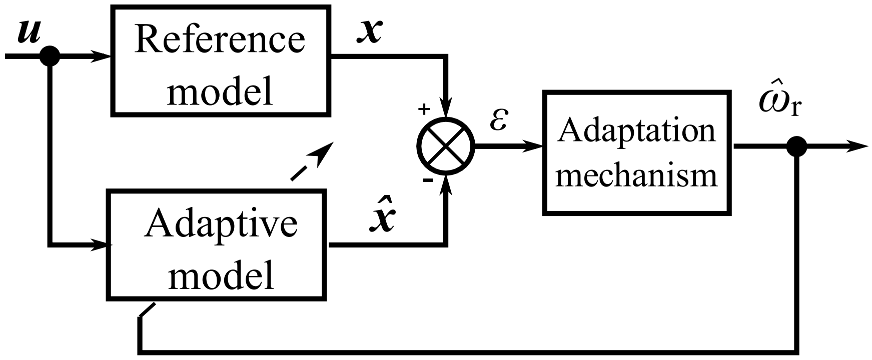

Fig. 6. Scheme of MRAS techniques.

The most straightforward and the most commonly used MRAS technique, in the case of IM speed determination, is the rotor flux based MRAS (RF-MRAS) [86], [87], [88]. The rotor flux vector is calculated from the measured voltage and current vectors by the so-called voltage model of IM. This model is considered the reference model and is calculated as

$$\frac{\mathrm{d}\boldsymbol{\psi_2}}{\mathrm{d}t} = \frac{L_2}{L_\mathrm{m}}\left(\boldsymbol{v}_1 - R_1\boldsymbol{i}_1 - L_1\sigma\frac{\mathrm{d}\boldsymbol{i}_1}{\mathrm{d}t}\right). \tag{13}$$

The adaptive model calculates the rotor flux vector from the measured current vector and from the estimated speed. The speed is unknown at the beginning and is treated as a parameter that will be estimated later. The adaptive model is based on the so-called current model of the IM and is calculated as

$$\frac{\mathrm{d}\widehat{\boldsymbol{\psi}}_2}{\mathrm{d}t} = \left(\widehat{\omega}_\mathrm{r} - \frac{1}{\tau_2}\right)\widehat{\boldsymbol{\psi}}_2 + \frac{L_\mathrm{m}}{\tau_2}\boldsymbol{i}_1. \tag{14}$$

The adaptation mechanism must ensure that the flux vectors calculated by both models are the same. The error between the two models create its input and is calculated as

$$e(t) = \hat{\psi}_{2\alpha}\psi_{2\beta} - \hat{\psi}_{2\beta}\psi_{2\alpha}. \tag{15}$$

The often-used adaptation mechanism is the PID or PI controller. It estimates the speed, which is then used for the adaptive model as

$$\hat{\omega}_{\mathrm{r}}(t) = K_{\mathrm{p}}\, e(t) + K_{\mathrm{i}} \int_{0}^{\tau} e(t)\mathrm{d}t, \tag{16}$$

where the K_{p} and K_{i} are the PI controller's proportional and integral, respectively, gains. The working scheme of the RF-MRAS is depicted in Fig. 7.

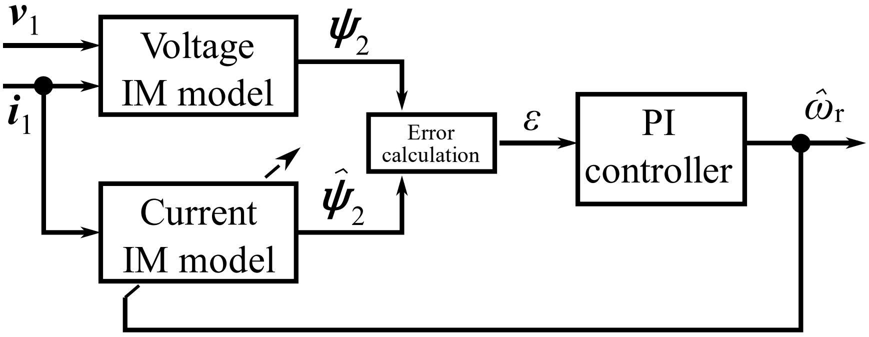

Fig. 7. Scheme of rotor flux based MRAS technique.

Since the equations contain integration, similar problems, as in the case with open-loop method, are introduced in the practical implementation of MRAS [74]. Another complication, which might result in offset in the estimated speed, arises from uncertainty in the motor parameters [89]. This is often eliminated by simultaneous estimation of speed and some motor parameters [81].

Other well-known MRAS algorithms are based on different quantities than the mentioned rotor flux. Most-often used ones are the reactive power (RP-MRAS) [81], back electromotive force (BEMF-MRAS), current-based (CB-MRAS) algorithms [87], and sliding mode (SM-MRAS) [90].

3.3. Speed Observers

Another commonly used method of determining the motor speed without the sensor is the speed observer [45], [46]. This type of speed estimation is more resistant to parameter deviation and measurement noise. The principle is based on designing a separate system (observer) that would duplicate the original system (motor). Then the error between the two systems' output is processed in an adaptive scheme, and the resulting signal (estimated speed of the motor) is used as a parameter in the observer. The adaptive scheme is defined to drive the error quickly to zero and therefore drive the estimated speed to the right value. [71].

Within the speed observer, the induction motor is considered to be a system where the voltage vector is its input, and the current vector is its output. The speed observer state description is the same as in the case of flux observer described in chapter 2.2.

The widely known speed observer methods for IM drive are Luenberger observer [71], Sliding mode observer [91], and Kubota's observer [70]. However, many other different types of observers for IM speed determination exist. In this thesis, the Luenberger observer was chosen as the typical speed observer and is further discussed. In the case of a standard Luenberger observer, the speed determination principle lies in combination with the MRAS algorithm. The controlled error is calculated from the difference between the system's and estimated output and from the estimated rotor flux as

$$e(t) = \hat{\psi}_{2\alpha}(i_{1\beta} - \hat{\imath}_{1\beta}) - \hat{\psi}_{2\beta}(i_{1\alpha} - \hat{\imath}_{1\alpha}). \tag{17}$$

and is then fed into a PI (proportional integral) controller or another adaptation mechanism, in case of PI controller, it is

$$\hat{\omega}_{\mathrm{r}}(t) = K_{\mathrm{p}}\, e(t) + K_{\mathrm{i}} \int_{0}^{\tau} e(t)\mathrm{d}t. \tag{18}$$

Then, the estimated speed changes the system matrix A and correction matrix K, which are updated every calculated sample time. The working principle of such speed observer is depicted in Fig. 8.

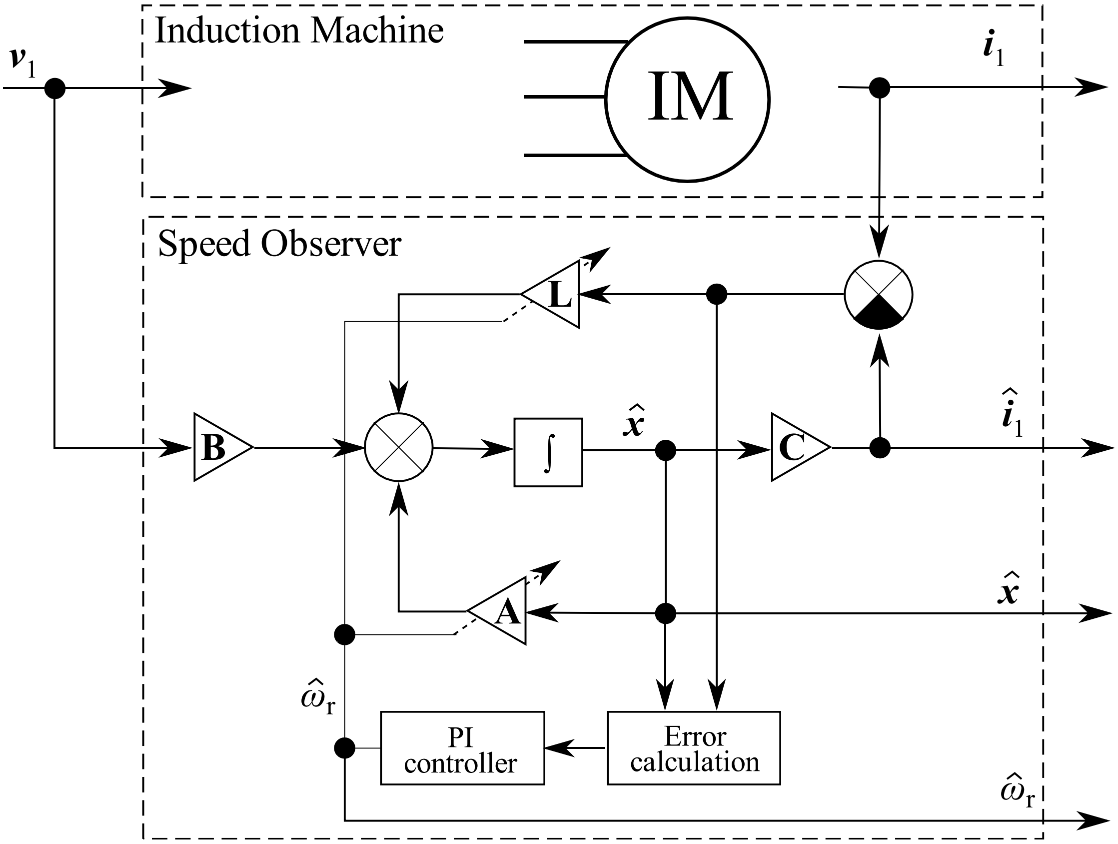

Fig. 8. Scheme of the speed observer.

This observer was realized on the real drive, and its practical implementation is added in Appendix A3.

3.4. Kalman Filter

The Kalman filter (KF) is a set of mathematical equations that recursively estimate the states of a system. Within the calculations, it minimizes the mean of the squared error. It is used in many applications [92]. For the KF, a few limitations exist. One of them is the limitation to only linear systems. Since the IM is not a linear system, the linearization near the actual working point must be performed. The Extended Kalman Filter (EKF) deals with nonlinearities in such way.

In connection with the induction motor drive, it is usually used for obtaining the rotational speed of the motor. However, other usages, such as an IM parameter identification [93], [94], fault detection [95] or stator voltage determination [96], are possible. In the case of the IM speed estimation [47], [97], the fifth or sixth-order system EKF is usually used. To the classical description of IM, where the states are current and flux vectors, the speed, and torque, respectively, are added to the states of the EKF. For the fifth-order EKF, the state matrix is then expanded to 5 rows and is defined as

$$\boldsymbol{x}(t) = \begin{bmatrix} i_{1\alpha} \\ i_{1\beta} \\ \psi_{2\alpha} \\ \psi_{2\beta} \\ \omega_{\mathrm{r}} \end{bmatrix}, \tag{19}$$

and, therefore, based on the IM equations, the state matrices A, B, and C change to

$$\mathbf{A} = \begin{bmatrix} -\frac{1}{\tau_{\mathrm{s}}} & 0 & \frac{k_{\mathrm{r}}}{\tau_{\mathrm{r}} L_1{}'} & -\frac{k_{\mathrm{r}}}{L_1{}'} p_{\mathrm{p}} \omega_{\mathrm{r}} & 0 \\ 0 & -\frac{1}{\tau_{\mathrm{s}}} & \frac{k_{\mathrm{r}}}{L_1{}'} p_{\mathrm{p}} \omega_{\mathrm{r}} & \frac{k_{\mathrm{r}}}{\tau_{\mathrm{r}} L_1{}'} & 0 \\ \frac{L_{\mathrm{m}}}{\tau_{\mathrm{r}}} & 0 & -\frac{1}{\tau_{\mathrm{r}}} & p_{\mathrm{p}} \omega_{\mathrm{r}} & 0 \\ 0 & \frac{L_{\mathrm{m}}}{\tau_{\mathrm{r}}} & -p_{\mathrm{p}} \omega_{\mathrm{r}} & -\frac{1}{\tau_{\mathrm{r}}} & 0 \\ -\frac{3}{2} \frac{p_{\mathrm{p}} L_{\mathrm{m}}}{L_2} \frac{1}{J} \psi_{2\beta} & \frac{3}{2} \frac{p_{\mathrm{p}} L_{\mathrm{m}}}{L_2} \frac{1}{J} \psi_{2\alpha} & 0 & 0 & -\frac{T_{\mathrm{L}}}{J} \end{bmatrix}, \tag{20}$$

$$\mathbf{B} = \begin{bmatrix} \frac{1}{L_1{}'} & 0 \\ 0 & \frac{1}{L_1{}'} \\ 0 & 0 \\ 0 & 0 \\ 0 & 0 \end{bmatrix},$$

$$\boldsymbol{C} = \begin{bmatrix} 1 & 0 & 0 & 0 & 0 \\ 0 & 1 & 0 & 0 & 0 \end{bmatrix}.$$

Because of the speed dependency of the first four rows and flux dependency of the last row of the matrix A, the system is nonlinear in this description.

Moreover, the J and T_{L} are usually unknown and cannot be used in the equation, unless they are estimated as well. For the Extended Kalman filter speed determination, the following state **F** and output matrix **H** are defined as

$$\mathbf{F}(k)=\begin{bmatrix} -\frac{1}{\tau_{\mathrm{s}}} & 0 & \frac{k_{\mathrm{r}}}{\tau_{\mathrm{r}}L_1{}'} & -\frac{k_{\mathrm{r}}}{L_1{}'}p_{\mathrm{p}}\omega_{\mathrm{r}} & 0 \\ 0 & -\frac{1}{\tau_{\mathrm{s}}} & \frac{k_{\mathrm{r}}}{L_1{}'}p_{\mathrm{p}}\omega_{\mathrm{r}} & \frac{k_{\mathrm{r}}}{\tau_{\mathrm{r}}L_1{}'} & 0 \\ \frac{L_{\mathrm{m}}}{\tau_{\mathrm{r}}} & 0 & -\frac{1}{\tau_{\mathrm{r}}} & p_{\mathrm{p}}\omega_{\mathrm{r}} & 0 \\ 0 & \frac{L_{\mathrm{m}}}{\tau_{\mathrm{r}}} & -p_{\mathrm{p}}\omega_{\mathrm{r}} & -\frac{1}{\tau_{\mathrm{r}}} & 0 \\ 0 & 0 & 0 & 0 & 0 \end{bmatrix}, \tag{21}$$

$$\mathbf{H}(k)=\begin{bmatrix} 1 & 0 & 0 & 0 & 0 \\ 0 & 1 & 0 & 0 & 0 \end{bmatrix}.$$

This matrices definition eliminated the J and T_{L}. Further, with this description, the speed ω_r is considered constant and is not influenced by anything in the system and will be estimated by the EKF as a noise.

The EKF algorithm consists of two stages – prediction and correction. At first, the estimate is calculated from the knowledge of the system description, which is given by the system matrix **F** and **B.** This is expressed by function f as

$$\hat{\boldsymbol{x}}(k|k-1)=f(\boldsymbol{x}(k-1|k-1),\boldsymbol{u}(k)), \tag{22}$$

where brackets $(k|k-1)$ refer to the calculation timing, in this case, the calculation was performed at time instant k based on the values from the time instant $k-1$. Then, the first estimate (a priori) of the covariance matrix **P** is calculated as

$$\mathbf{P}(k|k-1)=\mathbf{F}(k-1)\mathbf{P}(k-1|k-1)\mathbf{F}(k-1)'+\mathbf{Q}(k) \tag{23}$$

where **Q** is the state noise matrix. Afterward, the a priori estimate is corrected by the so-called Kalman gain. The optimal Kalman gain **K** is calculated as

$$\mathbf{K}(k)=\mathbf{P}(k|k-1)\mathbf{H}(k)'(\mathbf{H}(k)\mathbf{P}(k|k-1)\mathbf{H}(k)+\mathbf{R}(k))^{-1}, \tag{24}$$

where **R** is the output noise matrix.

The final (a posteriori) estimate is calculated from the first estimate and is adjusted according to the Kalman gain and the error between the measured and the a priori estimated output as

$$\mathbf{x}(k|k)=\mathbf{x}(k|k-1)+\mathbf{K}(k)(\mathbf{y}(k)-\boldsymbol{H}(k)\mathbf{x}(k|k-1)) \tag{25}$$

In the final step, the covariance matrix **P** is updated

$$\mathbf{P}(k|k)=(\mathbf{I}_5-\mathbf{K}(k)\mathbf{H}(k))\mathbf{P}(k|k-1) \tag{26}$$

where $\mathbf{I}_5$ is the identity matrix with rank five.

The matrix **Q** is a diagonal matrix with rank 5 that expresses the noise in the system and determines how much the states are dependent on the system description given by the matrix **F**. The matrix tuning is crucial for the proper operation of the algorithm.

The matrix **R** reflects the measurement noise and is a diagonal matrix with rank 2. This matrix must also be tuned. The most common way is to derive the matrix values from the variance of the measured outputs.

3.5. Other Methods

Other methods for speed determination have been developed. However, they are not commonly used, so only a short introduction for the two most important ones is provided in the thesis.

The signal injection method is one of them. Its principle is the following. The low amplitude signal is injected into the supply voltage of the induction [98] or synchronous motor [99]. Then, thanks to the anisotropy of the machine, the speed and position of the rotor are then calculated from the response in the current waveform [100]. Injecting a signal brings some problems. The relatively high amplitude of the injected signal would create additional torque waveform ripple and could negatively affect the precision of the control. On the other side, a small, injected signal amplitude is becoming harder to detect in the current waveform.

Another method is called the Rotor Slot Harmonics method, which is based on detecting the space harmonics induced by rotor slots in the air gap [74], [75]. Their frequency is proportional to the rotor speed and to the number of rotor slots. A rotor slot frequency signal is then processed in the same as an incremental encoder.

3.6. Sensorless Speed Determination Summary

IM speed determination is without a speed sensor a difficult task. The most common sensorless speed determination techniques were introduced in this chapter: MRAS, speed observers, and Kalman filter. All of the above-mentioned methods are able to deliver information about the speed with a certain precision. The comparison of different estimators and their accuracy is a common topic among researchers [72], [73], [75], [101]. However, their precision will always be worse than the traditional approach with the speed sensor unless all of the IM parameters are known with very high accuracy. Therefore, the selection between different methods or between the sensor and sensorless operation is always dependent on the specific application. The selection of a method suitable for the examined IM drive is discussed later in the thesis.

4. Induction Motor Drive Control Methods

This chapter presents the modern torque and speed control methods of the IM drive. Many control schemes have been proposed in the literature so far [68]. The basic classification is presented in Fig. 9.

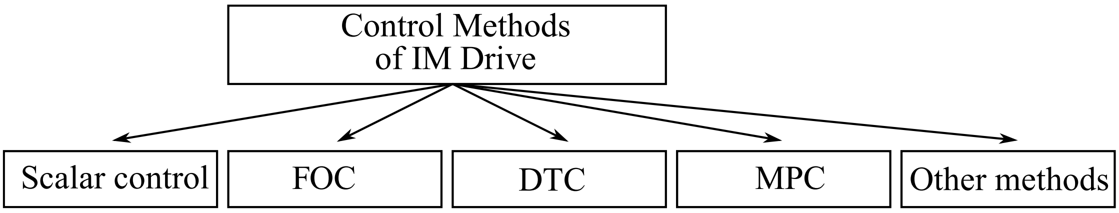

Fig. 9. IM drive control methods classification.

In this section, a big emphasis is put on the DTC since it shares a lot of its properties with predictive control, which is the main focus of the thesis. Further, the scalar control and field-oriented control are presented as well since they are very often used for the IM drive control. Their working principles, mathematical backgrounds, and some popular modifications are presented. Many other methods exist, but they are not so commonly used. For example, the fuzzy control, which may be beneficial in applications where the system or some parameters are unknown [53]. The sliding mode, which increases the robustness of the system and takes the switching nature of the power converter into account [53]. And many others like the neural networks, neuro-fuzzy control, or genetic algorithm control [102]. However, since they are not widely used, nor are they the focus of the thesis, they are not further discussed.

The control of the IM drive is realized by the voltage and its frequency. These two possibilities are connected in a scalar control. The scalar control of the induction motor is the oldest from the modern control strategies and is very simple. Only the frequency and amplitude of the stator voltage are controlled. Then, it could be applied through the PWM modulator. The request for constant flux amplitude in the IM is common. Then, according to the speed reference and voltage to frequency dependency, the voltage reference for the motor is determined. This dependency is not linear but is usually substituted with linear approximation where voltage to frequency ratio remains constant. Because of the voltage source limitation and because of the voltage drop on the stator winding, the ratio is not held constant during the whole operation area. It is adjusted at low frequencies and at a nominal voltage level.

Scalar control can be realized in either an open loop or in a closed loop. Open-loop control does not contain feedback from the motor, so the resulting speed may slightly differ from its reference. When higher accuracy is required, the speed feedback may be utilized. This is then closed-loop scalar control. The scalar control methods provide good performance only in steady states, but the behavior in the transients is rather worse. The benefit of this method is a simple implementation and is depicted in Fig. 10.

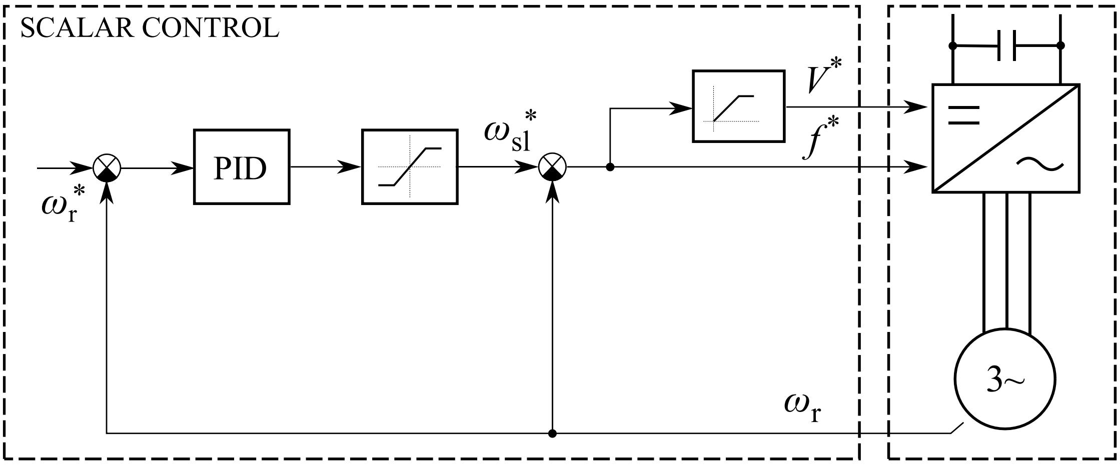

Fig. 10. The working principle of scalar control.

4.1. Field-Oriented Control

The FOC [8] is based on the idea of controlling the induction motor in the same way as a separately excited DC motor, i.e., the torque and the magnetic field are controlled independently. Within the FOC, the stator current is the control variable. This current vector is then decomposed into two orthogonal components. One component is linked to the flux, the other with the developed torque. The coordinates, in which the flux and torque components of the current are separated, are rotating synchronously with the flux vector [68]. In such representation, the two components appear as DC signals and can be individually controlled by separate controllers. The torque developed by the motor is calculated as the dot product between the two current components. The flux component usually assures constant value of rotor flux amplitude and, therefore, only the torque component can be used for the torque control.

For the coordinate transformation, the so-called transformation angle must be obtained. According to the way of transformation angle calculation, several types of FOC are recognized. The direct FOC reconstructs the flux vector from the measured electrical quantities [9], whereas the indirect FOC utilizes measured speed and estimates the slip to obtain the flux vector [103]. The principle of indirect field-oriented control is shown in Fig. 11.

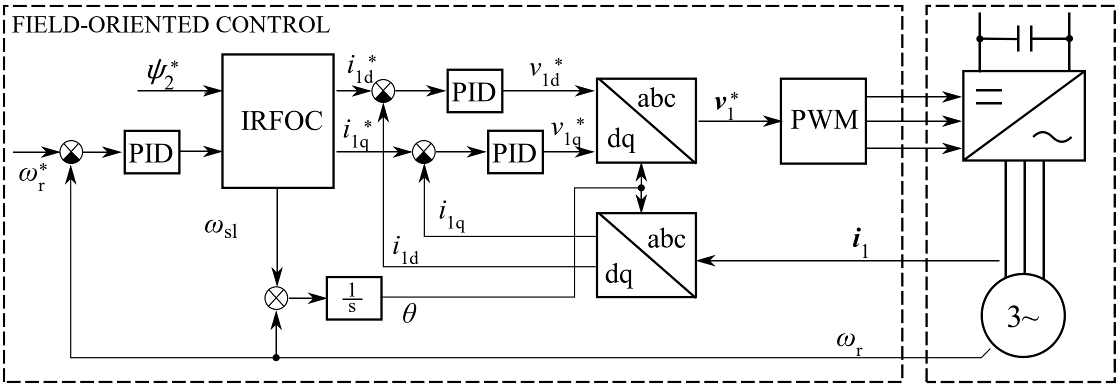

Fig. 11. The working principle of FOC.

The benefits of this method [68] consist in drive's optimal conditions in both the steady states and transients and in reaching high dynamism and precision of control. Other advantages lie in the fixed (and adjustable) switching frequency and small torque and current waveform ripple.

The disadvantage is the complexity of the algorithm since the mathematical model of the motor is utilized, coordinate transformations must be performed, and the PWM modulation is necessary. Moreover, multiple cascaded PID controllers are present, which brings other problems with correct tuning. Therefore, high computational time is required. Another disadvantage consists in the speed sensor, which must be present even if the speed control is not required.

4.2. Direct Torque Control

Within the DTC [8], the control variables are the torque and the flux amplitude. A specific transistor combination is selected within each sample time to change the torque and flux in a demanding direction. As in the case of FOC, the DTC has gone through many years of development, and many variants of the DTC methods were developed. Two main approaches were introduced. The first one was presented in Germany by Depenbrock [11], and the flux is controlled on a hexagon trajectory. The second one came from Japan and was developed by Takahashi [10], at which the flux vector is kept on a circular trajectory. For the thesis, the Takahashi's approach is more of interest since this control shares many properties with predictive control.

The torque of the IM can be expressed in many ways from different quantities. One of them is based on the vectors of stator and rotor fluxes. It shows that by maintaining both the flux vectors amplitudes constant, the torque is then dependent only on angle between the two vectors

$$T = \frac{L_\mathrm{m}}{L_\sigma^2} p_\mathrm{p} |\boldsymbol{\psi}_1 \times \boldsymbol{\psi}_2| = \frac{L_\mathrm{m}}{L_\sigma^2} p_\mathrm{p} |\boldsymbol{\psi}_1||\boldsymbol{\psi}_2| \sin\theta = \frac{L_\mathrm{m}}{L_\sigma^2} p_\mathrm{p} \psi_1 \psi_2 \sin\theta \tag{27}$$

where $L_\sigma \, is$ expressed as $L_\sigma = L_1 L_2 - L_m^2$.

When a certain voltage vector is applied, the stator flux vector moves in the direction of the applied voltage vector. The rotor flux vector then follows the same direction slowly with a delay. Then, the proper control of the stator flux vector changes the angle between stator and rotor flux vectors and can maintain the desired torque of the motor. The simple mathematical model for obtaining the torque and the stator flux vector is utilized as

$$\begin{gathered} \boldsymbol{\psi}_1 = \int (\boldsymbol{v}_1 - R_1 \boldsymbol{i}_1) \mathrm{d}t \\ T = \frac{3}{2} p_\mathrm{p} |\boldsymbol{\psi}_1 \times \boldsymbol{i}_1| = \frac{3}{2} p_\mathrm{p} (\psi_{1\alpha} i_{1\beta} - \psi_{1\beta} i_{1\alpha}) \end{gathered} \tag{28}$$

This model's benefit is the requirement of stator resistance knowledge only. On the other side, the performance in the low-speed area is worse. The usage of different model may bring better performance [104], [105].

After the torque and flux are estimated, the amplitude of the flux vector and its angle are determined. The angle is then used to determine the flux sector, which is depicted in Fig. 12.

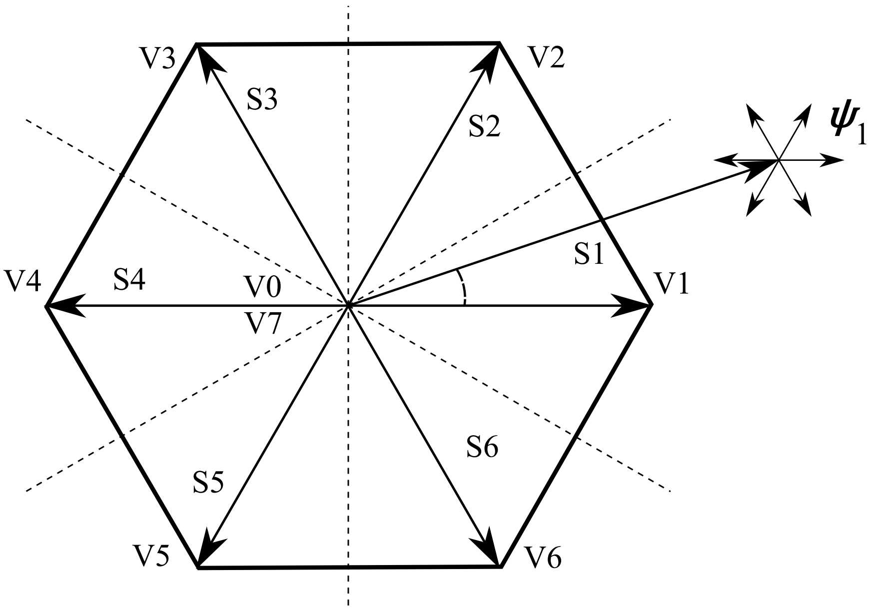

Fig. 12. Definition of sectors (S1 – S6, their borders are marked by the dashed line) and voltage vectors in the DTC case.

The controlled variables (torque and flux amplitude) are compared to their references with hysteresis controllers. The flux controller usually has only two possible outputs (increase or decrease), whereas the torque controller is usually implemented with three outputs (increase, decrease, do not change). Then, the most suitable vector is selected from the switching table presented in Table 1 and is applied by the inverter [106].

Table 1: Switching table of DTC

Demands		**Flux vector position**					
Flux	**Torque**	**1**	**2**	**3**	**4**	**5**	**6**
dψ = 0	dT = 1	V2	V3	V4	V5	V6	V1
	dT = 0	V7	V0	V7	V0	V7	V0
	dT = –1	V6	V1	V2	V3	V4	V5
dψ = 1	d* = 1	V3	V4	V5	V6	V1	V2
	dT = 0	V0	V7	V0	V7	V0	V7
	dT = –1	V5	V6	V1	V2	V3	V4

Many modifications of the basic DTC were developed [107], but most of them preserve the presented principle. The method’s block scheme, with its working principle, is depicted in Fig. 13.

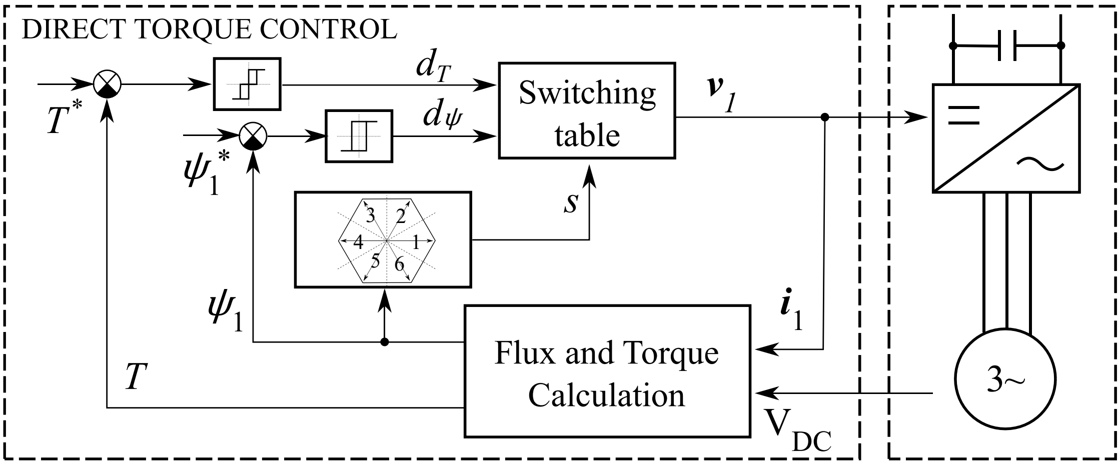

Fig. 13. The working principle of DTC.

The benefits of the DTC are good performance in both steady state and transient. Another advantage lies in the simplicity of the algorithm, since, compared to the FOC, the transformation to rotating coordinates is not required, the model of the induction motor is much simpler, and the PWM modulator is absent. Moreover, it uses hysteresis controllers instead of more complicated PID (proportional integral derivative) controllers. If the speed control is not required, the motor speed doesn’t have to be measured.

On the contrary, since the PWM modulator is not present, the faster the control calculations must be updated. Moreover, the absence of the PWM modulator also causes varying switching frequency. This may cause problems in specific applications, at which specific frequencies may cause incompatibility with other circuits. Another common problem of the drive with DTC is higher torque ripple and high current THD.

4.3. Predictive Control

The new approach to the control of the induction motor drive is predictive control. Many different types of classifications exist, but, very often, three main approaches of the predictive control in connection with the power electronics and motor control are distinguished [53], [108]. They are the hysteresis-based, trajectory-based, and model-based strategies. These approaches are not always fully separated, and in many methods, the transitions between them occur. The hysteresis-based and trajectory-based were the first attempts to bring predictive control to the field of electric drives in the past. The model-based predictive control, on the contrary, is a modern predictive strategy, which was introduced in electric drives very recently, and quickly became the most widely used predictive control within the area of the electric drive.

4.3.1. Hysteresis-Based Predictive Control

A hysteresis-based predictive strategy aims to keep the controlled variable within a tolerance area [53], [108]. The most straightforward implementation of the strategy is the hysteresis or bang-bang controller. A specific form of a hysteresis-based predictive operational principle with a circular hysteresis boundary was proposed in the predictive current control scheme [14]. It is illustrated in Fig. 14. On the left side, the block diagram is presented, and on the right side, the principle is explained. The circular boundary of the controlled stator current vector reference is shown. When the real stator current vector gets outside the boundary circle, another switching state must be applied. At this point, the trajectory of the stator current vector must be calculated for each possible switching state. The time it takes for each possible trajectory to touch the circle trajectory is predicted, and the switching state associated with the longest time is chosen. Also, the stator current reference and its boundary circle moves within the predicted amount of time and must be predicted as well. The dotted curve indicates this in the figure.

The advantage of this control is that the precise knowledge of the system is not necessary. Even with some uncertainties, the control error can be maintained small.

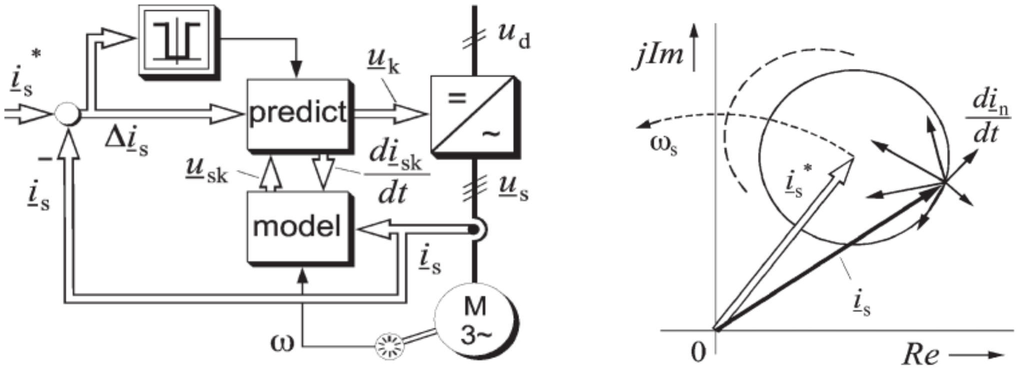

Fig. 14. Hysteresis-based predictive control, taken from [53].

4.3.2. Trajectory-Based Predictive Control

The trajectory-based predictive principle forces the controlled variables onto the precalculated trajectories [108]. Then, once the variables are on the trajectories, it remains there thanks to its own properties until some changes are enforced.

This strategy is not often utilized within electric drive control. One of a few examples of trajectory-based operational principle is Direct Speed Control [15]. In the method for a short time interval, the system inertia and derivatives of the load and motor torque are assumed to be constant. Under these conditions, parabolas curves in the speed error and acceleration axes can represent the system. The situation is shown in Fig. 15.

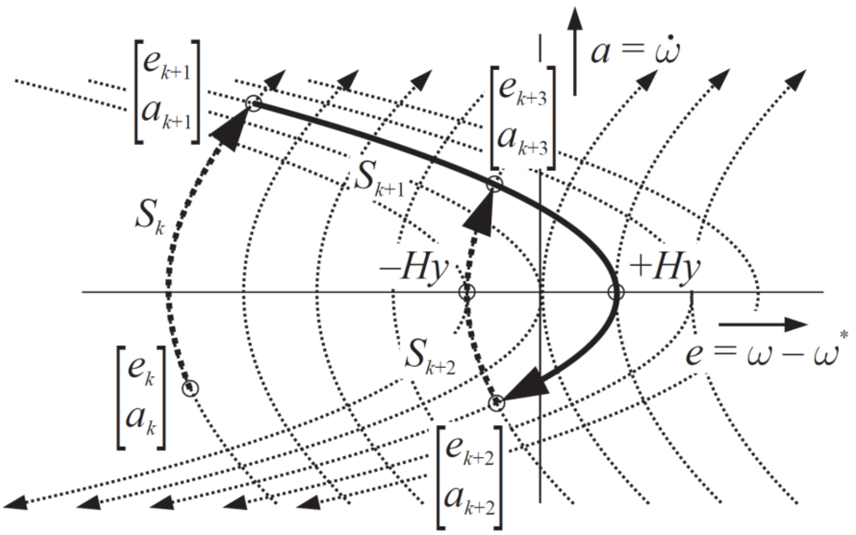

Fig. 15. Direct Speed Control principle, taken from [108].

The desired state is at the origin of the coordinate system, at which the error and the speed derivative are zero. To keep the system at this point, the infinite switching frequency would have to be reached. For that reason, some kind of hysteresis has to be defined. In the figure, we assume the initial system state is at point e_k a_k. To reach the desired state, firstly, the switching state S_k (torque increasing) is chosen, and the system moves along the dotted curve to e_{k+1} a_{k+1} point. At this point, another switching state S_{k+2} (torque decreasing) is chosen, and the trajectory moves along the bold curve until it reaches e_{k+2} a_{k+2} point. By this switching principle, the system is maintained close to the ideals state. In steady-state operation, the system moves on just two curves. The intersection points and the trajectories are predicted in every sampling time to prevent the system from exceeding the defined hysteresis.

The trajectory-based predictive principle predicts the trajectories for every switching state, so a more precise system model is required compared to the hysteresis-based principle.

4.3.3. Model-Based Predictive Control

The model-based predictive principle is not new; it has been introduced already in the 1970s. However, it was used only in application with large time constants (in range of minutes), such as the chemical industry, where it nowadays plays an important role [12]. In the area of the electric drive, there are much shorter time constants, so the computing demand is greater, and the calculations must be performed much faster. Because of that, the model-based predictive control could not have been developed until recent times. Then, the mathematical background was described [109] and the usage in electric drive were publicized [58], [110], [111].

The basic working principle of a model-based controller is depicted in Fig. 16. The algorithm utilizes past inputs and outputs, and the controlled variables are then predicted for the set of feasible future inputs. For such prediction, a good system knowledge is required. The predicted variables are compared with their references to yield a future error. The errors are then evaluated by the so-called cost function, which defines the optimization criteria for the choice of the best input. Moreover, some constraints can be implemented within the cost function. The candidate chosen by the cost function is then applied to the plant, and the cycle starts again.

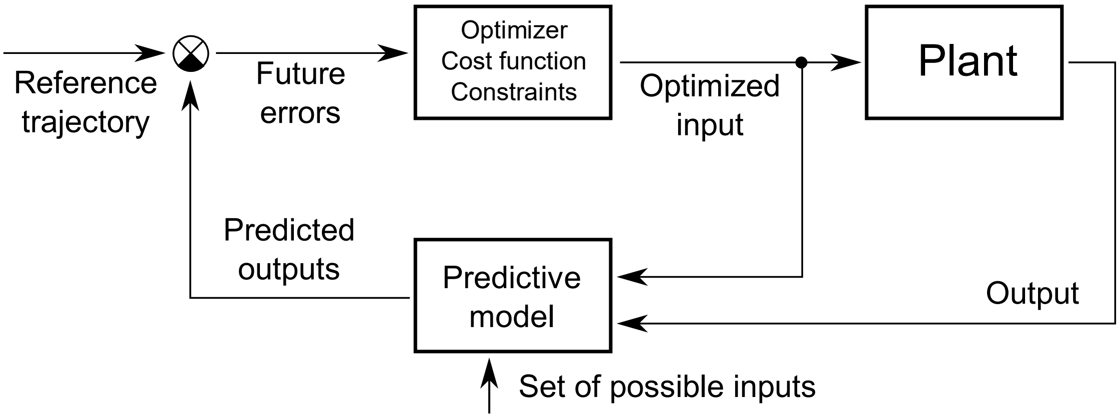

Fig. 16. The working principle of MPC.

The two main approaches based on the feasible control set of model predictive control (MPC) are distinguished for the control of IM drive. Finite set model predictive control (FS-MPC) and continuous set model predictive control (CS-MPC) [1], [19], [20], [25]. The FS-MPC considers a finite number of candidates. In the case of VSI, usually, the eight basic voltage vectors are the eight candidates. Therefore, the control variables are also predicted finite number times, in case of VSI, eight times. From them, the most suitable candidate is selected according to the given criteria expressed as the cost function. The cost function minimization is relatively easy since the cost function can be enumerated for all candidates. On the contrary, CS-MPC considers the infinite number of candidates. Then, the selection must perform differently. The prediction model and the cost function are expressed as a function, and the function is then the subject of an analytical minimization. The candidate that corresponds to this minimum is the best candidate and is applied. In the case of VSI, the selected voltage vector is applied through the PWM modulator. With increased system complexity, it becomes difficult to express the function minimum, and sometimes the FPGAs (field-programmable gate arrays) must be utilized [112].

Another classification of the model predictive control within IM control is possible, a classification based on a control variable. Two main approaches are distinguished. The predictive current control (PCC) [24], [113], [114] and the predictive torque control (PTC) [19], [21]. Usually, because of the smaller computational burden, they are both implemented as the FS-MPC, even though the CS-MPC implementation is also possible. Therefore, as the feasible candidates, only the eight voltage vectors are considered [115]. The difference between the two strategies is the controlled variable [25]. In the case of PCC, the stator current vector is decomposed into two parts by transformation to the rotating coordinates, and they are the subject of control. This control corresponds to the FOC [23], [24]. In the case of the PTC, the torque and stator flux amplitude are controlled, which corresponds to the DTC strategy [21].

An essential part of the MPC is the cost function, in which the control variables are expressed. The characteristic of the whole drive is then determined by the cost function design [19]. At each sampling time, the cost function over a finite horizon of sampling times for the whole feasible set of the considered candidates is minimized. The candidate, corresponding with the minimum cost function value, is then selected as the input for the next sampling time. The cost function can contain multiple parameters, which enables multivariable optimization. This brings an interesting problem because the individual control variables, sometimes each with different units, must be somehow joined.

In the case of IM control with PCC, where the individual parts of the current are controlled, the commonly used cost function [113] is

$$g(n) = |i_{1\alpha}(k+1) - i_{1\alpha}^*| + \left|i_{1\beta}(k+1) - i_{1\beta}^*\right|. \tag{29}$$

where k denotes the discrete time sample. Such cost function contains two equal parts with the same relevance; the two parts of the stator current. The error between the predicted values and their references are minimized within each step.

However, these individual elements could be more complex, for example, quadratic. This would force the control variables to their references faster. Such relation is used, for example, in PWM inverters, where the power flow control is required [116]. Moreover, such cost function shows another possible expression of the control variable. In the case of the active power part of the cost function, the error between the reference and predicted values is forced to zero. But, in the case of reactive power part, the reference reactive power is zero, so the whole part is forced to zero. The typical cost function implementation in the case of PWM rectifier is

$$g(n) = \left(P^* - P(k+1)\right)^2 + \left(Q(k+1)\right)^2. \tag{30}$$

Another cost function design aspect is the importance of the individual cost function's elements to its other elements. A good example is the PTC, where the flux and torque are controlled. Since the flux and torque have different dimensions, the cost function must contain a constant to unite these parts with some relevance. A typical cost function [21] used within PTC is

$$g(n) = k_{\mathrm{CF}}|\psi_1(k+1) - {\psi_1}^*| + |T_{\mathrm{e}}(k+1) - T_{\mathrm{e}}^*|, \tag{31}$$

where the choice of the k_{CF} constant determines the relevance of flux and torque settings. With adjusting the constant, the torque, and flux waveforms ripple are influenced. This was not the case with PCC and PWM rectifier since the controlled variables are of the same dimension.

Other elements may be included in the cost function. The proper weighting constant tuning is then another optimization problem. Multiple methods for the coefficients settings were proposed [61], [117], [118], [119], [121].

4.4. IM Drive Control Methods Summary

For the high-power applications, the proper control of the drive with IM is necessary. Two control strategies are nowadays standards in the industry, the FOC and DTC. Both of them have gone through years of development and optimizations. The most common implementations of each method were introduced in this chapter, and the working principle was explained.

Within the last few years, a new approach of motor control started to become popular, the so-called predictive control. The predictive control is divided into several types (hysteresis, trajectory, and model-based), and they are described in the chapter. The most popular within the area of the electric drive is nowadays the model predictive control. This can be further divided according to the number of feasible candidates, i.e., voltage vectors, to finite and infinite set MPC or according to the control variable to current and torque control. An important aspect of the MPC is the cost function, which defines the behavior of the whole drive. The cost function value expresses how far the system is from the ideal state. The lower it is, the closer the system is from the ideal state. According to the feasible set, the different methods can be used for cost function minimization.

5. Finite Set Predictive Torque Control

The FS-PTC is one of the often-utilized predictive control methods used with IM drives [17] and is of the greater interest of the thesis. This chapter provides a mathematical description of the method, deals with multiple issues arisen in the practical implementation, compares its properties with DTC method, and shows the possible improvement for torque ripple and current THD reduction.

In the case of a two-level inverter, the feasible set of inputs for the prediction consists of six active and two passive basic voltage vectors. By the application of each vector, the control variables, i.e., the developed torque and stator flux amplitude, are influenced in a specific manner. The PTC predicts this influence for each of these eight voltage vectors for the next sampling time. Therefore, a predictive model of the IM must be known. When the future torque and stator flux amplitude are predicted, the most suitable voltage vector is selected according to some criteria [25], [26], [120]. The so-called cost function expresses the criteria and, if required, some constraints. The inverter then applies the selected voltage vector [19]. The PTC working principle is depicted in Fig. 17.

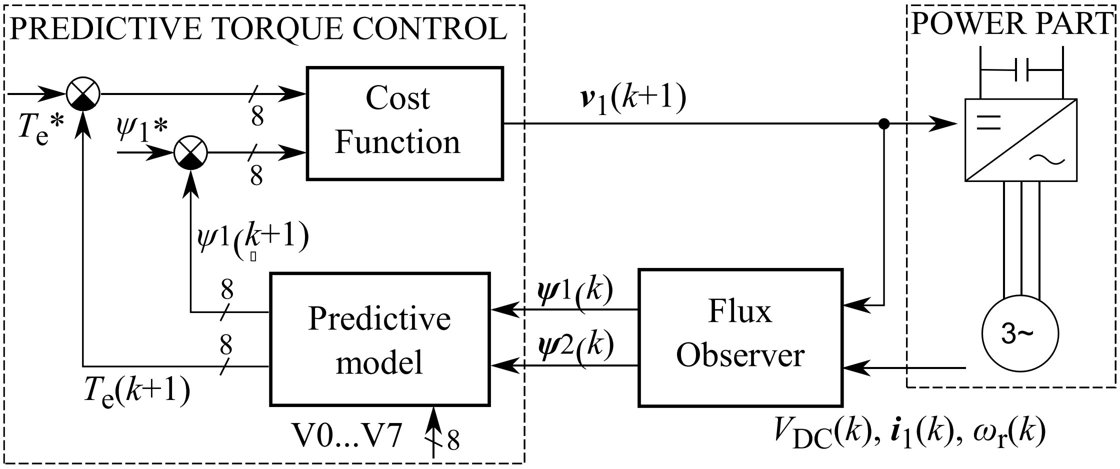

Fig. 17. The working principle of the PTC. Published by the author [21].

At first, the current state of the motor must be calculated. The control variables prediction (the torque and stator flux) requires the estimation of some non-measurable IM quantities. The knowledge of the stator and rotor flux vectors at the present sampling time are required. The estimation of the flux vectors explained in chapter 2.2 can be used for this.

Second, the prediction of the torque and flux vector takes place. [19], [120], [122], The stator flux vector prediction is based on the voltage equation of the IM equivalent circuit presented in section 2.1. After its discretization and replacing the derivative by the Euler approximation,

$$\boldsymbol{v}_1(k) = R_1 \boldsymbol{i}_1(k) + \frac{\boldsymbol{\psi}_1(k+1) + \boldsymbol{\psi}_1(k)}{\Delta T} \tag{32}$$

applies. The symbol k denotes to the time instant and ΔT is the time difference between the two samples. Because this time difference is equal to the sampling time, it is substituted by this sampling time T_{s}. Moreover, since the voltage vector $\boldsymbol{v}_1(k)$ is the object of searching, it is replaced by $\boldsymbol{v}_{\mathbf{1}}(n)$, where n is the considered voltage vector number. Finally, the stator flux vector is then predicted as

$$\boldsymbol{\psi}_1(k+1) = \boldsymbol{\psi}_1(k) + T_{\mathrm{s}}\boldsymbol{v}_1(n) - T_{\mathrm{s}}R_1\boldsymbol{i}_1(k). \tag{33}$$

Since the torque prediction is dependent on the stator current prediction, it must be predicted as well. According to [123], the equation of stator dynamic of a squirrel-cage IM in general coordinates rotating at speed ω_k is obtained as

$$\boldsymbol{i}_1 + \tau_\sigma \frac{\mathrm{d}\boldsymbol{i}_1}{\mathrm{d}t} = -\mathrm{j}\omega_{\mathrm{k}}\tau_\sigma\boldsymbol{i}_1 + \frac{k_{\mathrm{r}}}{R_\sigma}\left(\frac{1}{\tau_{\mathrm{r}}} - \mathrm{j}\omega_{\mathrm{r}}\right)\boldsymbol{\psi}_2 + \frac{\boldsymbol{v}_1}{R_\sigma}. \tag{34}$$

After discretization and replacing the derivatives with the Euler approximation, the current vector $\boldsymbol{i}_1(k+1)$ in a stationary coordinate system can be predicted as

$$\boldsymbol{i}_1(k+1) = \left(1 + \frac{T_{\mathrm{s}}}{\tau_\sigma}\right)\boldsymbol{i}_1(\mathrm{k}) + \frac{T_{\mathrm{s}}}{(\tau_\sigma + T_{\mathrm{s}})R_\sigma}\left[\left(\frac{k_{\mathrm{r}}}{\tau_{\mathrm{r}}} - k_{\mathrm{r}}\mathrm{j}\omega_{\mathrm{r}}(k)\right)\boldsymbol{\psi}_2(k) + \boldsymbol{v}_1(n)\right], \tag{35}$$

where $\tau_\sigma = \sigma L_1/R_\sigma$, $R_\sigma = R_1 + R_2k_{\mathrm{r}}^2$. The stator current vector prediction requires the rotational speed information which can be easily measured (as shown in Fig. 17) or estimated (as presented in section 3).

With the predicted stator current and flux vectors, the torque can be easily predicted as

$$T_e(k+1) = \frac{3}{2}p_p|\boldsymbol{\psi}_1(k+1) \times \boldsymbol{i}_1(k+1)|. \tag{36}$$

Then, the predicted control variables from (33) and (36) are compared to their references and are to be evaluated by the cost function. In the case of PTC, the cost function is defined as

$$g(n) = k_{CF}|\psi_1(k+1) - {\psi_1}^*| + |T_{\mathrm{e}}(k+1) - T_{\mathrm{e}}^*|, \tag{37}$$

where k_{CF} is the cost function weighting coefficient. It determines the importance of the correct flux setting to the correct torque setting. It is usually chosen as

$$k_{\mathrm{CF}} = \frac{T_{\mathrm{n}}}{\psi_{1\mathrm{n}}}, \tag{38}$$

where T_{n} is the machine nominal torque and $\psi_{1\mathrm{n}}$ is the nominal stator flux amplitude. Such choice of k_{CF} assures the same importance of the flux and torque setting.

The VSI then applies the voltage vector candidate selected by the cost function. It is kept on the motor terminals for the whole duration of the following sample time. Meanwhile, the calculation cycle starts again with the next prediction.

The practical implementation in Matlab code is presented in Appendix A3.

5.1. Common Implementation Issues

In a practical implementation of the PTC strategy, some aspects must be considered. This section brings the most important ones and shows how the cost function and constraints might solve the arisen problems.

5.1.1. Current Limitation

The fast changes of torque or flux reference may lead to very high current peaks, which, if not suppressed, may be harmful to the motor or the inverter. To ensure that the current stays within reasonable boundaries, the cost function can be designed in a way to suppress high current. The implementation of overcurrent protection [19] can be expressed as

$$g(n) = k_{CF}|\psi_1(k+1) - \psi_1{}^*| + |T_\mathrm{e}(k+1) - T_\mathrm{e}^*| + i_\mathrm{constr}, \tag{39}$$

where

$$i_\mathrm{constr} = \begin{Bmatrix} \infty & \text{if } |\boldsymbol{i}_\mathrm{s}(k+1)| > i_\mathrm{limit} \\ 0 & \text{if } |\boldsymbol{i}_\mathrm{s}(k+1)| \le i_\mathrm{limit} \end{Bmatrix}. \tag{40}$$

The overcurrent protection was tested experimentally, and the results are presented in Fig. 18. In the figure, the motor was disconnected from the inverter at first. Then, the flux amplitude reference changed to 1.2 Wb. In the case of current limitation, the flux increases much slower than in case of no limitation, but the current does not exceed the limit.

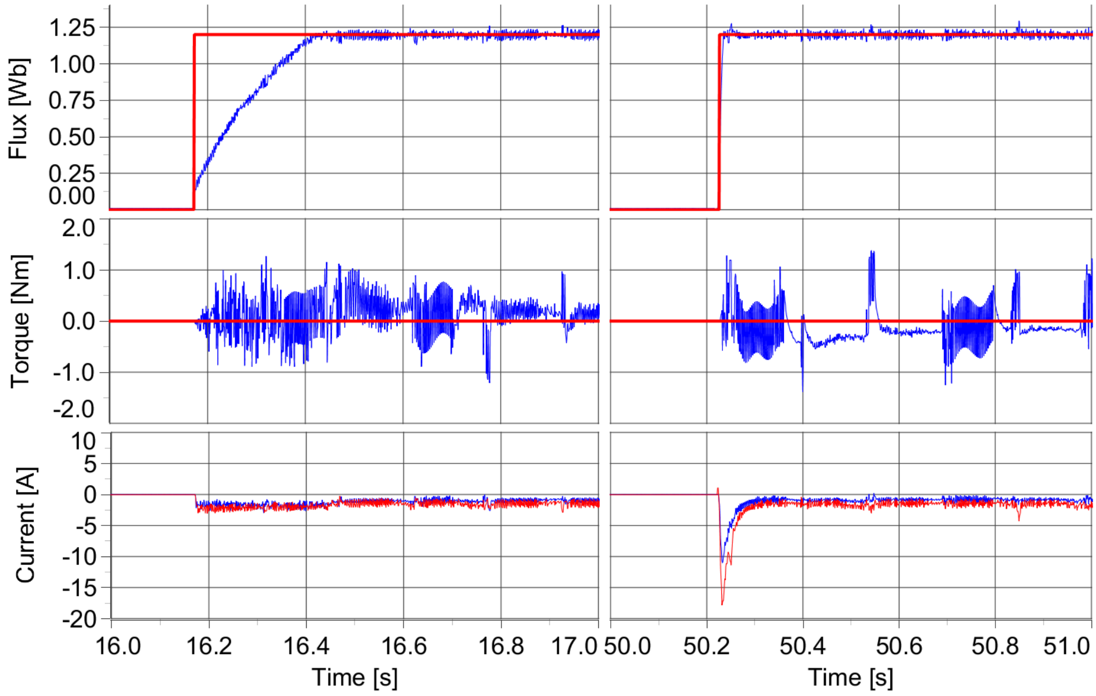

a) b)

Fig. 18. The waveforms of flux amplitude, torque and stator currents at a run a) with 3 A limitation and b) without current limitation.

5.1.2. Switching Losses Reduction

The switching of the inverter is always associated with losses. The higher the switching frequency is, the higher the losses are. Therefore, in many high-power applications, the switching frequency must be as low as possible. It is not a simple task to reduce the switching frequency of the inverter within the PTC. The most straight-forward way of its decrease lies in the sampling time increase. However, it is not the right solution since the performance of the drive decreases heavily [38], and the current harmonic distortion increases.

Another approach lies within the proper selection of the passive voltage vectors. There are eight possible voltage vectors in typical two-level VSI. Six of them are active, and two of them are passive. Since both passive vectors have the same influence on the motor, the cost function evaluates them in the same way, in case of the basic PTC implementation. However, from the point of view of the switching combination, the difference between these two vectors exists. If the cost function selects the passive vector, the proper distinguishing between the vectors can reduce the switching frequency. Such an approach is proposed in [124], where the following logic enhances the cost function. If the passive vector is selected, the one that requires a smaller amount of transistor switching changes is selected. The particular solution is depicted in Table 2.

Table 2: Efficient passive-voltage vector selection

Previous voltage vector	Selected voltage vector
V0, V1, V3, V5	V0
V2, V4, V6, V7	V7

A more sophisticated solution lies within the proper cost function design. A specific part regarding the voltage vector change may be added to the cost function. When the voltage vector within one sample time does not change, zero is added to the cost function, and the result is unaffected. However, if some transistor changes its state (another voltage vector is considered as a candidate), the cost function result increases, which gives disadvantages for the considered candidate. The more transistors change its state, the higher the disadvantage for the considered candidate. The modified cost function is then following

$$\begin{aligned} g(n) = k_{CF}|\psi_1(k+1) - {\psi_1}^*| + |T_\mathrm{e}(k+1) - T_\mathrm{e}^*| \\ + k_\mathrm{v}|(\boldsymbol{v}(k+1) - \boldsymbol{v}(k))|, \end{aligned} \tag{41}$$

where $\boldsymbol{v}$ is the applied or predicted voltage vector and k_v is the coefficient respecting the importance of switching frequency reduction. The higher is the k_v coefficient, the lower switching frequency is reached. However, this is always at the cost of worse torque and flux setting.

Another way of decreasing the inverter losses lies within the predictive loss model of an inverter [125]. The losses of the transistors are predicted for each feasible switching state, and they are included in the cost function as

$$g(n) = k_{CF}|\psi_1(k+1) - {\psi_1}^*| + |T_\mathrm{e}(k+1) - T_\mathrm{e}^*| + k_\mathrm{I}E_\mathrm{I}(k+1) \tag{42}$$

where E_{I} is the complete inverter loss that occurs during the transition from the actual state to the considered voltage vector and k_{I} is a weighting coefficient for loss reduction.

5.1.3. Processing Delay Compensation

The calculation of flux and torque for all candidates is a time-consuming task for a microcontroller. In an ideal case, at the time *k*, the currents are measured, the cost function selects, and the inverter immediately applies the optimal voltage for time duration from *k* to *k*+1. In such an ideal case, this would take no time, and the desired voltage vector would be applied for the duration from time *k* to time *k*+1. However, in the real situation, the calculation of all mentioned tasks takes a certain time. Then, the currents are measured in time *k*, and the cost function selects the optimal voltage for time *k*. However, the voltage cannot be applied immediately; it is applied at the next possible sample time, which is *k*+1. Therefore, the voltage meant for the duration from time *k* to time *k*+1 is applied from time *k*+1 to *k*+2. The longer the sample time is, the greater influence on the performance of the drive is.

The possible solution lies in a simple compensation of this one sample time [126]. At the time *k*, the currents are measured. Then, the necessary quantities are calculated for the time *k*+1 for voltage selected by the cost function in the previous step (since this is the voltage that is actually on the motor). Afterward, the prediction is made for all eight candidates for time *k*+2, which is then applied for the duration between the time *k*+1 and time *k*+2. All three cases, the ideal, the real, and the compensated, are depicted in Fig. 19. In the figure, the selection of a wrong voltage vector is shown in the case of a real situation without compensation.

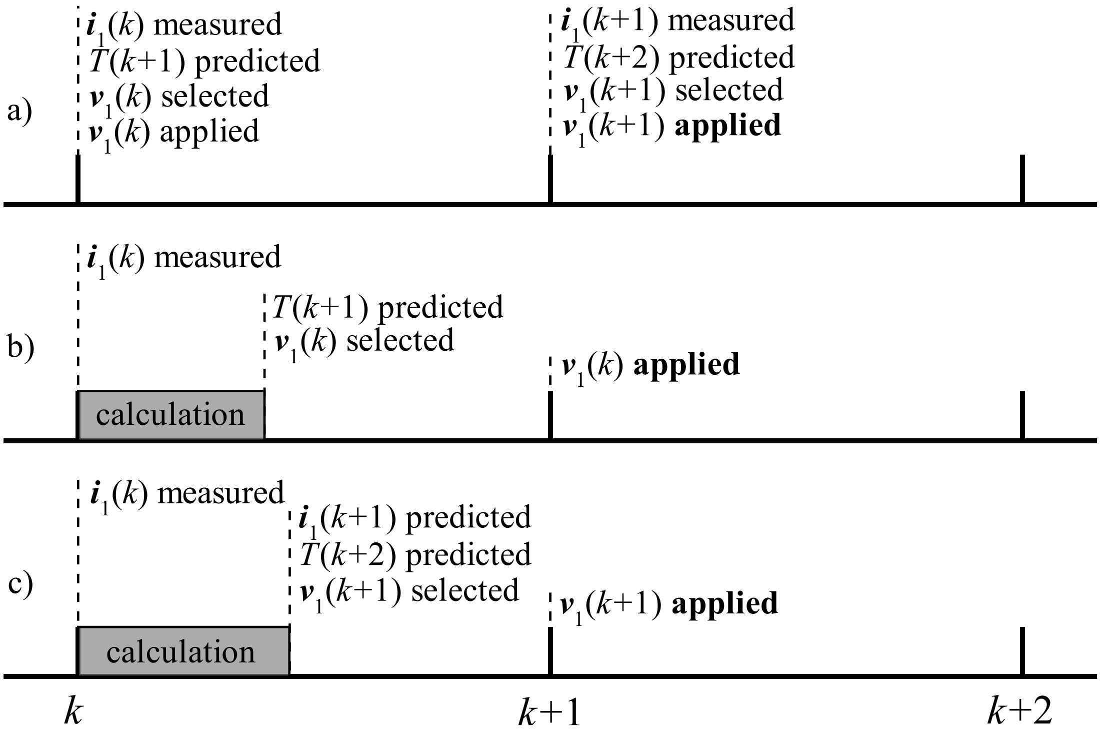

Fig. 19. Processing delay compensation in a) ideal case b) real case without compensation c) real case with compensation.

5.1.4. *Frequency Bandpass Filter*

The implementation of the PTC does not determine any pattern of the switching signals, as the control strategies using PWM does. The algorithm aims at reaching the optimal state in the next switching period, and the maximum switching frequency is limited by the sampling frequency only. However, not every switching time, the transistors change its state every. Therefore, the switching frequency is not constant, and the frequency spectra of many quantities are wide. In specific applications, such as railways, some frequencies in the current waveform are undesirable and must be suppressed [127], [128]. By incorporating a proper band-stop or band-pass filter into a cost function, the spectrum can be shaped, and undesired frequencies might be limited or desired frequencies included [19], [129]. The cost function that includes the band-stop or band-pass filter can be written as

$$g(n) = k_{CF}|\psi_1(k+1) - \psi_1^*| + |T_\mathrm{e}(k+1) - T_\mathrm{e}^*| + k_F|F(x^* - x^p)|, \tag{43}$$

where F is a digital band-stop or band-pass filter, which is defined by its transfer function. Coefficient k_F is the filter weighting coefficient, and x is the variable that is an object of the filtering, usually a stator current. An example of a current waveform with a band-pass filter at 2 kHz frequency is presented in Fig. 20.

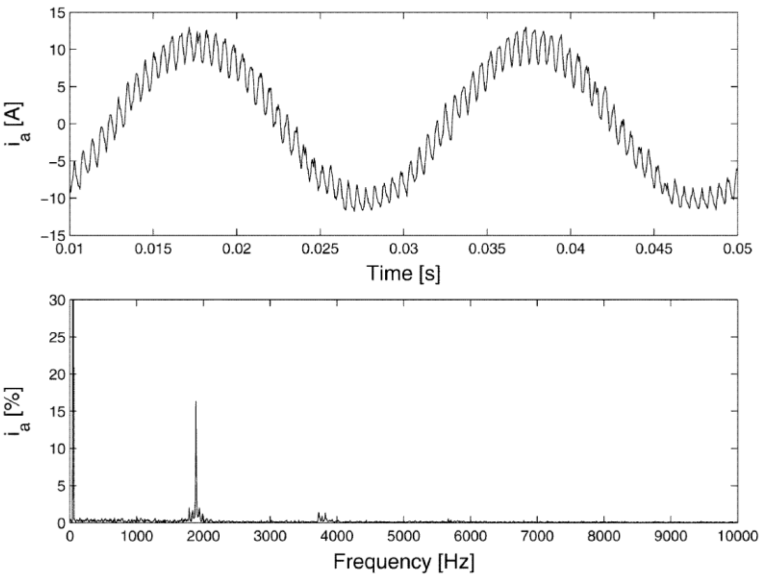

Fig. 20. Current waveform of PTC with 2 kHz band-pass filter included in the cost function, taken from [129].

5.2. Comparison of PTC and DTC

PTC and DTC strategies share many properties. The controlled variables, the generated torque and stator flux amplitude, are the same. Even the equation for obtaining these controlled variables are very similar (compare (27) with (31) and (33)). The predefined set of rules for voltage vector selection exists, even though it is expressed differently, switching table in the case of the DTC and cost function in the case of the PTC. Moreover, none of them uses the modulator, so the VSI is treated as a source of only eight fundamental voltage vectors that are applied for the whole sampling time. In recent times, many authors try to compare the DTC and PTC methods [21], [25], [130], [131]. The smaller ripple in the waveforms of the torque, the flux amplitude, and the current were achieved utilizing the PTC [132], [133], [134], [135]. An example is depicted in Fig. 21. However, the comparisons are usually based on the behavior comparison rather than on the roots of the different behavior. This would be more important for the understanding of the ripple decrease.

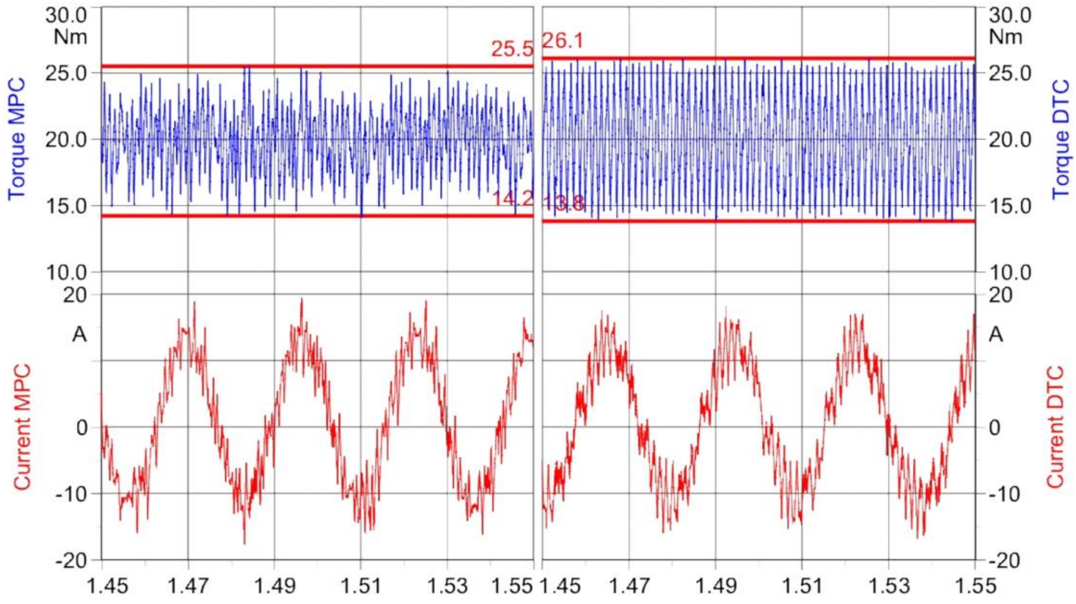

Fig. 21. Comparison of the ripples in the torque and current waveforms at DTC (right) and at predictive control (left). Published by the author [21].

The most significant difference lies in the fact that the DTC chooses the voltage vector based on the actual state only, but the PTC is based on the future state of the IM. Since the control variables are the same and one of the only eight fundamental voltage vectors is the feasible set, the chosen voltage vector is usually the same within both strategies. However, there are cases in which the worse vector is selected in the case of the DTC.

In the case of DTC, the flux plane is divided into six sectors, and the valid sector must be known at every moment. This may be problematic at the boundaries of two sectors. It is assumed that after the voltage vector application and during the whole following sampling time, the stator flux vector stays in the same sector. However, if this condition does not apply, then, in the following sector, the selected voltage vector causes different behavior than it was initially intended. This issue becomes more important with lower switching frequency. From the detailed switching pattern analysis [21], it follows that PTC overcomes this problem since the effect of the voltage vector is evaluated based on the final position of the stator flux vector rather than at its initial position. The effects of the voltage vectors on the stator flux vector are shown in Fig. 22. The figure shows that the sector evaluation at the initial and final position of the flux causes changes in the flux sectors, and, therefore, the selected vector within the DTC strategy.

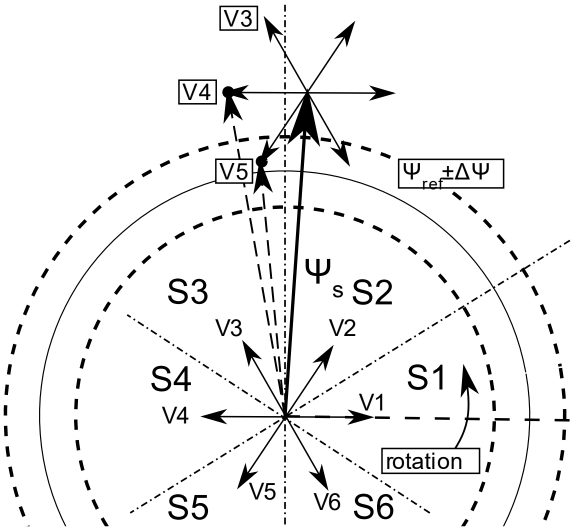

Fig. 22. The effect of each voltage vector on the flux vector at the flux sector transition. Published by the author [21].

A simulation was carried in Fig. 23, which depicts the stator flux vector trajectory in the case of the DTC. The rotation of the vector is counterclockwise. On the left side of the figure, the flux vector trajectory is shown. On the right side, detail of one border crossings is depicted. This detail shows the crossing of the stator flux vector from flux sector S3 to S4. In sector S3, the reference error is evaluated, and the flux decrease must be demanded. According to the switching table, voltage vector V5 is selected. However, after crossing to the flux sector S4, the V5 increases the flux rather than decreases. The result is that the intended flux amplitude decrease was not achieved in the case of the DTC.

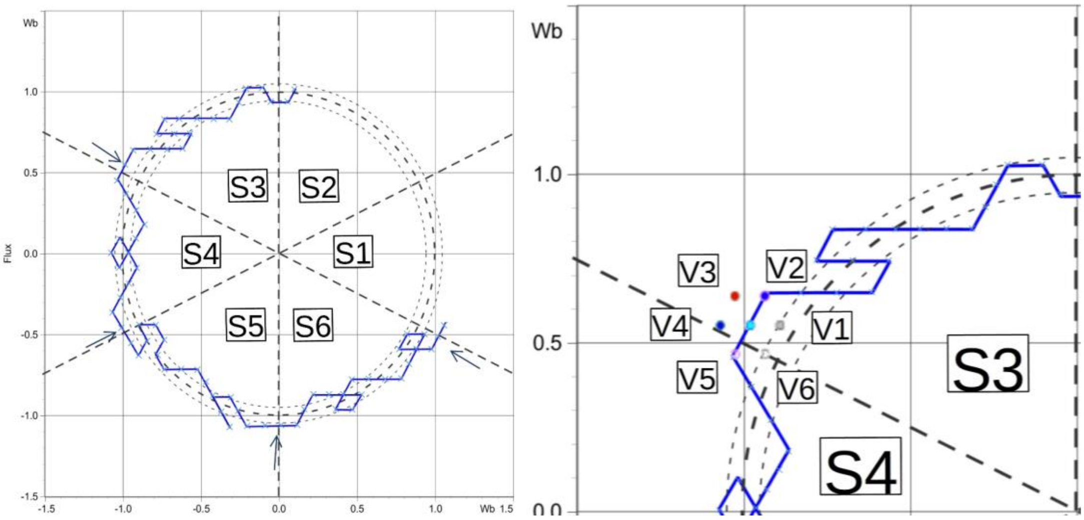

Fig. 23. The part of the flux vector tip trajectory at DTC run with the detail of the flux transition. The voltage vector V5 is selected at the marked point, but this vector increases the flux amplitude instead of its decrease. Published by the author [21].

The same simulation was performed within the PTC strategy. Fig. 24 presents the voltage vector selection at the border crossing. The voltage vector V6 selected at the marked point brings the flux vector position closer to its references. The worse vector V5 would be selected in the case of the DTC.

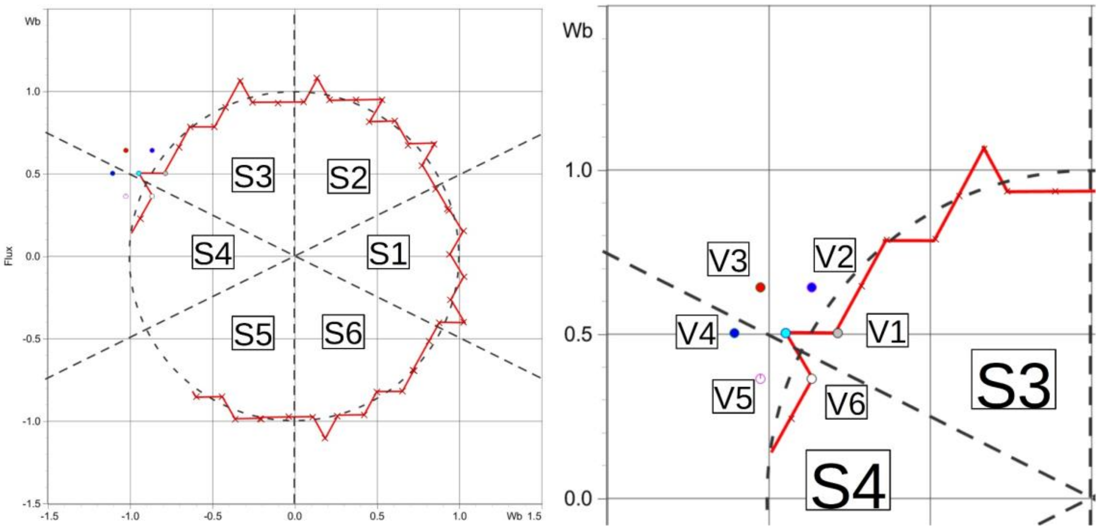

Fig. 24. The part of the flux vector tip trajectory at PTC run with the detail of the sector transition. At the marked point, the voltage vector V6 is applied to decrease flux amplitude and increase torque, but the DTC would choose V5. Published by the author [21].

Another problem arises from the different feasible voltage vectors sets. In the case of the DTC, the two voltage vectors are a priori neglected in every situation. As stated in Table 1, in every flux sector, one of the six voltage vectors may be selected, even though eight voltage vectors exist. The two vectors are always omitted. This is shown in Fig. 25.

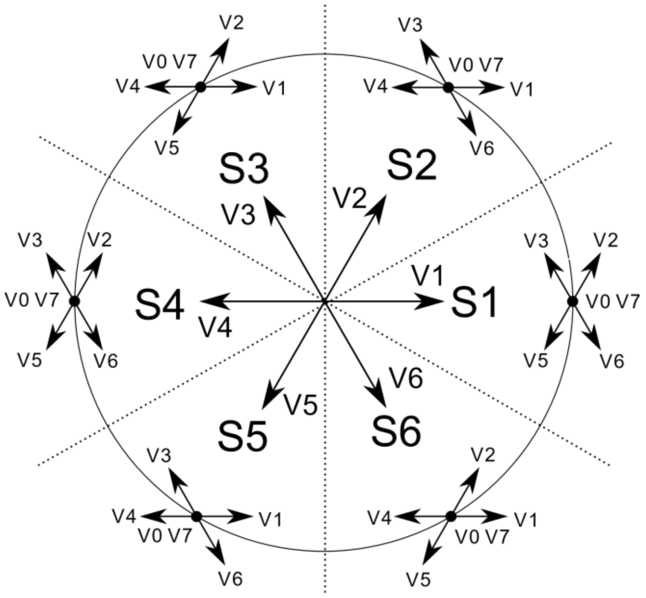

Fig. 25. The feasible set of voltage vectors in the DTC. Published by the author [21].

The simulation of such a case was performed. Fig. 26 shows the trajectory of the stator flux vector within the PTC strategy. On the right side, the detail of the trajectory in the flux sector S2 is depicted. In the sector, the voltage vectors neglected by the DTC (V2 and V5) were selected three times. At the marked position, the voltage vector V2 was selected.

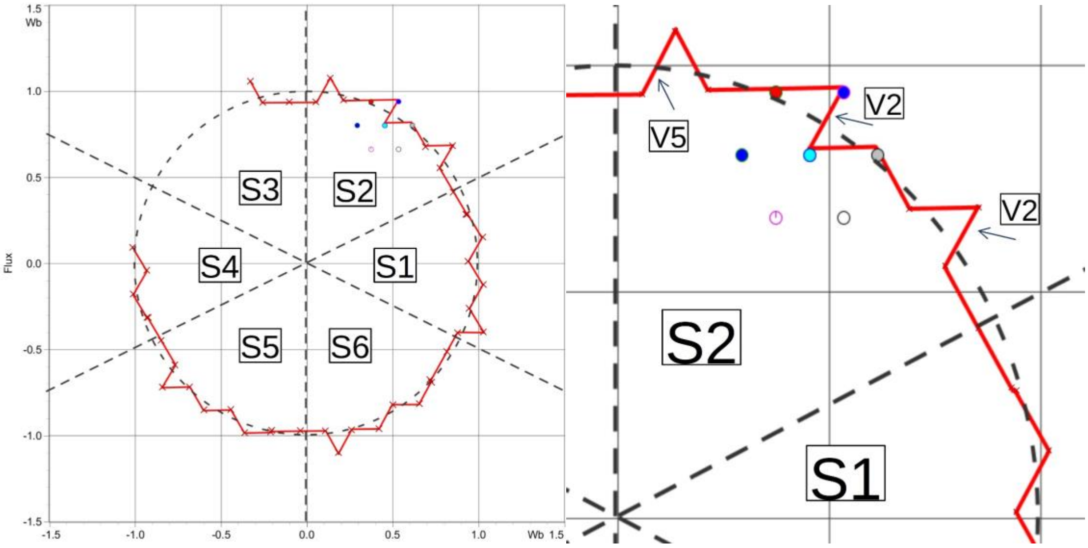

Fig. 26. The part of the flux vector tip trajectory at PTC run with its detail. The arrows mark where the PTC selects the voltage vectors neglected by the DTC. Published by the author [21].

Fig. 27 shows the effect of every voltage vector in the situation from Fig. 26 on the flux amplitude and torque waveforms. The PTC selected the neglected voltage vector V2. The DTC would select the voltage vector V3, which significantly increases the torque above its reference. It was shown in [21], that such neglection might cause an additional ripple in the torque waveforms. This undesired effect is not present at PTC since the selection is based on a larger feasible set of voltage vectors.

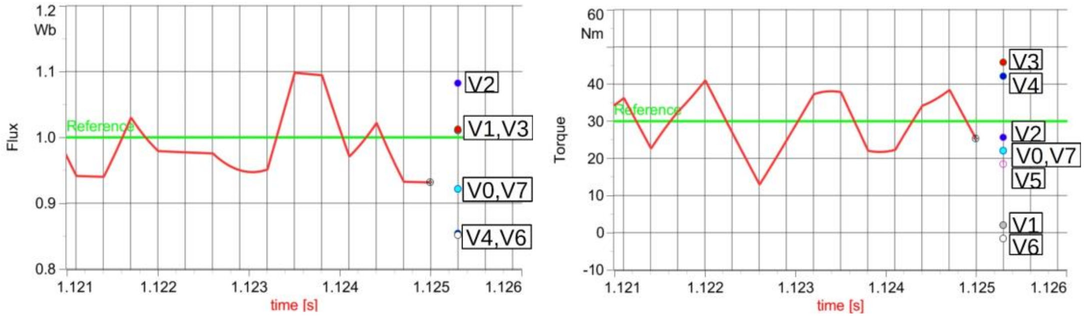

Fig. 27. The flux amplitude (left side) and the torque waveforms at PTC run with the predicted effects of all voltage vectors. Published by the author [21].

5.3. Torque and Current Ripple Decrease

The current ripple and high THD are a common drawback of all control methods utilizing the inverter [136]. Moreover, with the current ripple, the higher torque waveform ripple is connected. This is particularly the case of the DTC since no modulator is used. The PTC shares the same idea of fundamental voltage vector switching, so it also shares these drawbacks. Several methods to suppress the ripple have been developed so far. They are described in the following section, and their performances are shown.

5.3.1. Long-Horizon Prediction

The predictive control horizon defines how many sample times ahead are predicted. Even though the typical PTC implementation deals with only a one-step horizon, it is not limited to it [36], [137], [138]. In the case of PTC, optimum searching is usually solved by enumerating all possible solutions [53]. However, with the increased step horizon, the number of candidates for which the control variables must be predicted increases exponentially. In practical implementations, this would be impossible, even if many duplicate switching sequences were omitted. An efficient optimization solving for prediction with a longer horizon is still a challenge for the researchers. One solution is to restrict the feasible set [139]. However, then, it is not guaranteed that the optimal solution will be found, and dealing with suboptimal solutions will arise [140]. Other solutions based on sphere-decoding [141] has been proposed in [35], [50], [51]. Such an approach can, on average, enumerate the prediction with horizon ten as quickly as the traditional approach enumerates prediction with horizon one.

The principle of the prolonged horizon is explained in Fig. 28 with a simplified situation for prediction horizon k+5, where the system with only one input $\boldsymbol{U}_{\mathrm{pred}}(k)$ with two possible candidates and one output $\boldsymbol{Y}_{\mathrm{pred}}(k)$ is depicted.

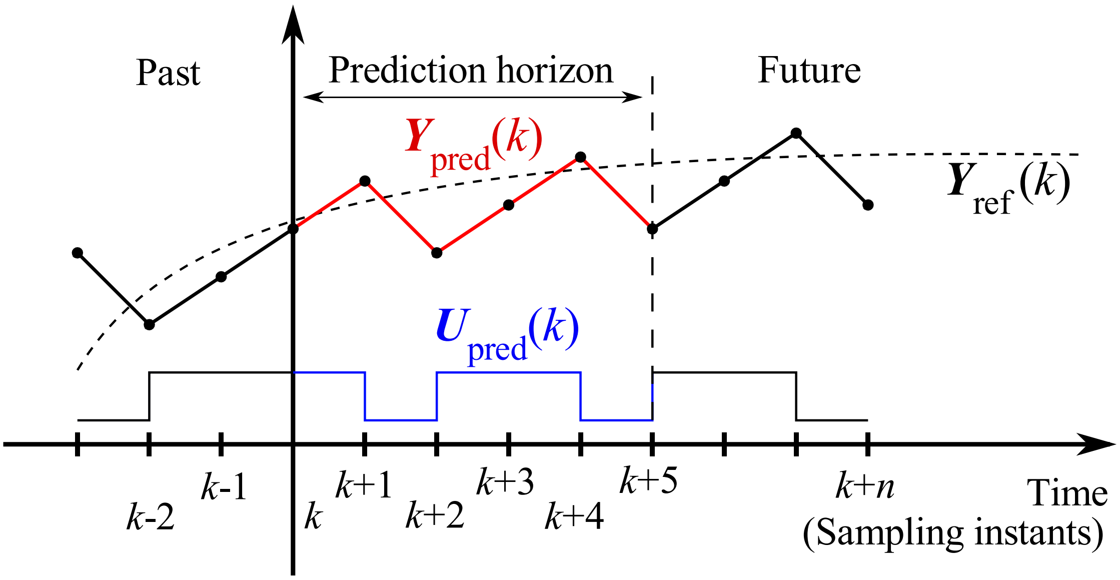

Fig. 28. Prolonged horizon for a system with one input and one output.

The long-horizon prediction brings some advantages at the cost of complexity increase. However, it has been experimentally proven that for first-order systems such as an induction motor with VSI, the long horizon prediction does not bring much performance increase. This would be beneficial for more complex systems, such as VSI with induction motor and LC filter (third-order system) [38]. In Fig. 28, the comparison of MPC with a one-step and ten-step horizon along with SVM is presented. The figure shows the dependency of the THD of the stator current on the switching frequency for these three strategies. It shows that the horizon increase does not significantly improve the performance, especially in the switching frequencies above 1 kHz. The computational burden and small improvement usually limit the prediction horizon to one.

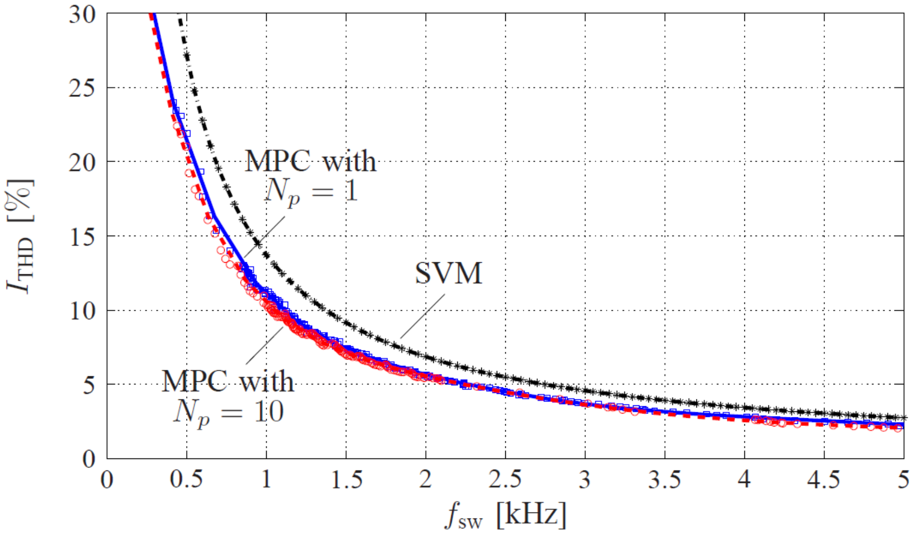

Fig. 29. Stator current THD comparison for three cases. MPC with a one-step, ten-step horizon, and SVM technique, taken from [38].

5.3.2. *Variable Switching Point*

Within PTC, each switching state is applied for at least one sampling time. An active voltage vector usually causes higher current and torque changes compared to the passive voltage vector. If it could be applied for a time interval shorter than one sampling time, then the torque waveform ripple could be reduced. Such a principle was proposed in [51], [52] and is shown in Fig. 30. For simplicity, only two voltage vectors are considered in the figure; the active vector, causing higher positive change in the torque and passive vector, causing lower negative change. The active vector leads to high ripple, and the longer time it is applied, the higher the ripple. If the switching takes place during the sampling time, the ripple could be reduced. However, as seen in the figure, such an approach increases switching frequency.

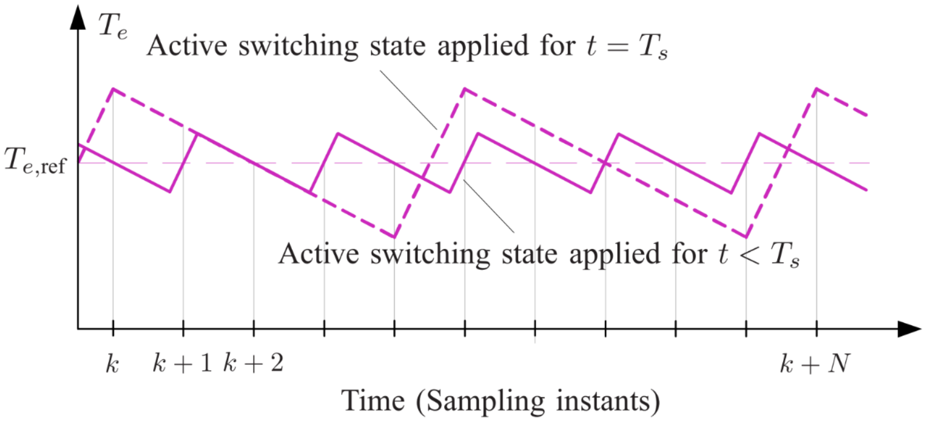

Fig. 30. Variable switching point method operational principle, taken from [52].

The effect of this method on the torque ripple and on the current THD was measured in [52] and is presented in Fig. 31. In the figure, the blue curve represents the traditional PTC, and the red curve the PTC with a variable switching point. The figure shows the ripple decrease in all measured operating points.

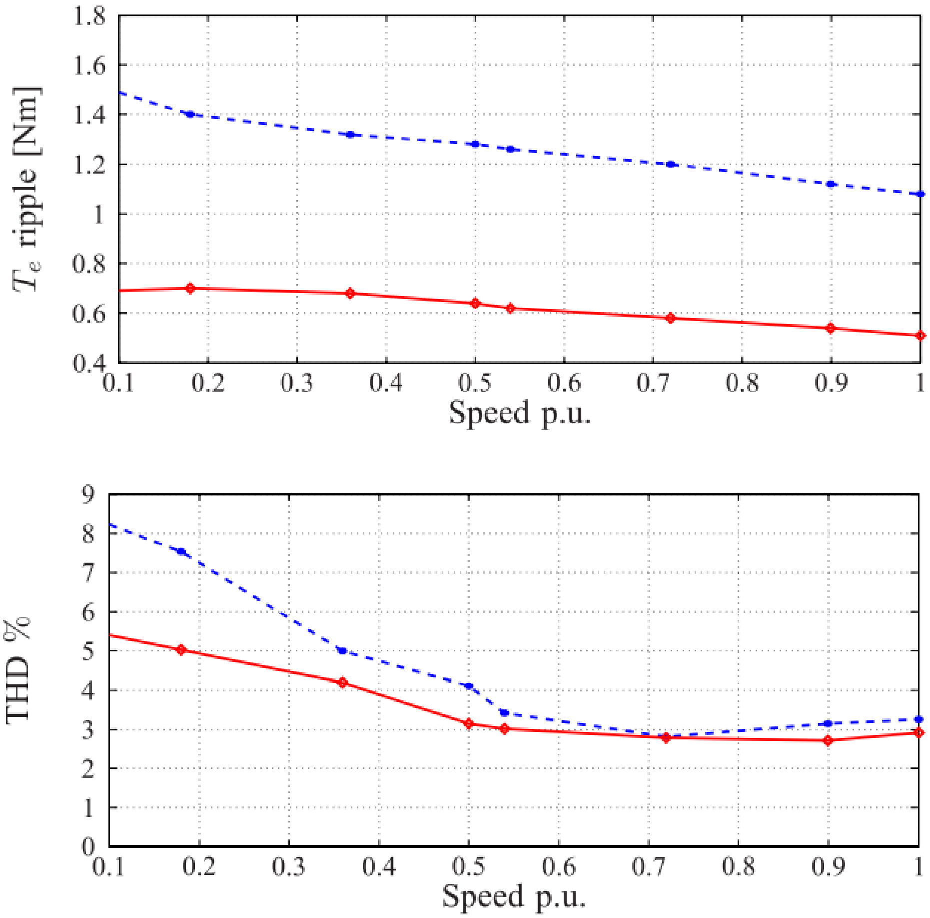

Fig. 31. Torque ripple (top) and current THD (bottom) reduction, taken from [52]. Blue curve – traditional PTC, red curve – PTC with variable switching point.

5.3.3. Voltage Vector Optimization with Space Vector Modulation

Using the space vector modulation (SVM), an infinite number of voltage vectors are the feasible candidates. Therefore, the more suitable vector can be applied than in the case of only eight vectors. Since the prediction of an infinite number of candidates is the case of CS-MPC, another approach is usually utilized in the case of FS-MPC. An example is presented in [39], where an algorithm for the ripple minimization using SVM is proposed. At first, one of the eight arbitrary voltage vectors ($\boldsymbol{u}_\mathrm{s}^*$ in the figure) is selected by the predictive control. Then, the stator flux error ($\Delta\lambda_\mathrm{s}$ in the figure) is evaluated, and the previously selected voltage vector is adjusted in its d-component (*dq* coordinates are rotating with the magnetic field and are linked to the rotor flux vector λ_r) in order to reach the stator flux reference. Therefore, instead of the whole sample time T_s the reduced time T_k is used, which changes the selected voltage vector $\boldsymbol{u}_\mathrm{s}^*$ to $\boldsymbol{u}_\mathrm{mod}^*$. The principle is depicted in Fig. 32.

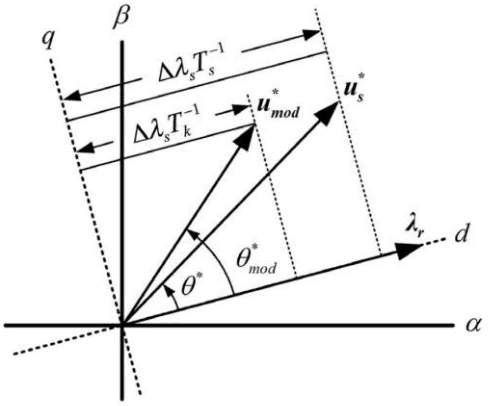

Fig. 32. Principle of voltage vector optimization method suppressing the ripple, taken from [39].

Since the resulting voltage vector has a modified angle (θ_mod^*) and amplitude, it is not one of the eight arbitrary ones, and the SVM must be used for its application. Fig. 33 shows the decrease of the flux (bottom) and torque (top) waveforms. On the top, the fundamental PTC, and, on the bottom, the optimized method are shown.

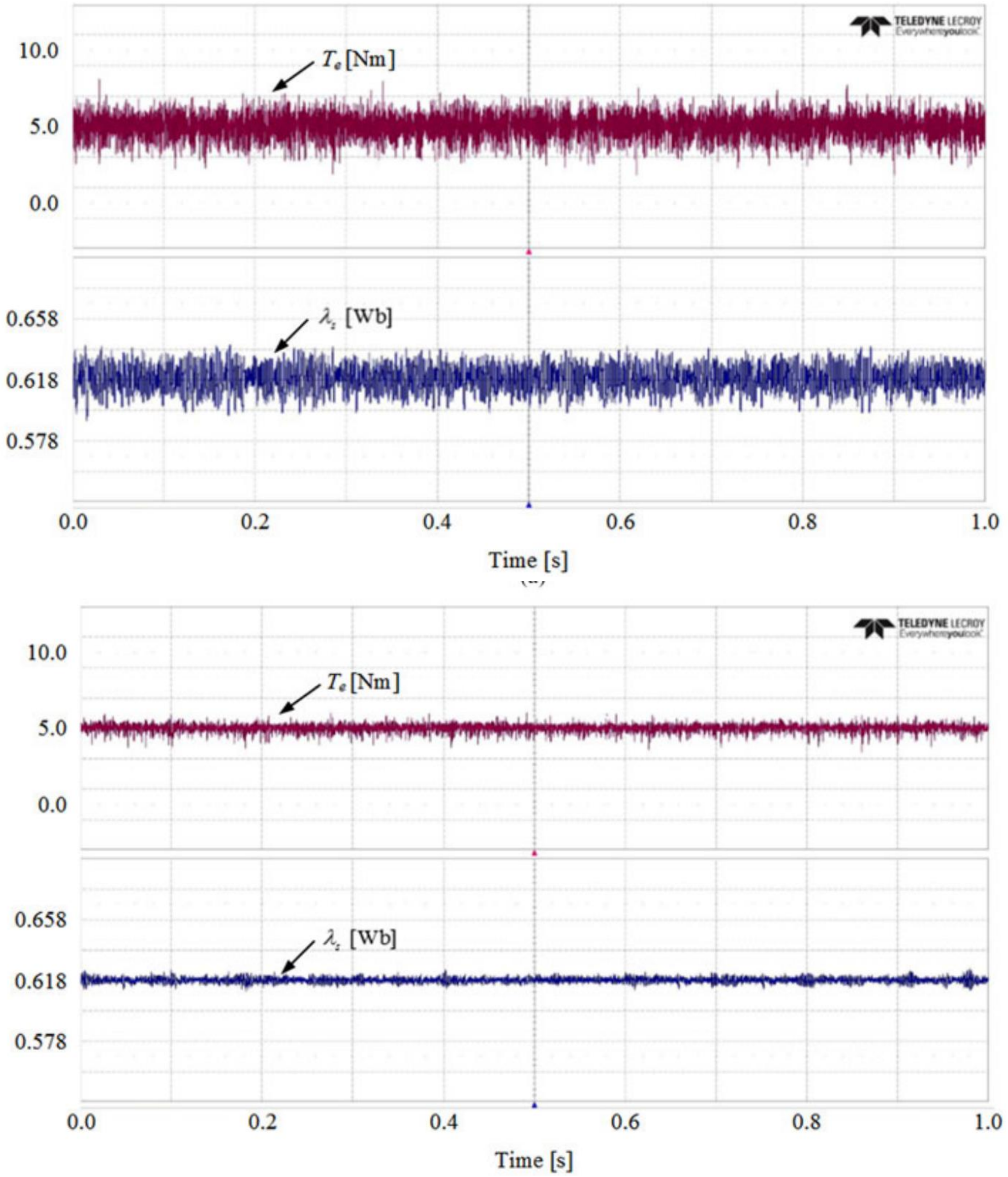

Fig. 33. Torque and flux ripple comparison of traditional PTC and PTC with voltage optimization, taken from [39]. Top – traditional PTC, bottom – optimized method.

5.3.4. Finite Set Expansion

The most common implementation of PTC utilizes the two-level inverter, which creates eight fundamental voltage vectors. These fundamental vectors are treated as feasible voltage vector candidates. However, using vector modulation, more voltage vectors can be created. For example, in [142], the 36 voltage vectors are defined, and in [33], two different sets of voltage vectors, with 18 and 12 vectors, are defined. The definition of the latter case is depicted in Fig. 34.

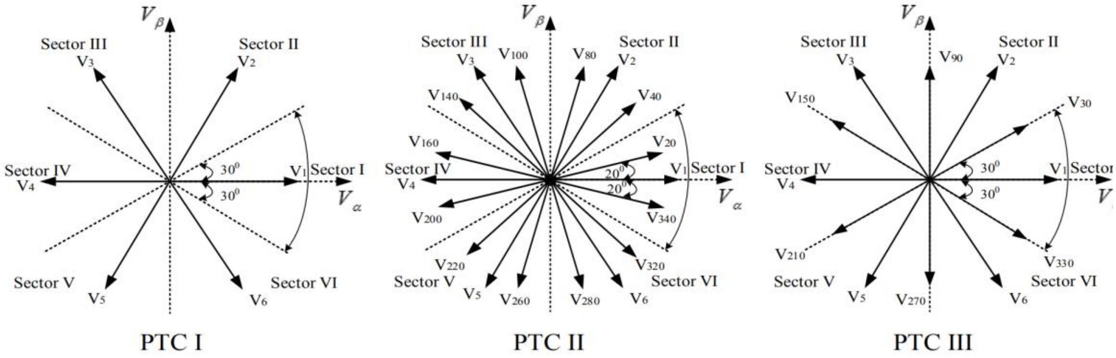

Fig. 34. Definition of voltage space vector using modulation, taken from [33].

The experiment conducted in [33] showed that the finite set expansion utilizing modulation could decrease the current THD. The performance is shown in Fig. 35. However, within this strategy, the switching frequency increases, which is not always possible, especially in high power applications. Another disadvantage lies the computational burden since the control variables must be predicted for more candidates.

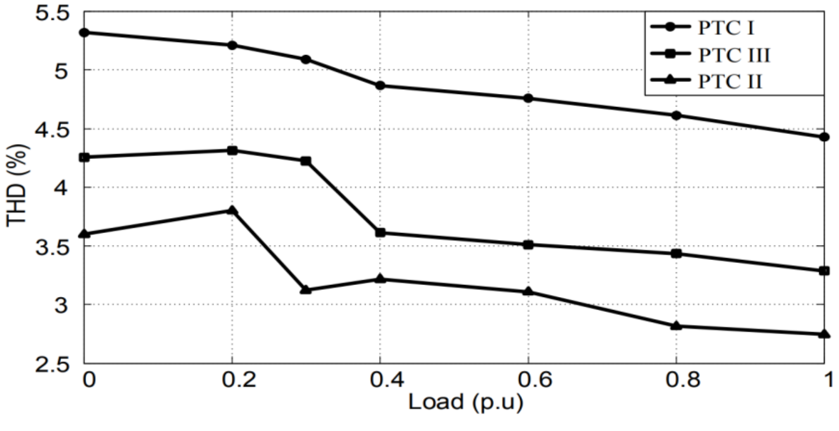

Fig. 35. Current THD comparison for PTC and PTC with a higher feasible set of candidates. PTC I – traditional PTC, PTC II – PTC with 18 voltage vectors, PTC III - PTC with 12 candidates. Taken from [33].

Allowing hardware modification of the inverter, the finite set of feasible voltage vectors can be increased without the increase in the switching frequency. The most common two-level inverter replacements are the multilevel inverters [34],[35], and matrix converters [5]. However, their usage is not the object of this thesis.

5.3.5. DC-Link Voltage Optimization

With the utilization of the controlled rectifier or additional DC-DC convertor, the torque and current ripple of IM and permanent magnet synchronous motor (PMSM) can be reduced with the optimization of the DC-link voltage. This applies regardless of the used control strategy. The AC motor can be considered as an inductive load; therefore, it follows, that lowering the DC-link lowers the current and torque waveforms ripples. This applies especially in the area of rotational speed lower than the motor's rated speed because the induced voltage is lower. Moreover, lowering the DC-link voltage reduces other losses, such as motor losses [66], [143], [144] and insulation stress [145]. The optimal DC-link voltage can be calculated from the voltage vector reference coming from the current controllers [146], [147], [148], [149]. However, this is possible only in such control strategies where the reference voltage vector amplitude is explicitly expressed, i.e., strategies using modulators. Other approaches utilizing the DC-link voltage optimization determine the optimal DC-link voltage from the measured quantities and motor parameters [150], [151], [152], [153]. The disadvantage of such an approach is the open-loop algorithm that deteriorates the performance. Moreover, with such an approach, the lower torque and current ripples are only the consequences of the reduced voltage; the DC-link voltage is not the result of torque ripple minimizing algorithm, so the lowest possible ripple is not guaranteed. However, good results were obtained using this approach. An example of the performance with the open-loop DC-link voltage optimization compared to full DC-link voltage is provided in Fig. 36. The test was carried in [152], and the results presented in the figure show that the torque, the flux amplitude, and the speed waveforms ripples for the full DC-link (top) are higher than for the optimized DC-link (bottom).

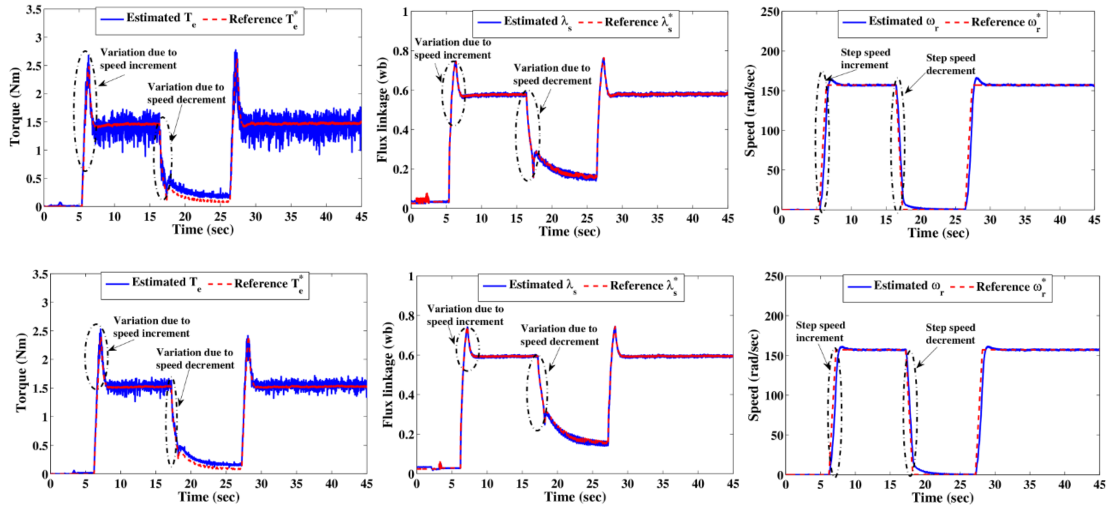

Fig. 36. Torque, flux amplitude and speed waveforms of the drive with full DC-link (top) and DC-link voltage optimized in an open loop (bottom), taken from [152].

Concerning the DC-link voltage optimization as the direct consequence of the torque ripples, the analysis and proposed optimization method are presented in section 6.

Another approach of the DC-link voltage optimization lies in the virtual voltage level decrease achieved by the modulation of the output vector. The advantage is that no additional hardware is required. However, the modulator must be present, and the switching frequency of the inverter increases. Literature [40] proposes optimal duty cycle control. During each sampling time, the selected voltage vector is applied for a specific time, and, for the remaining time, the passive vector is applied. The time durations of the selected and passive voltage vectors are based on the deadbeat torque control principle. To reach the same effect, [41] proposes the selected voltage vector time duration determined by another cost function, the so-called tracking cost index. Such approaches virtually decrease the amplitude of the applied vector. An example of these ripple minimizing strategies is presented in Fig. 37.

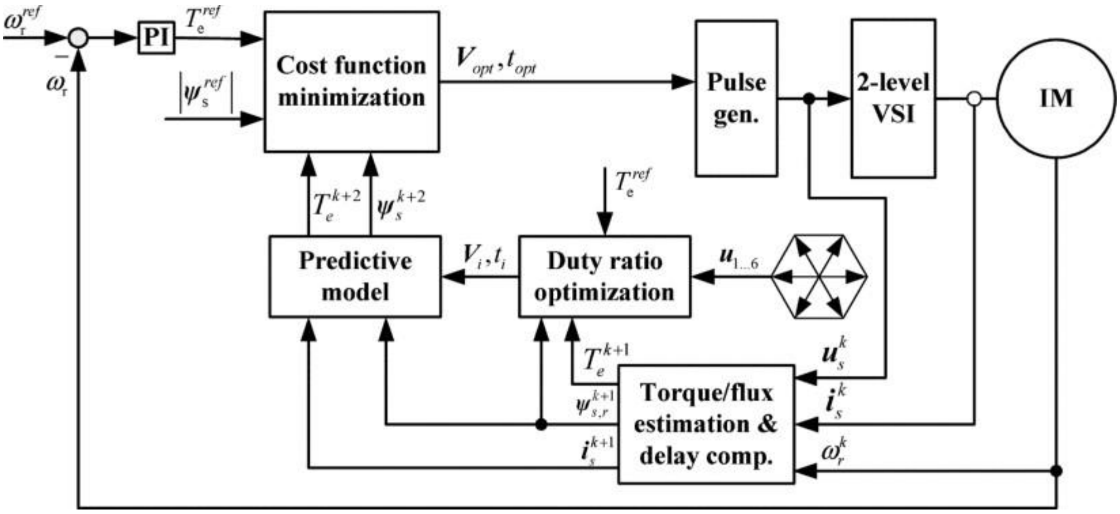

Fig. 37. PTC with duty cycle optimization, taken from [40].

The current THD and torque ripple are shown in Fig. 38 for three different operation points. The tests were performed in [40] and the results for traditional PTC (Conventional MPTC in the figure) with 20 kHz sampling frequency and for optimal duty cycle PTC with 20 kHz (MPTC I) and 10 kHz (MPTC II) sampling frequency are presented in the figure.

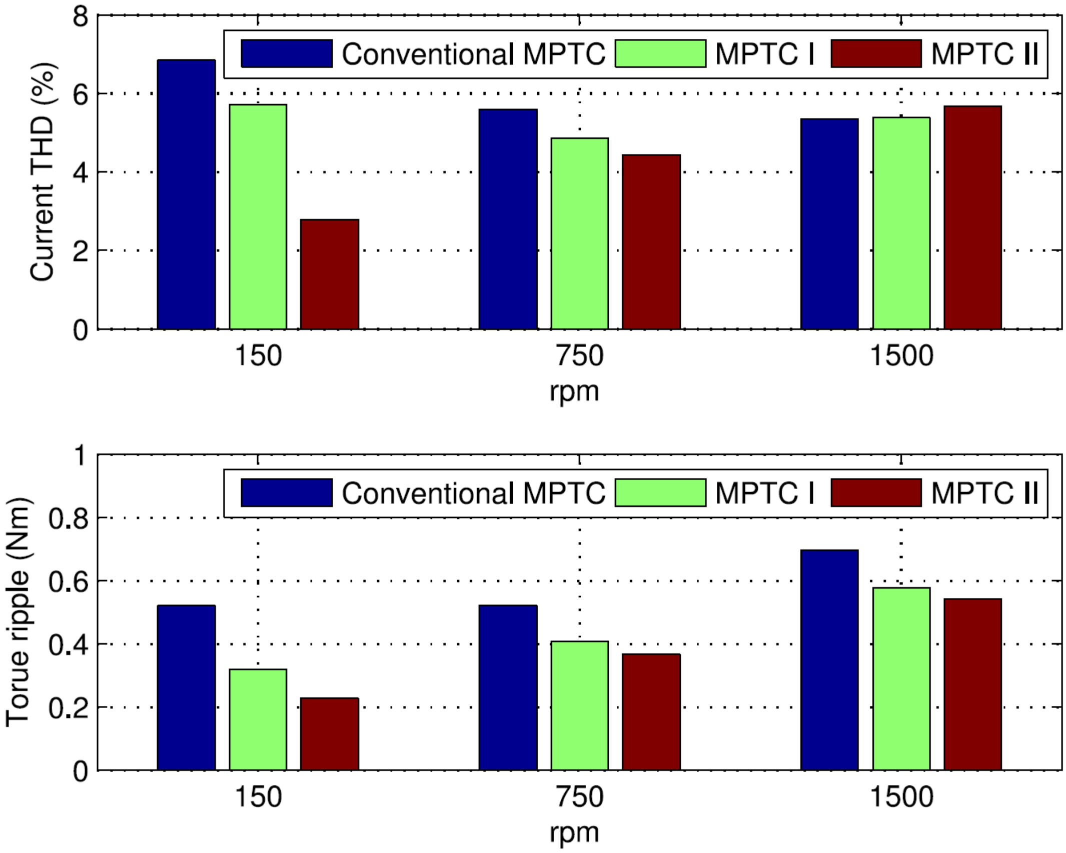

Fig. 38. Torque ripple (bottom) and current THD (top) comparison of traditional PTC and optimal duty cycle PTC with different sampling times, taken from [40].

5.4. Predictive Torque Control Summary

The FS-PTC is the most common implementation of MPC in the field of electric drives and power electronics. The working principle of the method, the predictive model, and cost function were described in this chapter. For the practical implementation of the control method, some important aspects must be considered. The current limitation, processing delay compensation, and switching frequency adjustment issues with their typical solutions were described.

The PTC's control variables are the torque and stator flux amplitude, which makes it similar to the DTC strategy. Moreover, none of them uses a modulator, which brings other common properties, such as a similar switching pattern. The detailed comparison between the two method was performed and was also published in [21].

One of the problematic behaviors of the PTC is a relatively high torque waveform ripple and high current THD. Since the thesis objective is to decrease this ripple, the existing solutions were introduced.

6. Predictive Torque Control with DC-Link Voltage Optimization

This chapter analyses the influence of the DC-link voltage on the torque and current ripple of IM drive. It proofs that with lower DC-link voltage, the torque and the current ripples decrease. Further, it derives the limitations for the minimum voltage. Finally, a new DC-link voltage optimization method based on model-based prediction is proposed. This optimization is then included into the PTC strategy.

6.1. DC-Link Voltage Control

A variable speed drive usually consists of a three-phase voltage source, a rectifier, DC-link capacitor with a coil, inverter, and the motor itself. The most common rectifier is just a simple diode bridge. The diode rectifier belongs to the group of uncontrolled rectifiers, and the output voltage depends on the input voltage only, i.e., the DC-link voltage is always constant, if the controlled machine is in the motoring mode [154]. However, in some applications, a solution enabling the DC-link voltage control can be required. The most advanced solution is the PWM rectifier consisting of transistors with antiparallel connected diodes in a bridge topology. Such topologies are called active front end (AFE), and the model predictive control of such a rectifier has also been developed [12], [155], [156]. They are usually controlled to reduce the reactive power drawn from the electrical grid, which is known as power factor correction (PFC) [157]. The suppression of the reactive power flow is their most significant advantage compared to other rectifiers. However, the disadvantage is the increased switching losses that are present due to the PWM operation. These topologies are utilized in some high-power applications, such as in railway vehicles with AC drives [158], [159]. The usage of high-power rectifiers enabling the DC-link voltage control is mentioned in the literature [160]. If the DC-link voltage control is required, a DC/DC converter is added between the rectifier and the inverter [155], [161]. This is not the only topology allowing the DC-link voltage control. Another one is, for example, a topology consisting of a middle frequency transformer, which was suggested in [162].

The commonly used simple controlled rectifier is the silicon controller rectifier (SCR) consisting of thyristors in a bridge configuration. Within such a rectifier, the output voltage is controlled by the pulses to the gates of the thyristors. The pulses must be synchronized with the grid voltage zero crossings of the and are delayed by a specific angle corresponding to the reference DC-link voltage. The disadvantage is the higher output voltage ripple and the reactive power drawn from the grid. On the other side, the advantage may be found in easier control. Also, the switching losses are smaller, since no PWM switching is used. In the case of drives with AC motors, the SCR is already present in many applications and is used for the initial charging of the DC-link capacitor. During the actual operation, it then operates with a zero-switching angle (as a diode rectifier) [163].

6.2. Influence of DC-Link Voltage on Torque Ripple

In the following section, the mathematical evaluation of the lower DC-link voltage on the torque ripple is provided. It shows that the lower voltage leads to lower torque ripple. For this purpose, the standard IM vector equations are used [164], [165].

The equation of the IM torque is based on the stator current and stator flux vectors. When Clarke's transformation with coefficient 2/3, the equation is

$$T_{\mathrm{e}} = \frac{3}{2} p_{\mathrm{p}} \Im\{\boldsymbol{i}_1 \overline{\boldsymbol{\psi}}_1\}, \tag{44}$$

where the overline denotes conjugate of the complex space vector. The time derivative of the torque can be then written as

$$\frac{\mathrm{d}T_{\mathrm{e}}}{\mathrm{d}t} = \frac{3}{2} p_{\mathrm{p}} \Im\left\{\frac{\mathrm{d}}{\mathrm{d}t}\left(\boldsymbol{i}_1 \overline{\boldsymbol{\psi}}_1\right)\right\} = \frac{3}{2} p_{\mathrm{p}} \Im\left\{\frac{\mathrm{d}\boldsymbol{i}_1}{\mathrm{d}t} \overline{\boldsymbol{\psi}}_1 + \boldsymbol{i}_1 \frac{\mathrm{d}\overline{\boldsymbol{\psi}}_1}{\mathrm{d}t}\right\}. \tag{45}$$

The derivative of the torque contains the time derivations stator flux and current vectors. The derivative of the stator flux vector is

$$\frac{\mathrm{d}\overline{\boldsymbol{\psi}}_1}{\mathrm{d}t} = \boldsymbol{v}_1 - R_1 \bar{\boldsymbol{i}}_1, \tag{46}$$

and the derivative of the stator current vector

$$\frac{\mathrm{d}\boldsymbol{i}_1}{\mathrm{d}t} = C_1 \boldsymbol{i}_1 + C_2 \boldsymbol{v}_1 + C_3 \boldsymbol{\psi}_2 - \mathrm{j}\omega C_4 \boldsymbol{\psi}_2, \tag{47}$$

where ω is the rotor electrical speed, and the coefficients are defined as

$$\begin{gathered} C_1 = -\frac{R_2 L_{\mathrm{m}}^2 + L_2^2 R_1}{\sigma L_1 L_2^2}, C_2 = \frac{1}{\sigma L_1}, C_3 = \frac{L_{\mathrm{m}} R_2}{\sigma L_1 L_2^2}, \\ C_4 = \frac{L_{\mathrm{m}}}{\sigma L_1 L_2}, \sigma = 1 - \frac{L_{\mathrm{m}}^2}{L_1 L_2}. \end{gathered} \tag{48}$$

The time derivative of the stator current is dependent on the rotor flux vector. Because the stator and rotor flux vector have the relationships given by

$$\boldsymbol{\psi}_2 = \frac{L_2}{L_{\mathrm{m}}} (\boldsymbol{\psi}_1 - \sigma L_1 \boldsymbol{i}_1), \tag{49}$$

the equation (49) can be substituted into (47), which gives

$$\frac{\mathrm{d}\boldsymbol{i}_1}{\mathrm{d}t} = C_1 \boldsymbol{i}_1 + C_2 \boldsymbol{v}_1 + C_5 \boldsymbol{\psi}_1 - \tau_{\mathrm{r}}^{-1} \boldsymbol{i}_1 - \mathrm{j}\omega C_2 \boldsymbol{\psi}_1 + \mathrm{j}\omega \boldsymbol{i}_1, \tag{50}$$

where

$$C_5 = \frac{R_2}{\sigma L_1 L_2}. \tag{51}$$

Now, the (50) and (46) can be put into (45), which yields the time derivative of the torque with dependence on the only stator flux and current vectors as

$$\frac{\mathrm{d}T_\mathrm{e}}{\mathrm{d}t} = \frac{3}{2}p_\mathrm{p}\Im\{C_1\boldsymbol{i}_1\overline{\boldsymbol{\psi}}_1 + C_2\boldsymbol{v}_1\overline{\boldsymbol{\psi}}_1 + C_5\boldsymbol{\psi}_1^2 - \tau_\mathrm{r}^{-1}\boldsymbol{i}_1\overline{\boldsymbol{\psi}}_1 - \mathrm{j}\omega C_2\boldsymbol{\psi}_1^2 + \mathrm{j}\omega\boldsymbol{i}_1\overline{\boldsymbol{\psi}}_1 \\ + \overline{\boldsymbol{v}}_1\boldsymbol{i}_1 - R_1\boldsymbol{i}_1^2\}. \tag{52}$$

The terms with no imaginary part are omitted and with (44), we get

$$\frac{\mathrm{d}T_\mathrm{e}}{\mathrm{d}t} = C_7T_\mathrm{e} + \frac{3}{2}p_\mathrm{p}\Im\{\mathrm{j}\omega\boldsymbol{i}_1\overline{\boldsymbol{\psi}}_1 + C_2\boldsymbol{v}_1\overline{\psi}_1 + \overline{\boldsymbol{v}}_1\boldsymbol{i}_1\}. \tag{53}$$

where

$$C_7 = C_1 - \tau_\mathrm{r}^{-1} \tag{54}$$

Only eight switching combinations can be created with a common two-level three-phase inverter. The control strategies operating without the modulator, such as the PTC, consider this set of eight fundamental voltage vectors as the feasible candidates. The magnitude of the two passive vector is zero and of the six active vectors depends on the DC-link voltage. When Clarke's transformation with coefficient 2/3 is used, the magnitude of the six active vectors is given as

$$|\boldsymbol{v}_1| = v_1 = \frac{2}{3}V_\mathrm{DCmax}, \tag{55}$$

where V_DCmax is the DC link voltage in the case of an uncontrolled rectifier, i.e., full DC-link voltage. The set of the feasible voltage vectors can be written in a complex form using Euler's formula as

$$\boldsymbol{v}_1 = v_1\mathrm{e}^{\mathrm{j}\gamma} = \frac{2}{3}V_\mathrm{DCmax}\mathrm{e}^{\mathrm{j}\gamma}, \tag{56}$$

where

$$\gamma \in \left\{0, \frac{\pi}{3}, \frac{2\pi}{3}, \pi, \frac{4\pi}{3}, \frac{5\pi}{3}\right\}. \tag{57}$$

The Euler's formula can be used on the stator current and flux vectors as well, which yields

$$\boldsymbol{i}_1 = i_1\mathrm{e}^{\mathrm{j}\delta}, \tag{58}$$

and

$$\boldsymbol{\psi}_1 = \psi_1\mathrm{e}^{\mathrm{j}\varepsilon}, \tag{59}$$

respectively.

In case of a SCR, the six active voltage vectors can be written as

$$\boldsymbol{v}_1' = k_\mathrm{DC}v_1\mathrm{e}^{\mathrm{j}\gamma} = k_\mathrm{DC}\frac{2}{3}V_\mathrm{DCmax}\mathrm{e}^{\mathrm{j}\gamma}, \tag{60}$$

where $k_\mathrm{DC} \in (0,1)$ is coefficient respecting the DC-link voltage amplitude ration to full DC link voltage V_DCmax. In case of the SCR, the torque derivative changes from (53) to

$$\frac{\mathrm{d}T_\mathrm{e}'}{\mathrm{d}t} = C_7T_\mathrm{e} + \frac{3}{2}p_\mathrm{p}\Im\{\mathrm{j}\omega\boldsymbol{i}_1\overline{\boldsymbol{\psi}}_1 + C_2\boldsymbol{v}_1'\overline{\boldsymbol{\psi}}_1 + \overline{\boldsymbol{v}}_1'\boldsymbol{i}_1\}. \tag{61}$$

If the voltage vectors (56) and (60) are applied at time $t = 0\,\mathrm{s}$, the torque derivatives (53) and (61), respectively, can be compared as

$$\Delta\dot{T}_\mathrm{e} = \lim_{t\to 0^+}\left(\frac{\mathrm{d}T_\mathrm{e}}{\mathrm{d}t} - \frac{\mathrm{d}T'_\mathrm{e}}{\mathrm{d}t}\right). \tag{62}$$

With his description, the state variables values will remain approximately the same in both cases. With utilizing (53) and (61), the equation (62) can be rewritten as

$$\Delta\dot{T}_\mathrm{e} = (1 - k_{DC})p_\mathrm{p}V_\mathrm{DCmax}C_2[\psi_1\sin\vartheta - i_1L_1\sigma\sin\varphi], \tag{63}$$

where the angles are defined as $\varphi = \gamma - \delta$ and $\vartheta = \gamma - \varepsilon$. The vector diagram with all utilized angles is presented in Fig. 39. The sine values of an angle can be expressed with their corresponding vectors. In this case, as

$$\Im\{\boldsymbol{v}_1\overline{\boldsymbol{\psi}}_1\} = \psi_1 v_1\sin\vartheta \Rightarrow \sin\vartheta = \frac{\Im\{\boldsymbol{v}_1\overline{\boldsymbol{\psi}}_1\}}{\psi_1 v_1} = \frac{\Im\{\mathrm{e}^{\mathrm{j}\gamma}\overline{\boldsymbol{\psi}}_1\}}{\psi_1}, \tag{64}$$

and

$$\Im\{\boldsymbol{v}_1\overline{\boldsymbol{i}}_1\} = i_1 v_1\sin\varphi \Rightarrow \sin\varphi = \frac{\Im\{\boldsymbol{v}_1\overline{\boldsymbol{i}}_1\}}{i_1 v_1} = \frac{\Im\{\mathrm{e}^{\mathrm{j}\gamma}\overline{\boldsymbol{i}}_1\}}{i_1}. \tag{65}$$

Then, (63) is written as

$$\Delta\dot{T}_\mathrm{e} = (1 - k_{DC})p_\mathrm{p}V_\mathrm{DCmax}C_2\Im\{\mathrm{e}^{\mathrm{j}\gamma}[\overline{\boldsymbol{\psi}}_1 - \sigma L_1\overline{\boldsymbol{i}}_1]\}. \tag{66}$$

The expression (49) is put into the equation and yields

$$\Delta\dot{T}_\mathrm{e} = (1 - k_{DC})p_\mathrm{p}V_\mathrm{DCmax}C_8\Im\{\mathrm{e}^{\mathrm{j}\gamma}\overline{\boldsymbol{\psi}}_2\} = (1 - k_{DC})p_\mathrm{p}V_\mathrm{DCmax}C_8\boldsymbol{\psi}_2\sin\xi, \tag{67}$$

where ξ is the angle between $\boldsymbol{v}_1$ and $\boldsymbol{\psi}_2$, and $C_8 = L_\mathrm{m}/L_1L_2 - L_\mathrm{m}^2$. The final equation expresses how much bigger the torque will in the case full DC-link voltage V_DCmax to the reduced DC-link voltage $k_\mathrm{DC}V_\mathrm{DCmax}$.

The influence of the angle ξ is explained in Fig. 40 in αβ complex plane. The figure shows the six active voltage vectors, and the stator flux vector trajectory as the two circles between which the vector tip is maintained. Further, the dot-dashed line divides the plane into six sectors in which the stator flux vector can be located. For each sector, each voltage vector has a specific impact on the flux vector amplitude and generated torque. This effect was explained in the section 4.2 within the DTC strategy description. If, for example, the stator flux vector is located in sector 1 and the torque demand is to increase, then voltage vectors V2 or V3 are selected. Vector V2 increases the flux amplitude whereas V3 decreases. Therefore, the theoretical minimum angle ξ (between the rotor flux and voltage) is $\pi/6$ when V2 is applied and flux vector is close to sector 2, and maximum angle is $5\pi/6$ when V3 is applied and stator flux vector is close to sector 6. Therefore, if the angle between the stator and rotor flux is smaller than $\pi/6$,

$$\xi \in (0, \pi) \Rightarrow \sin\xi \in (0{,}1). \tag{68}$$

applies.

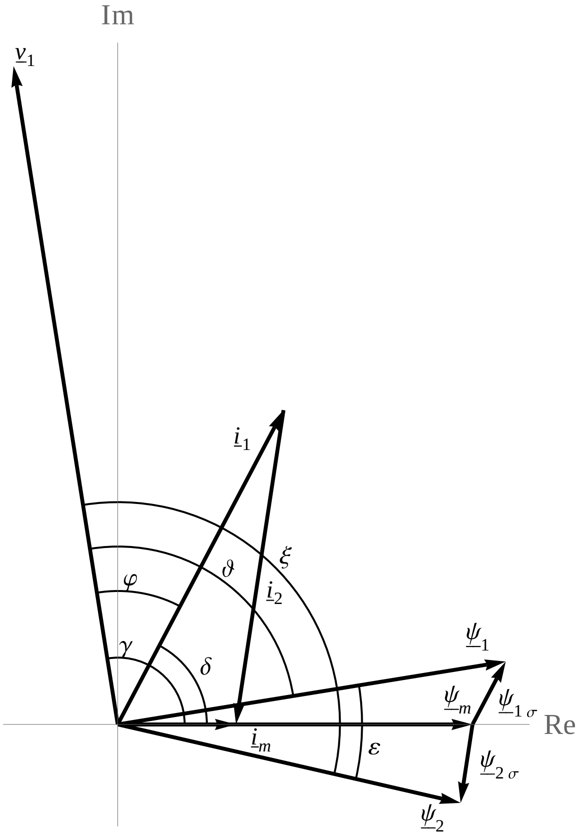

Fig. 39. IM vector diagram. Published by the author [166].

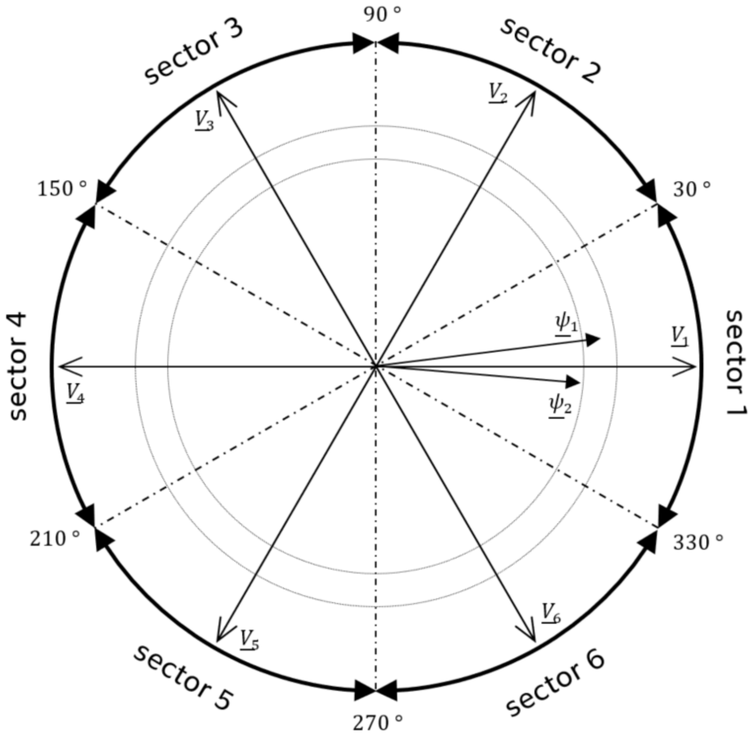

Fig. 40. Complex plane αβ with basic voltage vectors, stator and rotor flux linkage vectors and flux sectors. Published by the author [166].

From the torque equation based on the stator and rotor flux vectors

$$T_\mathrm{e} = \frac{3}{2} p_\mathrm{p} \frac{L_\mathrm{m}}{L_1 L_2 \sigma} \psi_1 \psi_2 \sin \varepsilon, \tag{69}$$

the angle ε can be expressed as

$$\varepsilon = \sin^{-1}\left(\frac{2}{3p_\mathrm{p}} \frac{L_1 L_2 \sigma}{L_\mathrm{m}} \frac{T_\mathrm{e}}{\psi_1 \psi_2}\right). \tag{70}$$

The rated values of the IM used in simulations and experiment report that $\varepsilon \approx 0.28 < \pi/6$. Therefore, with the reference torque increase, the condition (68) is met and $\sin \xi$ is positive.

The presented mathematical analyses confirm the assumption that lower DC-link voltage causes lower torque derivative and leads to lower torque ripple. However, for the explicit analytical expressions, some simplifying presumptions were adopted.

6.3. Influence of DC-Link Voltage on Current Ripple

In the following section, the mathematical evaluation of the lower DC-link voltage on the current ripple is provided. It shows that the lower voltage leads to lower current ripple.

The time derivative of the stator current vector in a general reference frame is

$$\frac{\mathrm{d}\boldsymbol{i}_1}{\mathrm{d}t} = C_1 \boldsymbol{i}_1 - \mathrm{j}\omega_\mathrm{k} \boldsymbol{i}_1 + C_2 \boldsymbol{v}_1 + C_3 \boldsymbol{\psi}_2 - \mathrm{j}\omega C_4 \boldsymbol{\psi}_2. \tag{71}$$

This derivative can be separated to the real and imaginary part. With the assumption of a reference frame fixed with the stator current vector, the d-component of the current vector is

$$\frac{\mathrm{d}i_1}{\mathrm{d}t} = C_1 i_1 + C_2 v_{1\mathrm{d}} + C_3 \psi_{2\mathrm{d}} + \omega C_4 \psi_{2\mathrm{q}} \tag{72}$$

where $i_1 = i_{1\mathrm{d}} = |\boldsymbol{i}_1|$. This changes (55) and (60) to

$$\boldsymbol{v}_1 = \frac{2}{3} V_\mathrm{DCmax} \mathrm{e}^{\mathrm{j}\varphi}, \tag{73}$$

$$\boldsymbol{v}_1' = k_\mathrm{DC} \frac{2}{3} V_\mathrm{DCmax} \mathrm{e}^{\mathrm{j}\varphi}. \tag{74}$$

The real part of (73) and (74), respectively, is put into (72), and gets

$$\frac{\mathrm{d}i_1}{\mathrm{d}t} = C_1 i_1 + C_2 \frac{2}{3} V_\mathrm{DCmax} \cos\varphi + C_3 \psi_{2\mathrm{d}} + \omega C_4 \psi_{2\mathrm{q}}, \tag{75}$$

and

$$\frac{\mathrm{d}i_1'}{\mathrm{d}t} = C_1 i_1 + C_2 k_\mathrm{DC} \frac{2}{3} V_\mathrm{DCmax} \cos\varphi + C_3 \psi_{2\mathrm{d}} + \omega C_4 \psi_{2\mathrm{q}}. \tag{76}$$

The comparison of (75) and (76) is done in the same way as in the case of the torque analysis as

$$\Delta \dot{i_1} = \lim_{t \to 0^+} \left(\frac{\mathrm{d}i_1}{\mathrm{d}t} - \frac{\mathrm{d}i_1'}{\mathrm{d}t} \right), \tag{77}$$

and is then rewritten as

$$\Delta \dot{i_1} = \frac{2}{3}(1-k)V_{\mathrm{DCmax}} C_2 \cos\varphi. \tag{78}$$

For the motoring mode of the IM, the $\cos\varphi \in (0,1)$ applies. The derived dependency (78) shows how much larger the current change is in the case of full DC-link voltage V_{DCmax} compared to the reduced voltage $k_{\mathrm{DC}} V_{\mathrm{DCmax}}$. Also, it mathematically confirms that lower DC-link voltage leads to lower changes in the IM current.

6.4. Minimal DC-Link Voltage Values

In this section, the minimum DC-link voltage for an operating point is derived. The operating point is defined by the reference speed, torque and flux. The simplifying assumption, that only fundamental components of voltage, current and flux waveforms contribute to the creation of the IM torque, is adopted.

In a coordinate system rotating oriented on the stator flux vector [164] (dq reference frame), the stator voltage equation is expressed as

$$\boldsymbol{v}_1 = R_1 \boldsymbol{i}_1 + \frac{\mathrm{d}\boldsymbol{\psi}_1}{\mathrm{d}t} + \mathrm{j}\omega_{\mathrm{s}} \boldsymbol{\psi}_1. \tag{79}$$

Within the dq reference frame, ($\psi_{1\mathrm{q}} = 0$) applies. Considering the steady state, the individual components of the stator voltage vector are

$$v_{1\mathrm{d}} = R_1 i_{1\mathrm{d}}, \tag{80}$$

$$v_{1\mathrm{q}} = R_1 i_{1\mathrm{q}} + \omega_{\mathrm{s}} \psi_{1\mathrm{d}}. \tag{81}$$

The magnitude of the fundamental voltage vector waveforms $v_{1\mathrm{fw}}$ is then

$$v_{1\mathrm{fw}} = \sqrt{v_{1\mathrm{d}}^2 + v_{1\mathrm{q}}^2} = \sqrt{R_1^2\left(i_{1\mathrm{d}}^2 + i_{1\mathrm{q}}^2\right) + 2R_1 i_{1\mathrm{q}} \omega_{\mathrm{s}} \psi_{1\mathrm{d}} + \omega_s^2 \psi_{1\mathrm{d}}^2}. \tag{82}$$

In this reference frame, the equations for the IM torque and stator flux vector d-component simplifies to

$$T_{\mathrm{e}} = \frac{3}{2} p_{\mathrm{p}} \psi_1 i_{1\mathrm{q}}, \tag{83}$$

$$\psi_{1\mathrm{d}} = L_1 i_{1\mathrm{d}} - \omega_{\mathrm{s}} L_1 \tau_{\mathrm{r}} \sigma i_{1\mathrm{q}}, \tag{84}$$

where $\psi_1 = |\boldsymbol{\psi}_1| = \psi_{1d}$.

For the torque and flux references T_{e}^* and ψ_1^*, the corresponding d-axis and q-axis current components can be written as

$$i_{1\mathrm{q}} = \frac{2}{3} \frac{T_{\mathrm{e}}^*}{p_{\mathrm{p}} \psi_1^*}, \tag{85}$$

$$i_{1\mathrm{d}} = \frac{1}{L_1}\psi_1^* + \omega_\mathrm{s}\tau_\mathrm{r}\sigma i_{1\mathrm{q}}. \tag{86}$$

The synchronous speed can be calculated as the sum of the rotor and slip speed

$$\omega_\mathrm{s} = p_\mathrm{p}\omega_\mathrm{r} + \omega_\mathrm{sl}. \tag{87}$$

In the stator flux-oriented coordinate system, the slip in the steady-state operation [165] is defined as

$$\omega_\mathrm{sl} = \frac{L_1 i_{1\mathrm{q}}}{\tau_\mathrm{r}(\psi_1^* - L_1\sigma i_{1\mathrm{d}})}. \tag{88}$$

In a steady-state, and with considering only the fundamental wave of the stator voltage, a voltage vector tip creates a circular trajectory of a magnitude given by (82). The six active voltage vectors create a hexagon of reachable voltage vectors. Decreasing the DC-link voltage shrinks the hexagon. At some threshold voltage $k_\mathrm{th}V_\mathrm{DCmax}$, the hexagon approaches the circular trajectory of the fundamental voltage wave, and touches the circle.

The formula for the circle inscribed in the hexagon gives the threshold coefficient

$$k_\mathrm{th} = \frac{\sqrt{3}v_{1\mathrm{fw}}}{V_\mathrm{DCmax}}. \tag{89}$$

Up to this point, the whole circle lies in the hexagon. It means, that the required fundamental voltage wave (the circle) can be modulated by the set of feasible vectors (the hexagon). In these operation points, the inverter is able to deliver the required power and the harmonic current waveform is maintained

Another significant coefficient value is at the point, when the inverter will no longer be able provide sufficient voltage to counter the back-emf. This critical DC-link voltage $k_\mathrm{crit}V_\mathrm{DCmax}$ can be deducted by the comparison of the surface of the fundamental voltage wave circle with the surface of the hexagon whose edge is equal to $2/3k_\mathrm{crit}V_\mathrm{DCmax}$ as

$$\pi v_{1\mathrm{fw}}^2 = \frac{3\sqrt{3}}{2}\left(\frac{2}{3}k_\mathrm{crit}V_\mathrm{DCmax}\right)^2, \tag{90}$$

and the critical coefficient k_crit is expressed as

$$k_\mathrm{crit} = \frac{\sqrt[4]{3}\sqrt{\frac{\pi}{2}}}{V_\mathrm{DCmax}}v_{1\mathrm{fw}}. \tag{91}$$

Since the equation contains quadratic term, two solutions exist. However, the negative root does not have physical sense so it was dropped.

Between the threshold and critical voltage values, the inverter provides sufficient voltage to the motor, so the operation point is maintained. However, parts of the circle are outside the hexagon, so they cannot be reached. This creates additional distortion in the stator current and the inverter will be approaching rectangular control strategy. Below the critical voltage value, the motor is not able to operate and the speed decreases.

It can be stated, that the optimal DC-link voltage value is determined by (89) since the torque and current ripples are minimized and no additional distortion in the current waveform is present. The situation is depicted in Fig. 41.

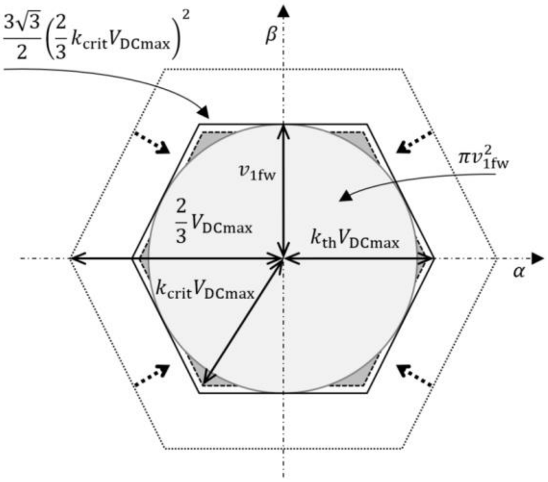

Fig. 41. Maximum, threshold and critical DC-link voltage with their corresponding hexagons along with the circular trajectory of the fundamental voltage wave. Published by the author [166].

6.5. DC-Link Voltage Optimization

The objective of the proposed predictive control method is to optimize the DC-link voltage at the value, at which the stator flux amplitude and developed torque waveform will have the lowest ripple [166]. The algorithm is based on the same principle as the PTC. At first, from the set of eight voltage vectors, the stator flux and torque are predicted, and the best candidate is selected by the same rules as in the case of the fundamental PTC method described in chapter 5. Then, this voltage vector candidate is applied. The switching state of the transistors that corresponds to the selected voltage vector is then considered as the only feasible switching state. Since the DC-link voltage is now the optimization object, the multiple different voltage vectors candidates can be created with the selected switching state and with the different DC-link voltage levels. In the thesis, the voltage vector with three different voltage levels was considered as the feasible set of candidates for the prediction; the lower, the same, and the higher magnitude. However, other options are available. For this feasible set of three candidates, the stator flux and torque are predicted, and by the cost function, the most suitable voltage vector magnitude is selected. The control principle of the proposed method of PTC with included DC-link voltage optimization is depicted in Fig. 42.

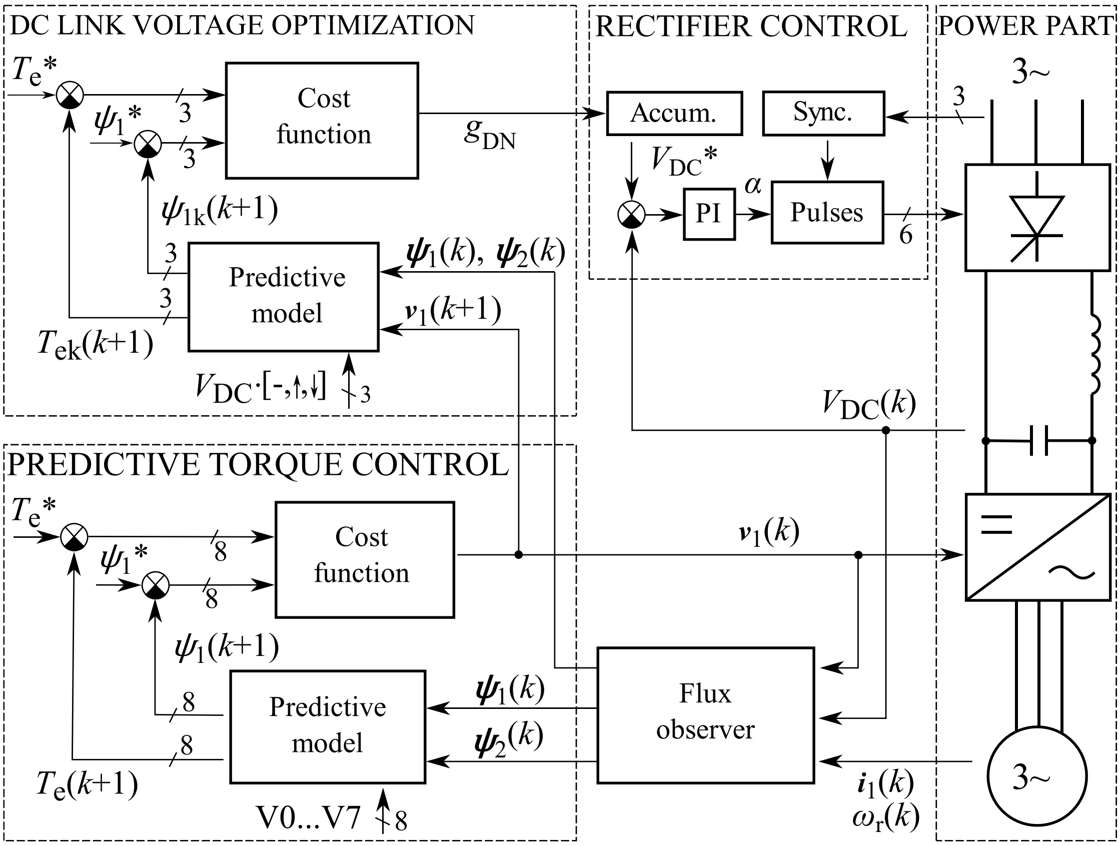

Fig. 42. The working principle of PTC with DC-link voltage optimization. Published by the author [166].

For the flux and torque prediction, the stator current prediction $\boldsymbol{i}_{1k}(k+1)$ is required. It is calculated similarly as in (35), i.e.,

$$\begin{aligned}\boldsymbol{i}_{1k}(k+1) = \left(1+\frac{T_s}{\tau_\sigma}\right)\boldsymbol{i}_1(k) + \frac{T_s}{(\tau_\sigma+T_s)R_\sigma} \\ \cdot\left[\left(\frac{k_r}{\tau_r} - k_r j\omega_r(k)\right)\boldsymbol{\psi}_2(k) + \boldsymbol{v}_{1k}(n_k)\right],\end{aligned} \tag{92}$$

where

$$\boldsymbol{v}_{1k}(n_k) = \frac{2}{3}V_{DC}k_{opt}\boldsymbol{c}_{sw}, \tag{93}$$

and where $\boldsymbol{c}_{sw}$ is the vector corresponding to the transistor switching combination that previously selected by the PTC, n_k is the number of the considered voltage vector candidate, and k_{opt} is the ratio of the DC-link voltage level candidate to the actual DC-link voltage. In the thesis, for the practical verification, k_{opt} is chosen as

$$k_{opt} \in \{0.98, 1, 1.02\}. \tag{94}$$

Such coefficient choices consider 98%, 100%, and 102%, respectively, of the actual DC-link voltage. Therefore, only small DC-link voltage changes are considered within each step.

The stator flux is predicted formally the same as in (33), i.e.,

$$\boldsymbol{\psi}_{1\mathrm{k}}(k+1)=\boldsymbol{\psi}_1(k)+T_\mathrm{s}\boldsymbol{v}_{1\mathrm{k}}(n_\mathrm{k})-T_\mathrm{s}R_1\boldsymbol{i}_1(k). \tag{95}$$

The torque $T_\mathrm{ek}(k+1)$ is finally predicted similarly as in (36), i.e.,

$$T_\mathrm{ek}(k+1)=\frac{3}{2}p_\mathrm{p}|\boldsymbol{\psi}_{1\mathrm{k}}(k+1)\times\boldsymbol{i}_{1\mathrm{k}}(k+1)|. \tag{96}$$

The three flux and torque candidates are calculated from (95) and (96) that are to be evaluated by the cost function. The proposed cost function is almost identical with the one used for the fundamental PTC itself, i.e.,

$$g_\mathrm{k}(n_\mathrm{k})=k_\mathrm{CF}|\psi_{1\mathrm{k}}(k+1)-\psi_1^*|+|T_\mathrm{ek}(k+1)-\ T_\mathrm{e}^*|. \tag{97}$$

The minimum of the cost function (97) specifies the DC-link voltage level that brings the system closest to the reference values. It also indirectly specifies the reference DC-link voltage. It is then used for the PI controller (depicted in Fig. 42), which adjusts the final DC-link voltage through the rectifier firing angle (in Fig. 42 marked as α).

However, the proposed algorithm is to be tested experimentally on a thyristor rectifier. In such a rectifier type, a variable time delay (the delay between the demanded control angle reference generation and its actual application) exists. Moreover, the reference DC-link voltage may change multiple times between the reaction times of the rectifier (since the optimization calculation is performed within every sampling time).

To compensate this phenomenon, an accumulator is placed between the prediction output and the PI controller reference. The cost function is then adjusted to output three numbers instead of the voltage magnitude; a positive number meaning accumulator output increase, a negative number meaning accumulator output decrease, and a zero meaning to preserve the last value. The most intuitive selection is

$$g_\mathrm{DN}(n_\mathrm{k})\in\{-1,0,1\}, \tag{98}$$

where g_DN is the cost function demand to the DC-link voltage.

The exact used values are a matter of tuning since they are strongly dependent on the controlled system. In the case of the considered rectifier type, the small shift towards the negative values is desirable. The thyristor allows only one direction of the current while blocks the other direction. Therefore, it is easy to control the DC-link voltage through the control angle α to increase its value, but it is impossible to decrease the voltage and discharge it. The voltage decrease is much slower and, when the self-discharge of the capacitor is neglected, is only performed by the current drawn by the load. The small shift towards negative values partly compensates for this issue.

The proposed control algorithm optimizing the DC-link voltage can be summarized in the following steps.

- Measurement of the phase currents, phase voltage angle, DC-link voltage and speed
- Current and voltage vector reconstruction
- Estimation of the actual stator and rotor flux linkage vector
- Prediction of possible stator flux amplitude and torque for all voltage vectors candidates
- Enumeration of the cost function with constraints for each of eight candidates and find the minimum cost function value
- Application of the selected voltage vector candidate on the inverter
- Prediction of possible stator flux amplitude and torque for applied voltage vector with three different DC-link voltages
- Enumeration of the cost function for the three voltage vector candidates and find the minimum cost function value
- Application of the requested change on the DC-link voltage reference accumulator
- The calculation of the rectifier's firing angle by the PID controller
- Adjustment of the controlled rectifier

This optimization algorithm was realized on the real drive, and its practical implementation in Matlab code is added in Appendix A3.

6.6. DC-Link Voltage Optimization Summary

The common topologies of controlling the DC-link voltage have been analyzed. Then, the influence of the DC-link voltage on the torque and current waveform ripple were examined. It was proofed that the torque and current ripples are decreasing with lowering the DC-link voltage down to certain limit values. The threshold and critical values of DC-link voltage for given operation points of the drive were defined, and calculation procedure was shown. At the end of the chapter, the predictive DC-link voltage optimization strategy was designed, and its integration into the PTC strategy was shown. These findings were also published in [166].

7. Simulation and Experimental Results

For the verification of the proposed PTC with the DC-link voltage optimization algorithm, the algorithm was implemented in the simulation environment Matlab/Simulink and was tested on the model of the drive. To further verify the results, it was implemented on the dSpace platform and tested experimentally on a laboratory drive with an IM of 5.5 kW output power. The experiment was done with and also without the speed sensor, for which the speed observer was utilized. The experiments in the steady states, the transients, and the field-weakening region were performed and the behavior compared with the PTC with full DC-link voltage. Finally, the motor losses were examined, and the influence of the proposed method on the motor loss distribution was evaluated.

7.1. Simulation Results

The proposed DC-link voltage optimization algorithm and its inclusion into the PTC method was verified in simulation environment Matlab/Simulink by the tests performed on the mathematical model of the IM.

The part concerning the control procedures, such as the flux estimator, the PTC control method, and the optimization algorithm, was constructed using the standard Simulink blocks and using the Matlab programming language. These were created as triggered subsystems that were triggered by the square clock signal with 100 µs period. The SimScape library was used for the simulation of the power part, i.e., the drive itself. This was simulated as a discrete model with a fixed step of 5 µs. The model of the drive consisted of a three-phase voltage source, a controlled rectifier, a DC-link capacitor with a choke, an IGBT (insulated gate bipolar transistor) inverter, a braking resistor, and the IM with parameters presented in Table 3. Within the simulations, only the measurable quantities (motor phase currents, DC-link voltage, input grid phase voltages, rotational speed) were regarded as inputs for the control algorithms. The simulation blocks overview in the Matlab Simulink is added in the Appendix A1.

7.1.1. Drive behavior during the DC-Link Voltage Decrease

The DC-link voltage decrease, and its effect on the torque developed by the IM are verified in Fig. 43 and Fig. 44. In Fig. 43, the DC-link voltage is slowly decreased from the full DC-link voltage down to zero. In Fig. 44, the detail near the threshold and critical voltage values is depicted. The motor is running at the speed 500 rpm that is kept by speed PI controller. The flux reference is 0.8 Wb and the applied load is 15 Nm. The figures show that when the voltage is above the threshold value, the motor is tracking the reference speed without problems. Below the threshold point, the motor speed still tracks the required one, but the phase current waveform’s shape deteriorates. When the voltage drops below the critical point, the speed decreases because the inverter is not able to counter the back emf.

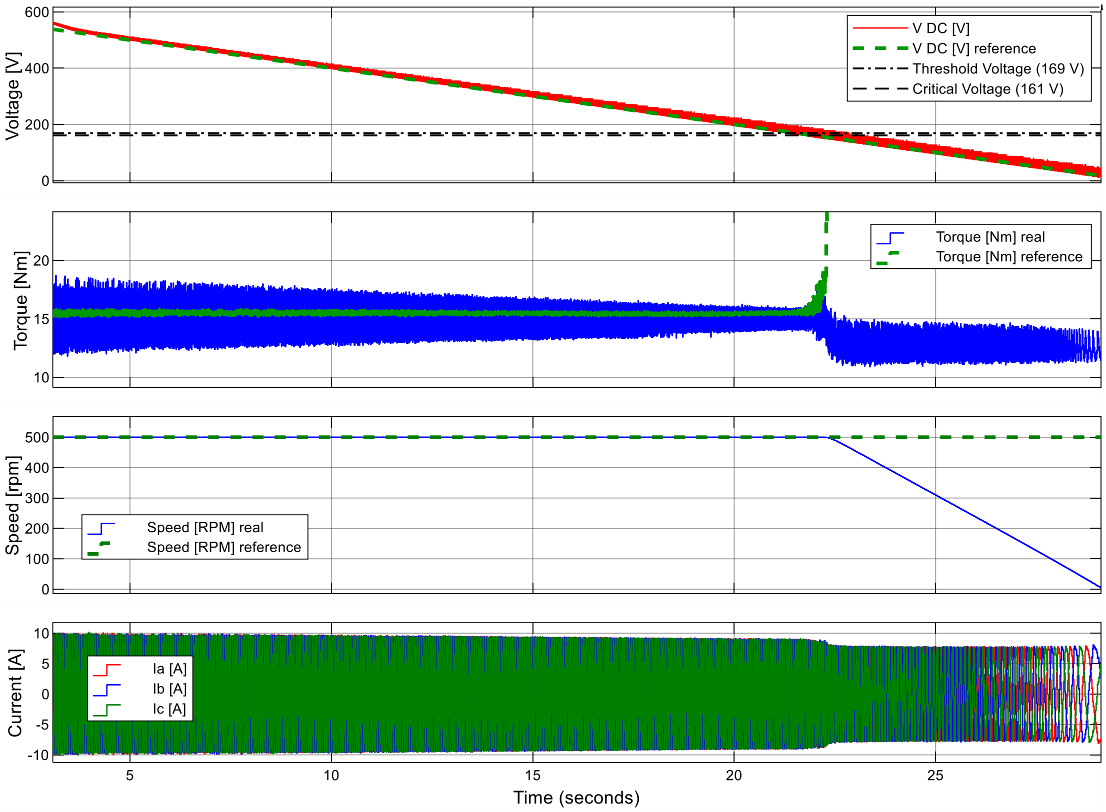

Fig. 43. Effect of the DC-Link voltage decrease on the torque ripple; speed 500 rpm, flux 0.8 Wb, load 15 Nm.

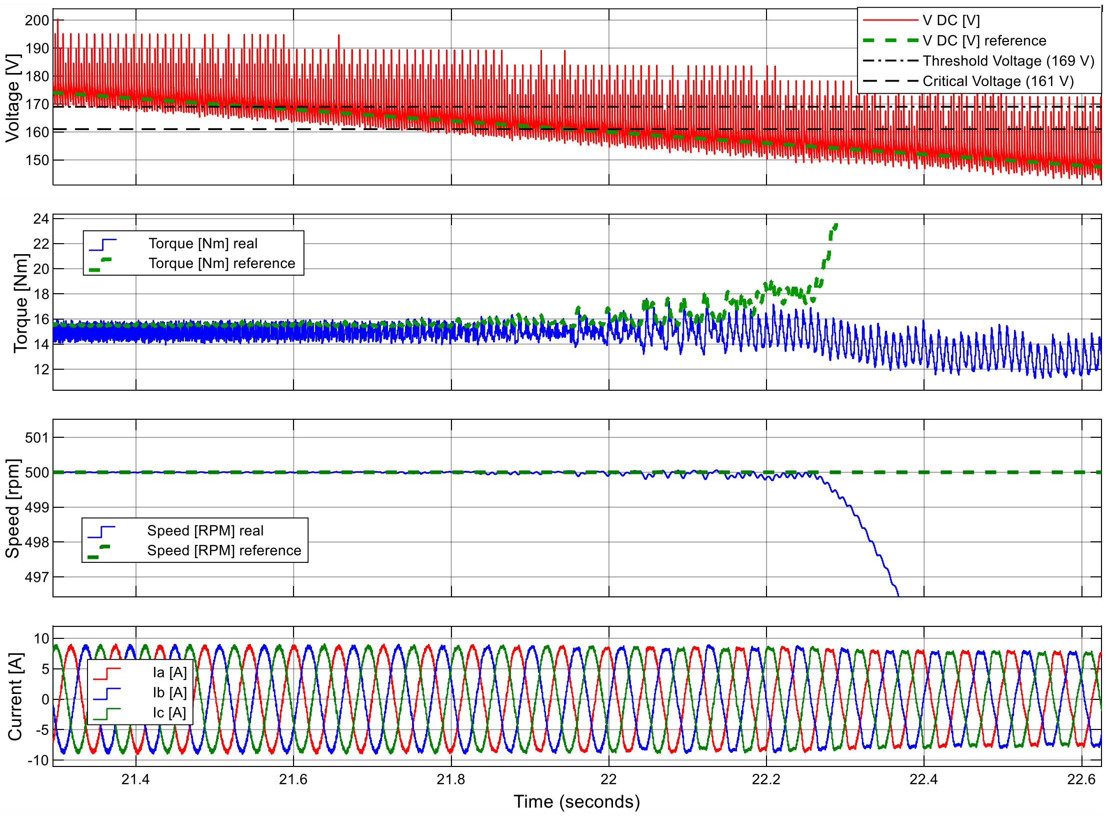

Fig. 44. Detail of Fig. 43 around threshold and critical DC-link voltage; speed 500 rpm, flux 0.8 Wb, load 15 Nm.

The threshold and critical DC-link voltage values calculations were derived in section 6.4 and the numeric calculation for the presented working point is presented below. For better comprehension, the most of the numbers are rounded. Since the d-component of the stator current vector $i_{1\mathrm{d}}$ depends on the synchronous speed ω_{s} and ω_{s} depends on $i_{1\mathrm{d}}$, the enumeration process must be performed iteratively. The chosen operating point from Fig. 43 and Fig. 44 is defined by the speed 500 rpm, the load torque 15 Nm and the stator flux amplitude 0.8 Wb. The steady-state where $T = T^*$ and $\psi_1 = \psi_1^*$ apply is assumed.

First, the q-component of the stator current vector $i_{1\mathrm{q}}$ is calculated from the torque and flux references according to (85) as

$$i_{1\mathrm{q}} = \frac{2}{3}\frac{T_{\mathrm{e}}^*}{p_{\mathrm{p}}\psi_1^*} = \frac{2}{3}\cdot\frac{15}{2\cdot 0.8} = 6.25\ \mathrm{A}. \tag{99}$$

The d-component of stator current vector $i_{1\mathrm{d}}$ is calculated according to (86). However, the synchronous frequency ω_{s} is not known. The first assumption might be that the slip frequency ω_{sl} is zero so for the synchronous speed

$$\omega_{\mathrm{s}} = p_{\mathrm{p}}\omega_{\mathrm{r}} + \omega_{\mathrm{sl}} = 2\frac{500\pi}{30} + 0 = 105\ \mathrm{rad/s} \tag{100}$$

applies. Therefore, the current $i_{1\mathrm{d}}$ is

$$i_{1\mathrm{d}} = \frac{\psi_1^*}{L_1} + \omega_{\mathrm{s}}\tau_{\mathrm{r}}\sigma i_{1\mathrm{q}} = \frac{0.8}{0.157} + 105\cdot 0.222\cdot 0.0923\cdot 6.25 = 18.5\ \mathrm{A}. \tag{101}$$

Afterward, the slip frequency ω_{sl} is adjusted from the stator current vector according to (88) as

$$\omega_{\mathrm{sl}} = \frac{L_1 i_{1\mathrm{q}}}{\tau_{\mathrm{r}}(\psi_1^* - L_1\sigma i_{1\mathrm{d}})} = \frac{0.157\cdot 6.25}{0.222(0.8 - 0.157\cdot 0.0923\cdot 18.5)} = 8.3\ \mathrm{rad/s}. \tag{102}$$

With the new value of the slip frequency, the current vector is calculated again recursively. The new synchronous speed is calculated as

$$\omega_{\mathrm{s}} = p_{\mathrm{p}}\omega_{\mathrm{r}} + \omega_{\mathrm{sl}} = 2\frac{500\pi}{30} + 8.3 = 113\ \mathrm{rad/s}. \tag{103}$$

The q-component of the current vector remains the same, but the q-component changes to

$$i_{1\mathrm{d}} = \frac{\psi_1^*}{L_1} + \omega_{\mathrm{s}}\tau_{\mathrm{r}}\sigma i_{1\mathrm{q}} = \frac{0.8}{0.157} + 113\cdot 0.222\cdot 0.0923\cdot 6.25 = 19.6\ \mathrm{A} \tag{104}$$

With this current, the slip frequency is changed again to

$$\omega_{\mathrm{sl}} = \frac{L_1 i_{1\mathrm{q}}}{\tau_{\mathrm{r}}(\psi_1^* - L_1\sigma i_{1\mathrm{d}})} = \frac{0.157\cdot 6.25}{0.222(0.8 - 0.157\cdot 0.0923\cdot 19.6)} = 8.6\ \mathrm{rad/s}. \tag{105}$$

The recursive algorithm could continue further, but, since the slip frequency changed minimally, the enumeration is stopped here.

Further, the voltage vector components are calculated from (80) and (81) as

$$v_{1\mathrm{d}} = R_1 i_{1\mathrm{d}} = 0.875 \cdot 19.6 = 17.1\ \mathrm{V}, \tag{106}$$

$$v_{1\mathrm{q}} = R_1 i_{1\mathrm{q}} + \omega_{\mathrm{s}} \psi_{1\mathrm{d}} = 0.875 \cdot 19.6 + 8.6 \cdot 0.8 = 95.9\ \mathrm{V}. \tag{107}$$

Then, the magnitude of the fundamental voltage vector waveform $v_{1\mathrm{fw}}$ (82) is

$$v_{1\mathrm{fw}} = \sqrt{v_{1\mathrm{d}}^2 + v_{1\mathrm{q}}^2} = \sqrt{17.1^2 + 95.9^2} = 97.4\ \mathrm{V}. \tag{108}$$

Finally, the threshold and critical values of the DC-link voltage are calculated from (89), and (91) as

$$V_{\mathrm{th}} = \sqrt{3} v_{1\mathrm{fw}} = \sqrt{3} \cdot 97.4 = 168.7\ \mathrm{V}, \tag{109}$$

and

$$V_{\mathrm{crit}} = \sqrt[4]{3} \sqrt{\frac{\pi}{2}} v_{1\mathrm{fw}} = \sqrt[4]{3} \sqrt{\frac{\pi}{2}} 97.4 = 160.7\ \mathrm{V} \tag{110}$$

respectively. These values correspond with the threshold and critical values for the operating point presented in the simulation.

7.1.2. Optimization Algorithm in Steady State

Fig. 45 shows the simulation of the DC-link voltage optimization process on a drive controlled by the PTC. The IM is operating with 500 rpm rotational speed reference that is kept by the speed PI controller. This controller creates the torque reference. The flux amplitude setpoint is 0.8 Wb and the applied load is 15 Nm for the whole simulation run. Initially, the full DC-link voltage 560 V is present and the optimization is turned off; therefore, the voltage reference is at 560 V. At time 1 s, the optimization process that controls the DC-link voltage reference is started. Immediately after, the voltage starts dropping and in about 600 ms it reaches its final value. This new voltage is close to the threshold point, which agrees with the theoretical analysis carried out in chapter 6.4.

Together with the voltage decrease, the current and the torque ripples are decreasing as well. A small delay between the DC-link voltage and its reference exists because the SCR cannot decrease the voltage. The current must be drawn by the motor to decrease the voltage. The comparison of the performances with and without the optimization is observable from the ripple on the left and right side of the figure.

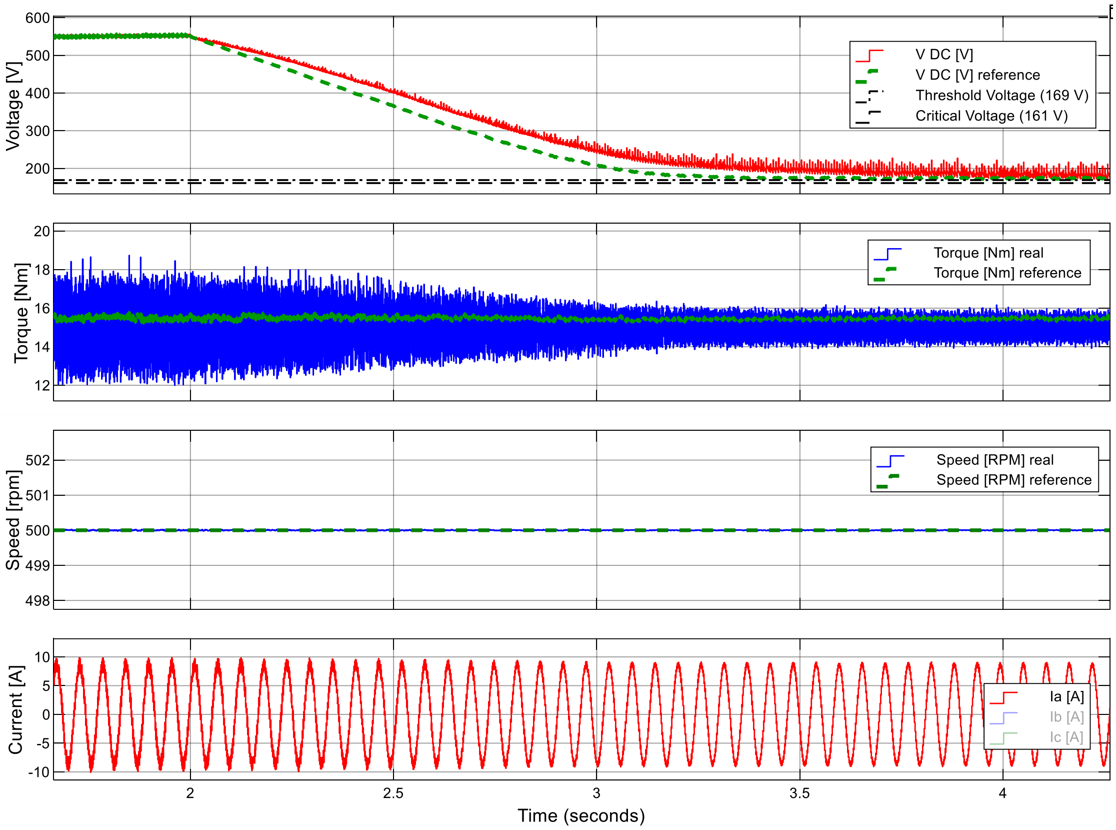

Fig. 45. Simulation of the optimization process in the steady-state; speed 500 rpm, load 15 Nm, flux 0.8 Wb.

The detail of the current and torque waveforms comparison between the run with and without optimization is presented in Fig. 46. The optimized voltage is present till time 5 s. Then, it is suddenly turned off, and the full DC-link is restored immediately. The additional torque and current ripple arise. The benefits of the run with the DC-link voltage optimization is seen from the torque ripple on the left (with the optimization) and right side (without the optimization) of the figure.

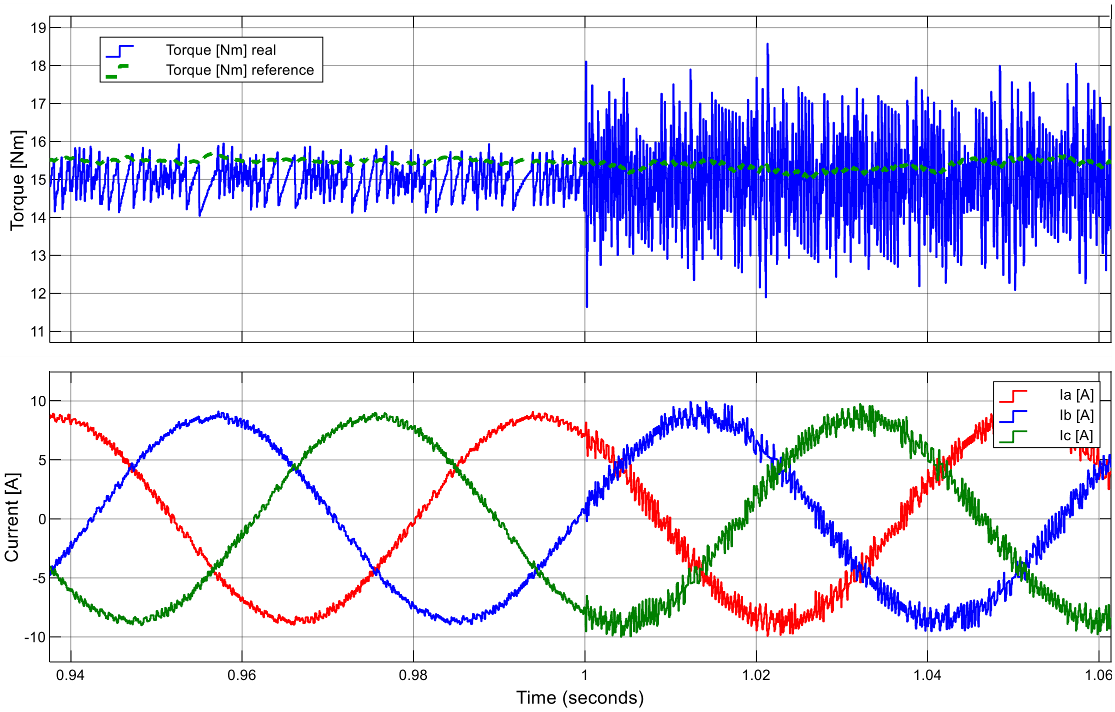

Fig. 46. Comparison of phase current and torque with and without the optimisation by simulation.

DC-link voltage optimization process in some other steady-state operating points are presented in Fig. 47 and Fig. 48. In Fig. 47, the speed of the motor is maintained at 500 rpm and in Fig. 48, at 1000 rpm. The motor is excited with 1 Wb stator flux amplitude and the rated load 37 Nm is applied for the whole time in both figures. At the time 2 s, the optimization is launched and the voltage decreases. The optimization process took around 1 s and the final voltage value is right above the threshold voltage. Together with the voltage decrease, the torque ripple decreases as well. Since the inverter must counter the back emf, the optimized voltage increases with higher speed. From the comparison of Fig. 47 and Fig. 48, it follows, that with higher motor speed the effect of the DC-link voltage optimization is less significant.

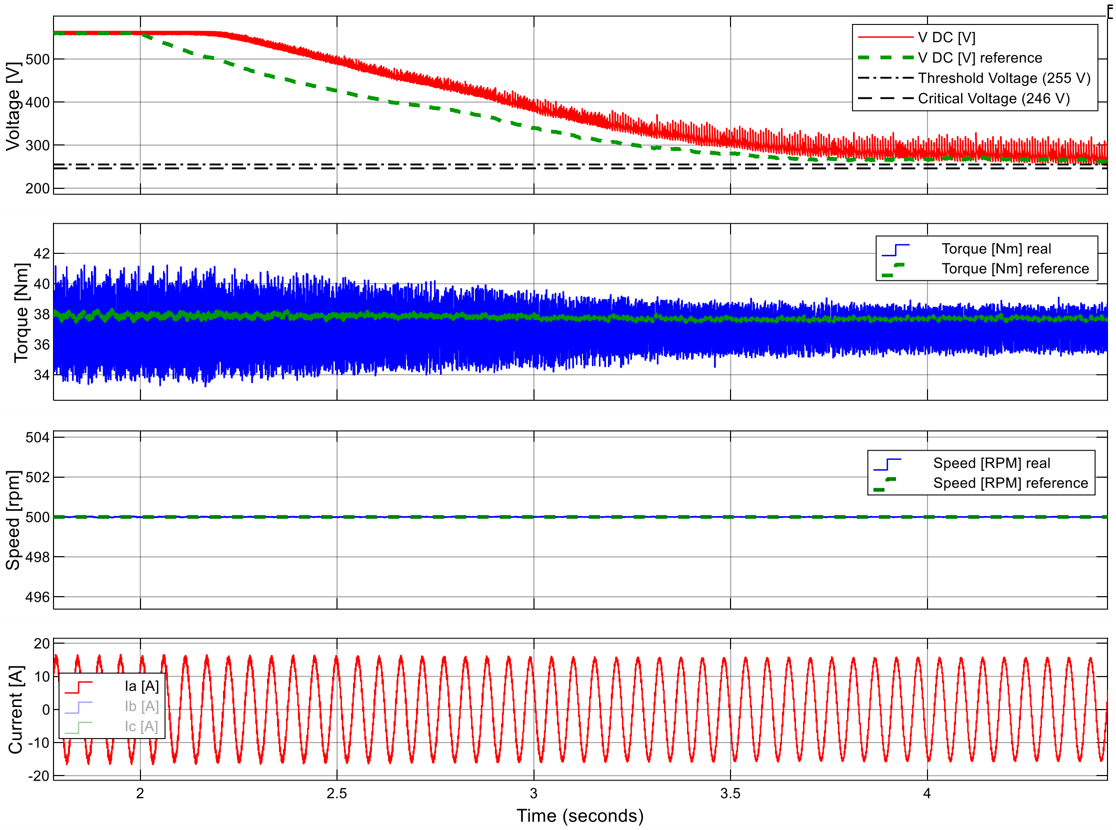

Fig. 47. Simulation of the optimization process in the steady-state; speed 500 rpm, rated load 37 Nm, flux 1 Wb.

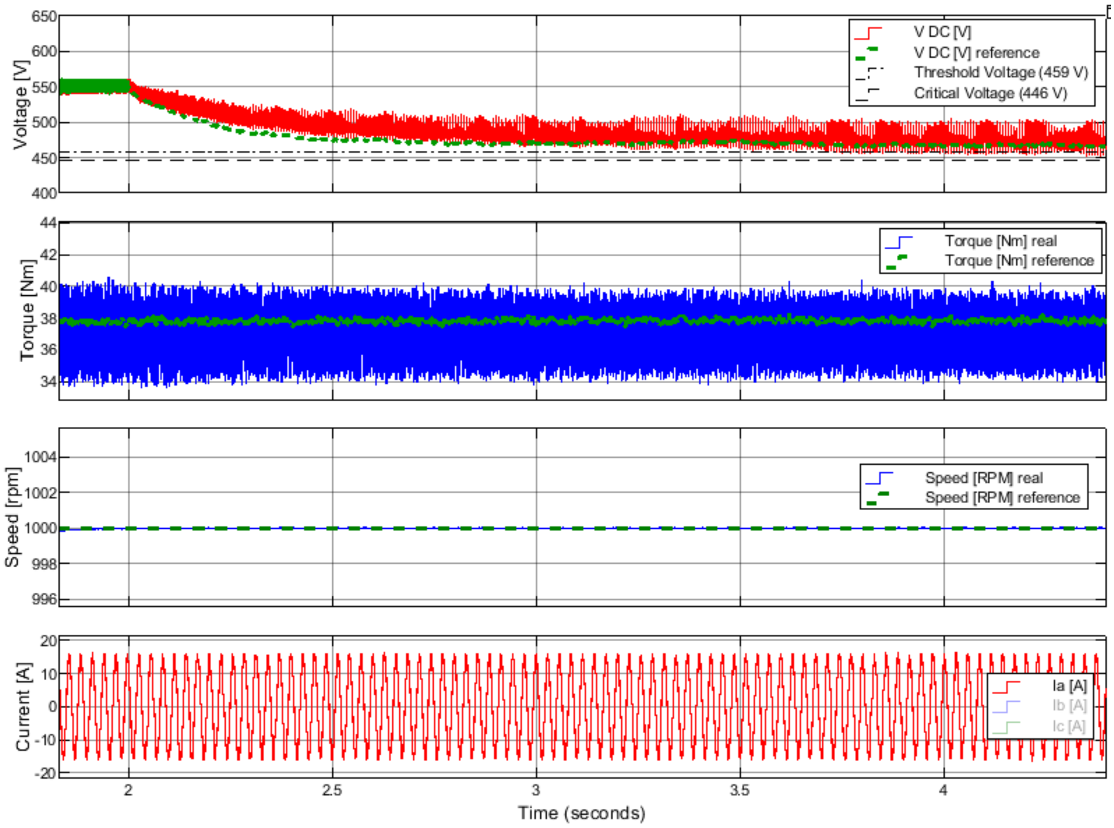

Fig. 48. Simulation of the optimization process in the steady-state; speed 1000 rpm, rated load 37 Nm, flux 1 Wb.

7.1.3. Optimization Algorithm in Transients

Fig. 49 and Fig. 50 present the performance of the optimization method during the speed transients. They show the simulation results of the motor startup in the cases of without DC-link voltage optimization and with optimization, respectively. Initially, the motor is at standstill with zero 0 rpm reference speed and flux excitation 0.8 Wb. The connected load is speed dependent. With zero speed, there is no load, and with the speed 1000 rpm, the rated load 37 Nm is applied. At time 1.5 s, the speed reference increases from 0 rpm to 1000 rpm. In the case without the optimization, the inverter supplies the motor with the sufficient voltage to develop the reference torque immediately. Therefore, the maximum torque is maintained for the whole process. In the case with the optimization, the DC-link voltage is almost zero in the beginning. Only a small voltage is needed for the motor excitation. When the speed reference increases, the inverter is unable to supply motor with sufficient voltage to develop the reference torque. The developed torque increases slower than in the case of no optimization. Therefore, the startup of the motor takes slightly longer time. This can be in some application considered to be a drawback of the proposed optimization method. This could be improved by changing the speed at which the DC-link voltage is adjusted, however, then the DC-link voltage would vary rapidly, and the steady-state performance could deteriorate.

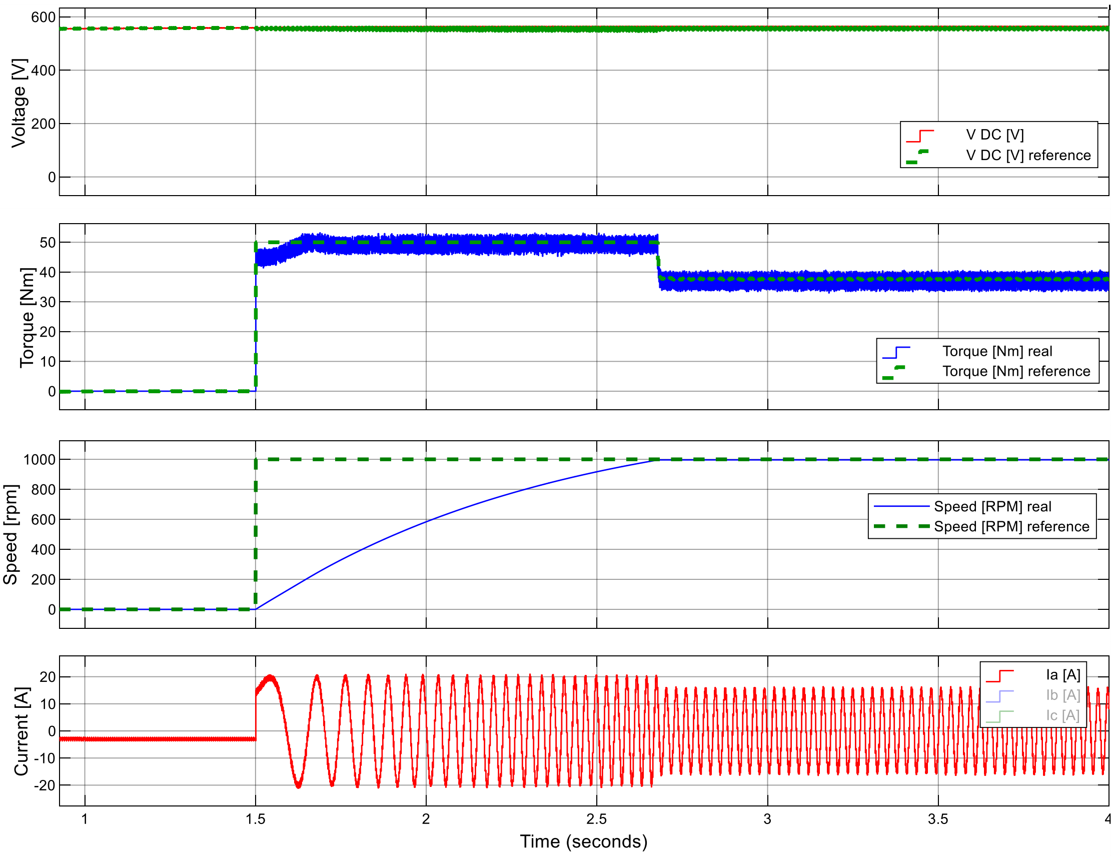

Fig. 49. Simulation run during motor start-up with full DC-link voltage; speed 0 - 1000 rpm, speed dependent load 0 – 37 Nm, flux 0.8 Wb.

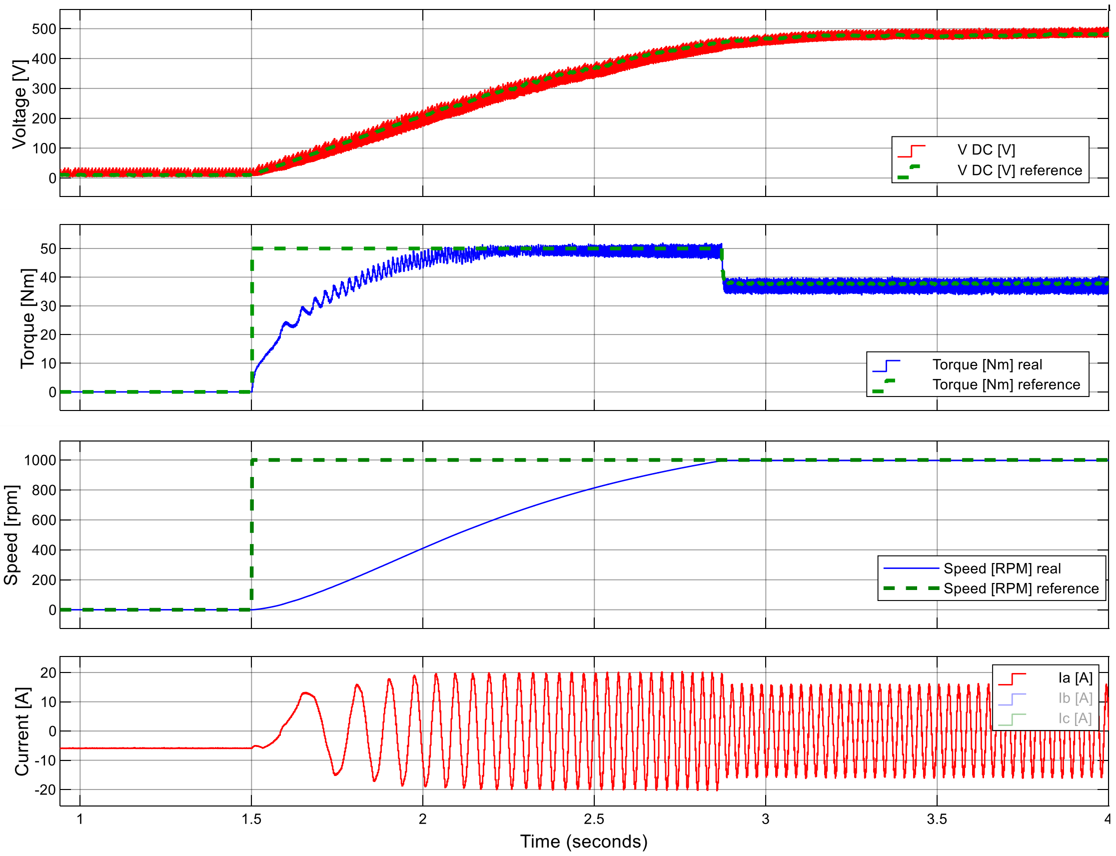

Fig. 50. Simulation run during motor start-up with optimized DC-link voltage; speed 0 - 1000 rpm, speed dependent load 0 – 37 Nm, flux 0.8 Wb.

Fig. 51 and Fig. 52 show the drive response on the speed reference change. The stator flux amplitude setpoint is 1 Wb for the whole simulation run. The rated load torque 37 Nm is applied at the time 0.5 s. In the beginning, the speed reference is zero and is gradually increased every second by 250 rpm. The final simulated speed value is the rated 1430 rpm. Both figures show very similar performance in reaching the reference speed. However, in the case of DC-link voltage optimization in Fig. 52, the torque and current ripples are lower compared to the simulation run with full DC-link voltage presented in Fig. 51.

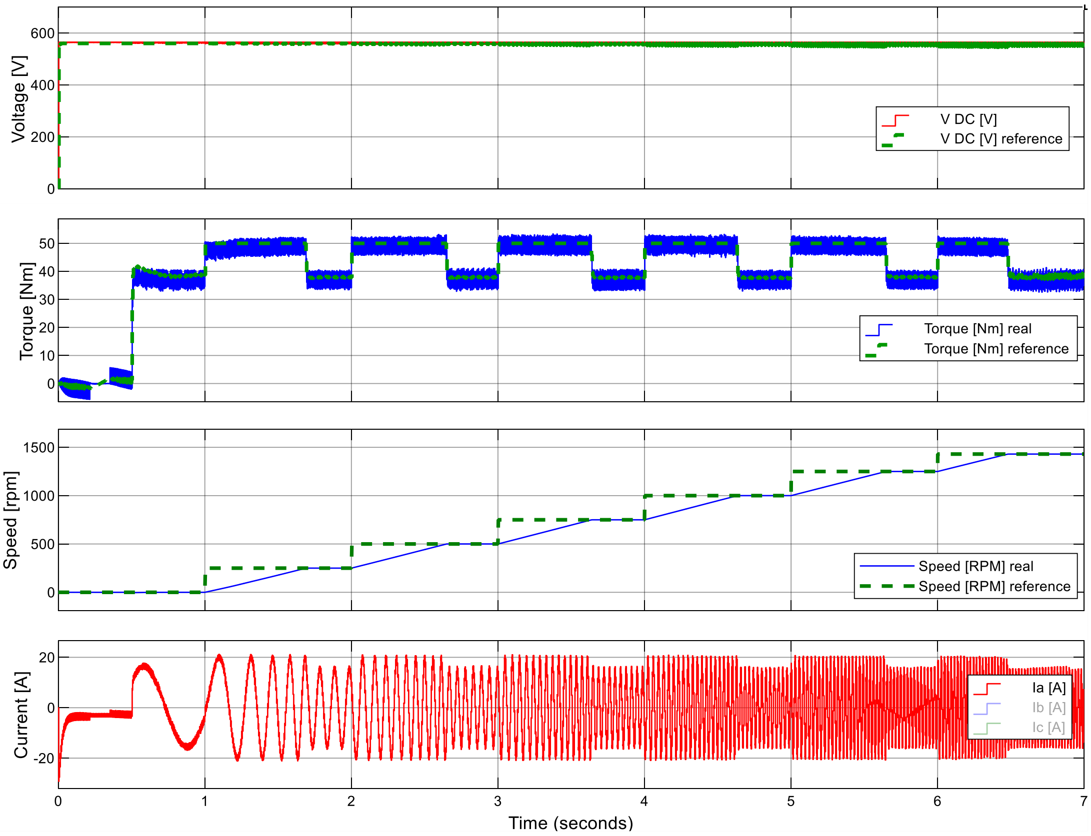

Fig. 51. Simulation run during speed transient with full DC-link voltage; speed gradually increased from 0 rpm to 1430 rpm, rated load 37 Nm, flux 1 Wb.

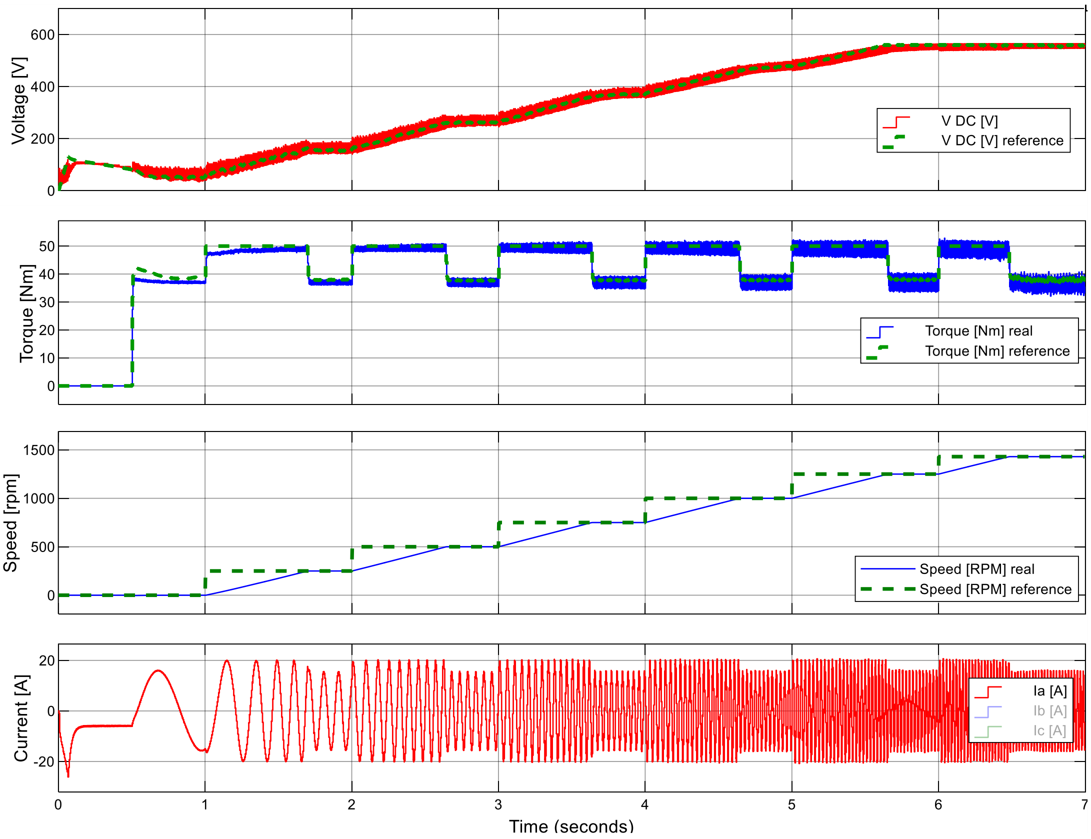

Fig. 52. Simulation run during speed transient with DC-link voltage optimization; speed gradually increased from 0 rpm to 1430 rpm, rated load 37 Nm, flux 1 Wb.

Fig. 53 and Fig. 54 present the drive behavior in the load torque transients. The figures show the performances in the cases of without the voltage optimization and with the optimization, respectively. The speed is maintained by the PI controller at 500 rpm and the motor is excited with flux 0.8 Wb for the whole time. In the beginning, no load is connected. At the time 1 s, the rated torque load 37 Nm is suddenly applied. With the load connected, the speed drops for a short time and is then brought back by the speed controller. Within the optimization, it takes slightly longer time to achieve the reference torque for the same reason as in the case of the speed transients. Moreover, the smoother waveforms of torque and phase current are observed in the case with the DC-link voltage optimization.

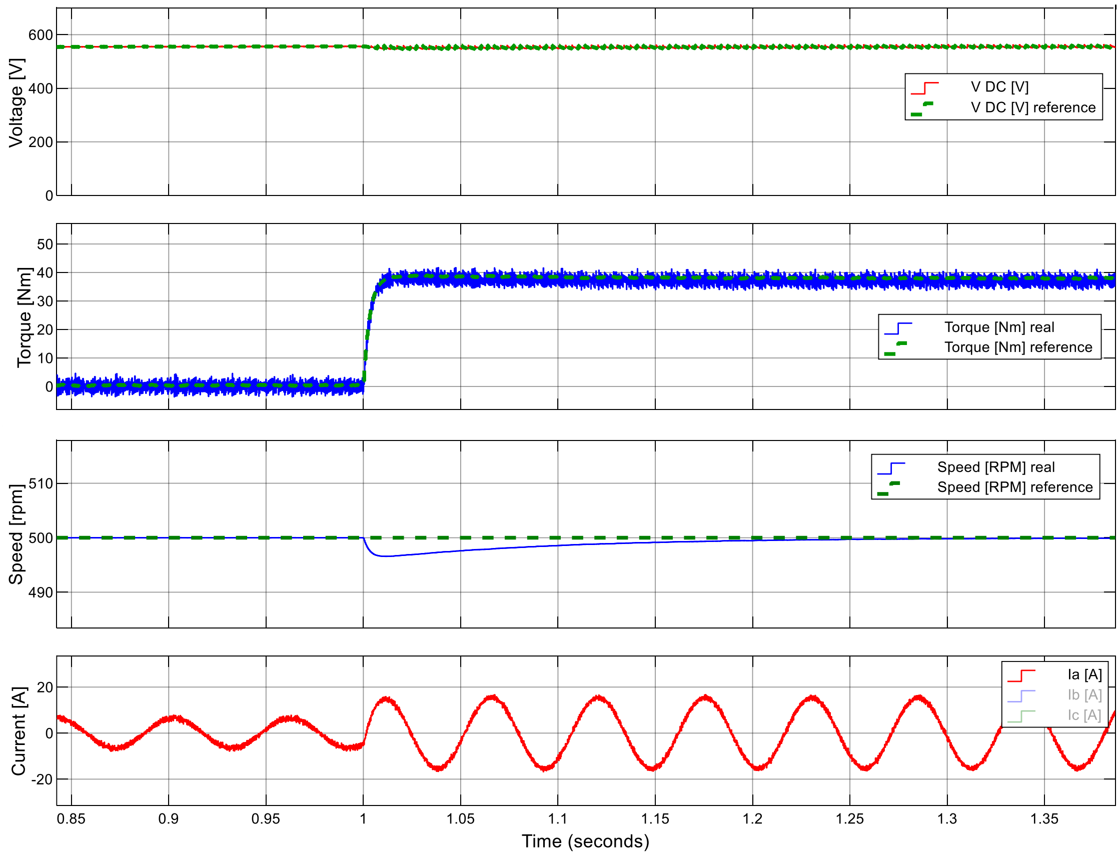

Fig. 53. Simulation run during torque transient with full DC-link voltage; speed 500 rpm, load 37 Nm, flux 0.8 Wb.

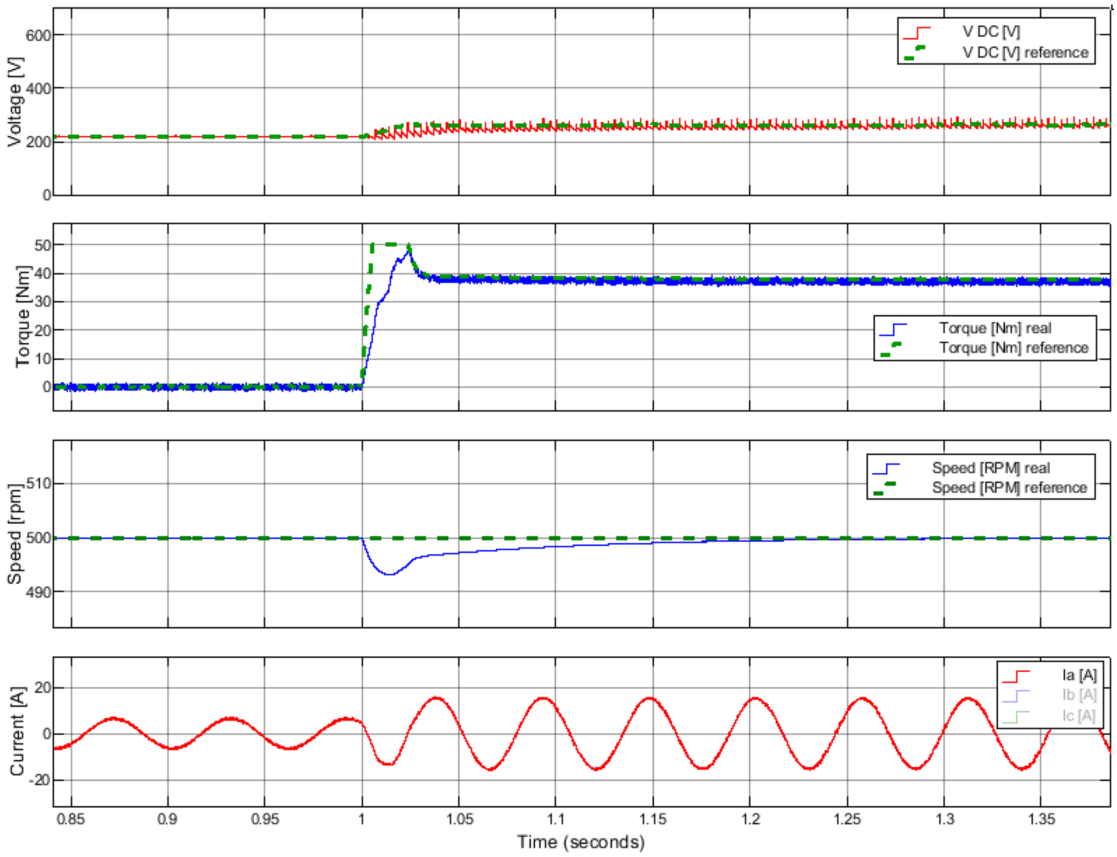

Fig. 54. Simulation run during torque transient with optimized DC-link voltage; speed 500 rpm, load 37 Nm, flux 0.8 Wb.

Fig. 55 and Fig. 56 present the drive response on the increasing load. The motor is excited with 1 Wb and is kept at the speed 500 rpm by the speed controller. In the beginning, the load torque is zero and is gradually increased by 5 Nm step up to the rated torque value 37 Nm. In the case of the run with DC-link voltage optimization (Fig. 56), the DC-link voltage is increasing and new optimized voltage is always found quickly. Moreover, the torque ripple is lower during the whole simulation than in the case of full DC-link voltage (Fig. 55).

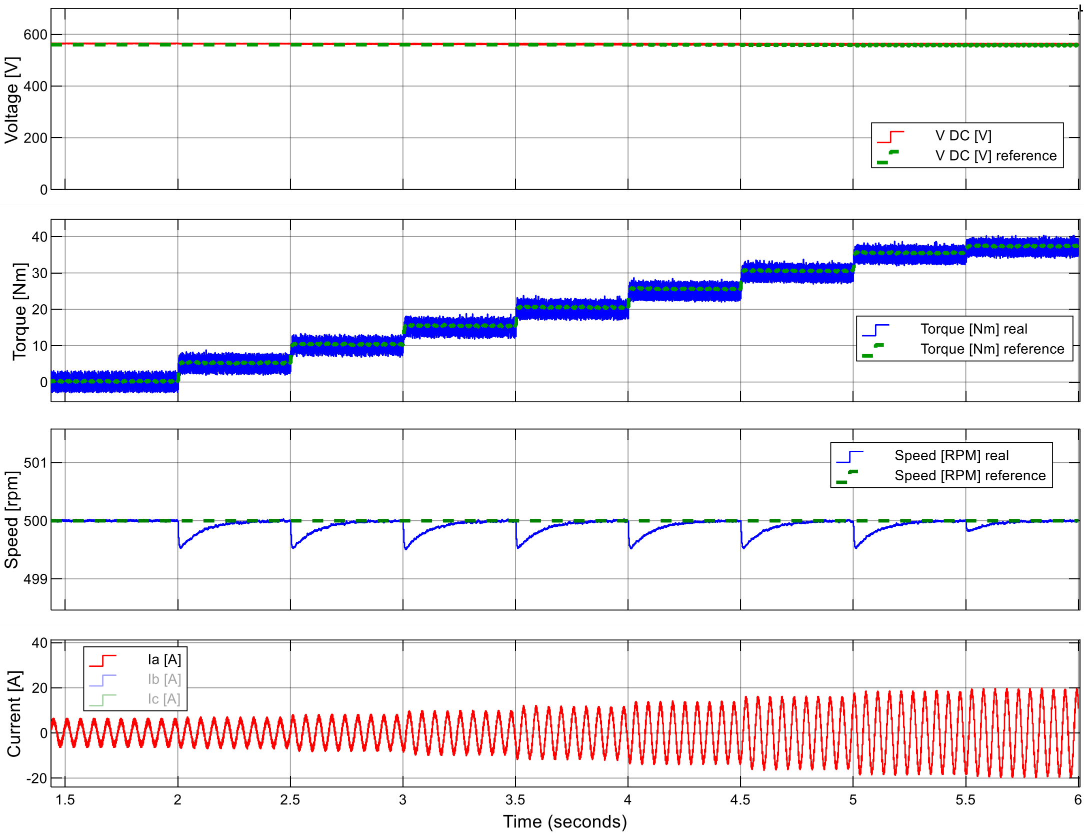

Fig. 55. Simulation run with increasing load and with full DC-link voltage; speed 500 rpm, load gradually increased from 0 to 37 Nm, flux 1 Wb.

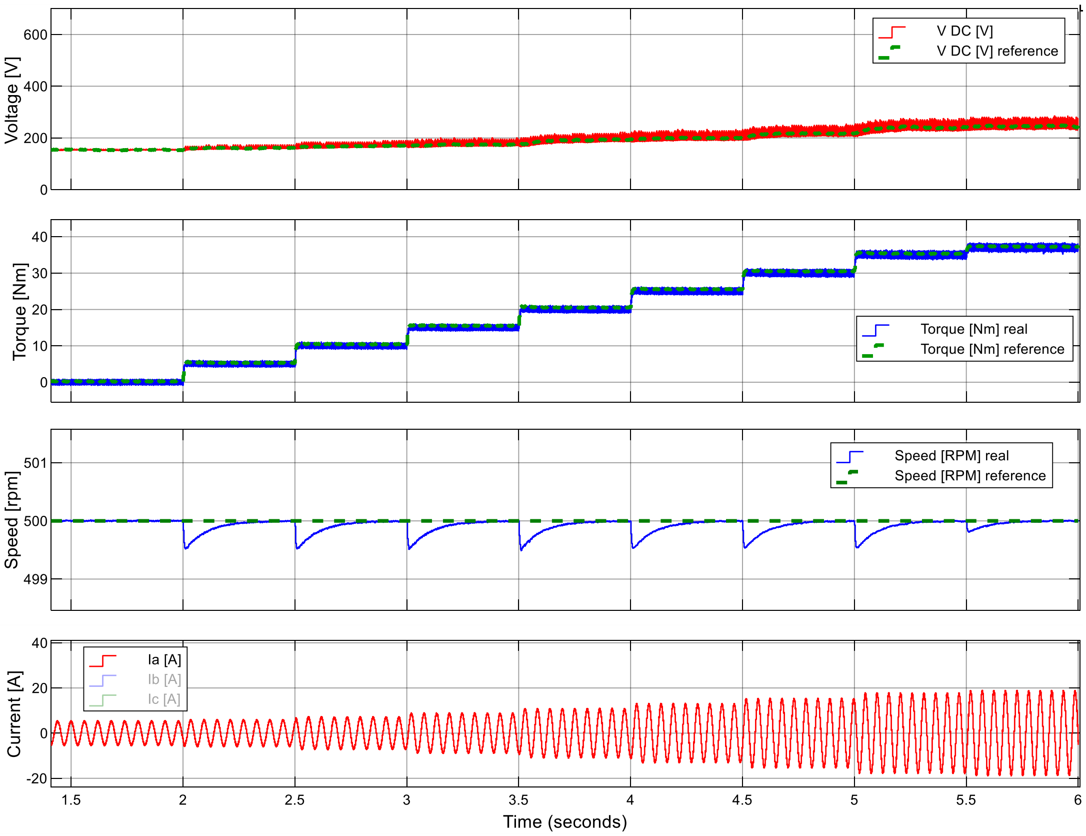

Fig. 56. Simulation run with increasing load and with DC-link voltage optimization; speed 500 rpm, load gradually increased from 0 to 37 Nm, flux 1 Wb.

Fig. 57 and Fig. 58 present the drive response during the transient, at which a lower speed reference is required. Fig. 58 shows the performance with the DC-link voltage optimization and Fig. 57 is for comparison with the full DC-link voltage operation. The load torque 15 Nm was applied and the IM was excited with 1 Wb for the whole time. The speed was kept at 1000 rpm in the beginning, and then, at the time 3 s, the speed reference quickly dropped to 500 rpm. The speed PI controller forces IM to create large negative torque, which brings the machine into the generator operation. Therefore, the energy from the machine is absorbed in the DC-link capacitor, which increases its voltage. The voltage increases up to 700 V, and, at this point, the switch controlling the brake resistor turns on so the energy is dissipated in the resistor. The simulation shows that within this process, the algorithm is unable to optimize the DC-link voltage. However, after the speed transient fades away, the optimization works again.

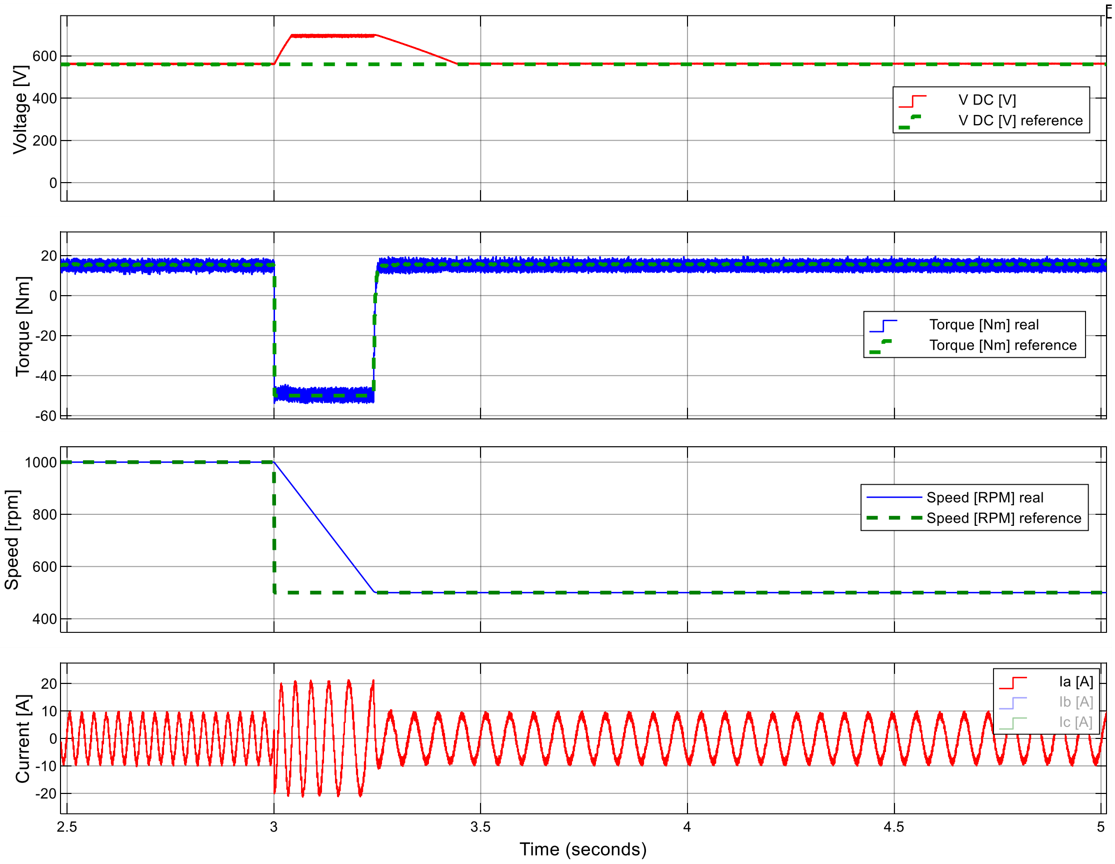

Fig. 57. Simulation run at speed reference decrease with full DC-link voltage; speed drop from 1000 to 500 rpm, load 15 Nm, flux 1 Wb.

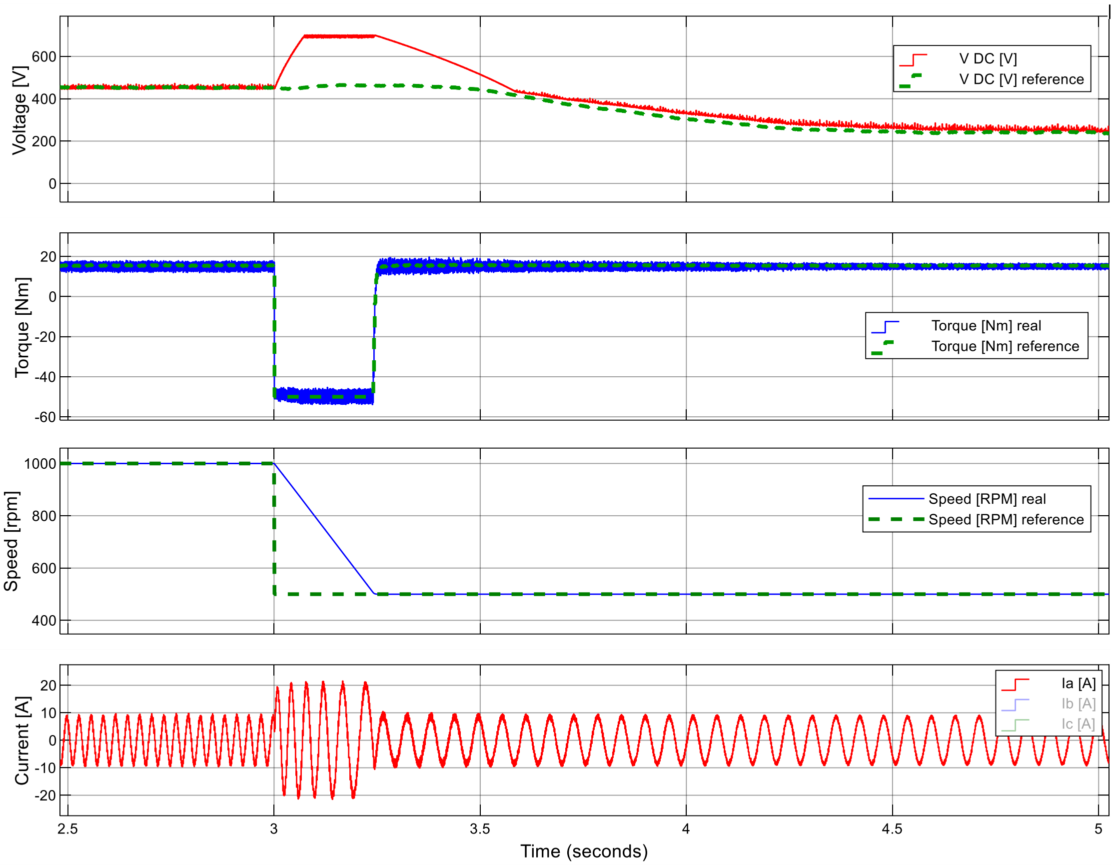

Fig. 58. Simulation run at speed reference decrease with DC-link voltage optimization; speed drop from 1000 to 500 rpm, load 15 Nm, flux 1 Wb.

7.1.4. Optimization in Field-Weakening Region

The field-weakening region is usually in the speed area above the rated speed. In this region, the flux excitement of the IM is lowered. This decreases the back emf so further speed increase is possible. However, the lower flux amplitude is always connected with lower maximum torque. The performance in the field-weakening region is presented in Fig. 59 and Fig. 60. The simulation verifies the proper behavior of the DC-link voltage optimization in that region. The drive speed is kept above its nominal value at 1600 rpm by the PI controller and the applied load torque is 15 Nm. The reference of the stator flux decreases from 0.9 to 0.35 Wb with the step 0.05 Wb. The figures compare the performances in the cases without (Fig. 59) and with the DC-link voltage optimization (Fig. 60). In both cases, the minimum flux, at which the drive is kept at the reference speed, is 0.4 Wb. Below that value, the speed decreases. In the case of the optimization, the DC-link voltage decreases with the flux, and makes the torque waveform slightly smoother. The improvement in this operating point is not that significant compared to the performance in the speed below the rated value.

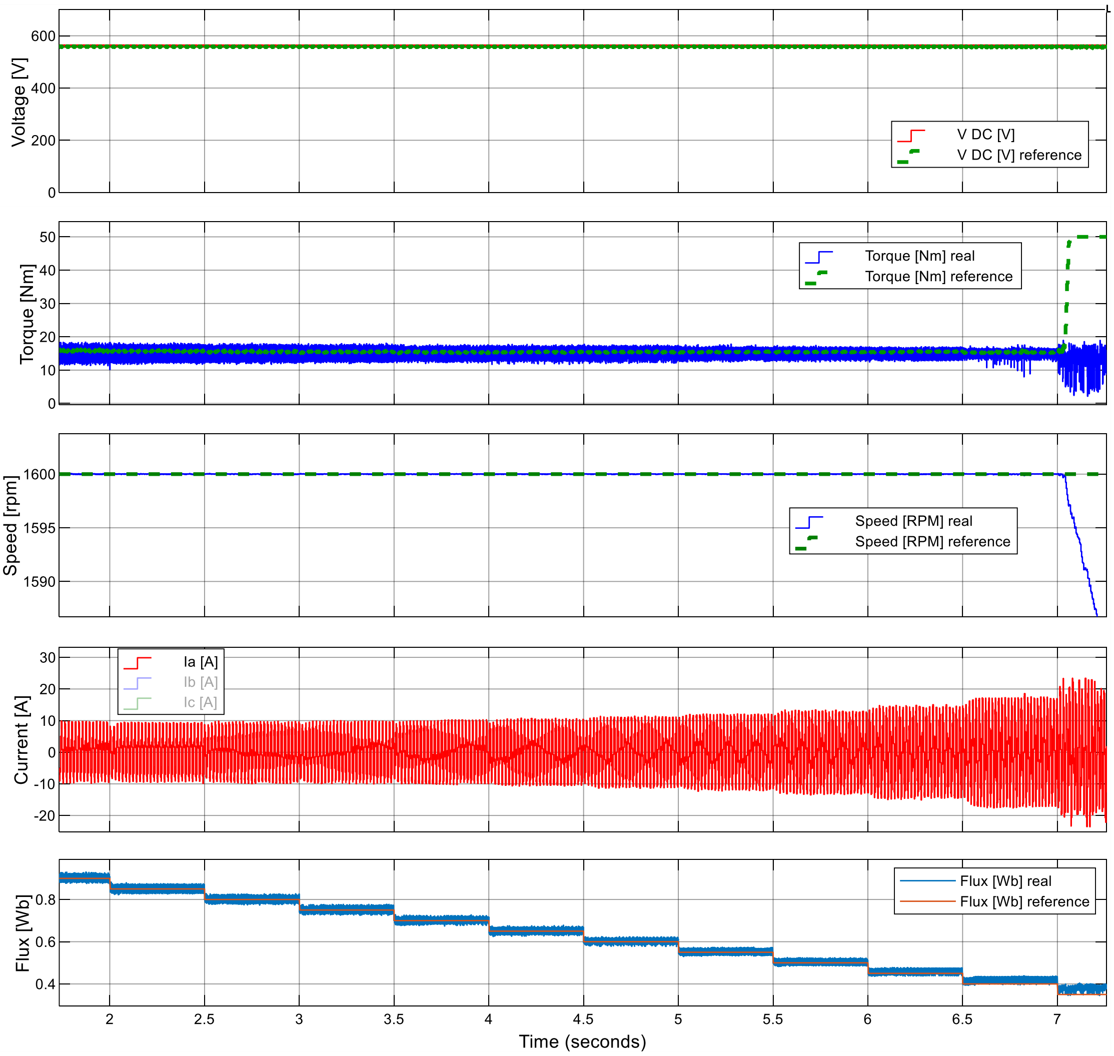

Fig. 59. Simulation run in the field-weakening region with full DC-link voltage; speed 1600 rpm, load 15 Nm, flux decreasing from 0.9 to 0.35 Wb.

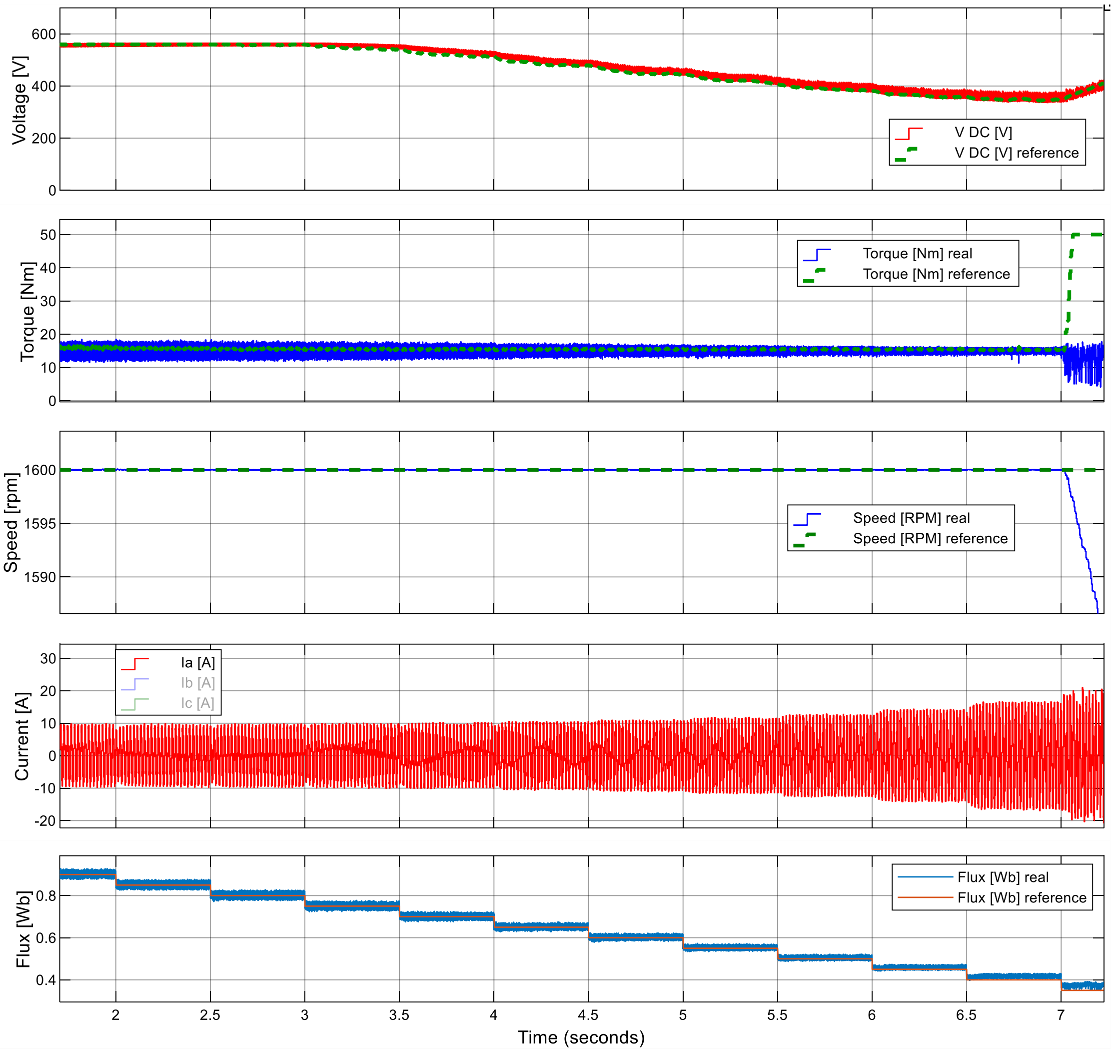

Fig. 60. Simulation run in the field-weakening region with optimized DC-link voltage; speed 1600 rpm, load 15 Nm, flux decreasing from 0.9 to 0.35 Wb.

7.2. Experimental Results with Speed Sensor

The proposed optimization strategy was further validated with an experiment on a laboratory drive with IM. As the controlled rectifier, the CKD MTT 431-63-12-LHO thyristors in a bridge topology is used. To ensure its grid synchronization, the grid voltage is measured with the step-down transformers. The resulting signals are brought to ADCs (analog digital converters) for the further angle calculation. The two electrolytic capacitors, each with capacitance 4700 µF and rated voltage 450 V, create the DC-link. To suppress the current peaks flowing to the DC-link, a DC-link coil with inductance around 1 H and 25 A rated current is used. As the inverter, the Infineon BSM100GB120DN2K IGBTs in a bridge topology are used and are driven by the Concept 2SD106AI driver. The same IGBT and driver are also used for the 100 Ω brake resistor. This IGBT turns on when the DC-link voltage exceeds 700 V. The DC-link voltage and two line currents are measured with their appropriate LEMs, and the resulting signals are then brought to the ADCs. The topology is presented in Fig. 61.

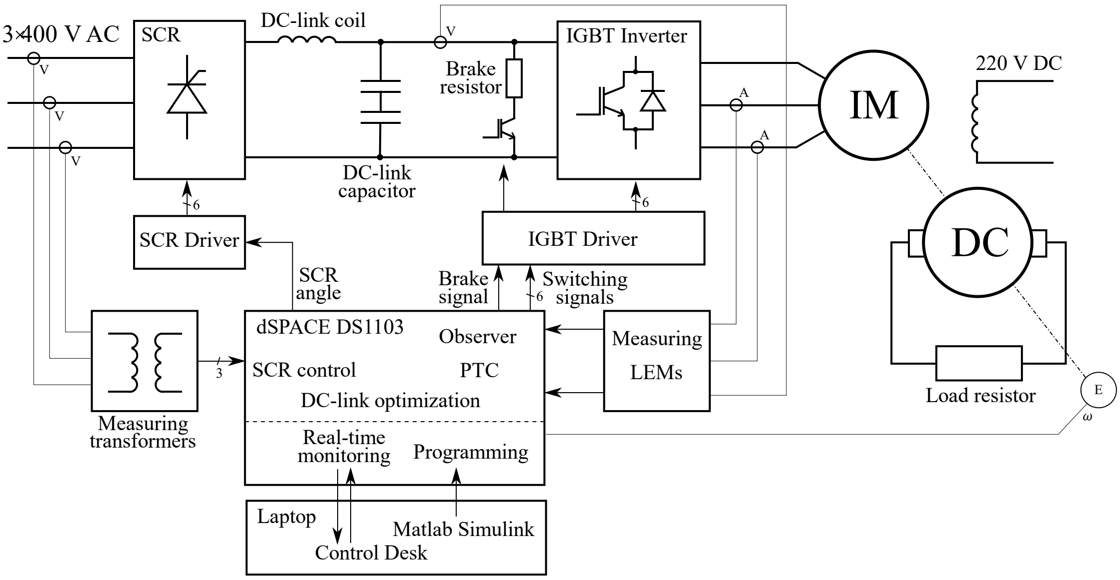

Fig. 61. The experimental setup.

A rapid prototyping board dSpace DS1103 is utilized for the drive control. The control model is developed in Matlab Simulink. It brings the advantage of using the same code with only minor changes for the simulation and experiment. It generates a C language code, compiles it, and uploads it to dSpace. Its most important properties are the 400 MHz PowerPC processor with 20 MHz TMS320F240 slave DSP (digital signal processing), 4 multiplexed (4x4 channels) and 4 individual 16-bit ADC inputs, 8 14-bit DAC (digital analog converter) outputs, 12 PWM outputs, incremental encoder support, multiple timers and hardware interrupts and CAN (controller area network) and serial interface. The sampling time of the algorithms implemented in dSpace was limited by the complexity of the algorithms and was set to 100 µs, which is the smallest operable value. The real-time communication between the dSpace and the computer after the code upload is managed by ControlDesk program. ControlDesk enables the read and write to the dSpace memory and to plot the waveforms of selected variables in real time. The

GUI (graphical user interface) developed in the ControlDesk environment is presented in Appendix A2. Since PTC doesn't use a modulator, the selected voltage vector, with necessary deadtime, was directly applied by the inverter for the duration of the whole sample time. Therefore, the switching frequency was not constant. The average switching frequency was measured to be around 1.8 kHz. The photography of the experimental setup with the description of the depicted parts is presented in Fig. 62.

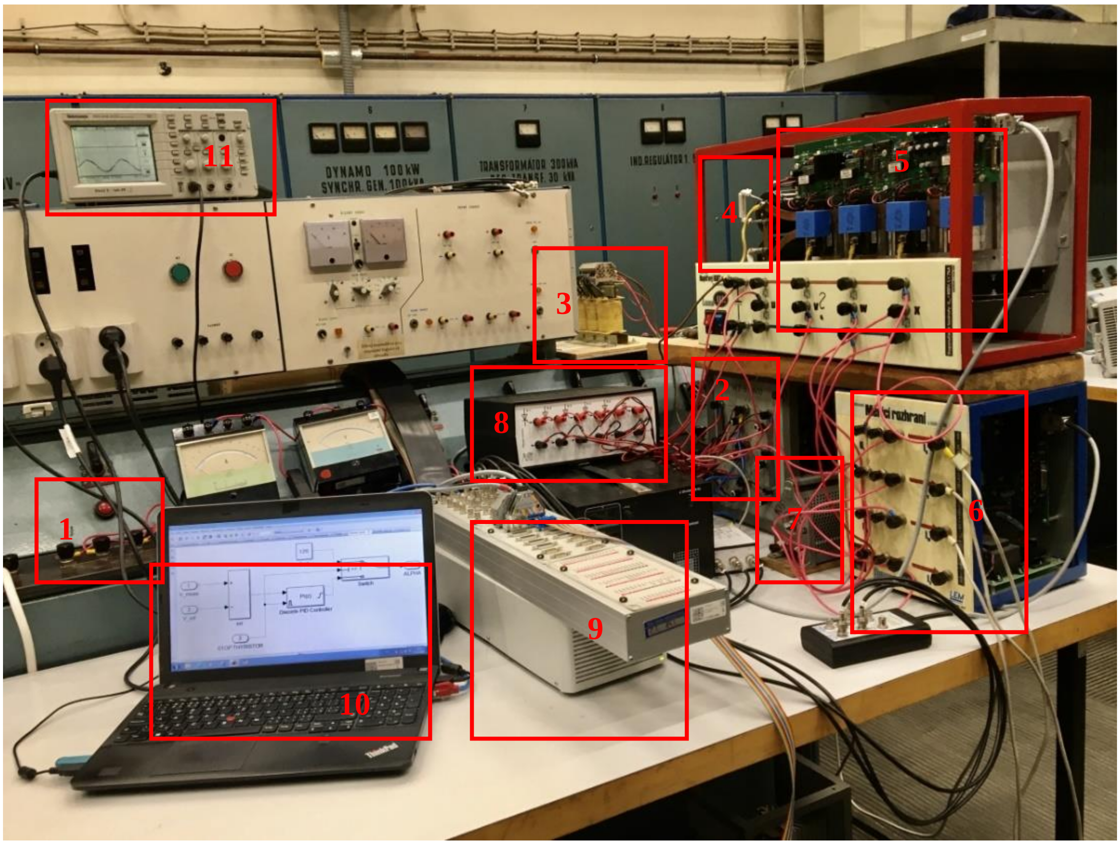

Fig. 62. The experimental setup, 1 – power source, 2 – SCR, 3 – DC-link choke, 4 – DC-link capacitors, 5 – IGBT inverter, 6 – Measuring interface, 7 – Brake resistor, 8 – SCR driver, 9 – dSpace DS1103, 10 – Laptop, 11 – Oscilloscope. Published by the author [166].

The three-phase four-pole squirrel-cage IM of 5.5 kW output power serves as a test motor. The load is created by the separately excited DC motor connected to the same shaft. The DC motor's terminals are electrically connected to a sliding resistor. Therefore, the load is speed-dependent and can be adjusted by the resistor value or by the excitation current. The rotational speed of the drive is measured by an optical incremental encoder with a 10-bit resolution. The rated values and parameters of the tested induction motor and DC motor that was used as a loading machine are listed in Table 3 and Table 4, respectively. Moreover, Table 4 presents the rated values of a synchronous generator that was utilized to create a harmonic voltage source with adjustable frequency and amplitude. The machines setup is depicted in Fig. 63.

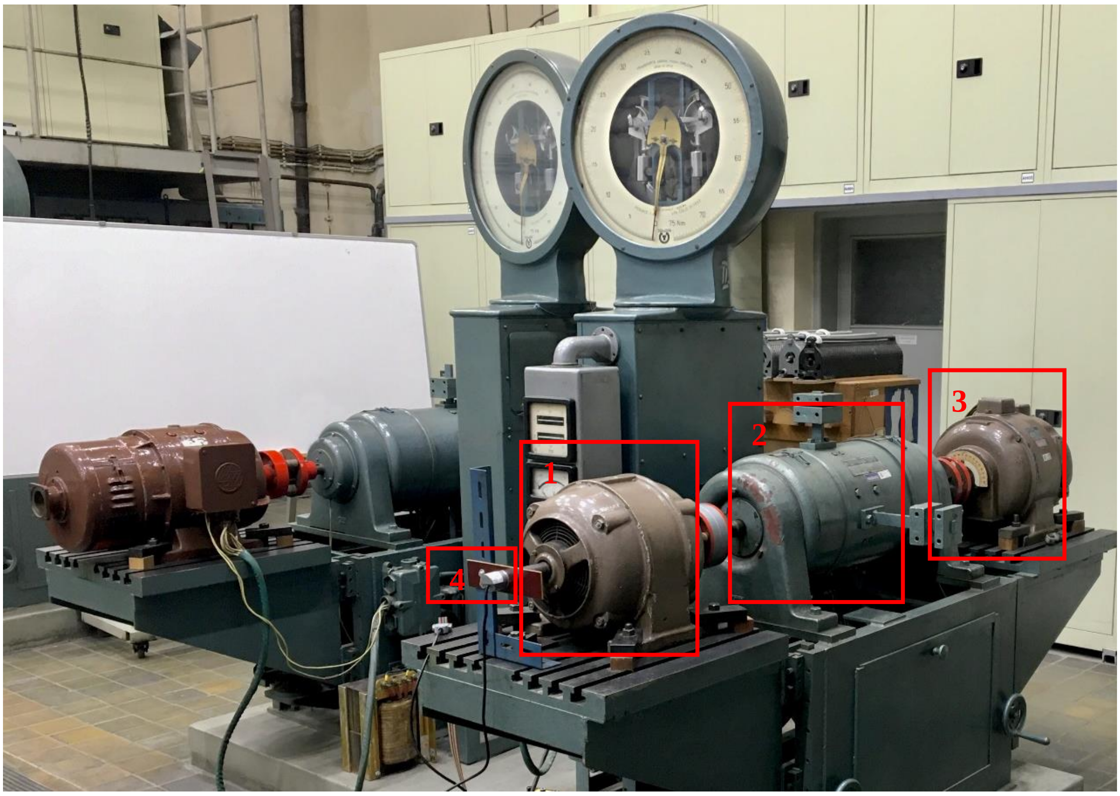

Fig. 63. The machines setup, 1 – Tested IM, 2 – Load DC motor, 3 – Synchronous generator, 4 – Optical encoder.

Table 3: Induction motor parameters and nameplate data.

Nameplate Data		Mathematical Model Parameters	
Nominal power	5.5 kW	Stator resistance	0.875 Ω
Nominal voltage	380 V	Rotor resistance	0.71 Ω
Nominal current	11.8 A	Stator inductance	0.15725 H
Nominal speed	1430 rpm	Rotor inductance	0.15763 H
Number of poles	4	Magnetizing inductance	0.15 H
		Iron core resistance	530 Ω

Table 4: DC dynamometer and synchronous generator nameplate data.

DC Dynamometer (Load DC motor)		Synchronous Generator	
Nominal power	6.7 kW	Nominal power	8 kW
Nominal armature voltage	220 V	Nominal stator voltage	400 V
Nominal armature current	32.6 A	Nominal stator current	14.5 A
Nominal speed	1500 rpm	Nominal speed	1500 rpm
Nominal excitation voltage	220 V	Nominal excitation voltage	32 V
Nominal excitation current	1.2 A	Nominal excitation current	7.6 A

7.2.1. Drive Behavior during DC-Link Voltage Decrease

The first experiment was performed to verify the behavior of the drive with decreasing DC-link voltage. The DC-link voltage, the calculated and the reference torque waveforms are presented in Fig. 64. In the experiment, the speed of the motor was kept at 500 rpm by the traditional PTC algorithm with the speed PI controller. The load was set 15 Nm. During that, the voltage was slowly decreasing from the full DC-link 550 V to 0 V. The figure shows, that with the full DC-link voltage, the torque ripple was high and was decreasing until the critical DC-link voltage was reached. At that point, the motor was no longer able to counter the back-emf and deliver the requested power. Therefore, the speed controller was not able to further keep the reference speed, and the speed dropped. For this operating point (500 rpm, 15 Nm, and 0.8 Wb), the threshold and critical DC-link voltage were calculated as 161 V and 169 V, respectively, and the enumeration is provided in 7.1.1.

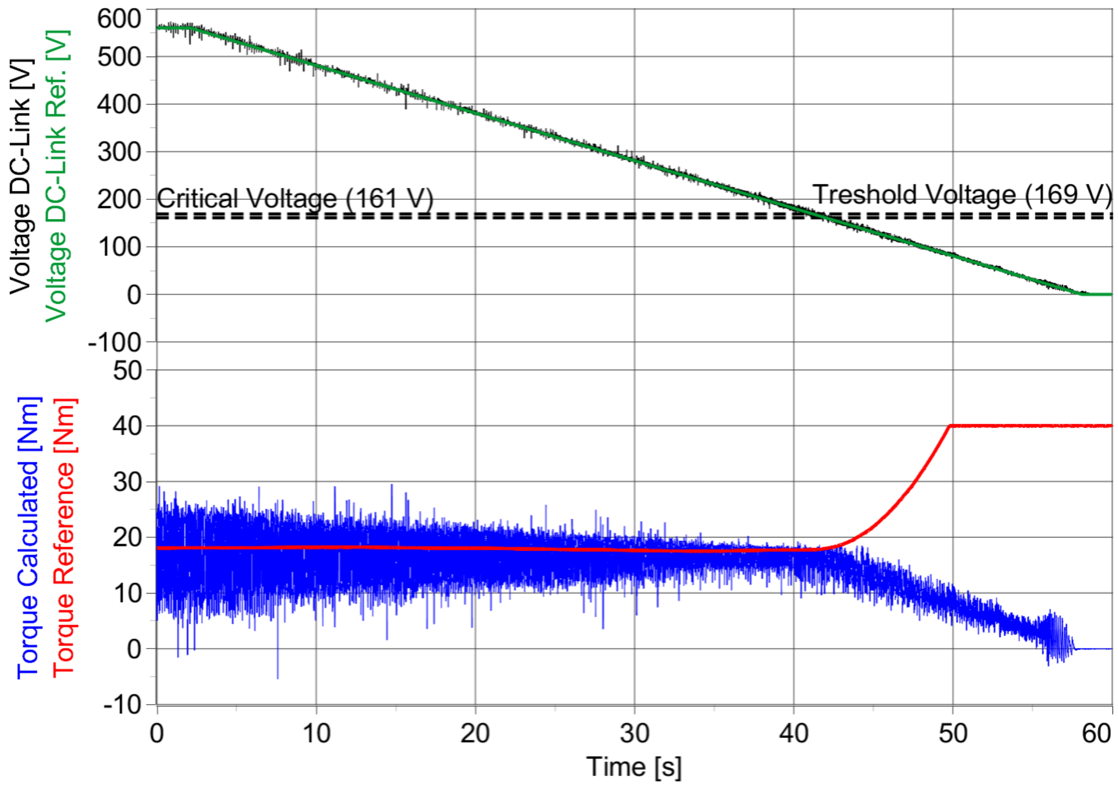

Fig. 64. Effect of the DC-Link voltage decrease on the calculated torque ripple; speed 500 rpm, flux 0.8 Wb, load 15 Nm. Published by the author [166].

Fig. 65 shows the detail of Fig. 64 around the threshold and critical DC-link voltages.

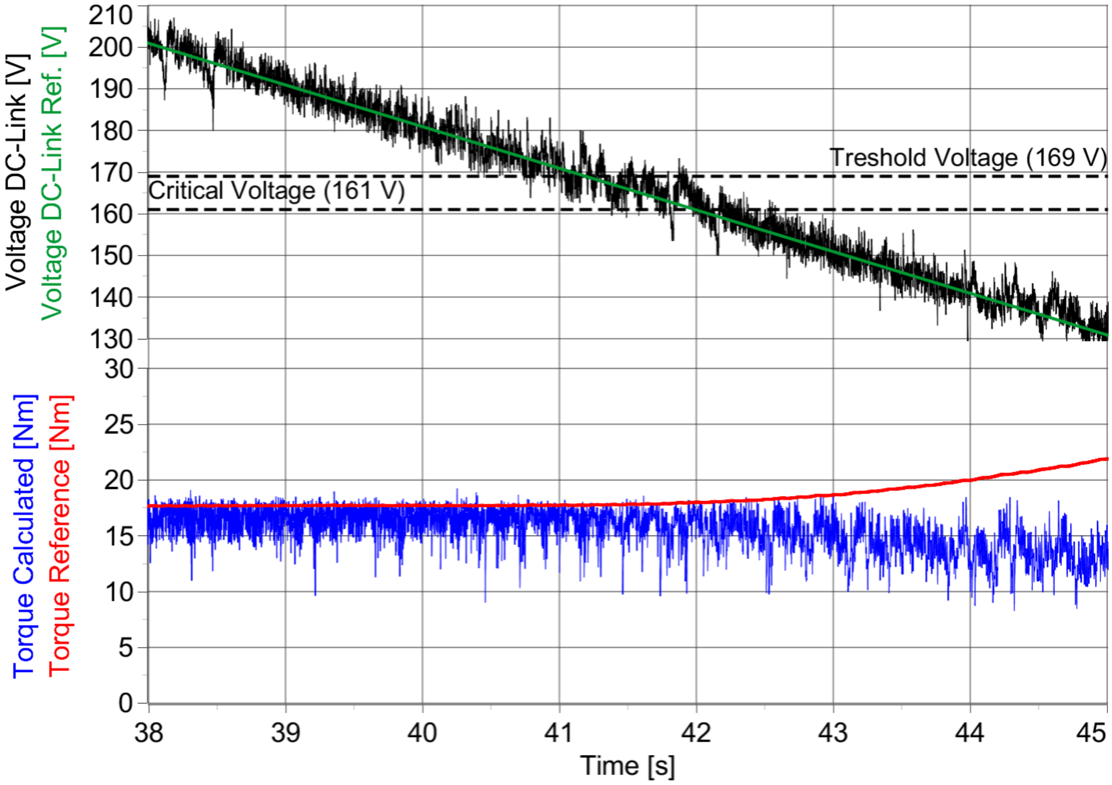

Fig. 65. Detail of Fig. 64 around threshold and critical DC-link voltage; speed 500 rpm, flux 0.8 Wb, load 15 Nm. Published by the author [166].

7.2.2. Optimization Algorithm in Steady State

In the following experiment, the DC-link voltage optimization was tested. In Fig. 66, the optimization process during the steady-state operation is depicted. Within the experiment, the speed was kept at 500 rpm by the speed PI controller, and the load torque was set to the rated value 37 Nm. At the beginning, the full DC-link voltage 550 V was present. Within this run, the torque ripple was high (around 21 Nm peak to peak ripple value). Then, the optimization algorithm was launched, and during the optimization, the torque ripple was decreasing. It took approximately 1 s to reach the DC-link voltage final value, which was found a little above the threshold value. The final torque ripple was significantly lower (around 6 Nm peak to peak ripple value).

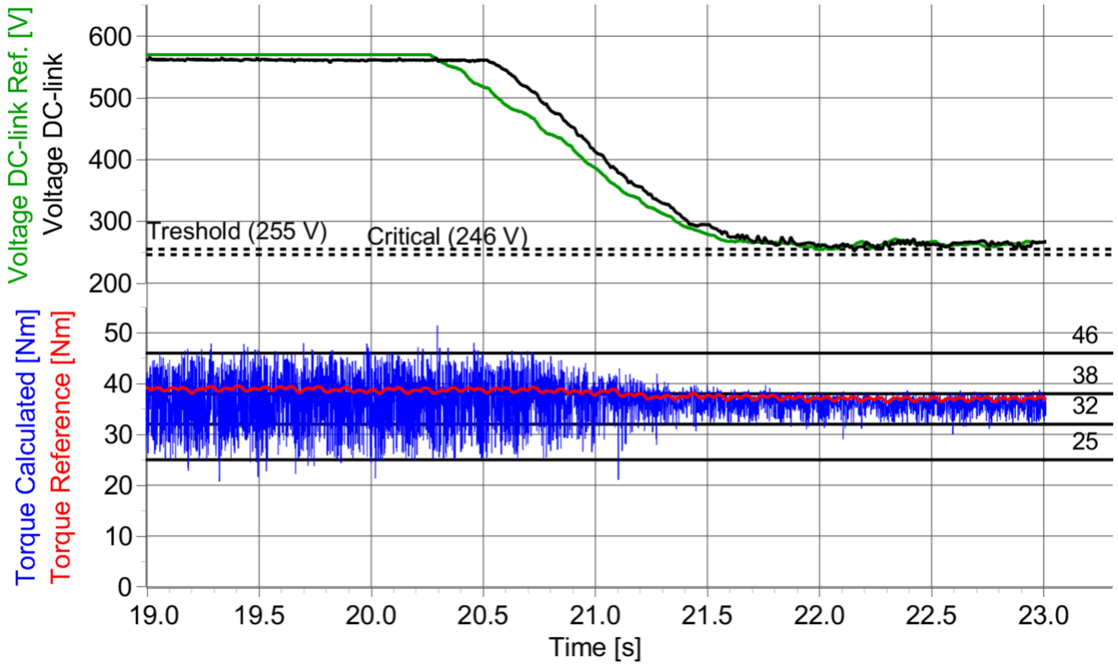

Fig. 66. Voltage optimization in steady-state; speed 500 rpm, flux 1 Wb, load 37 Nm. Published by the author [166].

Within the same condition (500 rpm, 37 Nm), the detail of the line current waveform was recorded for the cases of PTC with full DC-link and PTC with optimized DC-link. The waveforms are depicted in Fig. 67. The higher ripple with THD 4.6 % is observed with the full DC-link (top waveform) than in the case of running with optimized DC-link (bottom waveform) where the THD decreased to 2.9 %.

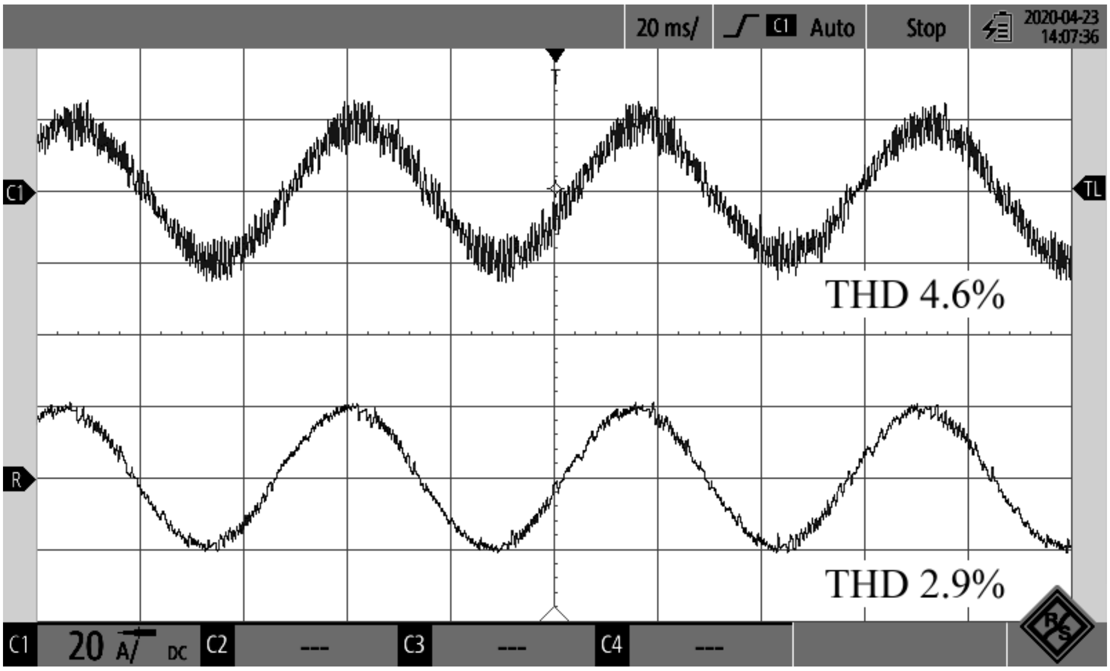

Fig. 67. Line current comparison for PTC with (bottom waveform) and without (top waveform) optimization; speed 500 rpm, flux 0.8 Wb, load 37 Nm. Published by the author [166].

The waveforms of the line current were recorded for multiple operating points. Some of them are presented in Fig. 68 (500 rpm, no-load operation), Fig. 69 (1000 rpm, 37 Nm) and Fig. 70 (1000 rpm, no-load operation). In all of the operating points, the THD is lower in the case of PTC with DC-link voltage optimization.

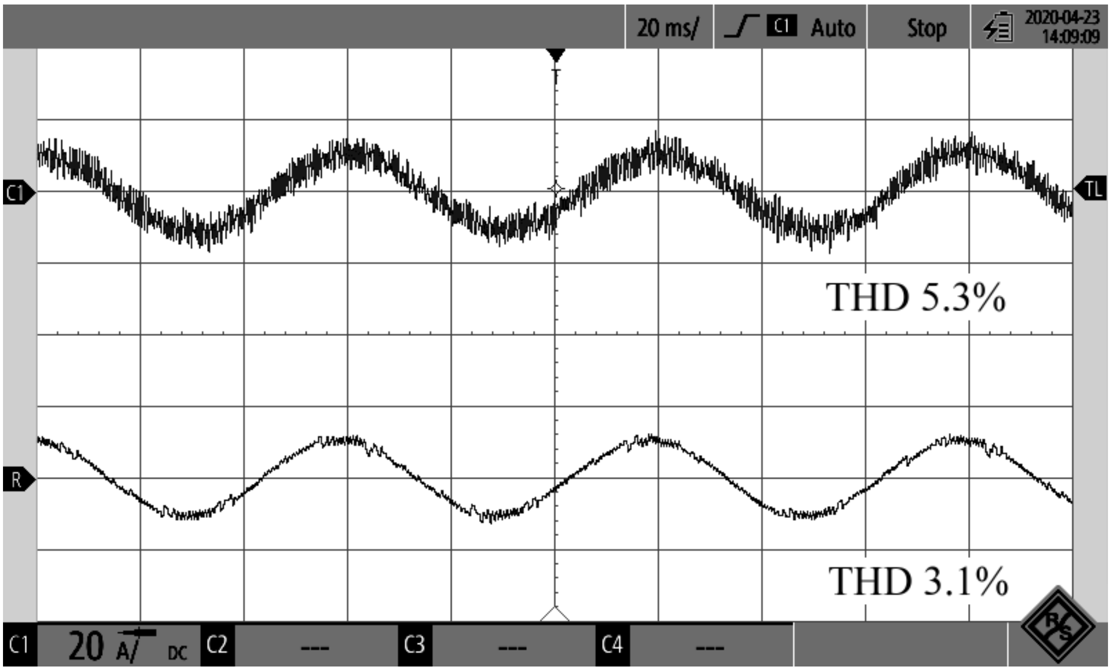

Fig. 68. Line current comparison for PTC with (bottom waveform) and without (top waveform) optimization; speed 500 rpm, flux 0.8 Wb, load 0 Nm. Published by the author [166].

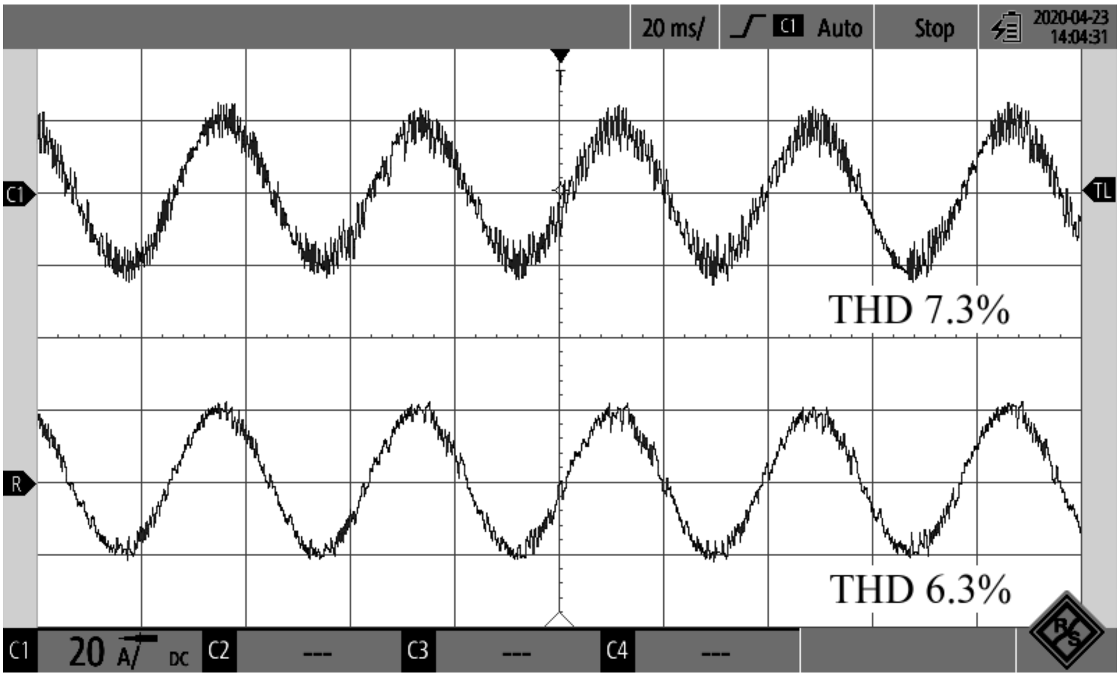

Fig. 69. Line current comparison for PTC with (bottom waveform) and without (top waveform) optimization; speed 1000 rpm, flux 0.8 Wb, load 37 Nm.

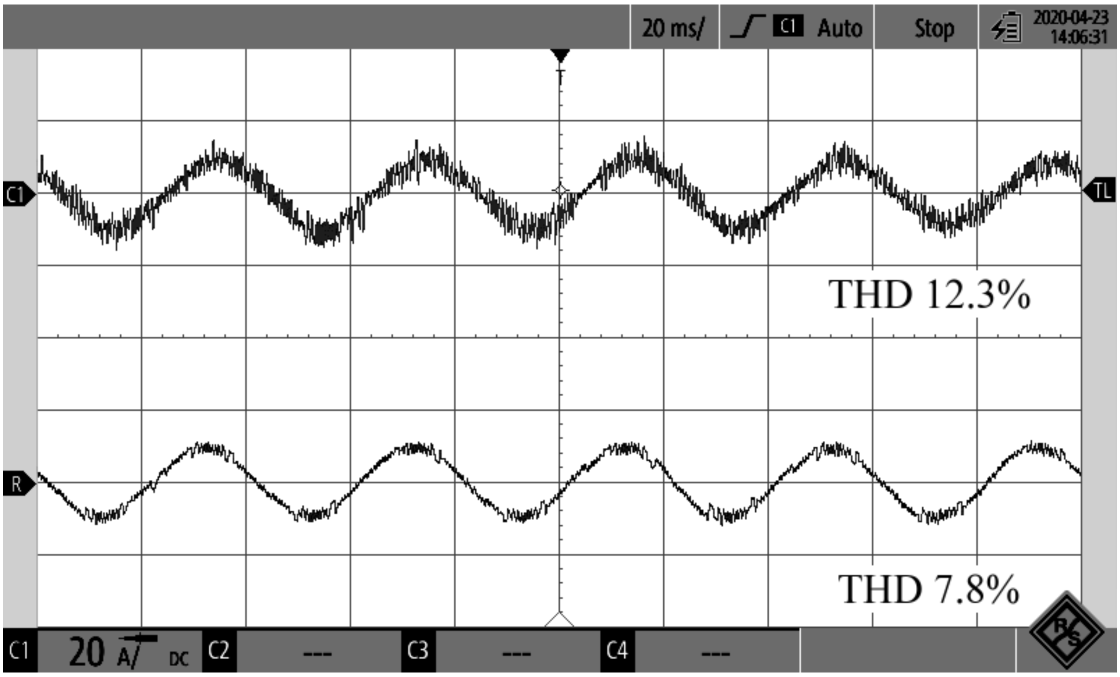

Fig. 70. Line current comparison for PTC with (bottom waveform) and without (top waveform) optimization; speed 1000 rpm, flux 0.8 Wb, load 0 Nm.

For better comprehension of the proposed optimization performance, the effect of the method on the line current THD is summarized in Fig. 71 and in Table 5. Fig. 71 shows the dependence of line current THD on load from no-load operation to the rated torque 37 Nm. The speed was kept at 500 rpm by the speed controller for the whole time. The PTC with full DC-link is shown as red points, and PTC with optimization is shown as blue points. In both cases, the THD slightly decreases with the load, and in the case of the PTC with optimization, the THD is around 2.5 - 3 % lower compared to the full DC-link operation.

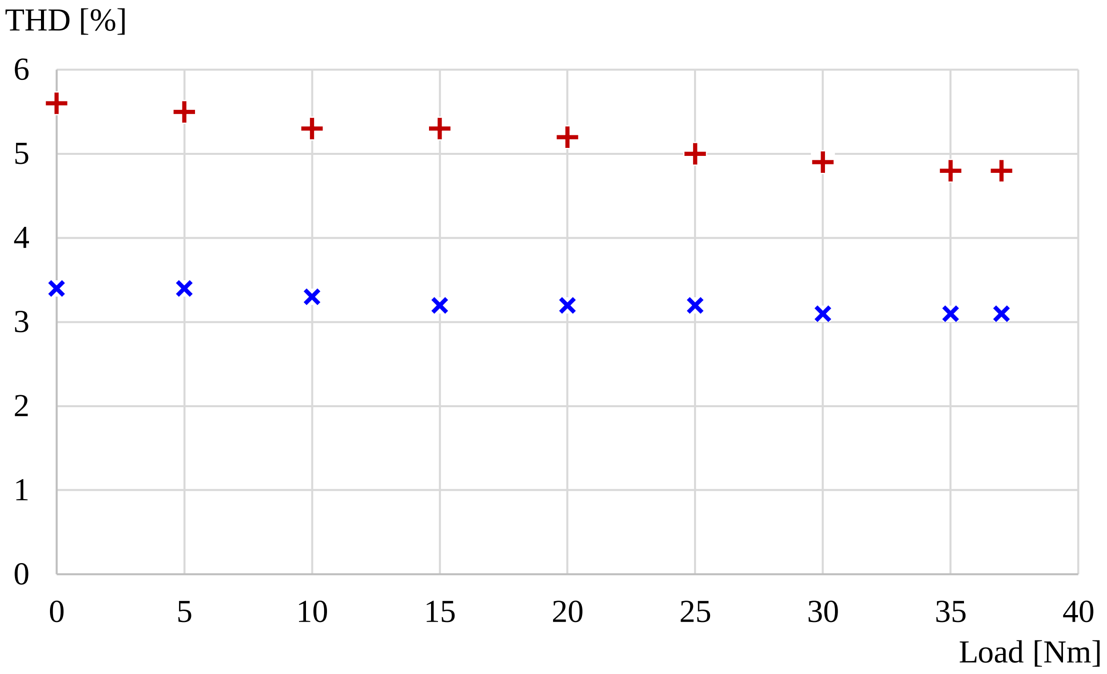

Fig. 71. Dependence of the line current THD on load; speed 500 rpm and for full (red) and optimized (blue) DC-link voltage. Published by the author [166].

The overview of multiple operating points is presented in Table 5. The table compares the THD in the case of full DC-link voltage with the THD in case of optimized voltage. Further, it shows the optimal DC-link voltage found by the algorithm for each of the operating points. The choice of operating points includes different speeds (500, 750, 1000, 1250, and rated value 1430 rpm) and different load torques (no load, 20 Nm, and rated value 37 Nm). The table shows lower THD of the line current for the case with the optimization than for the operation with full DC-link voltage for most operating points. Only within 1250 and 1430 rpm with rated load, the THD of the current remained the same with and without optimization. This happened because the algorithm found the full DC-link voltage as optimum value and, therefore, no difference between the two cases occurred.

Table 5: Line current THD in different operating points.

Speed [rpm]	Load [Nm]	THD (full V_{DC}) [%]	Optimized V_{DC} [V]	THD (optimized V_{DC}) [%]
500	0	5.3	200	3.1
	20	5.0	230	3.0
	37	4.6	260	2.9
750	0	11.3	290	5.4
	20	9.7	330	4.9
	37	7.8	360	4.7
1000	0	12.3	380	7.8
	20	9.2	415	6.6
	37	7.3	460	6.3
1250	0	12.7	460	10.6
	20	10.3	500	8.2
	37	9.1	560	9.1
1430	0	15	470	12
	20	9.7	510	8.5
	37	8.0	560	8.0

The detail of the stator flux vector trajectory in the stationary $\alpha\beta$ coordinate system during one electrical turn is depicted in Fig. 72. The objective of the control algorithm is to maintain the stator flux vector trajectory circular. However, this would be possible only in an ideal case with infinite switching frequency and zero sample time. The figure compares the trajectories of the PTC with (blue curve) and without (red curve) optimization for the operating point of speed 500 rpm, flux 0.8 Wb, and no load. The much smoother trajectory with lower deviation from the ideal circular trajectory is observed with the voltage optimization.

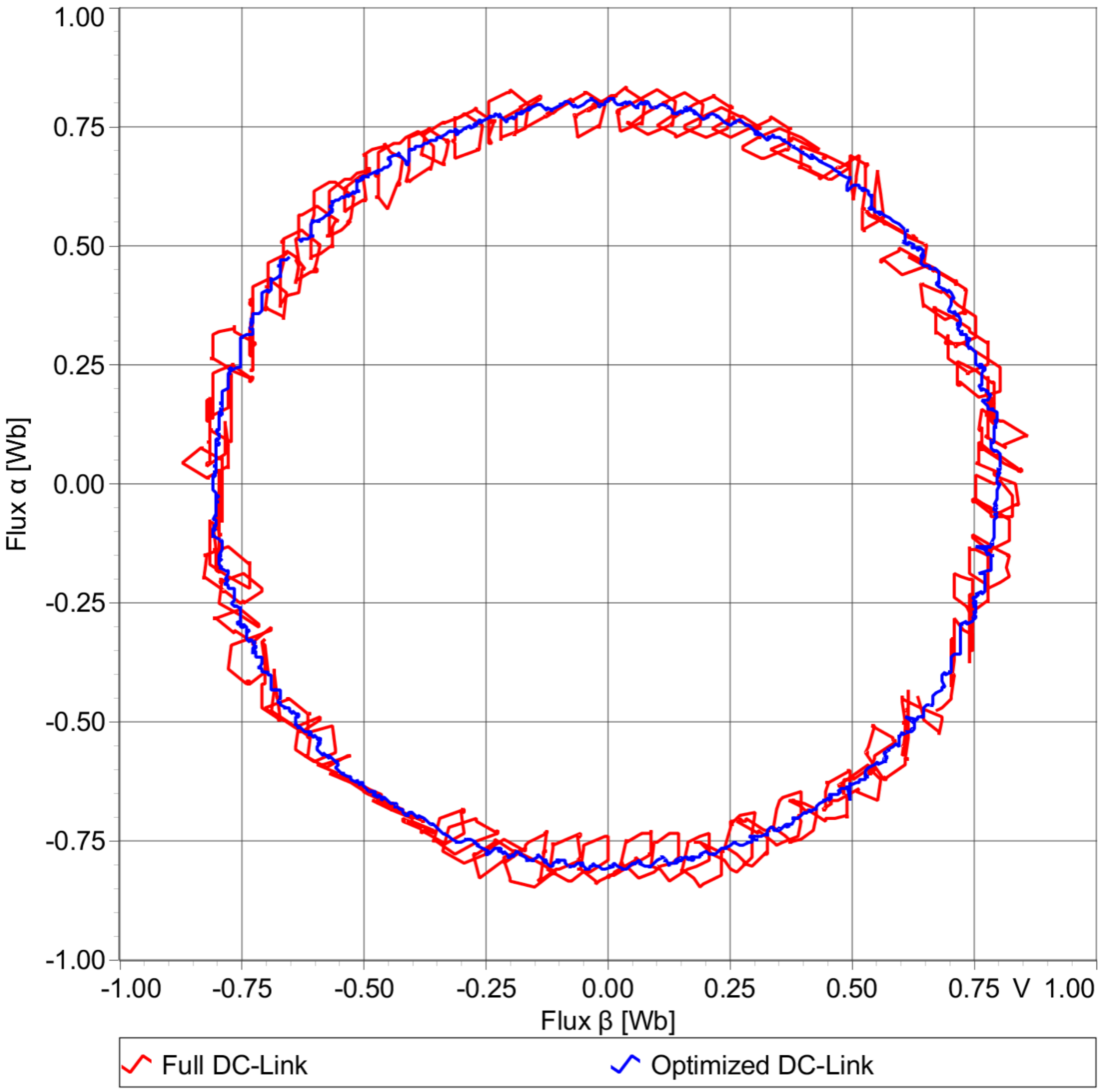

Fig. 72. Flux vector trajectory in the stationary αβ coordinate system for PTC with and without optimization; speed 500 rpm, flux 0.8 Wb, load 0 Nm. Published by the author [166].

For the same conditions (speed 500 rpm, flux 0.8 Wb, load 0 Nm), the FFT (fast Fourier transform) of the current was performed and is presented in Fig. 73. The figure shows that the amplitude of the fundamental frequency is the same for both cases. But, in the higher frequencies, the higher amplitude is observed in the case of PTC with full DC-link (red curve) than with optimized voltage (blue curve). The highest difference is observed around 1.5 and 2 kHz, which is the approximate switching frequency of the transistor.

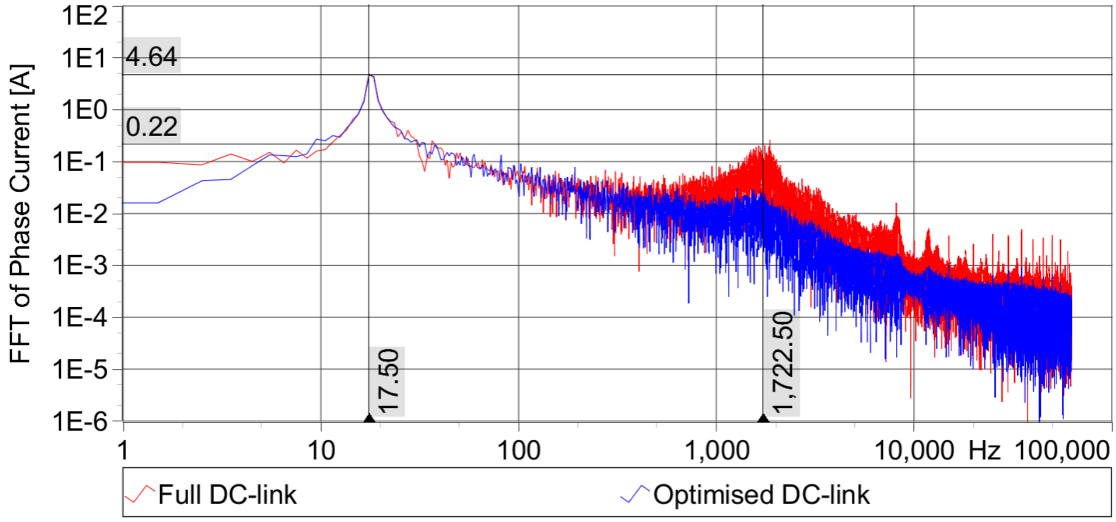

Fig. 73. FFT analysis of the line current for PTC with and without optimization; speed 500 rpm, flux 0.8 Wb, load 0 Nm. Published by the author [166].

7.2.3. Optimization Algorithm in Transients

The behavior of the drive with voltage optimization during the sudden change of the reference speed is depicted in Fig. 74. Initially, the motor is at a standstill with zero speed. During the standstill, the motor is still excited with 0.8 Wb. For that, only a small voltage is needed. The loading machine is the separately excited DC motor with load resistors in the armature winding; therefore, at 0 rpm, the load is 0 Nm. Shortly, the reference speed quickly changed from 0 rpm to 1000 rpm (speed is shown at the bottom). With increasing speed, the load also increases up to the setpoint 30 Nm (middle). In the case of the PTC with optimization, the DC-link voltage converges to its new optimal value (top), and the reference speed is reached. The figure shows that in the case of full DC-link voltage, the reference speed is reached faster compared to the optimized voltage by about 0.5 s. Therefore, the drive response, in the case of a reference speed step change towards a higher value, is slightly deteriorated with the optimization. However, in many applications, this is not an issue since the maximum acceleration is often limited by other factors, such as adhesion characteristics or relevant standards.

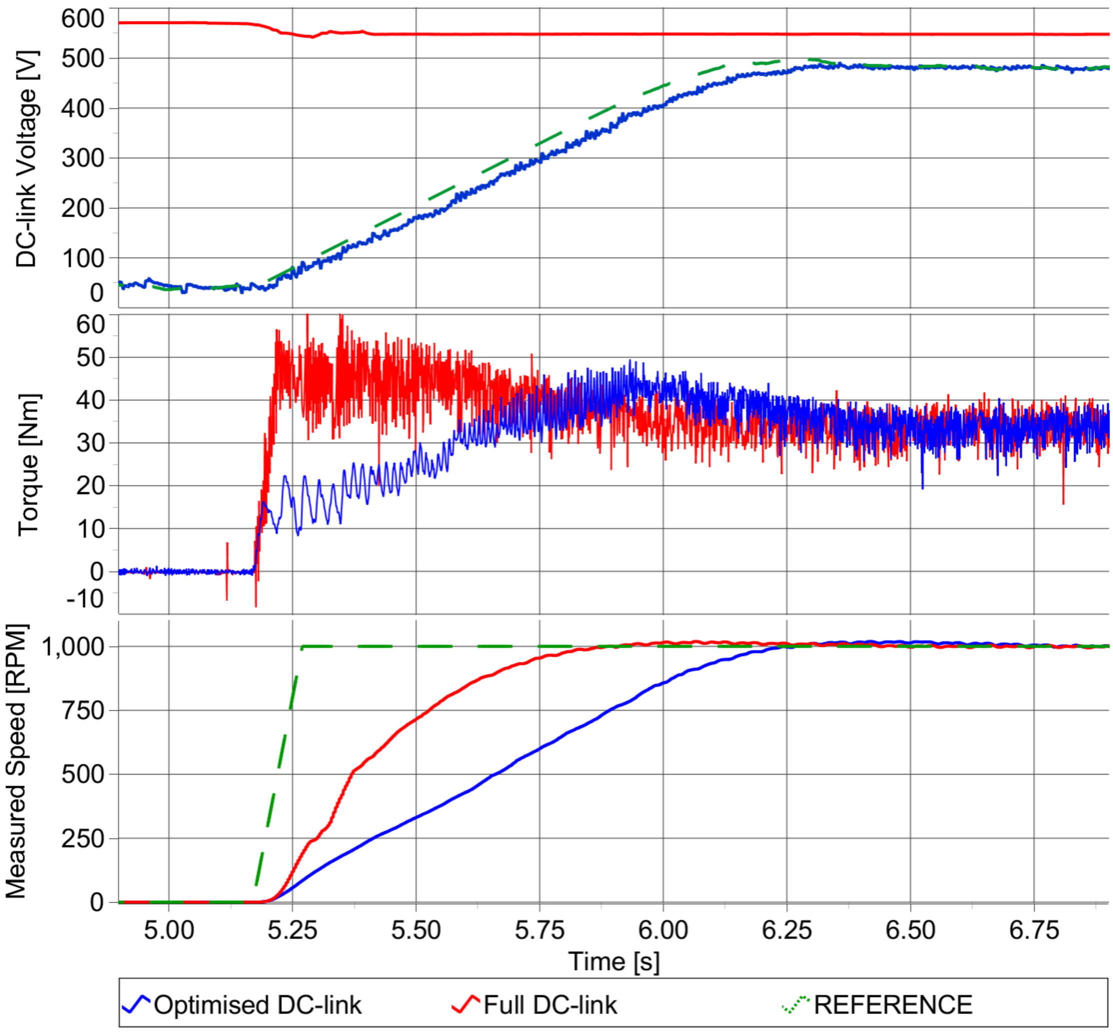

Fig. 74. Voltage optimization during motor start-up from a standstill (speed 0 rpm, no load) to speed 1000 rpm and rated load 37 Nm). Published by the author [166].

The performance during the change of speed towards a smaller value is depicted in Fig. 75. The drive was operating at speed 1000 rpm and loaded with 30 Nm. Then, the speed reference (green curve) decreased to zero. Since the load is speed-dependent, the final load was 0 Nm. In the zero-speed operation, the motor was still with excitation 0.8 Wb. The figure shows a good response in case of speed and torque. Also, it can be seen that the actual DC-link voltage does not adequately track the reference one. This is caused by the fact that the SCR allows only one polarity of current, and, during the drive braking, the DC-link voltage has to wait until the motor absorbs this energy. Moreover, during the braking, the machine behaves as a generator for a short time, so the DC-link voltage even slightly increases at one point. However, when the motor absorbs the energy from the DC-link, the DC-link voltage tracking continues without further problems.

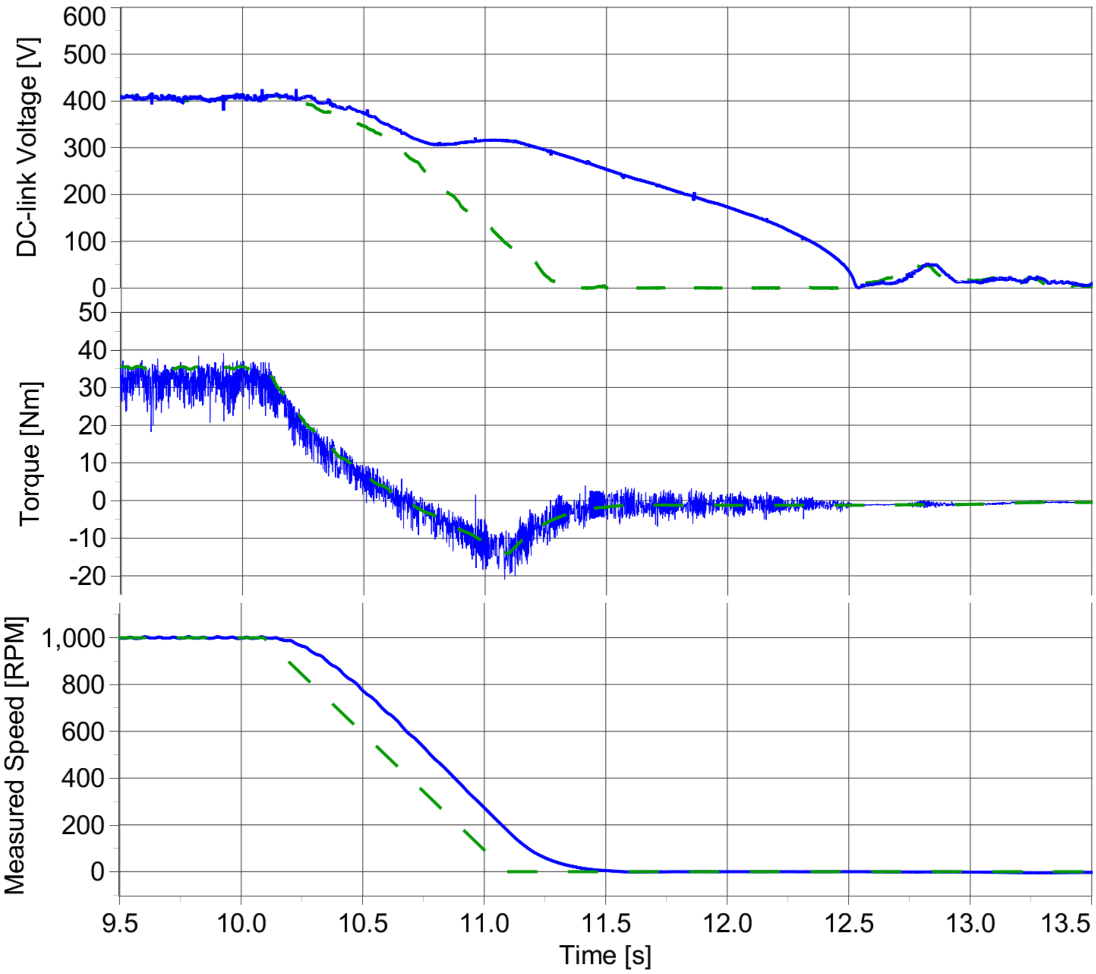

Fig. 75. Voltage optimization during motor brake from speed 1000 rpm to 0 rpm and with speed dependent load from 37 Nm to 0 Nm.

7.2.4. Optimization in Nominal Operating Point

To evaluate the behavior of the drive in the motor nominal working point (1430 rpm, 37 Nm), the start-up from zero speed to the rated point is presented in Fig. 76. Similar to the previous case, it was performed for the cases with and without DC-link voltage optimization. The start-up is slower in the case of the optimized DC-link voltage. By the time the nominal working point is reached, the DC-link voltage is already at its maximum value. Therefore, at high speed and high torque, the optimization method selects maximum voltage, so the performance of the drive is the same as without optimization.

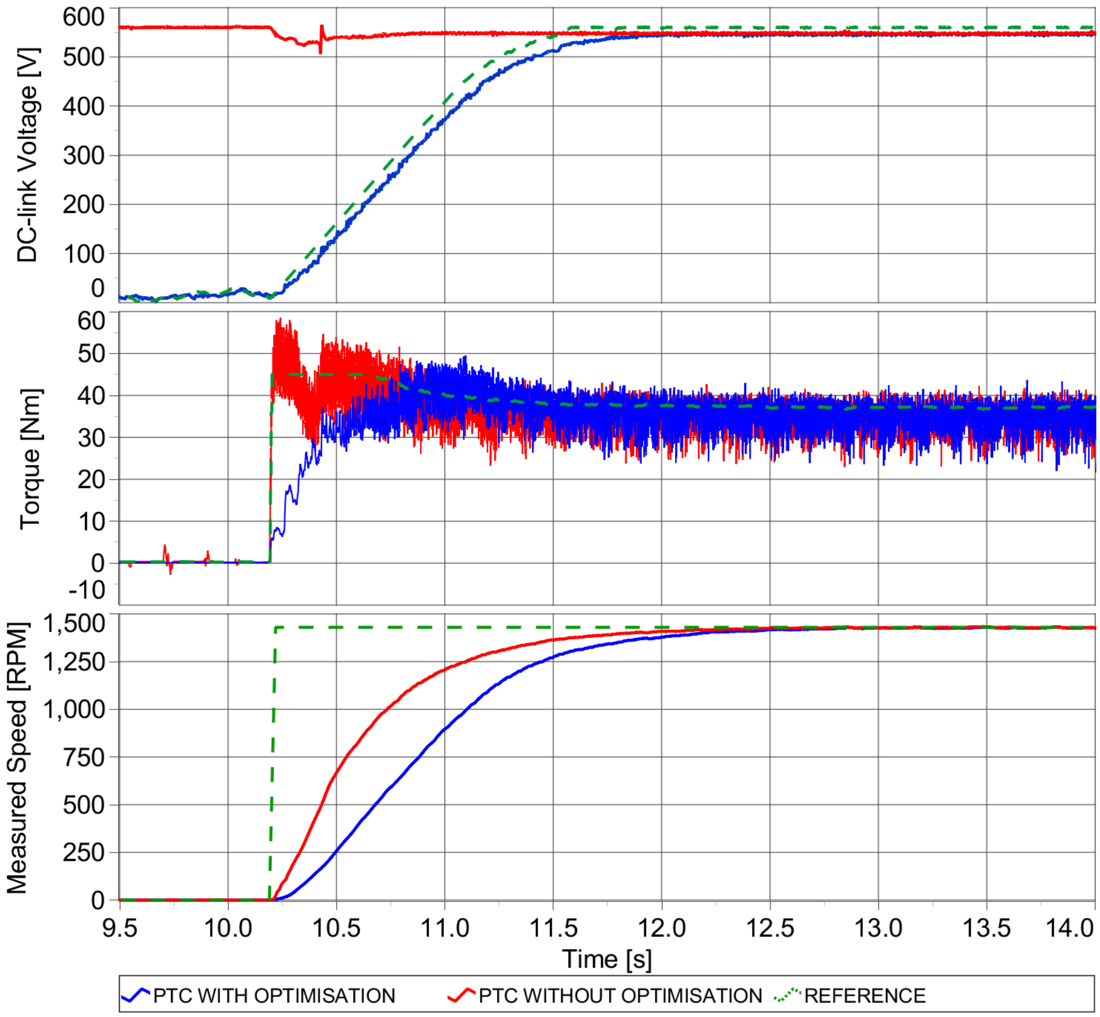

Fig. 76. Voltage optimization during motor start-up from a standstill (speed 0 rpm, no load) to nominal power condition (speed 1430 rpm, load 37 Nm). Published by the author [166].

7.2.5. Optimization in Field-Weakening Region

The ultimate experiment evaluated the performance in the field-weakening region. The motor was rotating with 1600 rpm, which is the speed above the rated value, with the load 15 Nm. Fig. 77 shows the DC-link voltage found by the optimization algorithm for different lowered flux amplitudes (measured from 0.9 to 0.4 Wb). The figure shows that the voltage can also be optimized in the field-weakening area up to some point. Behind this point, the optimized voltage starts to increase. Moreover, behind the point, the phase current amplitude starts to increase significantly.

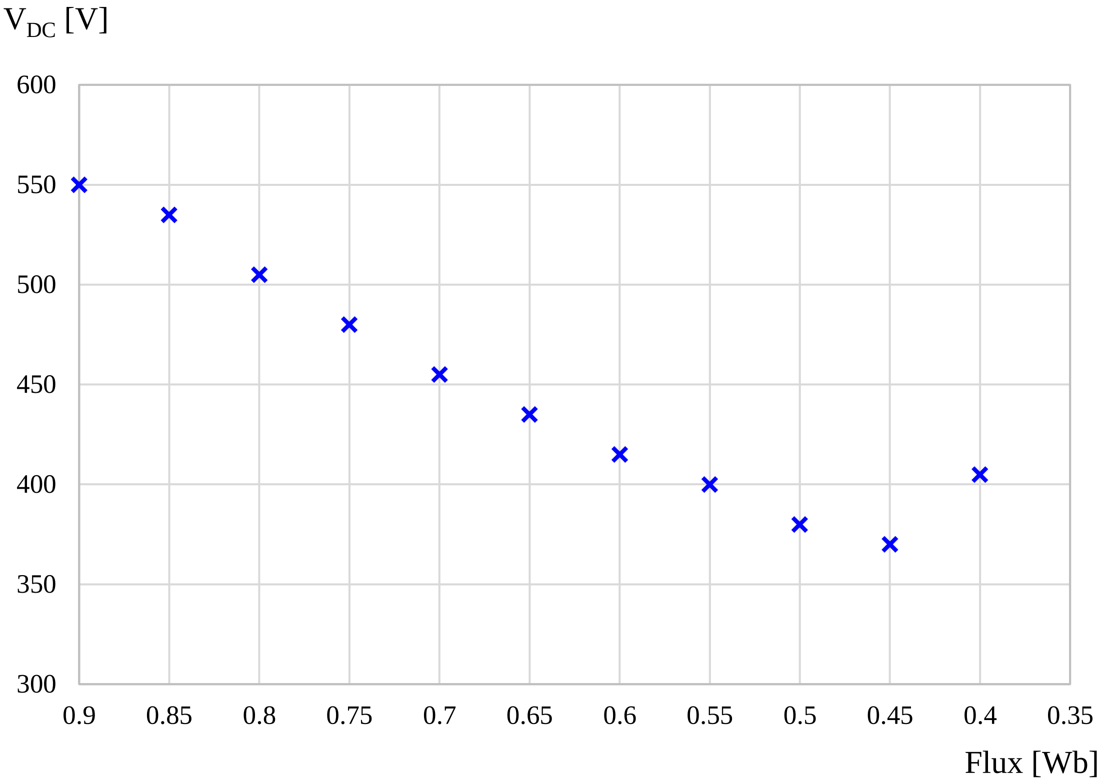

Fig. 77. Resulting DC-link voltage found by the predictive optimization algorithm in the field weakening region; speed 1600 rpm and load 15 Nm. Published by the author [166].

Fig. 78 shows the dependency of the line current THD on the decreasing flux amplitude in the field-weakening region. For the same situation as in Fig. 77 (1600 rpm, 15 Nm), the comparison of the THD between the PTC with (blue points) and without (red points) optimization is presented. The THD is decreasing in both cases; however, in the case of PTC with optimization, the THD is lower, especially with smaller flux amplitude.

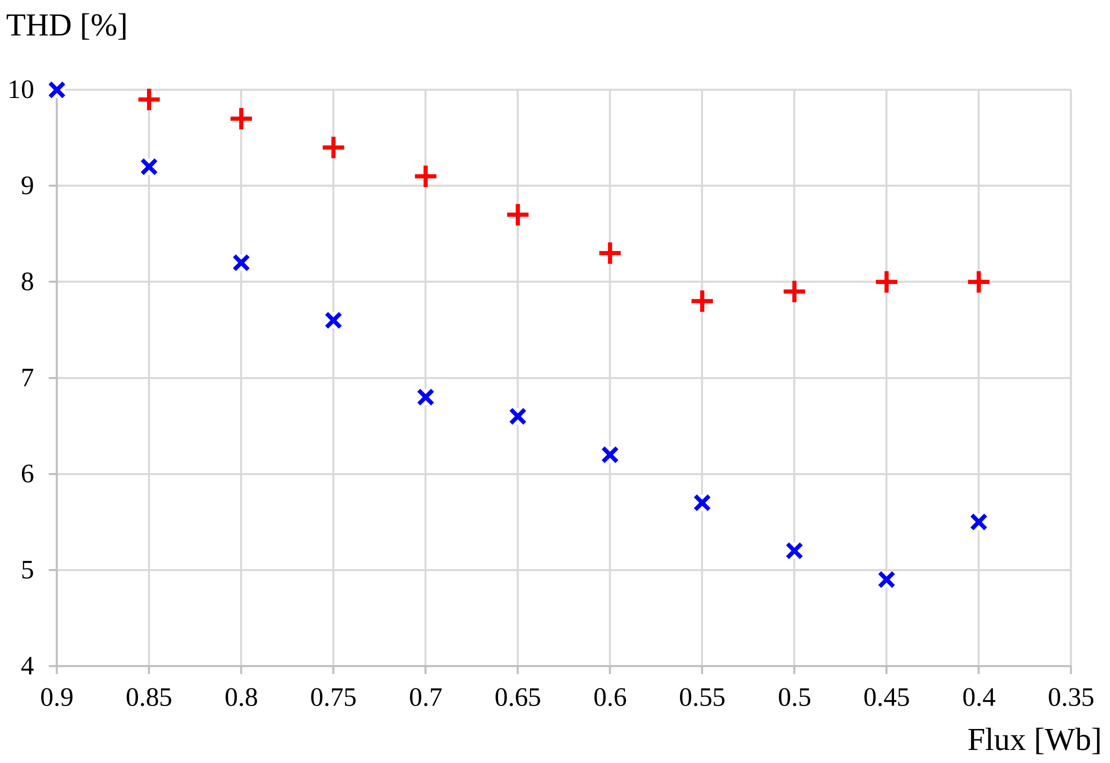

Fig. 78. THD of line current in field weakening region for optimized (blue) and full (red) DC-link voltage; speed 1600 rpm and load 15 Nm. Published by the author [166].

7.3. Experimental Results without the Speed Sensor

Since the operation without the speed sensor is a common requirement in many drive applications and since the sensorless operation is one of the thesis objectives, the proposed PTC with DC-link voltage optimization method was experimentally tested without the speed sensor. For the evaluation of the optimization algorithm performance, the hardware setup remained the same as in operation with the sensor. However, the information from the speed sensor was not used for the control algorithm, but only for the evaluation of the estimated speed accuracy. The speed determination was then done in the controller by the software only.

For the sensorless speed estimation, several methods were developed; rotor flux based MRAS, speed observer, and EKF. Their description has already been introduced in chapter 3. All three algorithms are able to determine the speed with similar errors in steady state. Fig. 79 shows the performance of the three methods, EKF (top part), MRAS (middle part), and speed observer (bottom part).

The practical realization of the MRAS method was published by the author at two conferences [86], [88] and of LO at another conference [101]. The EKF was tested by student Ranjan Tiwari as part of his diploma thesis [167] under the supervision of author of this thesis. For the verification of the DC-link voltage optimization algorithm, the speed observer was selected since its implementation into the tested control method is the simplest. The speed observer is just an extension of the flux observer that is already present in the control algorithm. With this choice, the computational burden of the controller is not significantly increased so the sampling time doesn't have to be increased. The error between the observed and measured speed of the IM is mainly caused by the uncertainty of the IM equivalent scheme parameters or by their change during the motor operation.

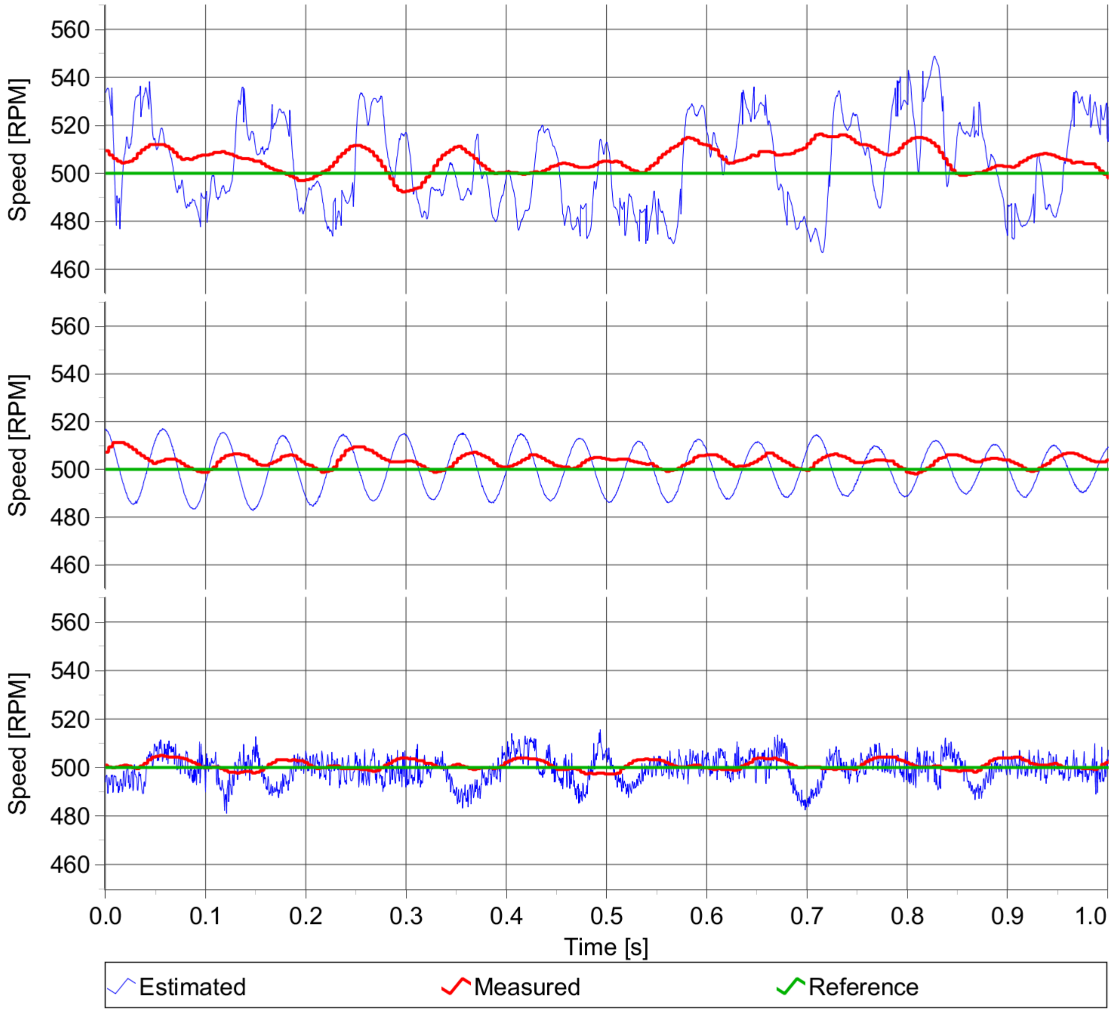

Fig. 79. Sensorless run in steady state without load. From the top: Kalman filter, MRAS, Speed observer.

7.3.1. Optimization Algorithm in Steady State

The experimental results of the DC-link voltage optimization without speed sensor and its comparison with the sensor operation in the steady-state are presented in Fig. 80. The performance without the speed sensor is shown on the right side of the figure. Even though the real and estimated speed in the top part of the figure show small offset, the optimization algorithm works well as shown in the middle part, where the torque ripple decreased and in the bottom part, where the DC-link voltage found the optimum. The left side of the figure shows the comparison with the conventional run with the speed sensor. The algorithm operation without the sensor is verified by the fact that the DC-link voltage optimum is found and that it is maintained at the same level as the run with the speed sensor.

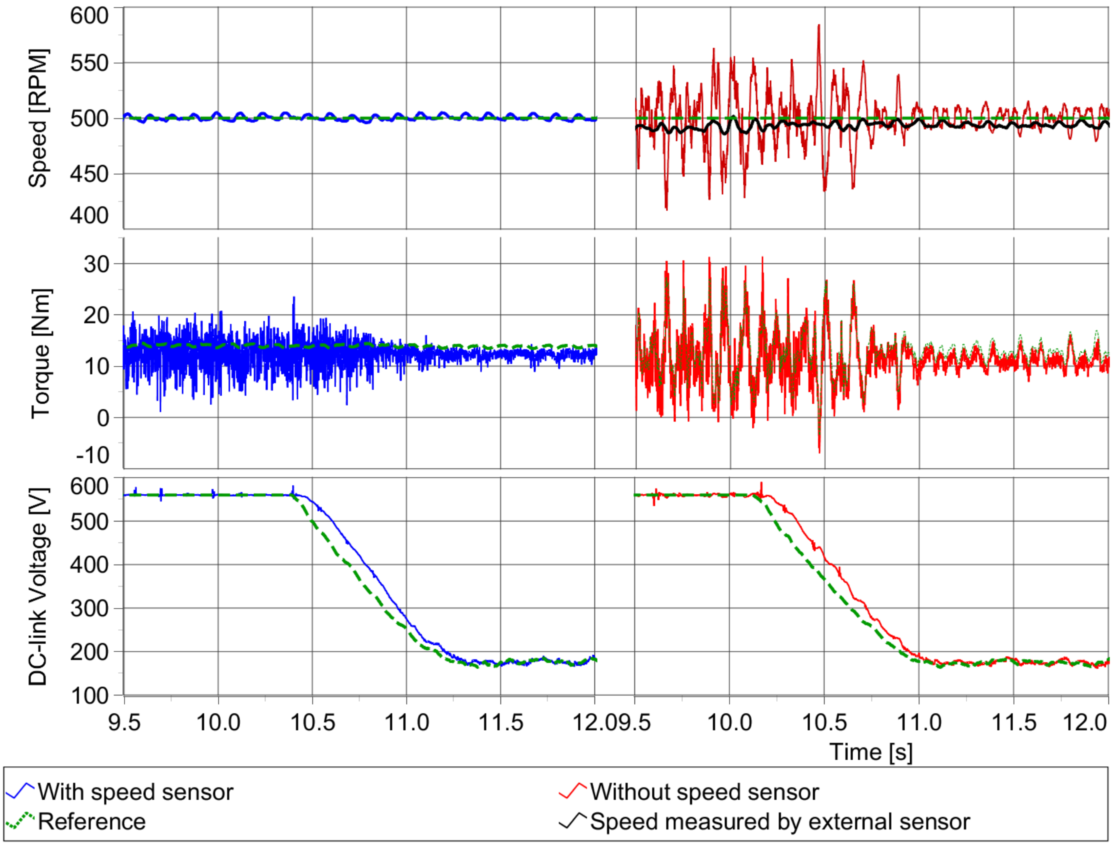

Fig. 80. Comparison between the sensor and sensorless operation during DC-link voltage optimization process in steady state; speed 500 rpm, flux 0.8 Wb, load 10 Nm.

Further steady-state verification without speed sensor is introduced in Fig. 81. The figure presents the trajectory of the stator flux vector tip during one electrical turn. The blue curve represents the operation with full DC-link and the red curve the operation with optimized DC-link voltage. Both of them are based on the operation without the speed sensor. The blue waveform (with the optimization) is smoother and has a smaller deviation from the circle trajectory than the red curve.

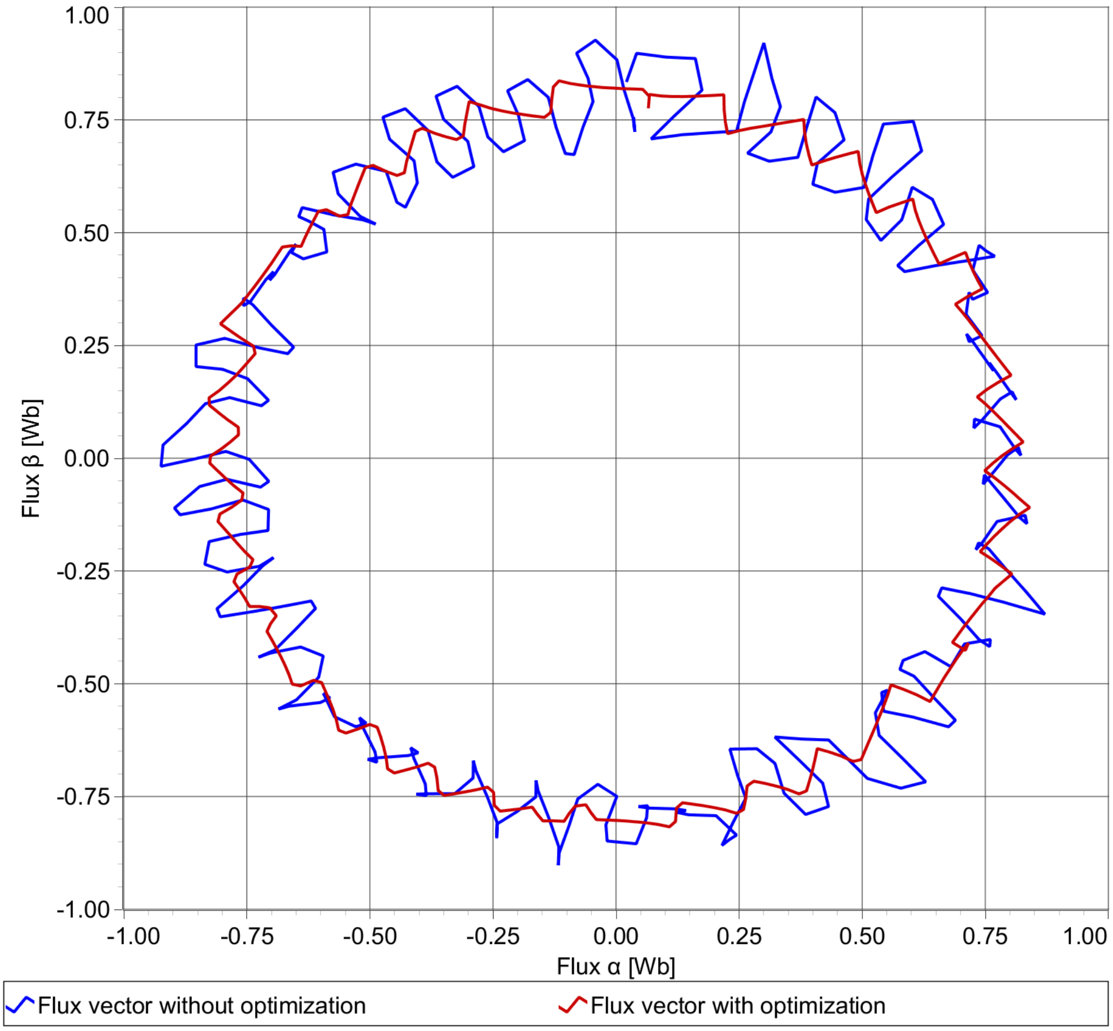

Fig. 81. Comparison between operation with and without DC-link voltage optimization without speed sensor in steady-state; speed 1000 rpm, flux 0.8 Wb, load 0 Nm

7.3.1. Optimization Algorithm in Low-speed Area

One of the problematic areas within the sensorless operation is typically a low-speed area. The performance of the proposed optimization algorithm without the speed sensor in the low-speed area was examined in Fig. 82. In the experiment, the reference speed was slowly changing from 50 to -50 rpm (middle part of the figure). According to the theoretical analysis from previous chapters, the optimized DC-link voltage (top part) should be decreasing with speed. However, in a very low-speed area, this trend is not always maintained, especially within the sensorless operation. However, after the speed was increased again, the optimization operates correctly. The absolute error of the observed speed to the measured speed is presented in the bottom part of the figure.

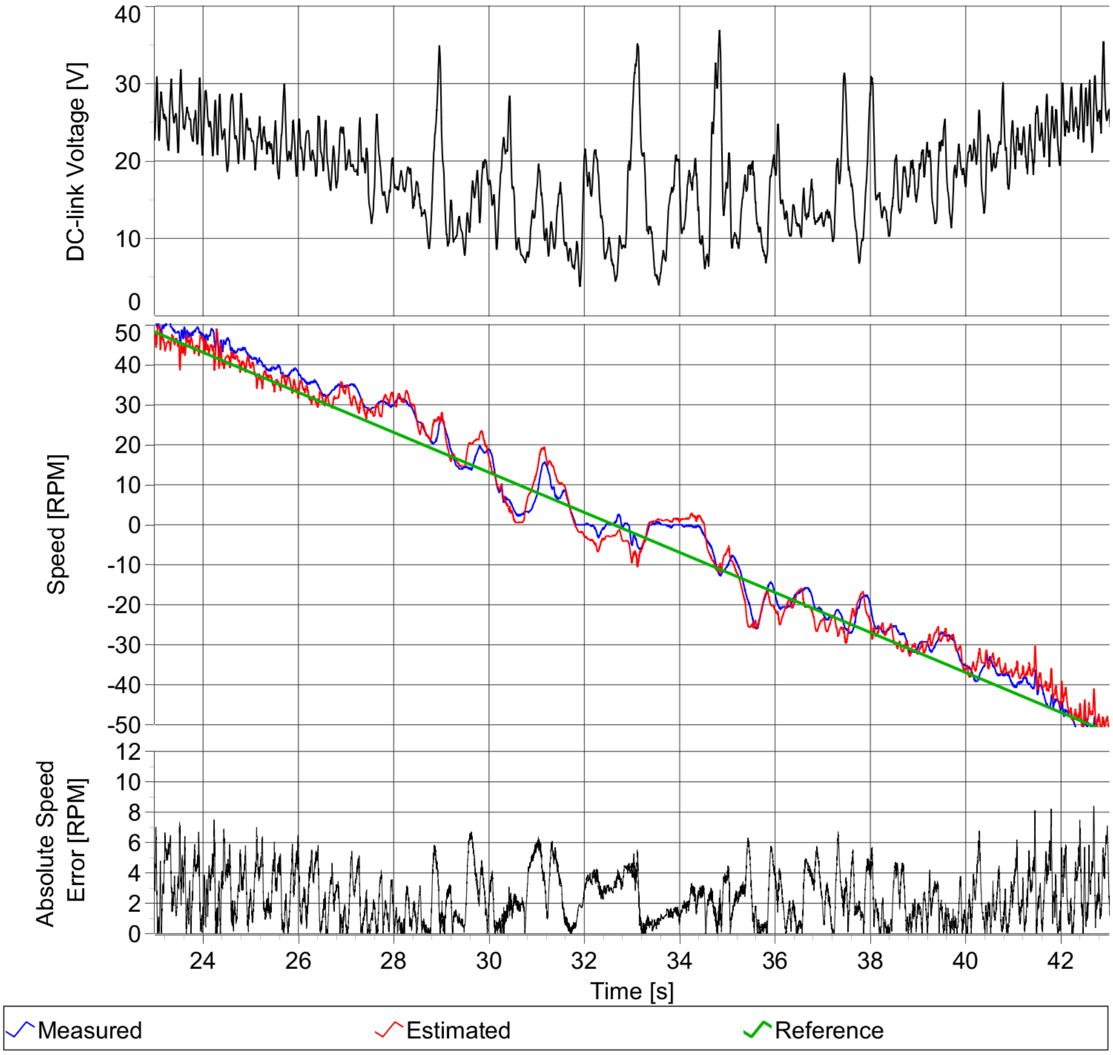

Fig. 82. DC-link voltage optimization without speed sensor in low-speed area; flux 0.8 Wb, load 0 Nm.

7.3.2. Optimization Algorithm in Transients

The performance of the sensorless operation during the motor start-up is presented in Fig. 83. At the beginning, the motor is at a standstill with only a flux excitation of 0.8 Wb. Then, the speed reference suddenly changes from 0 to 500 rpm. No load is connected to the motor during the whole run. On the right side of the figure, the performance of the sensorless operation is depicted, whereas, on the left side, the operation with the speed sensor is shown for the comparison. In both cases, the new steady state is reached quickly with some overshoot in the speed waveforms, which is caused by the tuning of the PI controller.

At the beginning of the transient, the calculated machine's torque does not reach its reference because the DC-link voltage is too low. However, the DC-link voltage rises quickly. Moreover, the DC-link voltage also does not entirely track its reference because, during the transient, the machine work as a generator for a short time, which increases the DC-link voltage. Finally, the new optimized voltage is found, and the steady-state voltage value is the same for both cases.

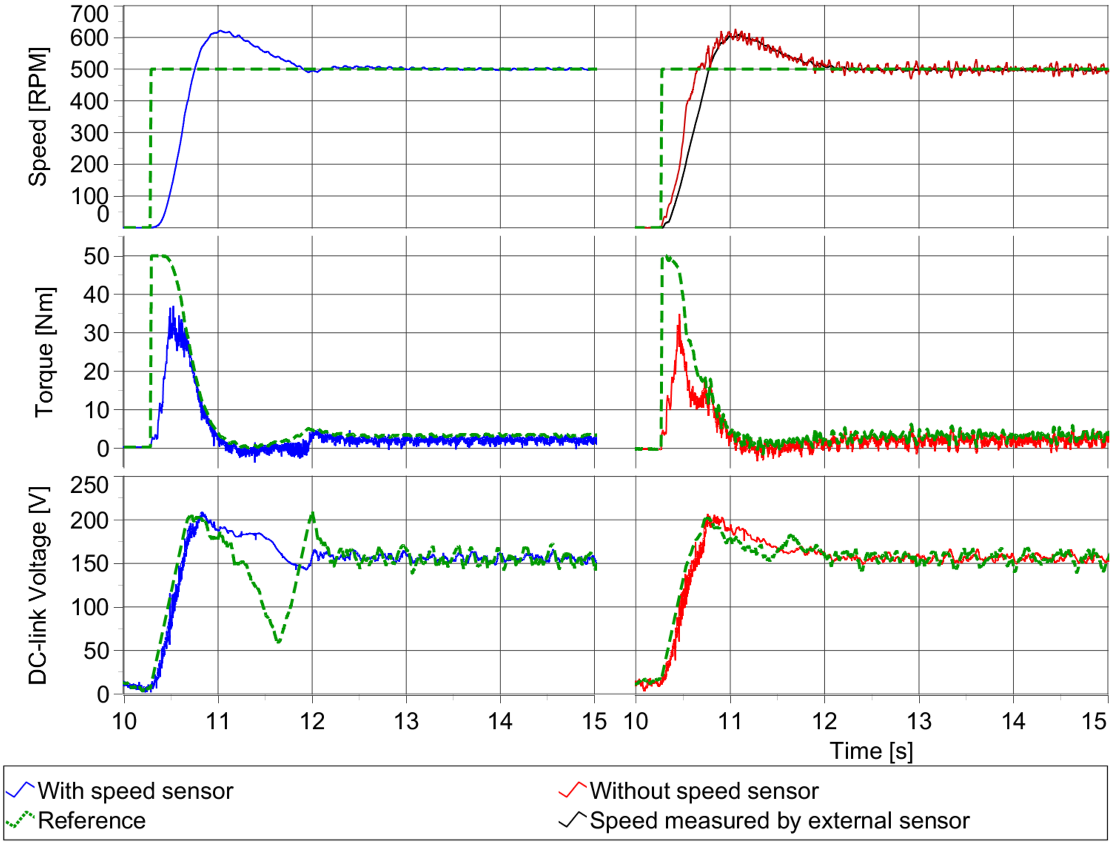

Fig. 83. Comparison between the sensor and sensorless operation during start-up for the case with DC-link voltage optimization; flux 0.8 Wb, no load.

The sensorless operation of the proposed algorithm during transient is further tested in Fig. 84. The left side of the figure shows the operation with full DC-link voltage, and the right side shows the operation with the optimized DC-link. Both of them are running without the speed sensor. The speed was kept at 500 rpm by PI speed controller, and the nominal load 37 Nm was suddenly applied. The transient after the load change is depicted in the figure. At that point, the speed (top curve) drops, but the PI controller brings the speed back to its reference afterward. The optimized DC-link voltage increased (bottom curve) along with the developed torque (middle curve) and found a new optimized value. Also, the torque ripple is lower in the case of the optimized operation, and the estimated speed waveform is smoother.

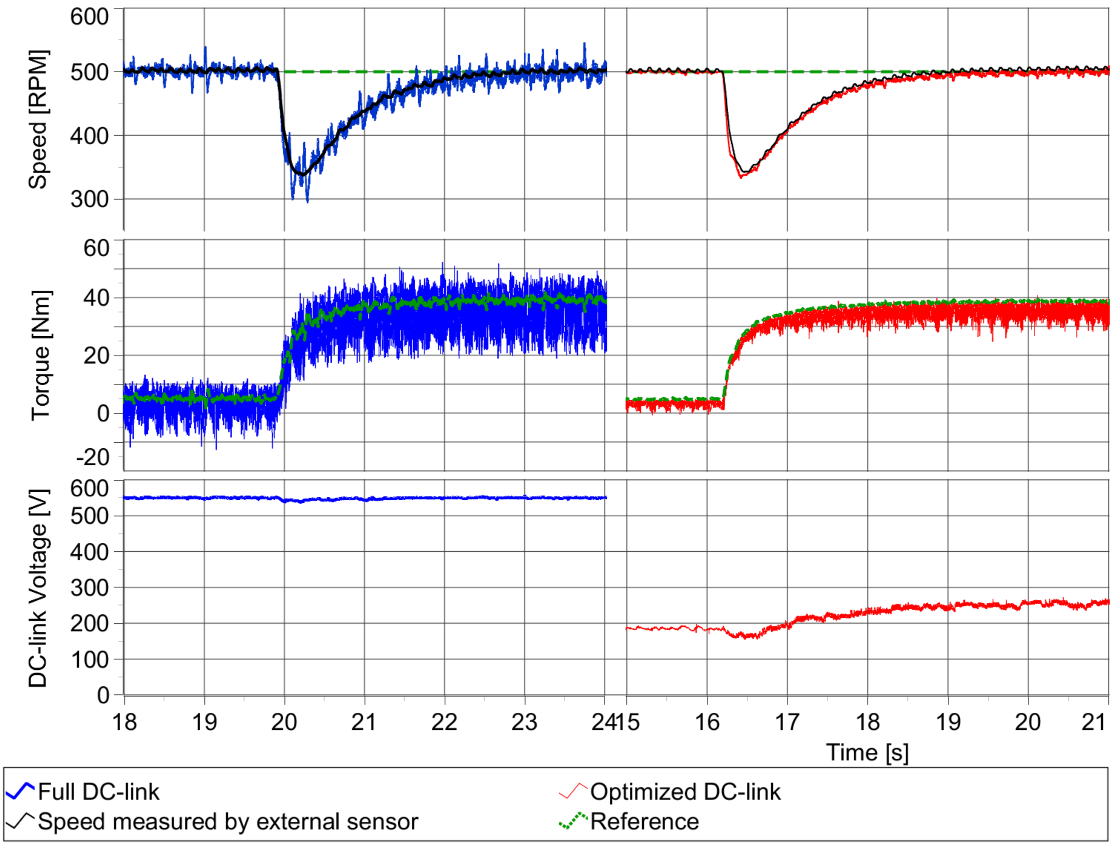

Fig. 84. Comparison between operation with and without DC-link voltage optimization without speed sensor during transients, speed 500 rpm, flux 0.8 Wb.

The DC-link voltage optimization algorithm without a speed sensor at varying load is further examined in Fig. 85. On the right side, the sensorless operation is presented, and on the left side, the comparison with the sensor operation is shown. In the figure, the IM is kept at speed 500 rpm by the PI controller, and no load is connected to the motor. Then, a load of 12 Nm is suddenly connected for a few seconds and disconnected afterward. The speed response is the same in both cases. With added load, it suddenly drops, and with disconnected load, it increases. After the transient, it always returns to its reference. With the load connected, the speed estimation shows a small offset in some operating points. Since the applied load is done by DC motor, the load torque is speed-dependent, and, therefore, the applied load is slightly smaller, and also the optimized DC-link voltage is a little lower. The similar behavior of the curves on the left and right side (sensor and sensorless operation) of the figure verifies the performance of the optimization algorithm in a sensorless operation. However, the performance is better with the speed sensor.

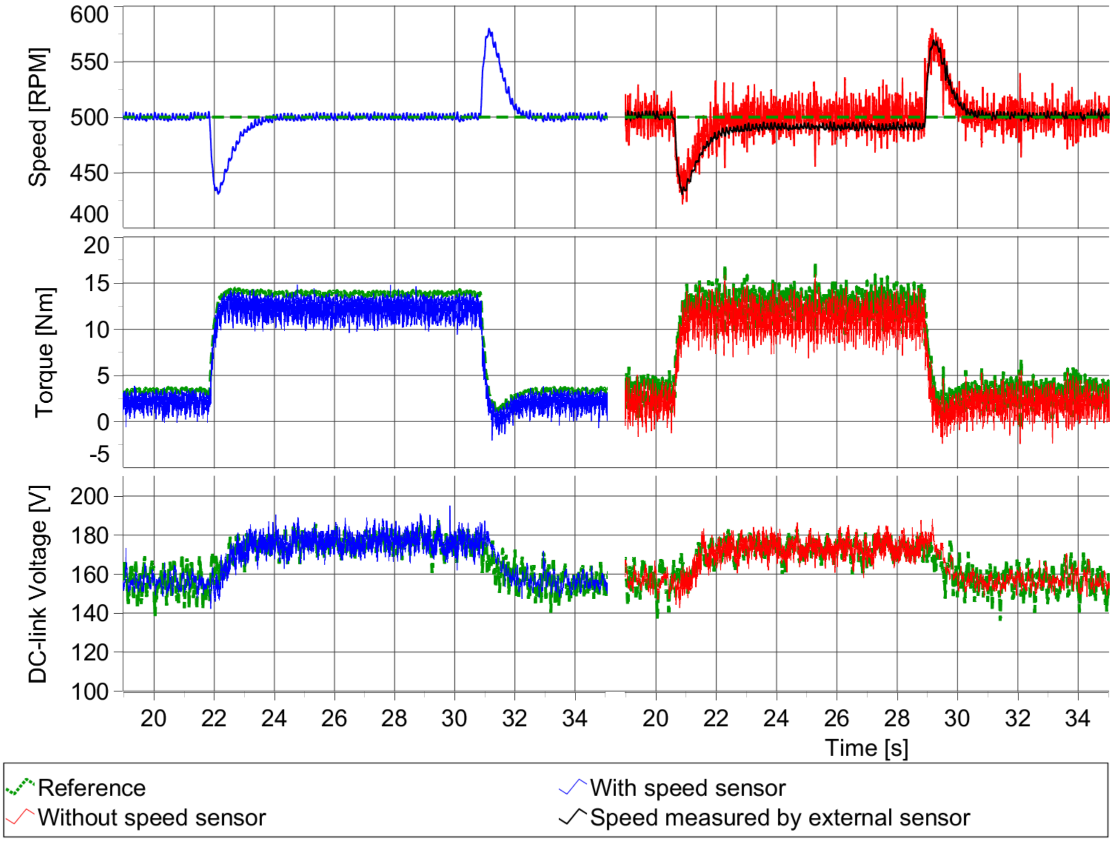

Fig. 85. Comparison between the sensor and sensorless operation with varying load and with DC-link voltage optimization; speed 500 rpm, 0.8 Wb.

7.4. Motor Losses Reduction

In the following section, the DC-link voltage optimization influence on the motor losses is examined. The loss distribution and their calculation are explained, and then the experiment with and without the voltage optimization is presented. The experimental results show the decrease of the losses, mainly the iron losses in the IM magnetic circuit, within the operation with the proposed DC-link voltage optimization algorithm [66].

The losses of the IM are usually divided into five categories. They are the stator winding losses, rotor winding losses, iron losses, mechanical losses, and additional losses [168], [169]. The IEC (International Electrotechnical Commission) standards give the methodology of the loss measurement and calculation. Since not all of the losses are easily measurable, some simplifications were assumed. The experimental validation was performed in a no-load condition so the rotor winding losses are minimized and assumed to be zero. The additional losses couldn't be distinguished from the constant losses so they are calculated together. The segregation of the losses into the categories was done in the following way.

The copper losses P_{Cu}in a three-phase stator winding are calculated as

$$P_{\mathrm{Cu}} = 3R_1 I_1^2, \tag{111}$$

where R_1 is the resistance of the stator winding and I_1 is the RMS value of the stator phase current. The resistance of the stator winding is easily obtained from the standard DC test and is presented in Table 3.

The constant losses can be written as

$$P_{\mathrm{c}} = P_0 - P_{\mathrm{Cu}} = P_{\mathrm{mech}} + P_{\mathrm{Fe}}, \tag{112}$$

where P_0 is the electric input power, P_{mech} are the friction and windage losses, and P_{Fe} are the iron losses.

The mechanical losses are calculated from at least four constant loss points between 30 % and 60 % of the rated motor voltage. Then, a curve against no-load voltage squared is developed and then linearly extrapolated to zero voltage [168], [169]. The mechanical losses are then read from the intersection of the extrapolated curve with the vertical axis. This is graphically depicted for speed 500 rpm in Fig. 86.

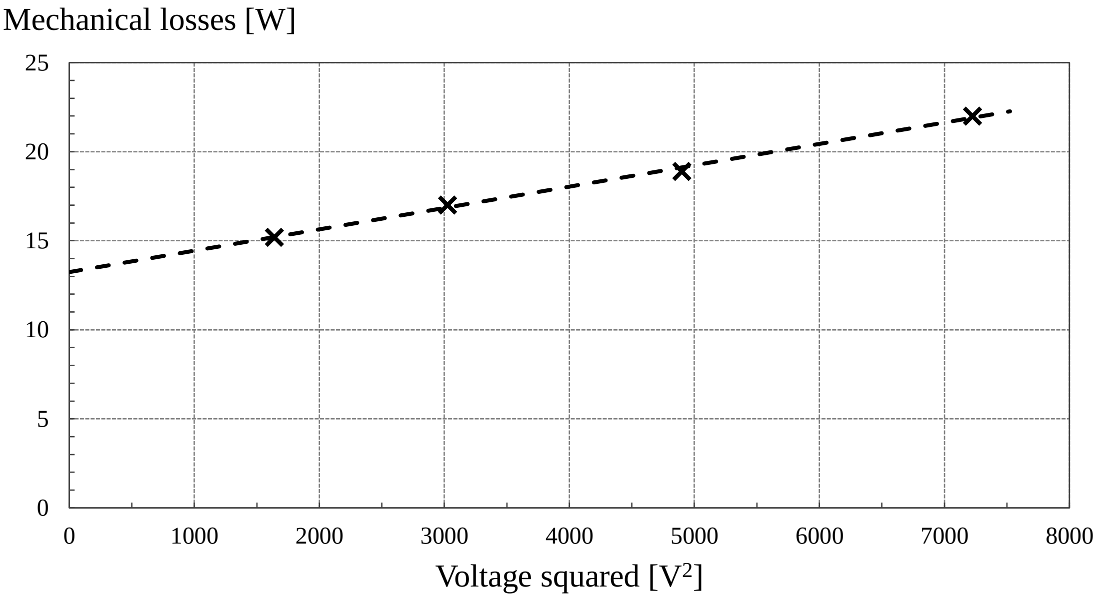

Fig. 86. Dependence of the measured mechanical losses on voltage squared for 500 rpm; crosses: measured data, dashed curve: linear fit.

Since the mechanical losses are speed and temperature-dependent [169], several tests were performed. For this measurement, the IM requires a variable amplitude and frequency harmonic power supply, which was created by the synchronous generator. The proper voltage to frequency ratio was maintained for each operating point. The measured dependence of mechanical losses on the drive speed is shown in Fig. 87.

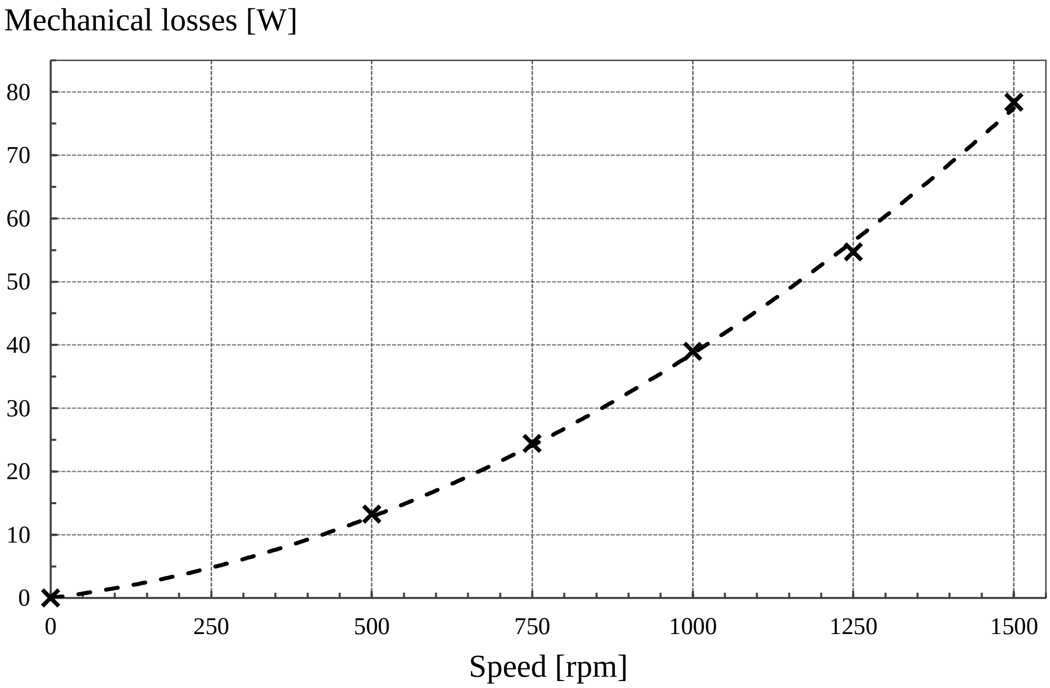

Fig. 87. Dependence of the measured mechanical losses on speed for a motor; crosses: measured data, dashed curve: second-order polynomial fit. Published by the author [66].

Iron losses are calculated from (112) and (111) as

$$P_{\mathrm{Fe}} = P_0 - P_{\mathrm{Cu}} - P_{\mathrm{mech}}. \tag{113}$$

The equation tells that to obtain the iron losses, the input power, stator winding copper losses, and mechanical losses must be determined.

The usage of VSI as the IM power supply introduces additional losses compared to sinusoidal supply [136], [168], [169]. The usage of the inverter increases the THD of the motor supply current and voltage, which directly causes the additional loss increase [170].

Since the IM represent an inductive load, the switching frequency directly influences the waveform of the current. This influence on the IM's iron losses is rather significant for small switching frequency, typically below 5 kHz [171], [172], [173]. Then, the current distortion increases rapidly, which leads to the IM internal flux density distortion [174], [175]. This iron loss increase caused by the non-sinusoidal power supply is mainly the consequence of the increased eddy currents [176] and slightly by the hysteresis loops [174].

For the iron loss analysis measurement, the two different hardware topologies were used. The first was similar to the measurement of the mechanical losses. The motor was connected to the SG, so the IM was supplied by a sinusoidal voltage with adjustable voltage and frequency. The setup is shown in Fig. 88. The electrical power was measured by power analyzer NORMA 4000 placed between the motor terminals and the respective source.

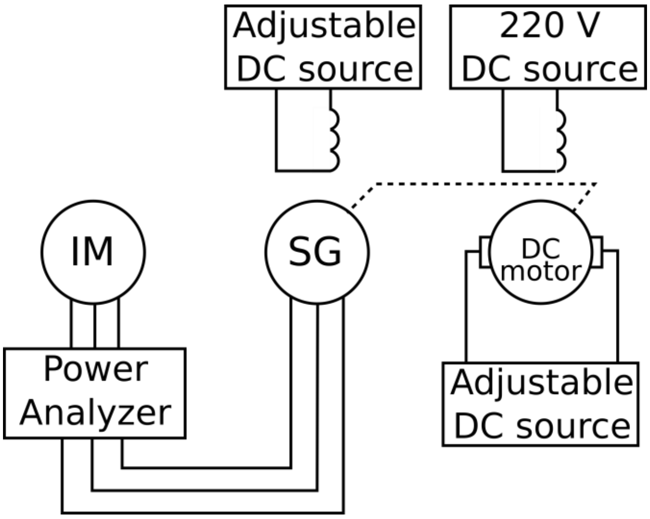

Fig. 88. Block diagram of the synchronous-generator-supplied induction motor. Published by the author [66].

Then, similarly as in the experimental verification of the DC-link voltage optimization, the IM was connected to the inverter and controlled by the PTC algorithm in a speed loop and without a mechanical load. The setup is presented in Fig. 89.

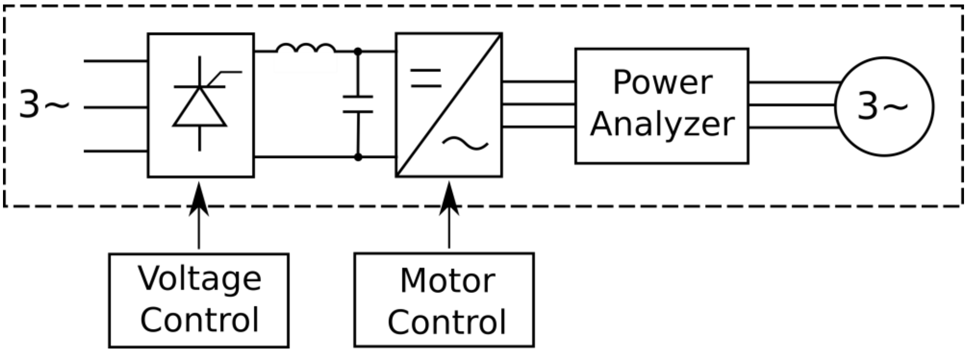

Fig. 89. Block diagram of the inverter-supplied induction motor. Published by the author [66].

In the case of PTC measurement, the reference speed and flux determine the operating point. The DC-link voltage was varied between the full DC-link and optimized DC-link voltage values for each operating point. In every measurement, the input power and the RMS (root mean square) value of the stator current were recorded. The losses were then divided according to the methodology mentioned above. Each operating point is associated with a specific frequency and RMS value of the supplying fundamental voltage wave. This value is then important for the comparison with the harmonic voltage source test.

Within the harmonic voltage source test, the SG (synchronous generator) output electrical frequency was adjusted by the connected DC motor, and the output voltage was adjusted by the field excitation of the SG. The measurement for the same condition as in the case with inverter run was repeated with this harmonic voltage source; the same frequency and the same RMS value of the voltage were set on the IM’s terminals and the input power, and RMS value of the current were recorded. The same methodology to obtain the losses was used.

The experiments were performed for three values of the speed (500, 750, and 1000 rpm). The reference flux in the case of run with the PTC algorithm was 1 Wb in all the cases.

Fig. 90, Fig. 91, and Fig. 92 show the loss distribution in the IM. The losses in the case of the sinusoidal power supply are shown on the left side. The losses measured with the PTC with full DC-link voltage and other voltage levels are shown on the right side. The lowest presented DC-link voltage is close to the voltage that was found by the proposed optimization algorithm. Measurement with lower DC-link voltage is not possible since the voltage is not high enough to counter the back emf. The number located above the columns are the total motor loss within the corresponding voltage supply. The loss distributions in the case of speeds 500, 750, and 1000 rpm are also presented in Table 6, Table 7, and Table 8, respectively.

The figures the table show that iron loss reduction was reached in the case of optimized DC-link voltage. With increasing voltage, the iron losses were increasing. With lowering the speed, the energy savings became more significant. In the speed area below the rated speed, the energy lost in the magnetic circuit was reduced by the DC-link voltage optimization. However, the higher the speed was, the less space remained for the voltage optimization since a higher voltage for back electromotive force compensation was required.

Table 6: Motor losses distribution for the speed 500 rpm

V_{DC} [V]	P_0 [W]	P_{mech} [W]	P_{Cu} [W]	P_{Fe} [W]
Harmonic supply	35.0	13.2	8.9	12.8
210	43.4	13.2	9.3	17.9
300	47.9	13.2	9.6	25.1
400	59.2	13.2	10.0	36.0
500	75.2	13.2	10.9	51.1
570	89.2	13.2	11.4	64.5

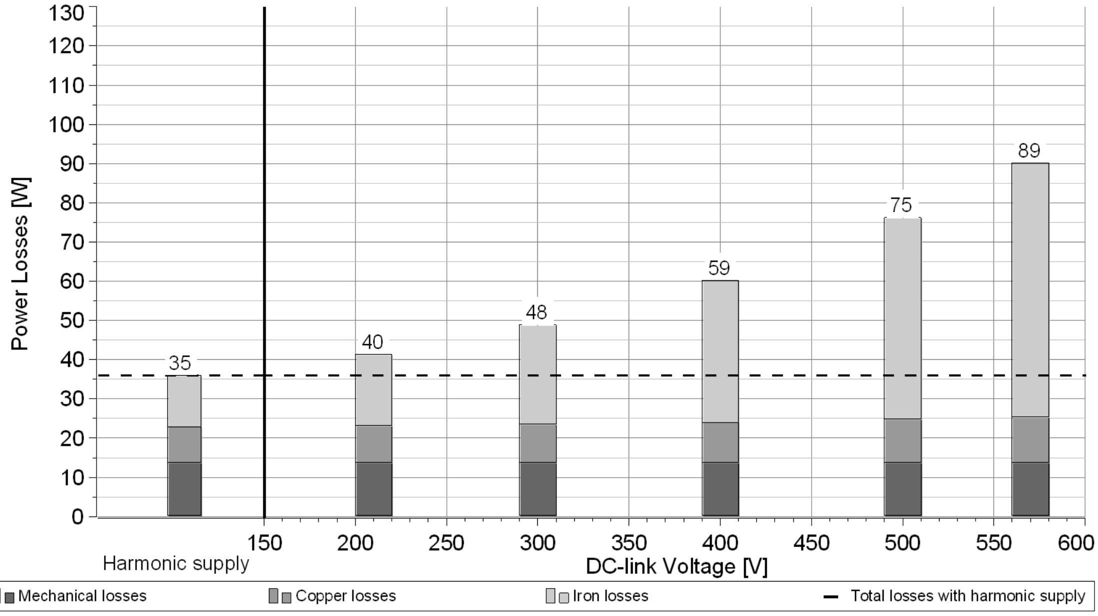

Fig. 90. Motor speed 500 rpm and no-load condition: loss distribution in the case of a sinusoidal supply (left) compared to a loss distribution of the PTC-controlled IM (right) with the reference stator flux 1 Wb and different values of DC-link voltage. Published by the author [66].

Table 7: Motor losses distribution for the speed 750 rpm

V_{DC} [V]	P_0 [W]	P_{mech} [W]	P_{Cu} [W]	P_{Fe} [W]
Harmonic supply	52.0	24.4	8.9	18.7
300	61.4	24.4	9.2	27.8
400	72.1	24.4	9.7	38.0
500	84.3	24.4	10.1	49.8
570	96.2	24.4	10.5	61.3

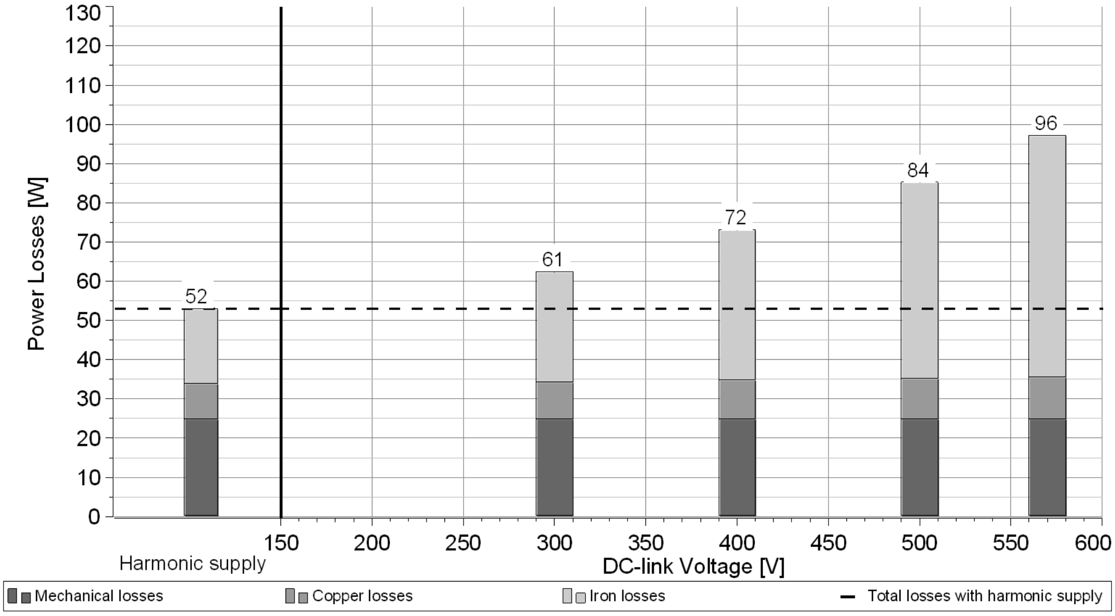

Fig. 91. Motor speed 750 rpm and no-load condition: loss distribution in the case of a sinusoidal supply (left) compared to a loss distribution of the PTC-controlled IM (right) with the reference stator flux 1 Wb and different values of DC-link voltage. Published by the author [66].

Table 8: Motor losses distribution for the speed 1000 rpm

V_{DC} [V]	P_0 [W]	P_{mech} [W]	P_{Cu} [W]	P_{Fe} [W]
Harmonic supply	73.2	38.9	8.5	25.7
400	88.4	38.9	9.2	40.2
500	102.2	38.9	9.7	53.4
570	113.7	38.9	10.3	64.4

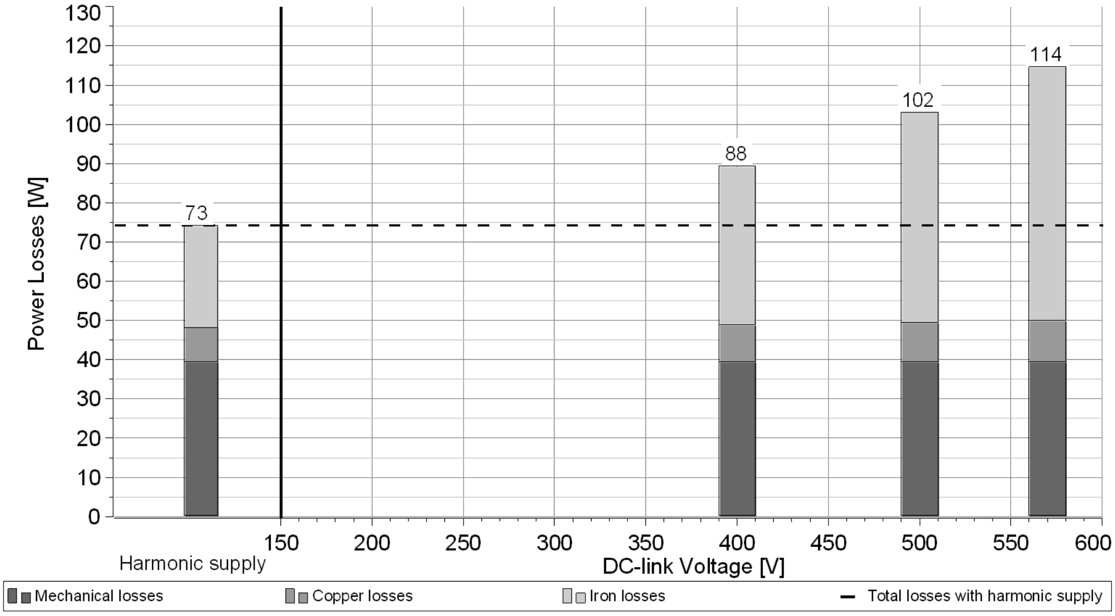

Fig. 92. Motor speed 1000 rpm and no-load condition: loss distribution in the case of a sinusoidal supply (left) compared to a loss distribution of the PTC-controlled IM (right) with the reference stator flux 1 Wb and different values of DC-link voltage. Published by the author [66].

7.5. DC-Link Voltage Optimization Results Summary

The effect of the DC-link voltage change on the ripple in the waveforms of torque and current is examined by simulation in Matlab Simulink environment and by experiment. The results support the analysis from sections 6.2, 6.3 and 6.4, that with the decreasing DC-link voltage level the torque and current waveforms ripple decreases down to a certain point, so-called threshold value. At this point, the DC-link voltage is still high enough to deliver the required power but is not able to maintain the sinusoidal shape of the current. With further DC-link voltage decrease down to so-called critical value, the DC-link voltage is not high enough to deliver the requested power, and the motor speed decreases, and reference torque increases. The simulation and experimental results proved the existence of these values.

Further, the proposed DC-link voltage optimization algorithm was implemented in Matlab Simulink on the mathematical model of the IM drive and on the laboratory drive. The simulation and experimental results proved the benefits of the operation with the optimization in steady-state and showed sufficient performance in multiple different operating points including speed and torque transients, and field-weakening region. Also, the disadvantages of the proposed algorithm, such as worse dynamics in some operating points, were presented. These findings were also published in [166].

The experimental validation of the proposed method was performed on the drive with and without the speed sensor. The sensorless operation was compared with the operation with the speed sensor. The results show that even without the speed sensor when the information about the motor speed is not precise, the DC-link voltage optimization algorithm provides better performance than the run with full DC-link voltage.

The last part of the chapter deals with loss distribution inside the motor and examines the influence of the DC-link voltage optimization on the motor losses. In the experiment, a significant loss decrease was measured within the proposed optimization. The highest energy savings were observed in the iron losses, and some small savings were found in ohmic losses due to the smaller RMS value of stator current. These findings were also published in [66].

8. Conclusions

The disadvantages of many IM drive control methods, including basic predictive torque control method, are high ripple of current and torque waveforms. This property is very undesirable because this, in consequence, contributes to additional electric, magnetic, and mechanic losses in the drive. In the thesis, a novel method of DC-link voltage optimization suppressing the torque and current ripple is developed, integrated into the predictive torque control algorithm, and then verified.

The first chapter mainly discusses the current state of art of induction motor control strategies. It provides an overview of the currently used control methods and main approaches of torque and current ripple reduction. Moreover, the world's top universities and researchers dealing with model predictive control are listed.

The next three chapters deal with the control of the IM drive. The second chapter presents the mathematical model of the IM and the observer used for estimation of the non-measurable quantities. The third chapter deals with different techniques for the determination of the induction motor speed without the use of a speed sensor. It discusses open-loop methods, different types of model reference adaptive systems, observers, and Kalman filters. The fourth chapter shows IM drive control methods. The FOC, the DTC, and the concept of predictive control are described. The classification of the predictive control method used for IM drives control is stated.

The fifth chapter describes the finite set predictive torque control of induction motor drives, which is the most common predictive control method in this area. Then, the common implementation issues, such as current limitation or switching frequency reduction, are addressed. Further, the comparison between PTC and DTC has been performed. Finally, the possibilities of torque and current waveforms ripples are shown.

The sixth chapter presents the influence of the DC-link voltage on the current and torque ripples. It is proved that with decreasing DC-link voltage, the ripples decrease as well. Finally, the novel DC-link voltage optimization for the current and torque ripples decrease is proposed, and the way of its integration into PTC is provided.

The seventh chapter shows the simulation and experimental results. The simulations are carried out in Matlab Simulink environment. The model of the drive is created with the SimScape library and consists of a three-phase power source, SCR, DC-link, IGBT inverter, and the motor itself. The control part, i.e., the flux observer, the PTC, and the voltage optimization, are constructed with standard Simulink library and were fed with a 100 µs clock signal. The experiment is conducted on a 5.5 kW IM drive. A three-phase thyristor bridge topology realizes the active rectifier, but other topologies, such as the PWM rectifier, are also possible. The simulations and experiments are performed in many different operating points, including steady states, transients, low-speed area, and field-weakening region. The experiments are then performed with and also without the speed sensor.

The results confirm the lower torque ripple and lower current THD in the case of PTC with DC-link voltage optimization. The best effect is achieved if the speed and the load, respectively, are lower than their rated values. The lower the speed and torque, the greater the effect. The experiment is also performed without the speed sensor. In this case, the speed is estimated by the speed observer, so the speed information has become less accurate compared to the operation with the sensor. However, the results of the sensorless operation also confirm the same benefits of voltage optimization. Furthermore, the experiment shows a significant decrease in the iron losses and a somewhat smaller decrease of the ohmic losses in the case of the PTC with DC-link voltage optimization.

The two main disadvantages of the PTC with the proposed DC-link voltage optimization have been stated. The first is the longer time constants in the transients when the sudden change of the torque is demanded. However, in many applications, the torque doesn’t change in a step manner, instead some ramp which eliminates the aforementioned problem is used. The second problem might arise from the requirement of the controlled rectifier. However, many industrial and traction drives are already equipped with the controlled rectifier used as a pre-charging circuit, or with the DC-DC converter.

The author considers the most significant contribution of the thesis to be the proposed DC-link voltage optimization integrated into predictive control and its analytical derivation. Compared to the conventional solution with full DC-link voltage, the proposed algorithm lowers the torque ripple, the current THD, and the drive losses. Compared to other algorithms reducing the DC-link voltage, the advantage of the proposed solution lies in the fact that the DC-link voltage value setpoint is a direct consequence of the torque ripple. With other algorithms, the torque ripple decrease is just an indirect consequence of the DC-link voltage reduction. Therefore, it is reasonable to assume that the proposed algorithm finds the solution with a smaller waveform ripple. Moreover, since the proposed algorithm is based on the MPC idea, other aspects or constrains may be easily included by the cost function modification. Another thesis contribution lies within the detailed DTC and PTC comparison, which clearly shows the benefits of the PTC.

8.1. Objective Fulfilment

I consider all objectives defined at the beginning of the thesis to be successfully fulfilled. Specifically, they were fulfilled in the following ways:

1. Sensorless IM drive predictive control method design.

The predictive torque control was selected as the perspective method of the IM drive control. The method was described in chapter 5, where also the main principle is explained, and the base equations are shown. The common implementation issues were discussed in chapter 5.1. This control method was implemented in a simulation environment and experimentally on a real drive. Since the selected method requires the rotational speed knowledge, the overview of sensorless speed determination methods was introduced in chapter 3. The source code is included in Appendix A3. The PTC method was tested and analyzed in chapters 5.2 and 7. This method then served as a base method for the DC-link voltage integration in chapter 6.5.

2. IM drive predictive torque control and direct torque control comparison.

This goal was fulfilled by the theoretical analysis, as well as by simulation and experiment in chapter 5.2. Many papers comparing the two methods were published by many authors; however, they focus mainly on the different behavior of these methods. The analysis performed in the thesis focuses more on the roots of the different behavior of both methods. These methods were tested in simulations and experimentally. The PTC showed better performance concerning the flux amplitude and the torque waveforms ripples. The analysis finds the root of the difference in the switching patterns. In the different set of feasible voltage vectors in each flux sector and in the vector selection principle near the flux sectors boundaries. These findings were also published in the journal Energies [21].

3. Predictive controlled IM drive VSI DC-link voltage optimization.

The influence of the DC-link voltage on the torque and current waveforms ripple was investigated in chapters 6.2 and 6.3, respectively. It was shown that with decreasing voltage, the ripples shrink. Then, in chapter 6.4, the minimal DC-link voltage for the given operating point was analytically derived. Finally, in chapter 6.5, the DC-link voltage optimization algorithm and its integration into the basic PTC were presented. The developed optimization algorithm predicts the ripple for the flux and torque waveforms and adjusts the DC-link voltage accordingly. This optimization method was published in the journal IET Power Electronics [166].

4. Proposed algorithms verification in Matlab Simulink environment.

The model of the drive was created using the SimScape library blocks. It consisted of the three-phase voltage source, the thyristor bridge rectifier, the DC-link with a capacitor and a choke, IGBT inverter, and the induction machine. The control part was created using standard Simulink blocks with a combination of Matlab code. For the IM drive control, the flux observer and PTC, and for the DC-link voltage control, the grid synchronization were realized. The proposed DC-link voltage optimization algorithm was then tested on this simulation setup. The overview of the simulated system is included in Appendix A1, and the code of the important blocks are included in Appendix A3. The verification of the proposed optimization algorithm was performed in multiple operating points, including steady states and transients. The field-weakening region operation is considered too. The simulation results are presented in chapter 7.1. The results confirmed the torque and current ripples decrease within the PTC with voltage optimization run compared to run with full DC-link voltage.

5. Experimental verification of proposed DC-link voltage optimization algorithm on laboratory IM drive system with the speed sensor.

The experimental verification of the predictive torque control with DC-link voltage optimization was done on a drive of 5.5 kW in the department’s laboratory. The drive consisted of the components with the same parameters as were used for the simulations. For the drive control, the dSpace DS1103 platform with 100 μs sampling time was selected. The setup is described in chapter 7.2 and in Appendix A2. The source codes of the important blocks remained the same as in the simulations and are presented in Appendix A3. Multiple experimental runs were performed. The performance in the steady states, in the transients, and in the field-weakening region were performed. The results are presented in chapter 7.2. The results confirmed the torque and current ripples decrease within the PTC with voltage optimization run compared to run with full DC-link voltage.

6. Experimental verification of proposed DC-link voltage optimization algorithm on laboratory IM drive without the speed sensor.

The verification of the proposed DC-link voltage optimization without the speed sensor was done on the same setup as with the sensor. The speed sensor was connected and was used only for estimated speed value verification; it was not used within any part of the control algorithm. To obtain the speed information, the speed observer described in chapter 3.3 and Appendix A3 was utilized. The experiments were performed in the steady states, the transients, the field-weakening region, and in the low-speed area. The results presented in chapter 7.3 show that the proposed optimization method reduces the torque and current ripples even if the estimated speed has certain inaccuracy compared to the real speed of the IM.

7. Reduction of the torque ripple, stator current THD, and drive losses.

With the developed DC-link voltage optimization algorithm, the THD of the current was reduced as well as a ripple in the torque waveform. The mathematical analysis of the influence of the DC-link voltage optimization on the torque and current waveform was performed in chapter 6. The verification is done by simulation and by experiment in chapter 7. The obtained performance improvement was published in the journal IET Power Electronics [166].

The effect of the DC-link voltage optimization on the drive losses was experimentally tested in chapter 7.4. The drive losses were calculated and distributed into three categories; ohmic losses, mechanical losses, and iron losses. The greatest improvement of the proposed strategy was recorded in the iron losses, and some minor improvements were observed in the ohmic losses. The findings were published in the journal Electronics [66].

8.2. Suggestions for Future Work

The proposed DC-link voltage optimization algorithm shows good performance, and I consider it perspective for further study.

Since the PTC doesn’t use a modulator it requires a very small sampling time. The predictive control algorithms generally require high computational power because of complex predictive models and cost function minimization. The potential for future work lies in the sample time reduction, which is possible thanks to the fast development of the microcontrollers.

The thesis showed the energy savings since the motor losses were reduced. However, other losses are influenced by the voltage optimization algorithm as well. Within the proposed algorithm, the rectifier losses may increase (and it depends on the rectifier type), and the inverter losses may decrease. Further research could include the calculation of the losses in the inverter and the rectifier, and try to balance these losses.

The stability of the IM drives predictive control methods are still under research. Only a few predictive control methods have been analyzed from the stability point of view so far. Therefore, future work might include stability analysis of the proposed optimization method.

For the further decrease of the current waveform ripple, the utilization of the proposed DC-link voltage optimization on the PCC might be useful since, within the PCC, the current is directly controlled.

Most of the control methods rely to some extent on the IM equivalent circuit. This circuit contains parameters that are known with some accuracy, not precisely. The last suggestion for future works is the analysis of the method robustness to the parameter mismatch.

References

[1] S. Vazquez, J. Rodriguez, M. Rivera, L. G. Franquelo and M. Norambuena, "Model Predictive Control for Power Converters and Drives: Advances and Trends," in *IEEE Transactions on Industrial Electronics*, vol. 64, no. 2, pp. 935-947, Feb. 2017.

[2] D. E. Quevedo, R. P. Aguilera, M. A. Perez, P. Cortes and R. Lizana, "Model Predictive Control of an AFE Rectifier With Dynamic References," in *IEEE Transactions on Power Electronics*, vol. 27, no. 7, pp. 3128-3136, July 2012.

[3] P. Cortes, G. Ortiz, J. I. Yuz, J. Rodriguez, S. Vazquez and L. G. Franquelo, "Model Predictive Control of an Inverter With Output LC Filter for UPS Applications," in *IEEE Transactions on Industrial Electronics*, vol. 56, no. 6, pp. 1875-1883, June 2009.

[4] J. Moon, J. Gwon, J. Park, D. Kang and J. Kim, "Model Predictive Control With a Reduced Number of Considered States in a Modular Multilevel Converter for HVDC System," in *IEEE Transactions on Power Delivery*, vol. 30, no. 2, pp. 608-617, April 2015.

[5] N. H. Viet, V. Minh Hung and N. PARASCHIV, "FS-PTC with Switching Table for Matrix Converter in Induction Motors Drive System," *2019 International Symposium on Electrical and Electronics Engineering (ISEE)*, Ho Chi Minh, Vietnam, 2019, pp. 298-303.

[6] C. D. Townsend, T. J. Summers, J. Vodden, A. J. Watson, R. E. Betz and J. C. Clare, "Optimization of Switching Losses and Capacitor Voltage Ripple Using Model Predictive Control of a Cascaded H-Bridge Multilevel StatCom," in *IEEE Transactions on Power Electronics*, vol. 28, no. 7, pp. 3077-3087, July 2013.

[7] M. Mosa, R. S. Balog and H. Abu-Rub, "High-Performance Predictive Control of Quasi-Impedance Source Inverter," in *IEEE Transactions on Power Electronics*, vol. 32, no. 4, pp. 3251-3262, April 2017.

[8] D. Casadei, F. Profumo, G. Serra and A. Tani, "FOC and DTC: two viable schemes for induction motors torque control," in *IEEE Transactions on Power Electronics*, vol. 17, no. 5, pp. 779-787, Sept. 2002.

[9] F. Blaschke, "The principle of field orientation as applied to the new TRANSVECTOR closed loop control system for rotating field machines, " in *Siemens Rev. 39*, pp. 217–220, 1972.

[10] I. Takahashi and T. Noguchi, "A New Quick-Response and High-Efficiency Control Strategy of an Induction Motor," in *IEEE Transactions on Industry Applications*, vol. IA-22, no. 5, pp. 820-827, Sept. 1986.

[11] M. Depenbrock, "Direct self-control (DSC) of inverter-fed induction machine," in *IEEE Transactions on Power Electronics*, vol. 3, no. 4, pp. 420-429, Oct. 1988.

[12] S. J. Qin and T. A. Badgwell, "A survey of industrial model predictive control technology, " in *Control Engineering Practice*, vol. 11, pp. 733–764, Jul. 2003.

[13] J. Rodriguez et al., "State of the Art of Finite Control Set Model Predictive Control in Power Electronics," in *IEEE Transactions on Industrial Informatics*, vol. 9, no. 2, pp. 1003-1016, May 2013.

[14] J. Holtz and S. Stadtfeld, "A Predictive Controller for the Stator Current Vector of AC-Machines fed from a Switched Voltage Source", *1983 International Power Electronics Conference IPEC*, vol. 2, pp. 1665–1675, Tokio, 1983.

[15] P. Mutschler, "Verfahren zur direkten Regelung der Geschwindigkeit eines elektrischen Antriebs (Principle for Direct Control of the Speed of an Electric Drive) ", *German Patent DE 196 35 981 C 2*, 1998.

[16] D. F. Schroder and R. Kennel, "Model-Control PROMC---A New Control Strategy with Microcomputer for Drive Applications," in *IEEE Transactions on Industry Applications*, vol. IA-21, no. 5, pp. 1162-1167, Sept. 1985.

[17] F. Wang, X. Mei, J. Rodriguez and R. Kennel, "Model predictive control for electrical drive systems-an overview," in *CES Transactions on Electrical Machines and Systems*, vol. 1, no. 3, pp. 219-230, September 2017.

[18] S. Vazquez et al., "Model Predictive Control: A Review of Its Applications in Power Electronics," in *IEEE Industrial Electronics Magazine*, vol. 8, no. 1, pp. 16-31, March 2014.

[19] J. Rodriguez and P. Cortes, "Predictive Control of Power Converters and Electrical Drives", *Wiley-IEEE Press*, Hoboken, NJ, USA, 2012, 246p.

[20] K. Wróbel, P. Serkies and K. Szabat, "Continuous and Finite Set Model Predictive Control of Induction Motor Drive," *IECON 2019 - 45th Annual Conference of the IEEE Industrial Electronics Society*, Lisbon, Portugal, 2019, pp. 963-968.

[21] P. Karlovsky and J. Lettl, "Induction Motor Drive Direct Torque Control and Predictive Torque Control Comparison Based on Switching Pattern Analysis", in *Energies*, vol. 11, no. 7, 1793, 2018.

[22] X. Yang, G. Liu, L. V. Dai and L.C. Quyen, "A novel model predictive direct control for induction motor drives," in *IEEJ Transactions on Electrical and Electronic Engineering*, vol. 14, no. 11, 2019.

[23] J. C. R. Martinez, R. M. Kennel and T. Geyer, "Model predictive direct current control," *2010 IEEE International Conference on Industrial Technology*, Vina del Mar, 2010, pp. 1808-1813,

[24] J. Wang and F. Wang, "Robust sensorless FCS-PCC control for inverter-based induction machine systems with high-order disturbance compensation, " in *Journal of Power Electronics*, 2020.

[25] F. Wang, Z. Zhang, X. Mei, J. Rodriguez and R. Kennel, "Advanced Control Strategies of Induction Machine: Field Oriented Control, Direct Torque Control and Model Predictive Control", in *Energies*, vol. 11, no. 1, 120, 2018.

[26] F. Wang, S. Li, X. Mei, W. Xie, J. Rodríguez and R. M. Kennel, "Model-Based Predictive Direct Control Strategies for Electrical Drives: An Experimental Evaluation of PTC and PCC Methods," in *IEEE Transactions on Industrial Informatics*, vol. 11, no. 3, pp. 671-681, June 2015.

[27] K. Wróbel, P. Serkies, K. Szabat, "Model Predictive Base Direct Speed Control of Induction Motor Drive—Continuous and Finite Set Approaches," in *Energies*, vol. 13, no. 5, 1193, 2020.

[28] P. Karlovský and J. Lettl, "Influence of switching frequency on torque ripples in model predictive control of induction motor drive," *2017 9th International Conference on Electronics, Computers and Artificial Intelligence (ECAI)*, Targoviste, 2017, pp. 1-4.

[29] M. Siami, D. A. Khaburi and J. Rodríguez, "Torque Ripple Reduction of Predictive Torque Control for PMSM Drives With Parameter Mismatch," in *IEEE Transactions on Power Electronics*, vol. 32, no. 9, pp. 7160-7168, Sept. 2017.

[30] P. Cortes, J. Rodriguez, D. E. Quevedo and C. Silva, "Predictive Current Control Strategy With Imposed Load Current Spectrum," in *IEEE Transactions on Power Electronics*, vol. 23, no. 2, pp. 612-618, March 2008.

[31] M. Kroneisl, V. Šmídl, Z. Peroutka and M. Janda, "Predictive Control of IM Drive Acoustic Noise," in *IEEE Transactions on Industrial Electronics*, vol. 67, no. 7, pp. 5666-5676, July 2020.

[32] M. Mamdouh, M. Abido and Z. Hamouz, "Weighting Factor Selection Techniques for Predictive Torque Control of Induction Motor Drives: A Comparison Study," in *Arabian Journal for Science and Engineering*. vol. 43. pp. 433-445, 2018.

[33] A. Bhowate, M. Aware and S. Sharma, "Synthetic Voltage Vector Selection Criteria in Predictive Torque Control for Performance Improvement of Three Phase Induction Motor Drive," *2019 10th International Conference on Power Electronics and ECCE Asia (ICPE 2019 - ECCE Asia)*, Busan, Korea (South), 2019, pp. 1263-1267.

[34] Y. Cho, W. J. Choi and K. Lee, "Model predictive control using a three-level inverter for induction motors with torque ripple reduction," *2014 IEEE International Conference on Industrial Technology (ICIT)*, Busan, 2014, pp. 187-192.

[35] S. R. Karpe, S. A. Deokar and A. M. Dixit, "Switching losses minimization and performance improvement of PCC and PTC methods of model predictive direct torque control drives with 15-level inverter," in *Journal of Electrical Systems and Information Technology*, vol. 5 no. 3, pp.759-776, 2018.

[36] T. Geyer and D. E. Quevedo, "Performance of Multistep Finite Control Set Model Predictive Control for Power Electronics," in *IEEE Transactions on Power Electronics*, vol. 30, no. 3, pp. 1633-1644, March 2015.

[37] S. A. Davari, D. A. Khaburi and R. Kennel, "Using a weighting factor table for FCS-MPC of induction motors with extended prediction horizon," *IECON 2012 - 38th Annual Conference on IEEE Industrial Electronics Society*, Montreal, QC, 2012, pp. 2086-2091.

[38] P. Karamanakos and T. Geyer, "Guidelines for the Design of Finite Control Set Model Predictive Controllers," in *IEEE Transactions on Power Electronics*, vol. 35, no. 7, pp. 7434-7450, July 2020.

[39] Y. Cho, Y. Bak and K. Lee, "Torque-Ripple Reduction and Fast Torque Response Strategy for Predictive Torque Control of Induction Motors," in *IEEE Transactions on Power Electronics*, vol. 33, no. 3, pp. 2458-2470, March 2018.

[40] Y. Zhang and H. Yang, "Model Predictive Torque Control of Induction Motor Drives With Optimal Duty Cycle Control," in *IEEE Transactions on Power Electronics*, vol. 29, no. 12, pp. 6593-6603, Dec. 2014.

[41] A. A. Ahmed, B. K. Koh, H. S. Park, K. Lee and Y. I. Lee, "Finite-Control Set Model Predictive Control Method for Torque Control of Induction Motors Using a State Tracking Cost Index," in *IEEE Transactions on Industrial Electronics*, vol. 64, no. 3, pp. 1916-1928, March 2017.

[42] F. Wang, Z. Chen, P. Stolze, J. Stumper, J. Rodríguez and R. Kennel, "Encoderless Finite-State Predictive Torque Control for Induction Machine With a Compensated MRAS," in *IEEE Transactions on Industrial Informatics*, vol. 10, no. 2, pp. 1097-1106, May 2014.

[43] F. Wang et al., "An Encoderless Predictive Torque Control for an Induction Machine With a Revised Prediction Model and EFOSMO," in *IEEE Transactions on Industrial Electronics*, vol. 61, no. 12, pp. 6635-6644, Dec. 2014.

[44] M. A. Mossa and S. Bolognani, "Effective model predictive current control for a sensorless IM drive," *2017 IEEE International Symposium on Sensorless Control for Electrical Drives (SLED)*, Catania, 2017, pp. 37-42.

[45] F. Wang et al., "Finite Control Set Model Predictive Torque Control of Induction Machine With a Robust Adaptive Observer," in *IEEE Transactions on Industrial Electronics*, vol. 64, no. 4, pp. 2631-2641, April 2017.

[46] S. A. Davari, D. A. Khaburi, F. Wang and R. M. Kennel, "Using Full Order and Reduced Order Observers for Robust Sensorless Predictive Torque Control of Induction Motors," in *IEEE Transactions on Power Electronics*, vol. 27, no. 7, pp. 3424-3433, July 2012.

[47] J. Li, L. Zhang, Y. Niu and H. Ren, "Model predictive control for extended Kalman filter based speed sensorless induction motor drives," *2016 IEEE Applied Power Electronics Conference and Exposition (APEC)*, Long Beach, CA, 2016, pp. 2770-2775.

[48] Y. B. Zbede, S. M. Gadoue and D. J. Atkinson, "Model Predictive MRAS Estimator for Sensorless Induction Motor Drives", *IEEE Transactions on Industrial Electronics*, vol. 63, no. 6, pp. 3511-3521, June 2016.

[49] F. Wang, Z. Zhang, J. Wang and J. Rodríguez, "Sensorless model-based PCC for induction machine", *IET Electric Power Applications*, vol. 11, no. 5, pp. 885-892, 2017.

[50] P. Karamanakos, T. Geyer, and R. P. Aguilera, “Computationally efficient long-horizon direct model predictive control for transient operation,” *2017 IEEE Energy Conversion Congress and Exposition (ECCE)*, Cincinnati, OH, USA, Oct. 2017, pp. 4642–4649.

[51] P. Karamanakos, T. Geyer, and R. P. Aguilera, “Long-horizon direct model predictive control: Modified sphere decoding for transient operation,” in *IEEE Transactions on Industry Applications*, vol. 54, no. 6, pp. 6060–6070, Nov 2018.

[52] P. Karamanakos, P. Stolze, R. M. Kennel, S. Manias and H. du Toit Mouton, "Variable Switching Point Predictive Torque Control of Induction Machines," in *IEEE Journal of Emerging and Selected Topics in Power Electronics*, vol. 2, no. 2, pp. 285-295, June 2014.

[53] P. Cortes, M. P. Kazmierkowski, R. M. Kennel, D. E. Quevedo and J. Rodriguez, "Predictive Control in Power Electronics and Drives," in *IEEE Transactions on Industrial Electronics*, vol. 55, no. 12, pp. 4312-4324, Dec. 2008.

[54] ECPE website, available 18.7.2020, https://www.ecpe.org/

[55] IEEE International Symposium on Predictive Control of Electrical Drives and Power Electronics (PRECEDE), available 18.7.2020, https://ieeexplore.ieee.org/xpl/conhome/1800554/all-proceedings

[56] IEEE 10th International Symposium on Sensorless Control for Electrical Drives (SLED), available 18.7.2020, https://ieeexplore.ieee.org/xpl/conhome/1800104/all-proceedings

[57] ABB website, available 18.7.2020, https://global.abb/

[58] T. Geyer, G. Papafotiou and M. Morari, "Model Predictive Direct Torque Control—Part I: Concept, Algorithm, and Analysis," in *IEEE Transactions on Industrial Electronics*, vol. 56, no. 6, pp. 1894-1905, June 2009.

[59] ABB website, available 12.7.2020, https://new.abb.com/drives/media/abbs-model-predictive-torque-control-mptc-protects-against-gas-supply-interruptions

[60] Š. Janouš, J. Talla, Z. Peroutka and V. Šmídl, "Predictive Control of Parallel Induction Motors Fed by Single Inverter with Common Current Sensors," *IECON 2018 - 44th Annual Conference of the IEEE Industrial Electronics Society*, Washington, DC, 2018.

[61] V. Šmídl, V. Mácha, Š. Janouš and Z. Peroutka, "Analysis of cost functions and setpoints for predictive speed control of PMSM drives," *2016 18th European Conference on Power Electronics and Applications (EPE'16 ECCE Europe)*, Karlsruhe, 2016, pp. 1-8.

[62] P. Vaclavek and P. Blaha, "PMSM model discretization for Model Predictive Control algorithms," *Proceedings of the 2013 IEEE/SICE International Symposium on System Integration*, Kobe, 2013, pp. 13-18.

[63] C. S. T. Dong, C. D. Tran, S. D. Ho, P. Brandstetter and M. Kuchar, "Robust sliding mode observer application in vector control of induction motor," *2018 ELEKTRO*, Mikulov, 2018, pp. 1-5.

[64] V. Valouch and P. Simek, "Comparison of Predictive Direct Power Control Methods for Grid-Connected Converter in B4 Configuration," *2019 International Conference on Electrical Drives & Power Electronics (EDPE)*, The High Tatras, Slovakia, 2019, pp. 87-92.

[65] M. Novak and Z. Novak, "Stability issues of high-speed PMSM feedback control systems," *2013 15th European Conference on Power Electronics and Applications (EPE)*, Lille, 2013, pp. 1-9.

[66] P. Karlovsky, O. Lipcak and J. Bauer, "Iron Loss Minimization Strategy for Predictive Torque Control of Induction Motor, " in *Electronics*, vol. 9, no 4, 566, 2020.

[67] J. Lettl, S. Fligl, J. Bauer and M. Vlcek, "*Comparison of Gamma and T Models for Convector Controlled Induction Machine Drives*", *Proceedings of PIERS 2012*, Cambridge, Electromagnetics Academy, 2012. pp. 925-928.

[68] B. K. Bose, "Power electronics and motor drives: advances and trends" *Elsevier*, 2010, 936 p.

[69] D. Luenberger, "An Introduction to Observers," in *IEEE Transactions on Automatic Control*, Vol. AC-16, No. 6, December 1971.

[70] H. Kubota, K. Matsuse, and T. Nakano, "DSP-Based Speed Adaptive Flux Observer of Induction Motor," in *IEEE Transactions on Industrial Applications*, Vol. 29, No. 2, pp. 344–348, 1993.

[71] J. Gacho, M. Zalman, "IM Based Speed Servodrive with Luenberger Observer," in *Journal of Electrical Engineering*, vol. 61, no. 3, pp. 149–156, 2016.

[72] Y. Zhang, Z. Zhao, T. Lu, L. Yuan, W. Xu and J. Zhu, "A comparative study of Luenberger observer, sliding mode observer and extended Kalman filter for sensorless vector control of induction motor drives," *2009 IEEE Energy Conversion Congress and Exposition*, San Jose, CA, 2009, pp. 2466-2473.

[73] D. Xu, B. Wang, G. Zhang, G. Wang and Y. Yu, "A review of sensorless control methods for AC motor drives," in *CES Transactions on Electrical Machines and Systems*, vol. 2, no. 1, pp. 104-115, March 2018.

[74] J. Holtz, "Sensorless Control of Induction Motor Drives," in *Proceedings of the IEEE*, vol. 90, no. 8, pp. 1359-1394, Aug. 2002.

[75] M. Zaky, M. Khater, H. Yasin, S. Shokralla and A. El-Sabbe, "Speed-Sensorless Control Of Induction Motor Drives (Review Paper)," in *Engineering Research Journal (ERJ)*, Faculty of Engineering, Minoufiya University, Egypt, 2007.

[76] S. Bolognani, L. Peretti and M. Zigliotto, "A novel open-loop speed estimation technique for low-cost IM drives," *2007 International Aegean Conference on Electrical Machines and Power Electronics*, Bodrum, 2007, pp. 754-759.

[77] M. Koteich, "Flux estimation algorithms for electric drives: A comparative study," *2016 3rd International Conference on Renewable Energies for Developing Countries (REDEC)*, Zouk Mosbeh, 2016, pp. 1-6.

[78] M. Zerbo, A. Ba-Razzouk and P. Sicard, "Open-loop speed estimators design for online induction machine synchronous speed tracking," *IEEE International Conference on Electric Machines and Drives*, 2005., San Antonio, TX, 2005, pp. 1089-1094.

[79] S. Bolognani, L. Peretti and M. Zigliotto, "Parameter Sensitivity Analysis of an Improved Open-Loop Speed Estimate for Induction Motor Drives," in *IEEE Transactions on Power Electronics*, vol. 23, no. 4, pp. 2127-2135, July 2008.

[80] A. Larabi, M. O. Mahmoudi and M. S. Boucherit, "Speed sonsorless vector control of induction motor using adaptive model reference method," *2008 International Symposium on Power Electronics, Electrical Drives, Automation and Motion*, Ischia, 2008, pp. 1120-1124

[81] S. Maiti, C. Chakraborty, Y. Hori and M. C. Ta, "Model Reference Adaptive Controller-Based Rotor Resistance and Speed Estimation Techniques for Vector Controlled Induction Motor Drive Utilizing Reactive Power," in *IEEE Transactions on Industrial Electronics*, vol. 55, no. 2, pp. 594-601, Feb. 2008.

[82] C. Schauder, “Adaptive Speed Identification for Vector Control of Induction Motors without Rotational Transducers,” in *IEEE Transactions on Industrial Electronics*, vol. 28, no. 5, pp. 1054-1061, 1992.

[83] C. E. de Carvalho, J. W. Lima Nerys, L. R. Lisita, E. G. Marra, M. De Bastos Guimarães. "MRAS Techniques Applied to Induction Motor Speed Estimation: A Comparative Analysis Based on a LabView Platform", Institute for Research and Education in Power Systems (IREP), Goiania, Brazil 2020

[84] S. Das, R. Kumar and A. Pal, "MRAS-Based Speed Estimation of Induction Motor Drive Utilizing Machines’ d- and q-Circuit Impedances," in *IEEE Transactions on Industrial Electronics*, vol. 66, no. 6, pp. 4286-4295, June 2019.

[85] Y. Wang, X. Deng and C. Wu, "A New Method for PI Parameter Adjustment of Induction Motor Based on MRAS," *2019 IEEE 4th Advanced Information Technology, Electronic and Automation Control Conference (IAEAC)*, Chengdu, China, 2019, pp. 500-504.

[86] P. Karlovský, R. Linhart and J. Lettl, "Sensorless determination of induction motor drive speed using MRAS method," *2016 8th International Conference on Electronics, Computers and Artificial Intelligence (ECAI)*, Ploiesti, 2016, pp. 1-4.

[87] M. Korzonek, G. Tarchala and T. Orlowska-Kowalska, "A review on MRAS-type speed estimators for reliable and efficient induction motor drives, " in *ISA Transactions*, vol. 93, pp. 1-13, 2019.

[88] P. Karlovský and J. Lettl, "Application of MRAS algorithm to replace the speed sensor in induction motor drive system," *12th International Scientific Conference Of Young Scientists On Sustainable, Modern and Safe Transport*, Elsevier BV, Linz, pp. 421-426, 2017.

[89] H. H. Vo, P. Brandstetter, T. C. Tran and C. S. T. Dong, "An Implementation of Rotor Speed Observer for Sensorless Induction Motor Drive in Case of Machine Parameter Uncertainty" in *Power Engineering and Electrical Engineering*, vol. 16, no. 4, Dec. 2018.

[90] H. Xie *et al.*, "Sliding-Mode MRAS based Encoderless Predictive Torque Control for Induction Machine," *2019 IEEE International Symposium on Predictive Control of Electrical Drives and Power Electronics (PRECEDE)*, Quanzhou, China, 2019, pp. 1-4.

[91] R. P. Vieira, C. C. Gastaldini, R. Z. Azzolin and H. A. Gründling, "Sensorless Sliding-Mode Rotor Speed Observer of Induction Machines Based on Magnetizing Current Estimation," in *IEEE Transactions on Industrial Electronics*, vol. 61, no. 9, pp. 4573-4582, Sept. 2014.

[92] F. Auger, M. Hilairet, J. M. Guerrero, E. Monmasson, T. Orlowska-Kowalska and S. Katsura, "Industrial Applications of the Kalman Filter: A Review," in *IEEE Transactions on Industrial Electronics*, vol. 60, no. 12, pp. 5458-5471, Dec. 2013.

[93] E. Ozsoy, M. Gokasan and S. Bogosyan, "Simultaneous rotor and stator resistance estimation of squirrel cage induction machine with a single extended kalman filter," in *Turkish Journal of Electrical Engineering and Computer Sciences*, vol. 18, pp. 853-864, 2010.

[94] J. Chen and J. Huang, "Stable Simultaneous Stator and Rotor Resistances Identification for Speed Sensorless IM Drives: Review and New Results," in *IEEE Transactions on Power Electronics*, vol. 33, no. 10, pp. 8695-8709, Oct. 2018.

[95] M. Rayyam, M. Zazi, Y. Hajji and I. Chtouki, "Stator and rotor faults detection in Induction Motor (IM) using the Extended Kaman Filter (EKF)," *2016 International Conference on Electrical and Information Technologies (ICEIT)*, Tangiers, 2016, pp. 148-152

[96] P. Karlovsky, O. Lipcak and J. Lettl " Estimation of Stator Voltage of Inverter-Supplied Induction Motor Using Kalman Filter," in *AETA 2019 - Recent Advances in Electrical Engineering and Related Sciences: Theory and Application*, Cham, Springer, 2020. p. 64-73.

[97] M. Barut, S. Bogosyan and M. Gokasan, "Speed-Sensorless Estimation for Induction Motors Using Extended Kalman Filters," in *IEEE Transactions on Industrial Electronics*, vol. 54, no. 1, pp. 272-280, Feb. 2007.

[98] Y. D. Yoon, S. K. Sul, S. Morimoto, and K. Ide, “High-Bandwidth Sensorless Algorithm for AC Machines Based on Square-Wave-Type Voltage Injection,” in *IEEE Transactions on Industry Applications*, vol. 47, no. 3, pp. 1361-1370, 2011.

[99] G. Wang, D. Xiao, N. Zhao, X. Zhang, W. Wang, and D. Xu, “Low-Frequency Pulse Voltage Injection Scheme-Based Sensorless Control of IPMSM Drives for Audible Noise Reduction,” in *IEEE Transactions on Industrial Electronics*, vol. 64, no. 11, pp. 8415-8426, 2017.

[100] P. L. Xu, and Z. Q. Zhu, “Carrier signal injection-based sensorless control for permanent-magnet synchronous machine drives considering machine parameter asymmetry,” in *IEEE Transactions on Industrial Electronics*, vol. 63, no. 5, pp. 2813-2824, 2016.

[101] P. Karlovsky and J. Lettl, "Comparison of sensorless AC drive operation using MRAS method or Luenberger observer," *2017 International Conference on Optimization of Electrical and Electronic Equipment (OPTIM) & 2017 Intl Aegean Conference on Electrical Machines and Power Electronics (ACEMP)*, Brasov, 2017, pp. 281-286.

[102] P. Vas, "Artificial—Intelligence-Based Electrical Machines and Drives: Applications of Fuzzy, Neural, Fuzzy-Neural and Genetic Algorithm Based Techniques", *Oxford University Press*, New York, 1999, 625p.

[103] K. Hasse, "Zur Dynamik Drehzahlgeregelter Antriebe mit strom-richtergespeisten Asynchron-kurschlusslafermaschinen", PhD thesis, Technical University Darmstadt, Germany, 1969.

[104] P. Karlovský and J. Lettl, "Improvement of DTC performance using luenberger observer for flux estimation," *2017 18th International Scientific Conference on Electric Power Engineering (EPE)*, Kouty nad Desnou, 2017, pp. 1-5.

[105] P. Karlovsky and J. Lettl, "Influence of speed and flux estimation by Luenberger observer on IM drive with DTC," 22nd International Conference on Applied Electronics, Pilsen, University of West Bohemia Pilsen, pp. 69-72, 2017.

[106] P. Vas, "Sensorless vector and direct torque control" Oxford University Press, Oxford, 1998.

[107] G. S. Buja and M. P. Kazmierkowski, "Direct torque control of PWM inverter-fed AC motors - a survey," in *IEEE Transactions on Industrial Electronics*, vol. 51, no. 4, pp. 744-757, Aug. 2004.

[108] A. Linder, R. Kanchan, R. Kennel and P. Stolze, "Model-Based Predictive Control of Electric Drives", Cuvillier Verlag, Göttingen, 2010.

[109] J. B. Rawlings, "Tutorial overview of model predictive control," in *IEEE Control Systems Magazine*, vol. 20, no. 3, pp. 38-52, June 2000.

[110] R. Kennel, A. Linder and M. Linke, "Generalized predictive control (GPC)-ready for use in drive applications?," *2001 IEEE 32nd Annual Power Electronics Specialists Conference (IEEE Cat. No.01CH37230)*, Vancouver, BC, 2001, pp. 1839-1844 vol. 4.

[111] L. Wang, S. Chai, D. Yoo, G. Lu, N. Ki, "PID and Predictive Control of Electrical Drives and Power Converters using MATLAB/Simulink". *Wiley-IEEE Press*, 2015.

[112] S. Saeidi and R. Kennel, "Continuous set nonlinear model predictive control for an induction motor," *2013 15th European Conference on Power Electronics and Applications (EPE)*, Lille, 2013, pp. 1-10.

[113] J. Retif, X. Lin-Shi and F. Morel, "Predictive Current Control for an Induction Motor," *2008 IEEE Power Electronics Specialists Conference,* Rhodes, 2008, pp. 3463-3468.

[114] J. Han, W. Li, H. Su, L. Zhou, Q. Meng and C. Liu, "An Improved Model Predictive Current Control Algorithm Considering Dynamic Response Performance of Torque and Speed," *2019 22nd International Conference on Electrical Machines and Systems (ICEMS)*, Harbin, China, 2019, pp. 1-4.

[115] J. Lettl and P. Karlovsky, "Induction motor drive predictive direct torque control method," *2015 25th International Conference Radioelektronika (RADIOELEKTRONIKA)*, Pardubice, 2015, pp. 70-74.

[116] J. Rodriguez, J. Pontt, P. Correa, P. Lezana and P. Cortes, "Predictive power control of an AC/DC/AC converter," *Fourtieth IAS Annual Meeting. Conference Record of the 2005 Industry Applications Conference*, 2005., Kowloon, Hong Kong, 2005, pp. 934-939 Vol. 2.

[117] M. Novak, H. Xie, T. Dragicevic, F. Wang, J. Rodriguez and F. Blaabjerg, "Optimal Cost Function Parameter Design in Predictive Torque Control (PTC) Using Artificial Neural Networks (ANN)," in *IEEE Transactions on Industrial Electronics,* 2020 (Early Access).

[118] P. Cortes *et al.*, "Guidelines for weighting factors design in Model Predictive Control of power converters and drives," *2009 IEEE International Conference on Industrial Technology*, Gippsland, VIC, 2009, pp. 1-7.

[119] A. Bhowate, M. Aware and S. Sharma, "Predictive Torque Control With Online Weighting Factor Computation Technique to Improve Performance of Induction Motor Drive in Low Speed Region," in *IEEE Access*, vol. 7*,* pp. 42309-42321, 2019.

[120] P. Karlovský and J. Lettl, "Predictive Control of Induction Motor Drive Using dSPACE Platform", in *Transaction on Electrical Engineering*, vol. 6, no. 2, pp. 44-48, 2017.

[121] P. R. U. Guazzelli, W. C. de Andrade Pereira, C. M. R. de Oliveira, A. G. de Castro and M. L. de Aguiar, "Weighting Factors Optimization of Predictive Torque Control of Induction Motor by Multiobjective Genetic Algorithm," in *IEEE Transactions on Power Electronics*, vol. 34, no. 7, pp. 6628-6638, July 2019.

[122] P. Karlovský and J. Lettl, "Rozbor prediktivní metody přímého řízení momentu pohonu s asynchroním motorem v prostředí Matlab Simulink", In *Sborník XXXIV. celostátní konference elektrické pohony,* University of West Bohemia, Pilsen, 2015.

[123] J. Holtz, "The dynamic representation of AC drive systems by complex signal flow graphs," *Proceedings of 1994 IEEE International Symposium on Industrial Electronics (ISIE '94)*, Santiago, Chile, 1994, pp. 1-6

[124] T. Himabindu, A. V. R. Teja, G. Bhuvaneswari and B. Singh, "Simplified predictive torque control of an IM drive with efficient zero vector placement," *2017 IEEE 26th International Symposium on Industrial Electronics (ISIE)*, Edinburgh, 2017, pp. 362-367.

[125] P. Karlovsky and J. Lettl, "Loss Reduction in Induction Motor Drive Using Model Predictive Control," *2018 10th International Conference on Electronics, Computers and Artificial Intelligence (ECAI)*, Iasi, Romania, 2018, pp. 1-4.

[126] H. Miranda, P. Cortes, J. I. Yuz and J. Rodriguez, "Predictive Torque Control of Induction Machines Based on State-Space Models," in *IEEE Transactions on Industrial Electronics*, vol. 56, no. 6, pp. 1916-1924, June 2009.

[127] H. Hu, Y. Shao, L. Tang, J. Ma, Z. He and S. Gao, "Overview of Harmonic and Resonance in Railway Electrification Systems," in *IEEE Transactions on Industry Applications*, vol. 54, no. 5, pp. 5227-5245, Sept.-Oct. 2018

[128] L. A. Frasco and F. R. Holmstrom, "EMC consequences of power electronics applied to rail transit", *IEE International Conference on Railways in the Electronic Age*, United Kingdom, pp. 117-127, 1981.

[129] P. Cortes, J. Rodriguez, D. E. Quevedo and C. Silva, "Predictive Current Control Strategy With Imposed Load Current Spectrum," in *IEEE Transactions on Power Electronics*, vol. 23, no. 2, pp. 612-618, March 2008.

[130] P. K. V. Kunisetti and T. V. Kumar, "Enhanced direct torque control and predictive torque control strategies of an open-End winding induction motor drive to eliminate common-mode voltage and weighting factors," in *IET Power Electronics*, vol. 12, no. 8, pp. 1986-1997, 10 7 2019

[131] F. Ban, G. Lian, H. Li, B. Chen and G. Gu, "Comparative Analysis of Torque and Flux Ripples for Several Direct Torque Control Strategies of PMSM," *2018 IEEE International Conference on Applied Superconductivity and Electromagnetic Devices (ASEMD)*, Tianjin, 2018, pp. 1-2

[132] R. Kennel, J. Rodríguez, J. Espinoza and M. Trincado, "High performance speed control methods for electrical machines: An assessment," *2010 IEEE International Conference on Industrial Technology*, Vina del Mar, 2010, pp. 1793-1799,

[133] P. Karlovsky and J. Bauer, "Wheel slip determination capability of locomotive driven by model predictive control," *2018 IEEE 18th International Power Electronics and Motion Control Conference (PEMC)*, Budapest, 2018, pp. 1-6.

[134] J. Lettl and P. Karlovsky, "Induction Motor Drive Predictive Control Method Analysis and Comparison with Fundamental Direct Torque Control Method," *PIERS 2015 Proceedings*, Electromagnetics Academy, Cambridge, pp. 2510-2513, 2015.

[135] P. Karlovský and J. Lettl, "Improvement of induction motor drive performance using predictive control method instead of DTC method," *2016 International Conference on Applied Electronics (AE)*, Pilsen, 2016, pp. 121-124.

[136] Z. Akhmetov and A. Ruderman, "Analytical current THD evaluation for three-phase voltage source inverters," in *IET Power Electronics*, vol. 13, no. 6, pp. 1286-1289, 6 5 2020.

[137] T. Geyer and D. E. Quevedo, "Multistep Finite Control Set Model Predictive Control for Power Electronics," in *IEEE Transactions on Power Electronics*, vol. 29, no. 12, pp. 6836-6846, Dec. 2014.

[138] P. Acuna, C. A. Rojas, R. Baidya, R. P. Aguilera and J. E. Fletcher, "On the Impact of Transients on Multistep Model Predictive Control for Medium-Voltage Drives," in *IEEE Transactions on Power Electronics*, vol. 34, no. 9, pp. 8342-8355, Sept. 2019.

[139] T. Geyer, "Computationally Efficient Model Predictive Direct Torque Control," in *IEEE Transactions on Power Electronics*, vol. 26, no. 10, pp. 2804-2816, Oct. 2011.

[140] R. Baidya *et al.*, "Dealing with Suboptimality in Multistep Model Predictive Control for Transient Operations," *2019 IEEE Energy Conversion Congress and Exposition (ECCE)*, Baltimore, MD, USA, 2019, pp. 3780-3785.

[141] B. Hassibi and H. Vikalo, "On the sphere-decoding algorithm I. Expected complexity," in *IEEE Transactions on Signal Processing*, vol. 53, no. 8, pp. 2806-2818, Aug. 2005.

[142] M. Amiri, J. Millimonfared, D. A. Khaburi and M. Khosravi, "A fixed switching frequency predictive torque control scheme for induction motors based on discrete space vector modulation" in *Electrical Engineering*, vol. 102, no. 4, pp. 845–857, 2020.

[143] M. Wilamowski, B. Irwin, J. David, "*Power Electronics and Motor Drives*", CRC Press, Baton Rouge, 2nd edition, 2018, 1015p.

[144] H. Van Khang, W. Pawlus and K. G. Robbersmyr, "Investigation and reduction of losses on inverter-fed induction motors," *2017 19th European Conference on Power Electronics and Applications (EPE'17 ECCE Europe)*, Warsaw, 2017, pp. P.1-P.9.

[145] Y. Xie, J. Zhang, F. Leonardi, A. R. Munoz, F. Liang and M. W. Degner, "Modeling and Verification of Electrical Stress in Inverter-Driven Electric Machine Windings," *2018 IEEE Energy Conversion Congress and Exposition (ECCE)*, Portland, OR, 2018, pp. 5742-5749.

[146] A. M. Howlader, N. Urasaki, T. Senjyu, A. Yona and A. Y. Saber, "Optimal PAM Control for a Buck Boost DC-DC Converter with a Wide-Speed-Range of Operation for a PMSM", in *Journal of Power Electronics*, vol. 5, no. 5, pp. 477-484, 2010.

[147] J. O. Estima and A. J. Marques Cardoso, "Efficiency Analysis of Drive Train Topologies Applied to Electric/Hybrid Vehicles," in *IEEE Transactions on Vehicular Technology*, vol. 61, no. 3, pp. 1021-1031, March 2012.

[148] H. Li, S. Huang, D. Luo, J. Gao and P. Fan "Dynamic DC-link Voltage Adjustment for Electric Vehicles Considering the Cross Saturation Effects", in *Energies*, vol. 11, no. 8, pp. 2046, 2018.

[149] Sang Kyoon Kim, Young Sam Kim and Young Ahn Kwon, "Improved performance of sensorless induction motor drive based on variable link voltage," *SICE 2003 Annual Conference (IEEE Cat. No.03TH8734)*, Fukui, Japan, 2003, pp. 1638-1643 Vol.2.

[150] K. Choo, I. Won, S. Hong, J. Lee and C. Won, "Novel DC-link voltage variation method for interior permanent magnet synchronous motor drive system with high-efficient DC-DC converter," *2017 20th International Conference on Electrical Machines and Systems (ICEMS)*, Sydney, NSW, 2017, pp. 1-6.

[151] T. H. Kim, J. H. Lee and C. Y. Won, "Design and Control Methods of Bidirectional DC-DC Converter for the Optimal DC-Link Voltage of PMSM Drive", in *Journal of Electrical Engineering and Technology*, vol. 9, no. 6, pp. 1944–1953, 2014.

[152] K. Choo, I. Won, S. Hong, J. Lee and C. Won, "Novel DC-link voltage variation method for interior permanent magnet synchronous motor drive system with high-efficient DC-DC converter," *2017 20th International Conference on Electrical Machines and Systems (ICEMS)*, Sydney, NSW, 2017, pp. 1-6.

[153] S. Sridharan and P. T. Krein, "Optimizing variable DC link voltage for an induction motor drive under dynamic conditions," *2015 IEEE Transportation Electrification Conference and Expo (ITEC)*, Dearborn, MI, 2015, pp. 1-6.

[154] P. Karlovsky and J. Lettl, "Capability of Predictive Torque Control Method to Control DC-link Voltage Level in Small Autonomous Power System with Induction Generator", in: *Lecture Notes in Electrical Engineering*, Springer, Cham, vol. 554, pp. 769-777, 2020.

[155] P. Cortés, J. Rodriguez, P. Antoniewicz and M. Kazmierkowski, "Direct Power Control of an AFE Using Predictive Control," in *IEEE Transactions on Power Electronics*, vol. 23, no. 5, pp. 2516-2523, Sept. 2008

[156] M. Parvez, S. Mekhilef, N. M. L. Tan and H. Akagi, "An improved active-front-end rectifier using model predictive control," *2015 IEEE Applied Power Electronics Conference and Exposition (APEC)*, Charlotte, NC, 2015, pp. 122-127.

[157] M. Perez, J. Rodriguez and A. Coccia, "Predictive current control in a single phase PFC boost rectifier," *2009 IEEE International Conference on Industrial Technology*, Gippsland, VIC, 2009, pp. 1-6.

[158] Youssef, A.B.; El Khil, S.K.; Slama-Belkhodja, I. State Observer-Based Sensor Fault Detection and Isolation, and Fault Tolerant Control of a Single-Phase PWM Rectifier for Electric Railway Traction. *IEEE Transactions on Power Electronics 2013*, 28, 5842-5853.

[159] L. He, J. Xiong, H. Ouyang, P. Zhang and K. Zhang, "High-Performance Indirect Current Control Scheme for Railway Traction Four-Quadrant Converters," in *IEEE Transactions on Industrial Electronics*, vol. 61, no. 12, pp. 6645-6654, Dec. 2014.

[160] S. Chakraborty, H.-N. Vu, M. M. Hasan, D.-D. Tran, M.E. Baghdadi and O. Hegazy, "DC-DC Converter Topologies for Electric Vehicles, Plug-in Hybrid Electric Vehicles and Fast Charging Stations: State of the Art and Future Trends". in *Energies*, vol. 12, no. 6, 1569, 2019.

[161] E. Fuentealba Vidal, I. Eidt Colling and I. Barbi, "A Bidirectional PWM Three-Phase Step-Down Rectifier Based on the Differential-Mode Power Conversion Principle," in *IEEE Transactions on Power Electronics*, vol. 24, no. 12, pp. 2951-2958, Dec. 2009.

[162] P. Drabek, Z. Peroutka, M. Pittermann and M. Cedl, "New Configuration of Traction Converter With Medium-Frequency Transformer Using Matrix Converters," in *IEEE Transactions on Industrial Electronics*, vol. 58, no. 11, pp. 5041-5048, Nov. 2011.

[163] Y. P. Patel *et al.*, "Mitigation of the effects of common-mode current on the operation of SCR-based rectifiers for AC drives," *2015 IEEE Energy Conversion Congress and Exposition (ECCE)*, Montreal, QC, 2015, pp. 2949-2955.

[164] X. Xu, R. De Doncker and D. W. Novotny, "A stator flux oriented induction machine drive," *PESC '88 Record., 19th Annual IEEE Power Electronics Specialists Conference*, Kyoto, Japan, 1988, pp. 870-876 vol.2.

[165] M. Popescu, "Induction motor modelling for vector control purposes," Helsinki University of Technology, Laboratory of Electromechanics, Report, Espoo, 2000, 144 p.

[166] P. Karlovsky, O. Lipcak, J. Bauer and J. Lettl, "Predictive Torque Control of Induction Motor with Integrated DC-Link Voltage Optimisation," in IET Power Electronics, 2020 (Early Access).

[167] R. Tiwari, Determination of Induction Motor Speed using Kalman Filter, Master's thesis, Faculty of Electrical Engineering, CTU in Prague, 2019.

[168] H. Karkkainen, L. Aarniovuori, M. Niemela and J. Pyrhonen, "Converter-Fed Induction Motor Efficiency: Practical Applicability of IEC Methods," in *IEEE Industrial Electronics Magazine*, vol. 11, no. 2, pp. 45-57, June 2017.

[169] L. Aarniovuori, P. Rasilo, M. Niemelä and J. J. Pyrhönen, "Analysis of 37-kW Converter-Fed Induction Motor Losses," in *IEEE Transactions on Industrial Electronics*, vol. 63, no. 9, pp. 5357-5365, Sept. 2016.

[170] D. Zhang, R. An and T. Wu, "Effect of voltage unbalance and distortion on the loss characteristics of three-phase cage induction motor," in *IET Electric Power Applications*, vol. 12, no. 2, pp. 264-270, 2 2018.

[171] A. Boglietti, P. Ferraris, M. Lazzari and M. Pastorelli, "Change of the iron losses with the switching supply frequency in soft magnetic materials supplied by PWM inverter," in *IEEE Transactions on Magnetics*, vol. 31, no. 6, pp. 4250-4252, Nov. 1995.

[172] D. Zhang, H. Dai, H. Zhao and T. Wu, "A Fast Identification Method for Rotor Flux Density Harmonics and Resulting Rotor Iron Losses of Inverter-Fed Induction Motors," in *IEEE Transactions on Industrial Electronics*, vol. 65, no. 7, pp. 5384-5394, July 2018.

[173] D. Zhang, T. Liu, H. Zhao and T. Wu, "An Analytical Iron Loss Calculation Model of Inverter-Fed Induction Motors Considering Supply and Slot Harmonics," in *IEEE Transactions on Industrial Electronics*, vol. 66, no. 12, pp. 9194-9204, Dec. 2019.

[174] S. Xue *et al.*, "Iron Loss Model for Electrical Machine Fed by Low Switching Frequency Inverter," in *IEEE Transactions on Magnetics*, vol. 53, no. 11, pp. 1-4, Nov. 2017, Art no. 2801004.

[175] A. Boglietti, P. Ferraris, M. Lazzari and M. Pastorelli, "Influence of the inverter characteristics on the iron losses in PWM inverter-fed induction motors," in *IEEE Transactions on Industry Applications*, vol. 32, no. 5, pp. 1190-1194, Sept.-Oct. 1996.

[176] A. Boglietti, P. Ferraris, M. Lazzari and F. Profumo, "Iron losses in magnetic materials with six-step and PWM inverter supply (induction motors)," in *IEEE Transactions on Magnetics*, vol. 27, no. 6, pp. 5334-5336, Nov. 1991.

List of Author’s Publications Related to the Thesis

Publications in Journals with Impact Factor

P. Karlovsky and J. Lettl, "Induction Motor Drive Direct Torque Control and Predictive Torque Control Comparison Based on Switching Pattern Analysis", in *Energies*, vol. 11, no. 7, 1793, 2018.
Impact factor 2017: 2.676 (Q2)
Contribution: 50 %
Number of citations in WoS: 5

P. Karlovsky, O. Lipcak and J. Bauer, "Iron Loss Minimization Strategy for Predictive Torque Control of Induction Motor, " in *Electronics*, vol. 9, no. 4, 566, 2020.
Impact factor 2019: 2.412 (Q2)
Contribution: 33.3 %
Number of citations in WoS: 0

P. Karlovsky, O. Lipcak, J. Bauer and J. Lettl, "Predictive Torque Control of Induction Motor with Integrated DC-Link Voltage Optimisation," in *IET Power Electronics*, 2020. (**accepted 7.7.2020**).
Impact factor 2019: 2.672 (Q2)
Contribution: 25 %
Number of citations in WoS: 0

Publications Excerpted in Web of Science

J. Lettl and P. Karlovsky, "Induction motor drive predictive direct torque control method," *2015 25th International Conference Radioelektronika*, Pardubice, 2015, pp. 70-74.
Contribution: 50 %
Number of citations in WoS: 4

P. Karlovsky and J. Lettl, "Improvement of induction motor drive performance using predictive control method instead of DTC method," *2016 International Conference on Applied Electronics (AE)*, Pilsen, 2016, pp. 121-124.
Contribution: 50 %
Number of citations in WoS: 2

P. Karlovsky, R. Linhart and J. Lettl, "Sensorless determination of induction motor drive speed using MRAS method," *2016 8th International Conference on Electronics, Computers and Artificial Intelligence (ECAI)*, Ploiesti, 2016, pp. 1-4.
Contribution: 33.3 %
Number of citations in WoS: 4

P. Karlovsky and J. Lettl, "Influence of switching frequency on torque ripples in model predictive control of induction motor drive," *2017 9th International Conference on Electronics, Computers and Artificial Intelligence (ECAI)*, Targoviste, 2017, pp. 1-4.
Contribution: 50 %

P. Karlovsky and J. Lettl, "Comparison of sensorless AC drive operation using MRAS method or Luenberger observer," *2017 International Conference on Optimization of Electrical and Electronic Equipment (OPTIM) & 2017 Intl Aegean Conference on Electrical Machines and Power Electronics (ACEMP)*, Brasov, 2017, pp. 281-286.
Contribution: 50 %
Number of citations in WoS: 1

P. Karlovsky and J. Lettl, "Application of MRAS algorithm to replace the speed sensor in induction motor drive system," *12th International Scientific Conference Of Young Scientists On Sustainable, Modern and Safe Transport*, Elsevier, Linz, pp. 421-426, 2017.
Contribution: 50 %
Number of citations in WoS: 3

P. Karlovsky and J. Lettl, "Improvement of DTC performance using Luenberger observer for flux estimation," *2017 18th International Scientific Conference on Electric Power Engineering (EPE)*, Kouty nad Desnou, 2017, pp. 1-5.
Contribution: 50 %
Number of citations in WoS: 2

P. Karlovsky and J. Lettl, "Influence of speed and flux estimation by Luenberger observer on IM drive with DTC," *22nd International Conference on Applied Electronics*, Pilsen, University of West Bohemia Pilsen, pp. 69-72, 2017.
Contribution: 50 %
Invited talk

P. Karlovsky and J. Lettl, "Loss Reduction in Induction Motor Drive Using Model Predictive Control," *2018 10th International Conference on Electronics, Computers and Artificial Intelligence (ECAI)*, Iasi, Romania, 2018, pp. 1-4.
Contribution: 50 %

P. Karlovsky and J. Bauer, "Wheel slip determination capability of locomotive driven by model predictive control," *2018 IEEE 18th International Power Electronics and Motion Control Conference (PEMC)*, Budapest, 2018, pp. 1-6.
Contribution: 50 %
Number of citations in WoS: 1

Other Publications

J. Lettl and P. Karlovsky, "Induction Motor Drive Predictive Control Method Analysis and Comparison with Fundamental Direct Torque Control Method," *PIERS 2015 Proceedings*, Electromagnetics Academy, Cambridge, pp. 2510-2513, 2015.
Contribution: 50 %
Number of citations in WoS: 2

P. Karlovsky and J. Lettl, "Rozbor prediktivní metody přímého řízení momentu pohonu s asynchroním motorem v prostředí Matlab Simulink", In *Sborník XXXIV. celostátní konference elektrické pohony*, University of West Bohemia, Pilsen, 2015.
Contribution: 50 %

P. Karlovsky and J. Lettl, "Predictive Control of Induction Motor Drive Using dSPACE Platform", in *Transaction on Electrical Engineering*, vol. 6, no. 2, pp. 44-48, 2017.
Contribution: 50 %

P. Karlovsky and J. Lettl, "Capability of Predictive Torque Control Method to Control DC-link Voltage Level in Small Autonomous Power System with Induction Generator", in: *Lecture Notes in Electrical Engineering*, Springer, Cham, vol. 554, pp. 769-777, 2020.
Contribution: 50 %

P. Karlovsky, O. Lipcak and J. Lettl, "Estimation of Stator Voltage of Inverter-Supplied Induction Motor Using Kalman Filter," in: *Lecture Notes in Electrical Engineering*, Springer, Cham, vol. 685, pp. 64-73, 2020.
Contribution: 33.3 %

P. Karlovsky, J. Lettl and J. Bauer, "Optimum Flux Search Control of Induction Motor Drive with Predictive Torque Control", *International Scientific Conference on Electric Power Engineering (EPE)*, Praha, Czech Republic, 2020, (**accepted**).
Contribution: 33.3 %

List of Author’s Other Publications

-

A. Appendices

A1. Simulink Model

The top layer of the simulation scheme made in Matlab Simulink environment is depicted in Fig. 93. On the right side, the components from SimScape library create the power part of the drive. In the middle, the control algorithms are depicted. From the top. they are the observer, the PTC strategy, and the DC-link voltage optimization. These components are driven by a clock signal with fixed frequency representing the microcontroller clock signal. On the left side, the references are entered. In the left bottom corner, the synchronization of the rectifier to the voltage grid, and the logic of the brake resistor switching are assured.

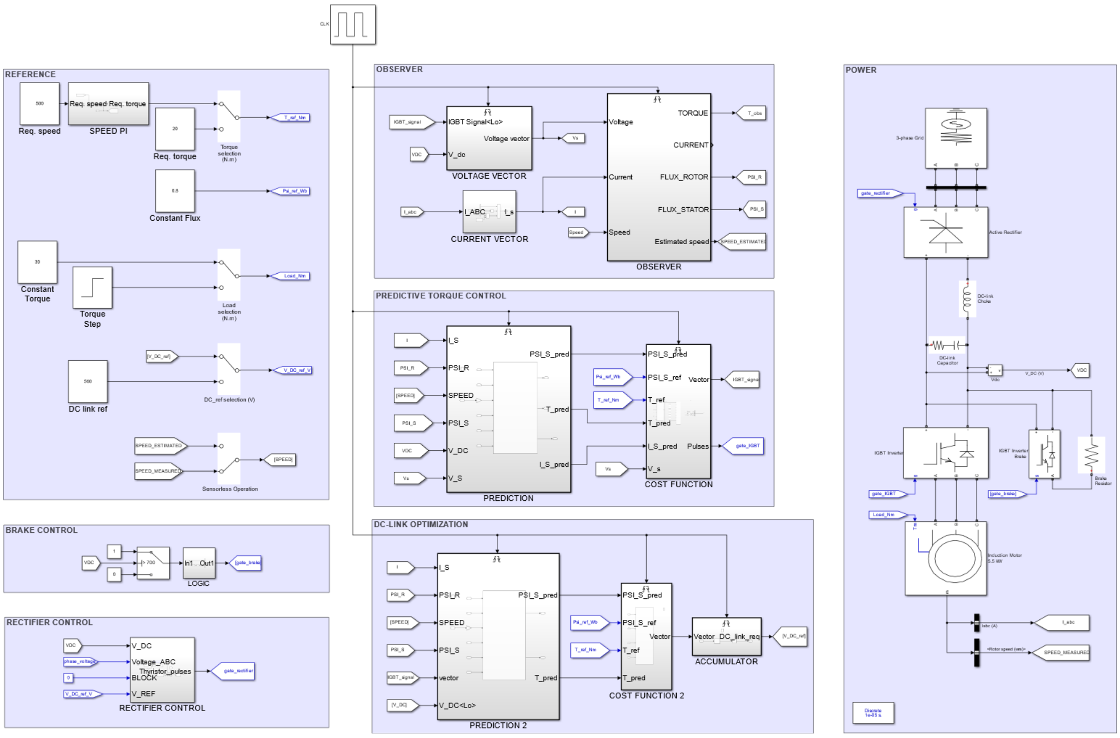

Fig. 93. Simulink model with SimScape library power components.

A2. ControlDesk GUI

A two screenshots of the GUI developed in ControlDesk program are presented in Fig. 94 and Fig. 95. The ControlDesk enables the communication between the laptop and the dSpace. A real-time monitoring, update and record of the selected variables are executed through this GUI. Fig. 94 shows the case with full DC-link voltage and Fig. 95 the case with the DC-link voltage optimization.

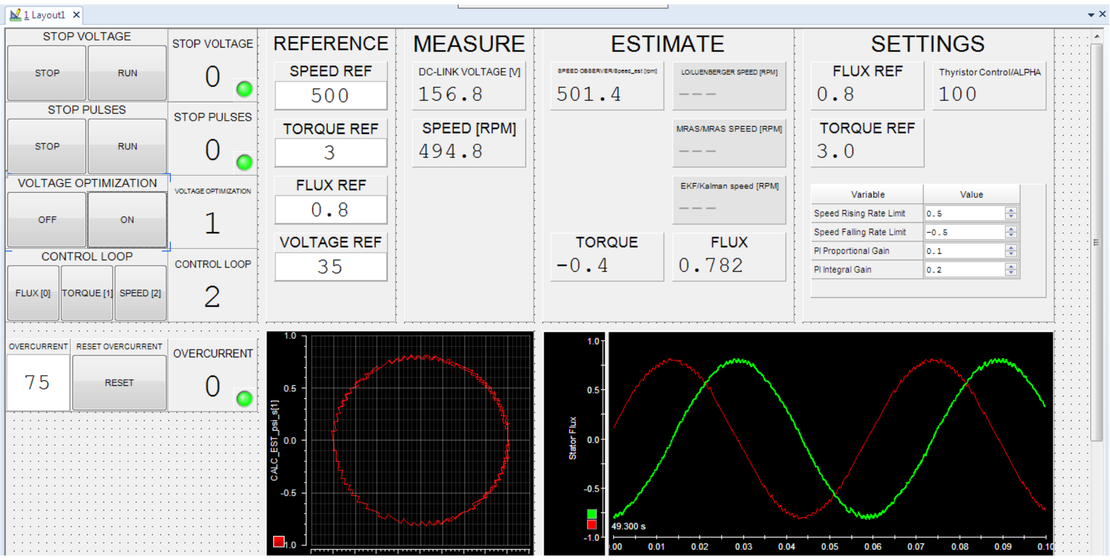

STOP VOLTAGE 0
STOP PULSES 0
VOLTAGE OPTIMIZATION 1
CONTROL LOOP 2
OVERCURRENT 75
OVERCURRENT 0

REFERENCE
SPEED REF 500
TORQUE REF 3
FLUX REF 0.8
VOLTAGE REF 35

MEASURE
DC-LINK VOLTAGE [V] 156.8
SPEED [RPM] 494.8

ESTIMATE
SPEED OBSERVER/Speed_est [rpm] 501.4
LO/LUENBERGER SPEED [RPM] ---
MRAS/MRAS SPEED [RPM] ---
EKF/Kalman speed [RPM] ---
TORQUE -0.4
FLUX 0.782

SETTINGS
FLUX REF 0.8
Thyristor Control/ALPHA 100
TORQUE REF 3.0

Variable	Value
Speed Rising Rate Limit	0.5
Speed Falling Rate Limit	-0.5
PI Proportional Gain	0.1
PI Integral Gain	0.2

Fig. 94. ControlDesk GUI; the DC-link voltage optimization is on.

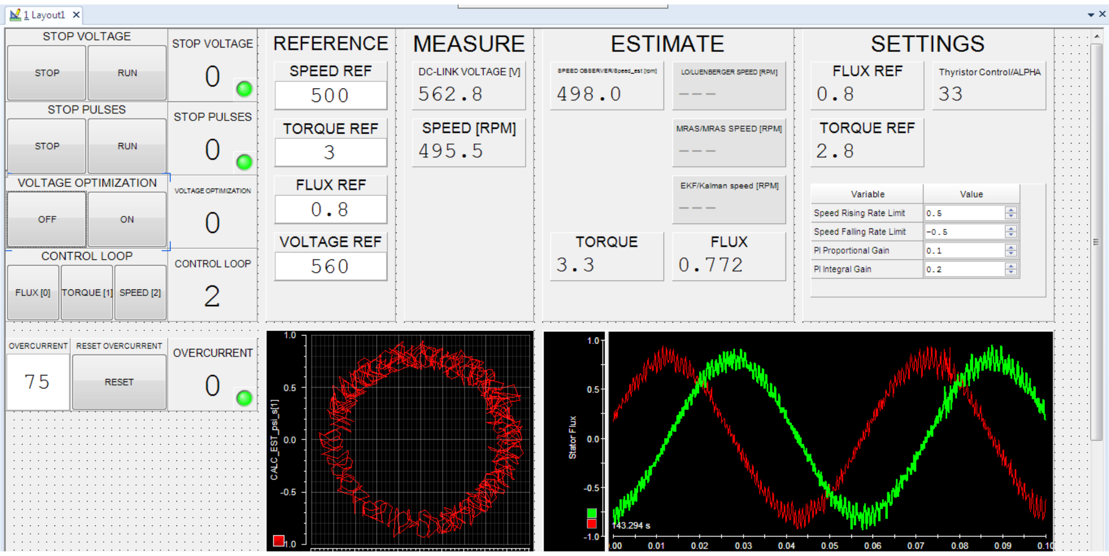

STOP VOLTAGE 0
STOP PULSES 0
VOLTAGE OPTIMIZATION 0
CONTROL LOOP 2
OVERCURRENT 75
OVERCURRENT 0

REFERENCE
SPEED REF 500
TORQUE REF 3
FLUX REF 0.8
VOLTAGE REF 560

MEASURE
DC-LINK VOLTAGE [V] 562.8
SPEED [RPM] 495.5

ESTIMATE
SPEED OBSERVER/Speed_est [rpm] 498.0
LO/LUENBERGER SPEED [RPM] ---
MRAS/MRAS SPEED [RPM] ---
EKF/Kalman speed [RPM] ---
TORQUE 3.3
FLUX 0.772

SETTINGS
FLUX REF 0.8
Thyristor Control/ALPHA 33
TORQUE REF 2.8

Variable	Value
Speed Rising Rate Limit	0.5
Speed Falling Rate Limit	-0.5
PI Proportional Gain	0.1
PI Integral Gain	0.2

Fig. 95. ControlDesk GUI; the DC-link voltage optimization is off.

A3. Matlab Codes of Selected Algorithms

The developed Matlab source codes and Simulink blocks of the most important algorithms, i.e., the flux observer, the speed observer, the predictive control, and the DC-link voltage optimization are presented below.

Flux observer

```
function psi2, i1_o, state_out = fcn(i1, v1, speed, state_in, k)

%Sampling time
Ts=100e-6;

%System matrices constants
a1=-R2/L2;
```

```
a2=Lm*R2/L2;
a3=Lm*R2/(1-Lm*Lm/L1/L2)/L1/L2/L2;
a4=Pp*Lm/(1-Lm*Lm/L1/L2)/L1/L2;
a5=R1/L1/(1-Lm*Lm/L1/L2)+Lm*Lm*R2/L1/sigma/L2/L2;
b1=1/sigma/L1;

%Correction matrix coefficients, correction coefficient k = 1 ... 1.5
k1=-(k-1)/(1-Lm*Lm/L1/L2)*((R2/L2)+(R1/L1));
k2=k-1;
k3=(k-1)/(1-(1-Lm*Lm/L1/L2))*(R2/L2-k*R1/L1);
k4=(k-1)*(1-Lm*Lm/L1/L2)/(1-(1-Lm*Lm/L1/L2));

%Matrices definition
A = (speed.*[0 -Pp 0 0;Pp 0 0 0;0 a4 0 0;-a4 0 0 0]) + [a1 0 a2 0;0 a1
0 a2;a3 0 -a5 0;0 a3 0 -a5];        %System matrix
B = [0 0;0 0;b1 0;0 b1];            %Input matrix
C = [0 0 1 0;0 0 0 1];              %Output matrix
C1 = [1 0 0 0;0 1 0 0];             %Matrix for observed flux
extraction

%Correction matrix
K = (speed.*[0 k4;-k4 0;0 k2;-k2 0]) + [k3 0;0 k3;k1 0;0 k1];


%Old observed current and flux extraction
i1_o = C*state_in;      %Current
psi2 = C1*state_in;     %Flux

state_der = B*v1 + A*state_in + K*(i1_o – i1); %State derivatives
state_out = state_in + state_der * Ts;          %New observed states

%New observed current and flux extraction
i1_o = C*state_out;     %Observed current
psi2 = C1*state_out;    %Observed flux
```

In Matlab Simulink, the above-mentioned code is placed in Simulink block in a way shown in Fig. 96.

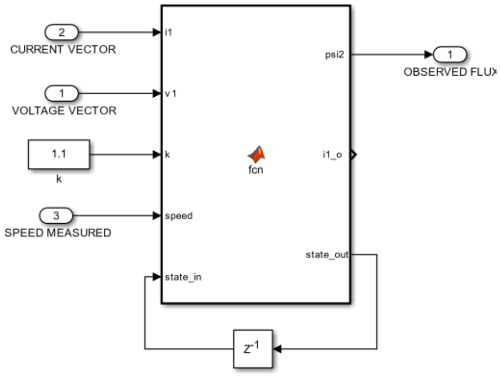

Fig. 96. Implementation of the flux observer in Matlab Simulink.

Speed observer

The Matlab code used for the sensorless speed determination is the same as in case of the flux observer. The difference lies in the treatment of the speed information. In the flux observer, it was taken from the measurement, in case of the speed observer, it is estimated by the PI controller. This is depicted in Fig. 97.

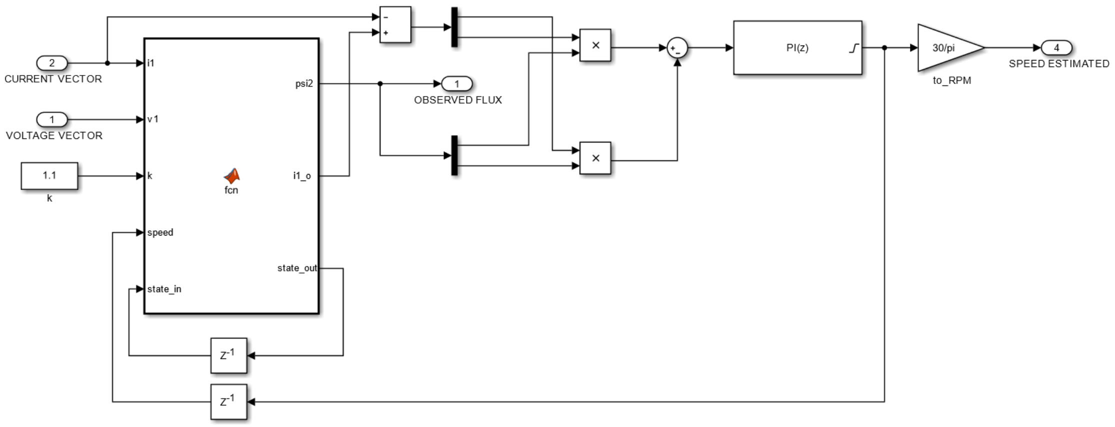

Fig. 97. Implementation of the speed observer in Matlab Simulink.

Predictive torque control – predictive model

```
function [psi1_p, T_p, i1_p] = fcn(i_s, psi_r, speed, v_dc, psi1)

%Sampling time
Ts=100e-6;

%Voltage vectors definition
v1 = v_dc*2/sqrt(3)*
[0+0j 0+1j -sqrt(3)/2+0.5*1j -sqrt(3)/2-0.5*1j 0-1j sqrt(3)/2-0.5*1j
sqrt(3)/2+0.5*1j 0+0j];

% Prediction for eight voltage vector candidates
for k = 1:8

    %Current Prediction
    i1_p(k) = (1+Ts/(1-Lm*Lm/L1/L2)*L1/(R1+R2*Lm/L2*Lm/L2))*i1
+Ts/((1-Lm*Lm/L1/L2)*L1/(R1+R2*Lm/L2*Lm/L2)+Ts)*(1/(R1+R2*Lm/L2*Lm/L2)
*((Lm/L2/L2/R2-Lm/L2*1j*Pp*speed)*psi_r+v1(k)));

    %Stator Flux Prediction
    psi1_p(k) = psi1 + Ts*v1(k) - R1*Ts*(i1);

    %Torque Flux Prediction
    T_p(k) = real(3/2*sqrt(3)*Pp*(real(psi1_p(k))*imag(i1_p(k)) -
imag(psi1_p(k))*real(i1_p(k))));

end
```

Predictive torque control – cost function

```
function [voltage_number] = fcn(psi1_p, T_p, psi1_ref, T_ref, i1_p, k, 
i1_limit)

%Penalize current higher than limit
for j = 1:8
    if (abs(i1_p(j)) > i1_limit)
        current_penal (j) = 100*abs(i_s_p(j));        %very high number
    else
        current_penal (j) = 0;                        %zero
    end
end

%Calculate Cost Function
 g = k*abs(abs(psi1_p)-psi1_ref) + abs(T_p - T_ref) + current_penal;

[~, v] = min(g);              %Find the minimum
voltage_number = v - 1;       %Indexing in Matlab starts at 1, voltage 
vector numbers start at 0
```

DC-link voltage optimization method – predictive model

```
function [psi1_p, T_p] = fcn(i1, psi2, speed, psi1, v_dc, 
vector_number)

%Sampling time
Ts=100e-6;

%Voltage vectors definition
vectors = v_dc*2/sqrt(3)*
[0+0j 0+1j -sqrt(3)/2+0.5*1j -sqrt(3)/2-0.5*1j 0-1j sqrt(3)/2-0.5*1j 
sqrt(3)/2+0.5*1j 0+0j];

%Create voltage vectors candidates with different amplitude
v1 = vectors(vector_number+1)*2/3*v_dc*[1 0.98 1.02]; %Indexing in 
Matlab starts at 1, voltage vector numbers start at 0

% Prediction for three voltage vector candidates
for k = 1:3

    %current prediction
    i1_p(k) = (1+Ts/(1-Lm*Lm/L1/L2)*L1/(R1+R2*Lm/L2*Lm/L2))*i1
+Ts/((1-Lm*Lm/L1/L2)*L1/(R1+R2*Lm/L2*Lm/L2)+Ts)*(1/(R1+R2*Lm/L2*Lm/L2)
*((Lm/L2/L2/R2-Lm/L2*1j*Pp*speed)*psi_r+v1(k)));

    %Stator flux prediction
    psi1_p(k) = psi1 + Ts*v1(k) - R1*Ts*(i1);

    %Torque prediction
    T_p(k) = real(3/2*sqrt(3)*Pp*(real(psi1_p(k))*imag(i1_p(k)) -
imag(psi1_p(k))*real(i1_p(k))));

end
```

DC-link voltage optimization method – cost function

```
function [vector] = fcn(psi1_p, T_p, psi1_ref, T_ref, k)

%Calculate Cost Function
g = k*abs(abs(psi1_p)-psi1_ref) + abs(T_p - T_ref);

[~, v] = min(g);              %Choose minimum
vectors = [0 -1 1];           %Commands for the integrator, the order
is the same as in the prediction
vector = vectors(v);          %Output the chosen command
```